Study of Oxygenases Structure and Function Relation



A thesis submitted to the Board of the Faculty of Mathematical, Physical & Life Sciences in partial fulfilment of the requirements for the degree of Doctor of Philosophy at the University of Oxford

Mohammadparsa Jabbary

Linacre College

Hillary term 2025



Study of Oxygenases Structure and Function Relation

Mohammadparsa Jabbary
Linacre College, University of Oxford

DPhil thesis
Hillary term 2025

Summary

This thesis concerns experimental studies on two structurally related $Fe^{(II)}$-utilizing oxidizing enzymes – isopenicillin N synthase (IPNS) which catalyzes the key ring forming steps in the microbial biosynthesis of the penicillin antibiotics and γ-butyrobetaine hydroxylase (BBOX) which catalyzes the final step in the biosynthesis of L-carnitine, a molecule vital in lipid metabolism. Chapter 1 gives an introduction to $Fe^{(II)}$-utilizing oxidizing enzymes, then summarizes relevant previous studies on IPNS and BBOX. Chapter 2 describes methods for the optimized production of IPNS including in labelled form. Chapter 3 describes studies on IPNS mutants designed to disrupt the substrate binding mode and/or conformational changes during catalysis. A striking outcome of the work was the discovery of a new mode of action for IPNS, giving a product isomeric with isopenicillin N. The use of NMR spectroscopy was a unifying theme in terms of analytical studies carried out, that is protein observed NMR as described in Chapter 2 and small-molecule NMR as described in Chapter 3, where NMR studies were essential for assignment of unanticipated product structures. Further, as described in Chapter 4, NMR was used to inform on inhibitor binding to BBOX and mechanism of action. Chapter 5 provides a summary of the work and suggests avenues for future research.

Acknowledgements

I hereby take this opportunity to express my gratitude to Professor Cristopher J. Schofield for the great opportunity to pursue my DPhil under his supervision. His unwavering support throughout my DPhil studies has been substantially helpful in my academic journey. Working in his lab has been a truly rewarding experience, offering numerous opportunities for scientific exploration.

I am also deeply thankful to Professor Timothy D. W. Claridge for his guidance and support in NMR techniques, which have greatly enriched my research.

I would like to thank Dr. Patrick Rabe, for his daily supervision in the lab. His exceptional support in developing my laboratory skills and his intellectual guidance on my research projects have been invaluable. I have thoroughly enjoyed learning from and collaborating with him.

I would like to thank Dr. Eidarus Salah and Dr. Shyam Basak for their assistance and support on the BBOX project, which allowed me to explore working on other enzymes structurally relevant to IPNS.

Finally, I would like to thank Professor Christopher J. Schofield and Dr. Patrick Rabe for their meticulous proofreading of my thesis and their ongoing comprehensive support throughout this process.

Declaration and Author Contributions

I declare that I carried out all of the work described in this thesis, except the following works:

Chapter 3:

- The cysteinyl ^{13}C-^{15}N labelled ACV was prepared by Dr. Patrick Rabe and Dr. Shyam Basak.
- The crystallography studies on S281A_IPNS, S281C_IPNS, and Q280A_L282A IPNS were carried out by Dr. Patrick Rabe, including crystal and data collection as well as structure refinements.
- The antibiotic assay on the S281A_IPNS turnover product was carried out by Dr. Karina Calvopina Tapia.

Chapter 4:

- All BBOX inhibitors stated in Chapter 4 were prepared by Dr. Shyam Basak.
- The recombinant human BBOX was prepared by Dr. Eidarus Salah.

Table of Contents

Abbreviations viii

Chapter 1: Introduction 1

1.1 Oxygenases 1

1.2 β-Lactam Antibiotics 3

1.3 Overview of β-Lactam Biosynthesis 3

1.4 Isopenicillin N Synthase (IPNS) 7

1.5 Reactions of Isopenicillin N Synthase with Substrate Analogues 11

1.6 Isopenicillin N Synthase Mechanism 15

1.7 Isopenicillin N Synthase from Different Species 16

1.8 L-Carnitine Biosynthesis by γ-Butyrobetaine Hydroxylase (BBOX) 17

1.9 Other Human 2OG Dependent Oxygenases 19

1.10 Mechanism of 2OG Dependent Oxygenases 21

1.11 Importance of Second Shell Residues in Oxygenases 22

1.12 Objectives of the Work Described in this Thesis 23

1.13 References 25

Chapter 2: Expression of Labelled IPNS for NMR Spectra Peak Assignment 32

2.1 Introduction 32

2.1.1 Protein 2-D NMR Spectroscopy 32

2.1.2 Preparation of Labelled Proteins Using Minimal Medium 33

2.2 Results and Discussion 36

2.2.1 Optimizing Production of Recombinant IPNS 36

2.2.2 Expression and Purification of ^{15}N Labelled IPNS 40

2.2.3 ^{1}H-^{15}N HSQC Spectra of IPNS 42

2.2.4 Examining IPNS Melting Temperature (T_m) 47

2.2.5 Second Batch of ^{15}N Labelled IPNS ^{1}H-^{15}N HSQC Spectra 50

2.2.6 Expression and Purification of Per-deuterated ^{15}N labelled IPNS 54

2.2.7 Effect of IPNS Per-deuteration on TROSY-Type ^{1}H-^{15}N HSQC Spectra 56

2.2.8 Production of Per-deuterated ^{13}C-^{15}N Labelled IPNS 58
2.2.9 Conclusion 59
2.3 Methods 61
2.3.1 Expression Trials of IPNS in Different Media 61
2.3.2 Small-Scale IPNS Purification 62
2.3.3 Large-Scale Purification of ^{15}N Labelled IPNS 63
2.3.4 IPNS NMR Studies 65
2.3.5 IPNS Thermal Stability Assays 66
2.4 References 67

Chapter 3: Isopenicillin N Synthase (IPNS) – A New Mode of Reactivity 70

3.1 Introduction 70
3.1.1 Key Interactions in the IPNS Active Site 70
3.1.2 Role of Ser_{281} in IPNS Mechanism 71
3.1.3 Observed Correlated Motions Through IPNS Structure in Catalysis 72
3.2 Results and Discussion 73
3.2.1 Mutations of Key Residues Involved in IPNS Dynamics 73
3.2.2 Expression and Purification of IPNS Mutants 73
3.2.3 Monitoring Turnover of WT and S281A_IPNS Using ^{1}H NMR and LC-MS 80
3.2.4 Purification of the S281A_IPNS Turnover Product with m/z=608.16 85
3.2.5 Purification of the S281A_IPNS Turnover Product with m/z=360.12 89
3.2.6 Turnover of Cysteinyl ^{13}C-^{15}N Labelled ACV with S281A_IPNS 93
3.2.7 Turnover of S281A_IPNS Using ^{18}O Isotope 100
3.2.8 Other Mutants of IPNS Giving the New Product 102
3.2.9 Examining S281T_IPNS Selectivity 108
3.2.10 Monitoring Possible Intermediates in S281T_IPNS Turnover 112
3.2.11 Treatment of the Thiazole Product With TCEP 117
3.2.12 Addition of TCEP to the Midpoint of S281T_IPNS Turnover 119
3.2.13 Formation of Thiazole and Oxazole Rings in Biological Processes 122
3.2.14 Proposed Mechanism of Formation of the Product with a Thiazole Ring 123
3.2.15 Antibiotic Activity Testing of the New Product 125

3.2.16 Examining The Role of Q280A_L282A Mutation on Transforming Active Site Dynamics to the Surface α-3 Helix 126
3.2.17 Crystallography Studies on IPNS Mutants 132
3.2.18 Conclusion 140
3.3 Methods 141
3.3.1 Preparation of ACV Substrate 141
3.3.2 Mutation of pCOLD_IPNS 141
3.3.3 Expression and Purification of IPNS Mutants 142
3.3.4 Preparation of BTFA Tagged S55C_Q280A_L282A IPNS 144
3.3.5 NMR Studies on IPNS Mutants 145
3.3.6 LC-MS Studies on IPNS Mutants Catalysis 147
3.3.7 Preparation and Isolation of S281A_IPNS Turnover Products 147
3.3.8 Turnover Experiments in D_2O 148
3.3.9 ^{18}O Isotope Studies 148
3.4 References 150
3.5 Appendix 3.I 153

Chapter 4: NMR Studies on γ-Butyrobetaine Hydroxylase 154

4.1 Introduction 154
4.1.1 γ-Butyrobetaine Hydroxylase 154
4.1.2 Examining Protein-Ligand Binding Using NMR Spectroscopy 156
4.2 Results and Discussion 157
4.2.1 BBOX Inhibitor Turnover Studies 157
4.2.2 BBOX Inhibitor Protein Binding Assay 159
4.2.3 Examining the Binding Mode of SB_133 165
4.2.4 Conclusion 168
4.3 Methods 169
4.3.1 Expression and Purification of Pseudomonas BBOX 169
4.3.2 BBOX NMR Studies 171
4.4 References 172
4.5 Appendix 4.I 175

4.6 Appendix 4.II 176

Chapter 5: Summary of Results and Suggestions for Future Work 177

5.1 Summary of Experiments in Chapter 2 and Future Work 177
5.2 Summary of Experiments in Chapter 3 178
5.3 Summary of Experiments in Chapter 4 182
5.4 References 184

Abbreviations

1D	1-dimensional
2D	2-dimensional
2OG	2-oxoglutarate
2YT	2 x tryptone / yeast extract
A[3-D_2]CV	L-α-(aminoadipoyl)-L-3,3-[D_2]-cysteinyl-D-valine
AC[3-D]V	L-α-(aminoadipoyl)-L-cysteinyl-D-3-[D]-valine
ACA	L-α-(aminoadipoyl)-L-cysteinyl-D-alanine
ACG	L-α-(aminoadipoyl)-L-cysteinyl-glycine
ACV	L-α-(aminoadipoyl)-L-cysteinyl-D-valine
ACVS	L-α-(aminoadipoyl)-L-cysteinyl-D-valine synthetase
AspH	asparaginyl / aspartyl hydroxylase
BBOX	γ-butyrobetaine hydroxylase
BLAs	β-lactam antibiotics
BLAST	basic local alignment search tool
BTFA	1-bromo-3,3,3-trifluoroacetone
COSY	correlated spectroscopy
CAR	L-carnitine
CPMG	carr-purcell-meibom-gill
CSA	chemical shift anisotropy
CV	column volume
Da	Dalton
DAAA	D-α-aminoadipoyl
DAC	deacetylcephalosporin C
DAOC	deacetoxycephalosporin C
DAOCS	deacetoxycephalosporin C synthase
DD	dipole-dipole
DMSO	dimethyl sulfoxide
DNA	deoxyribonucleic acid
Et	ethyl
eq.	equivalent

FIH	hypoxia-inducible factor asparagine hydroxylase
GBB	γ-butyrobetaine
h-BBOX	human γ-butyrobetaine hydroxylase
HIF	hypoxia-inducible factor
HMBC	heteronuclear multiple bond correlation
HPLC	high-performance liquid chromatography
HSQC	heteronuclear single quantum coherence
HTML	N^{ε}-trimethyl -2-hydroxy-L-lysine
INEPT	insensitive nuclei enhancement by polarization transfer
IPN	isopenicillin N
IPNS	isopenicillin N synthase
IPTG	isopropyl β-D-1-thiogalactopyranoside
JmjC	jomonji C
KDM	histone lysine demethylase
LAAA	L-α-aminoadypoyl
LC	liquid chromatography
Me	methyl
MS	mass spectrometry
N-OG	N-oxalylglycine
NAD^+	nicotinamide adenine dinucleotide
NADH	nicotinamide adenine dinucleotide + hydrogen
NIH	National Institute of Health
NMR	nuclear magnetic resonance
PAGE	polyacrylamide gel electrophoresis
PCR	polymerase chain reaction
PenN	penicillin N
ps-BBOX	pseudomonas γ-butyrobetaine hydroxylase
RFU	relative fluorescence units
RMSD	root mean square deviation
RNA	ribonucleic acid
SDS	sodium dodecyl sulfate

STD	saturation transfer difference
TB	terrific broth
TCEP	tris(2-carboxyethyl)phosphine
TET	Ten-Eleven Translocation subfamily
T_m	temperature of melting
TMABA	N^{δ}-trimethylaminobutyraldehyde
TML	N^{ε}-trimethyl-L-lysine
TMLH	N^{ε}-trimethyl-L-lysine hydroxylase
Tris	tris(hydroxymethyl)aminomethane
TROSY	transverse relaxation optimized spectroscopy
WaterLOGSY	water–ligand observed via gradient spectroscopy
WT	wildtype

Chapter 1: Introduction

1.1: Oxygenases

Oxygenases and oxidases are a wide group of enzymes that catalyze oxidation reactions using dioxygen (O_2) [1-3]. Oxygenases catalyze the transfer of one or two oxygen atoms from O_2 to their substrates(s); by contrast oxidases catalyze substrate oxidation (e.g. desaturation) without direct incorporation of oxygen from O_2 [1-3]. Both oxygenase and oxidase enzymes use the oxidative power of O_2 in catalysis [4]. A large set of oxygenases (and oxidases) are dependent on non-heme iron ions, that is their catalysis requires $Fe^{(II)}$ or $Fe^{(III)}$ as cofactors without the need for a prosthetic group [1,2]. With many non-heme oxygenases, $Fe^{(II)}$ is bound reversibly to the active site via coordination of two histidine residues and one aspartate/glutamate residue, an arrangement known as the 2-His-1-carboxylate facial triad [5,6] (Figure 1.1 a). The facial triad motif is common in $Fe^{(II)}$ dependent oxygenases and oxidases, with exceptions being the 2-oxoglutarate (2OG) dependent halogenases and aspartyl- / asparaginyl-hydroxylase, both of which employ only two histidine residues from the enzyme to chelate $Fe^{(II)}$ [7].In the 2OG dependent structural family of oxygenases, the facial triad is supported by a distorted double-stranded β-helix core fold, also known as a jelly-roll, cupin or jumonji C fold [8,9].

Oxygenases and oxidases can be subdivided into two categories, depending on whether 2OG is used for catalysis, with the majority being 2OG dependent [3], though some 2OG oxygenases can employ 2-oxo acids other than 2OG [10]. In the case of 2OG oxygenase dependent catalysis, the 2OG co-substrate undergoes oxidative decarboxylation giving succinate, and CO_2, with one oxygen atom from O_2 being incorporated into succinate [3]. In a typical 2OG oxygenase catalyzed hydroxylation reaction, the other oxygen atom from O_2 is incorporated into the alcohol product, although exchange with water has been observed in some cases (Figure 1.1 b) [11,12].

2OG oxygenase activity was first observed in 1960s in pioneering studies on the biosynthesis of hydroxylated-proteins during collagen production [13]. Work over subsequent decades has revealed 2OG oxygenases and structurally related oxygenases

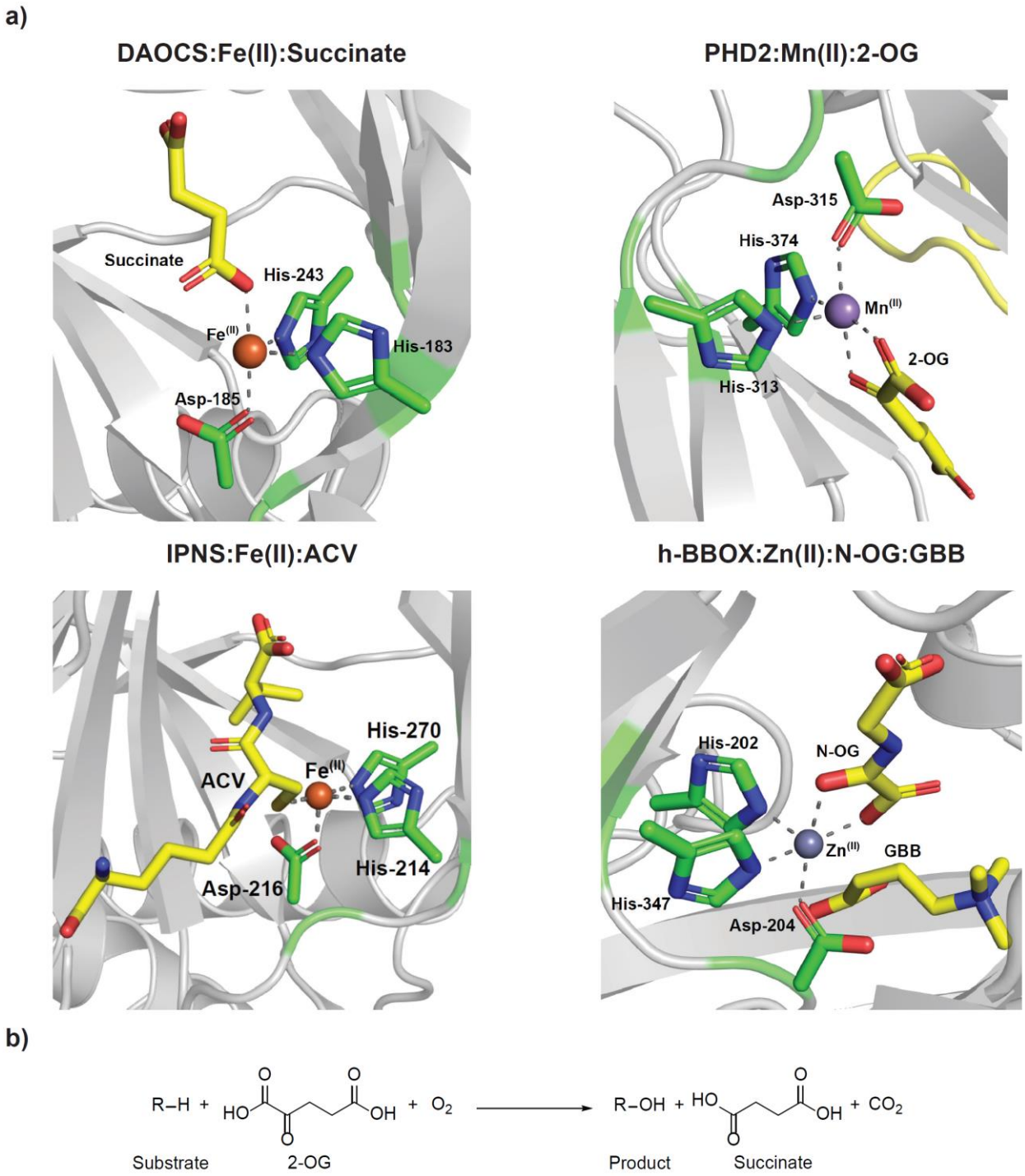


Figure 1.1: The 2-his-1-carboxylate facial triad in oxygenase and oxidase enzymes. **(a)** Crystal structure views from deacetoxycephalosporin C synthase (DAOCS) (PDB ID: 1UO9), human prolyl hydroxylase domain isoform 2 (PHD2) (PDB ID: 6YW1), isopenicillin N synthase (IPNS) (PDB ID: 6ZAE) and human gamma butyrobetaine hydroxylse (h-BBOX) (PDB ID:3O2G) are shown. **(b)** Stoichiometry of a typical reaction catalyzed by 2OG dependent oxygenases.

are widely distributed across most of biology. They catalyse reactions in secondary metabolite / antibiotic biosynthesis, multiple modifications to lipids, proteins, small-molecules and nucleic acids [14]. They have biological roles in important processes including lipid metabolism, hypoxia sensing, nucleic acid damage repair, signaling pathways in plants and, as described below, in likely the most important class of antibiotics yet discovered, that is the penicillins and other β-lactams [14].

1.2: β-Lactam Antibiotics

The β-lactam containing antibiotics (BLAs) are one of the most important and frequently used classes of antibiotics, all of which bear the four-membered β-lactam ring [15]. The structures of the major subfamilies of various β-lactam antibiotics are shown in Figure 1.2 a [15]. The common mechanism of action for BLAs is to disturb bacterial cell wall biosynthesis through inhibiting transpeptidases leading to bacterial cytolysis [15-17]. The transpeptidases catalyze cross-linking of linear peptidoglycan chains (peptidoglycan cross linking) through formation of a new peptide bond, a process essential in bacterial cell wall biosynthesis (Figure 1.2 b) [15-17]. The reactive and electrophilic nature of the β-lactam rings enables BLAs to bind to the transpeptidases and covalently react with the nucleophilic serine at their active sites to form a relatively stable acyl-enzyme complex (Figure 1.2 c) [18-20].

Many β-lactam antibiotics, including all clinically used penicillins and cephalosporins, are obtained either via isolation from fermentation mixtures, or by modification of isolated fermentation products [15]. The chemical synthesis of β-lactam antibiotics is challenging, in part because of the high level of enantioselectivity required and the density of their functionalization, and also because the β-lactam rings are relatively unstable compared to normal amides [15,21].

1.3: Overview of β-Lactam Biosynthesis

The biosynthetic pathway leading to the formation of penicillin, cephalosporin, cephamycin, and cephabacins in fungi and bacteria is shown in Figure 1.3 [11,15,22-24]. A key step in the biosynthetic pathway of penicillin antibiotics is the formation of a bicyclic product, isopenicillin N (IPN), which is a precursor to all naturally occurring penicillin- and

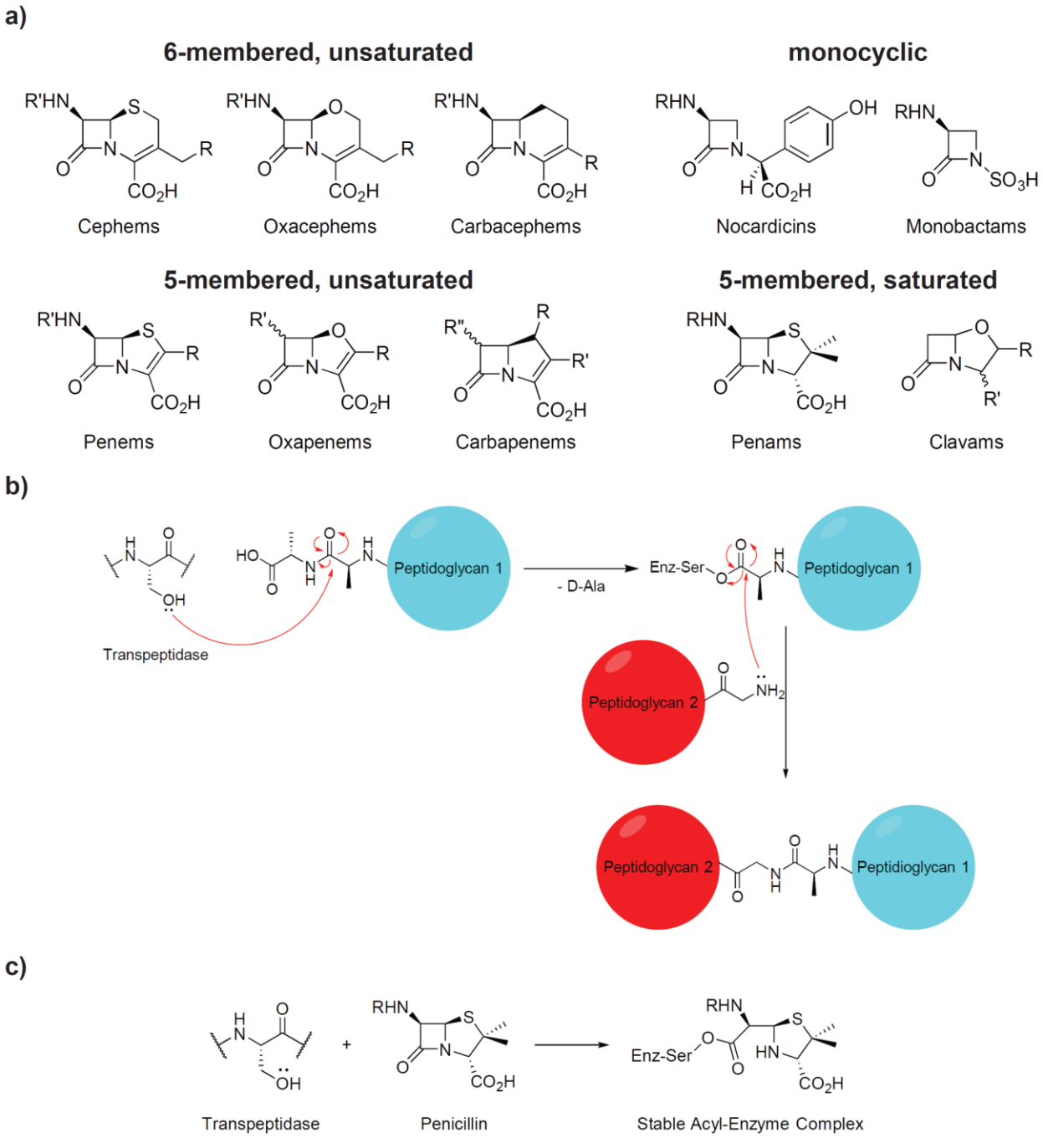


Figure 1.2: **(a)** Different sub-families of β-lactam antibiotics, adopted from reference [15]. **(b)** The transpeptidase activity to cross link peptidoglycans via peptide bond formation. **(c)** Inhibition of transpeptidase enzyme via stable acyl-enzyme complex formation occurs with β-lactam antibiotics. The figure was adapted from reference [15].

cephalosporin-derived antibiotics (Figure 1.3). IPN bears a β-lactam ring fused to a saturated five-membered thiazolidine ring and is not a potent broad-spectrum antibiotic; however, structural modifications of IPN forms modified penicillins, cephalosporins, cephamycins and cephabacins, which are powerful antibiotics (Figure 1.3) [15].

In the committed step of penicillin and cephalosporin biosynthesis, a tripeptide, L-α-aminoadipoyl)-L-cysteinyl-D-valine (ACV), is formed via assembly of L-α-aminoadipic acid, L-cysteine, and L-valine [23,24]. The ACV formation reaction is catalyzed by a multidomain non-ribosomal peptide synthetase enzyme, ACV synthetase (ACVS); during formation of ACV the stereochemistry of the L-valine precursor is inverted to the D-stereochemistry as observed in ACV [23,24].

Isopenicillin N synthase (IPNS) converts the ACV to give IPN, in a 4-electron oxidation reaction, involving two CH bond cleaving reactions to form a conformationally strained bicyclic structure through an oxidative-cyclization process (Figure 1.3) [11,12,15]. IPNS is a non-heme iron(II) dependent oxidase belonging to the 2OG oxygenase structural family, but which is 2OG independent [11,12,15]. In some fungi, IPN can subsequently undergo deacylation to form 6-aminopenicillanic acid (6-APA) which then undergoes reacylation to form penicillin G or related penicillins with hydrophobic side chains (as observed in some fungi). Alternatively, in bacteria and some fungi IPN can undergo epimerization to form penicillin N, which is a precursor to the cephalosporins (Figure 1.3) [15].

The first step in the cephalosporin biosynthesis pathway is expansion of the 5-membered ring of penicillin N to form deacetoxycephalosporin C (DAOC) [15], in a reaction catalyzed in bacteria by deacetoxycephalosporin C synthase (DAOCS) which is a 2OG dependent oxygenase. The product, DAOC, is hydroxylated by another bacterial 2OG dependent oxygenase, DAOC hydroxylase (DACS), to form deacetylcephalosporin C (Figure 1.3) [15]. In fungi a single bifunctional enzyme catalyzes both the ring expansion and hydroxylation reactions [25]. DAC is a precursor to cephalosporin C, cephamycin C, and the cephabacins (Figure 1.3) [15].

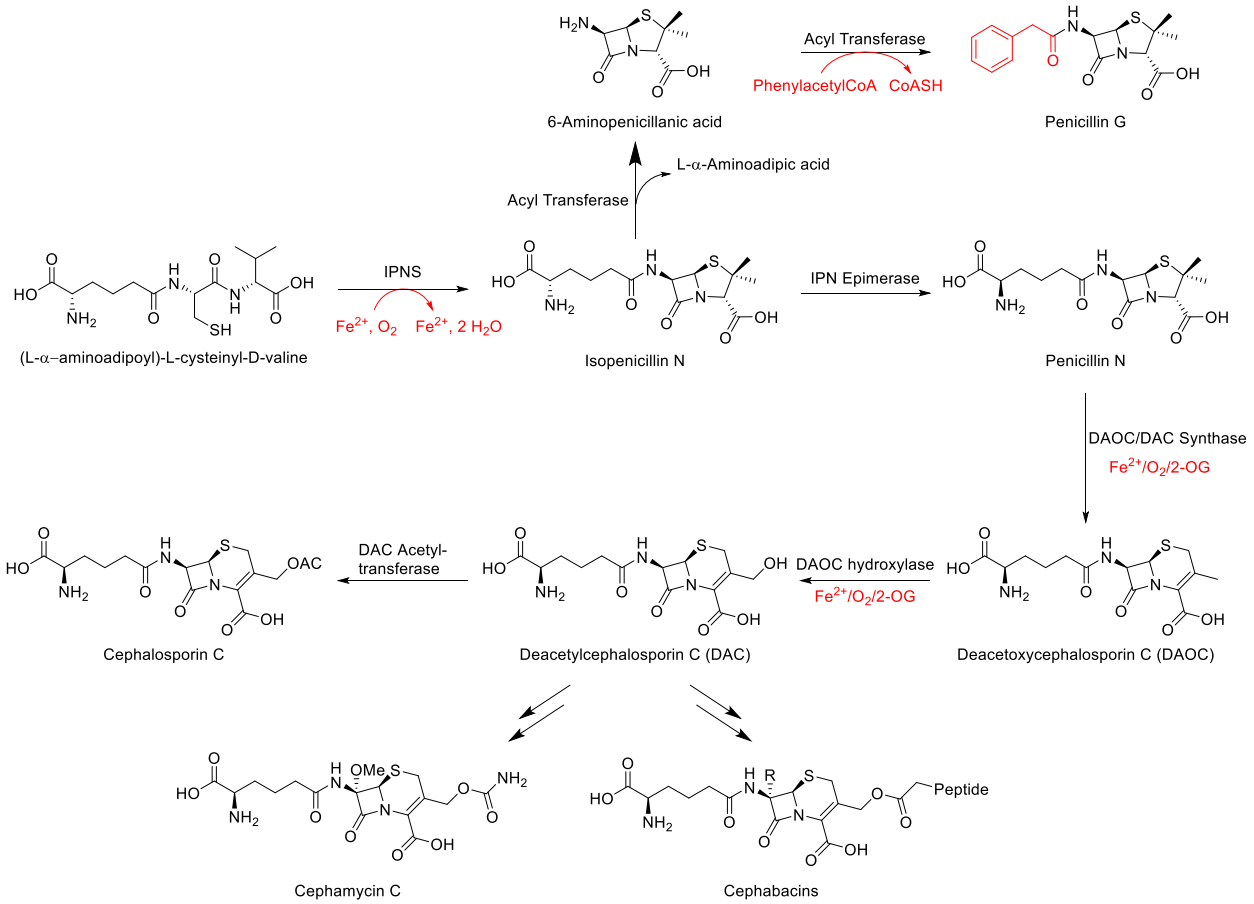


Figure 1.3: Key steps in the biosynthesis of penicillin and cephalosporin antibiotics in fungi and bacteria. Selected co-substrates / co-factors are shown in red. The scheme was adopted from reference [15].

Whereas the conversion of DAOC to DAC is a typical 2OG oxygenase catalyzed hydroxylation reaction, the rearrangement of penicillin N to form DAOC is an unusual enzyme catalyzed reaction, likely proceeding via a monocyclic intermediate. Figure 1.4 shows an outline mechanism for the DAOCS catalyzed ring expansion of the penicillin N five-membered ring to the six-membered ring [26]. The reaction begins with 2OG and penicillin N binding to the active site (in ternary complex mechanism), with 2OG substituting for two water molecules via bidentate coordination to $Fe^{(II)}$. Subsequently, after O_2 binding, 2OG undergoes oxidative decarboxylation to form succinate and CO_2 with $Fe^{(II)}$ being converted into an $Fe^{(IV)}$=O (ferroxo) species. Formation of a $Fe^{(IV)}$=O intermediate is proposed to be common in reactions catalyzed by 2OG dependent oxygenases and related oxidases, including IPNS. The $Fe^{(IV)}$=O species abstracts a hydrogen from one of penicillin N methyl groups forming a free radical with concomitant

reduction of the iron to $Fe^{(III)}$. The free radical on penicillin N undergoes ring expansion / rearrangement forming a six membered ring followed by a second hydrogen abstraction from the $Fe^{(III)}$-OH species to give the alkene of DAOC.

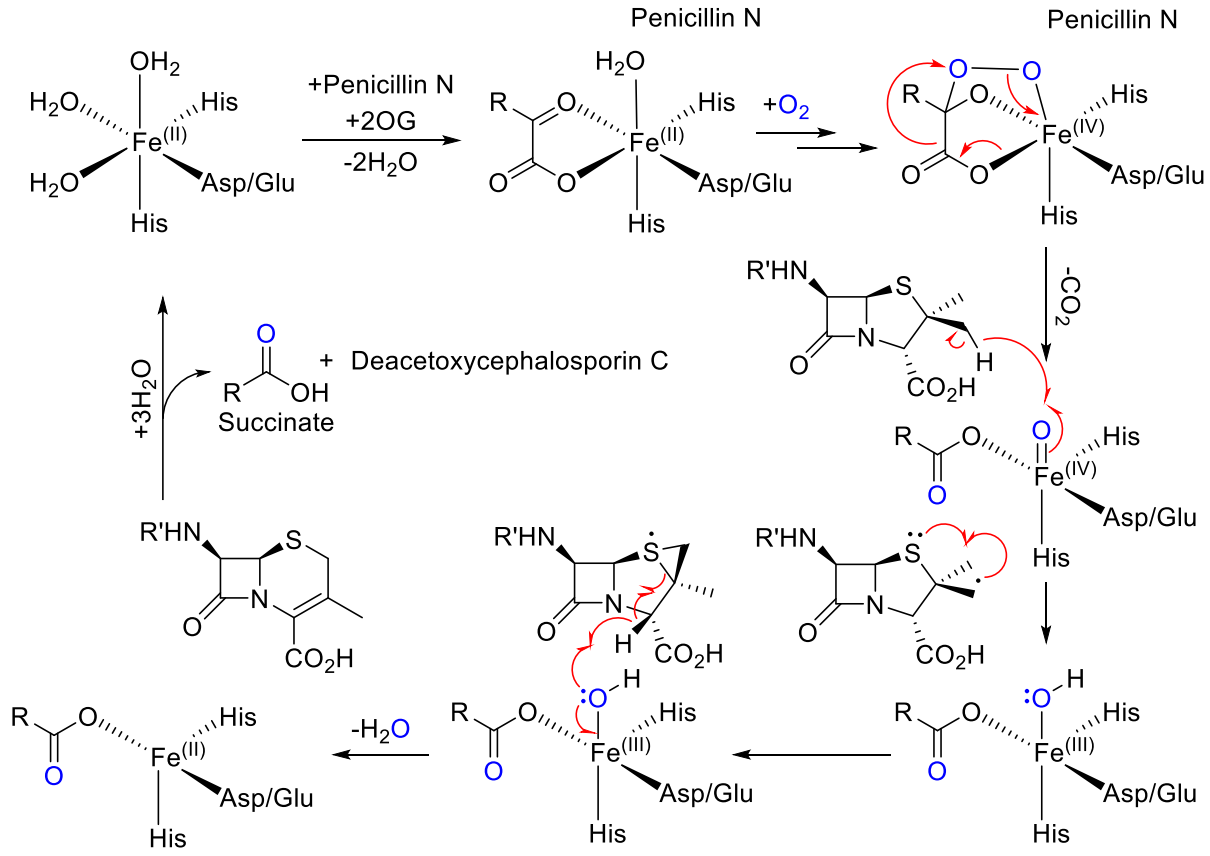


Figure 1.4: The proposed ternary complex mechanism for DAOCS enzyme, converting isopenicillin N and 2OG into deacetoxycephalosporin C, succinate, and CO_2. The oxygen atoms from dioxygen are coloured blue. The scheme was adopted from reference [26].

1.4: Isopenicillin N Synthase (IPNS)

As explained in Section 1.3, IPNS catalyzes the formation of IPN via the 4-electron oxidation of ACV in a process coupled with the reduction of O_2 into two H_2O molecules [9-11]. The oxidized disulfide form of ACV, which is dimerized through disulfide bond formation, does not react with IPNS, hence the activity of IPNS is elevated in the presence of reducing agents, that help maintain the thiol form of ACV, such as tris-(2-carboxyethyl)phosphine (TCEP) [15,27]. Although IPNS does not require 2OG [11,12-15],

its overall structure is similar to those of 2-OG dependent oxygenases (and oxidases), including the structures of DAOCS and DACS [28].

A crystal structure of IPNS was first solved in complex with $Mn^{(II)}$, used in order to prevent $Fe^{(II)}$ mediated catalysis [12]. Subsequently, IPNS was crystallized in complex with $Fe^{(II)}$ and ACV (IPNS:$Fe^{(II)}$:ACV) under anaerobic conditions, giving a structure revealing valuable information about the active conformation of the IPNS structure, the ACV binding mode, and the IPNS reaction mechanism [29]. The IPNS structures revealed a distorted double 8-stranded β-helix (jelly-roll) core as observed in all studied 2OG dependent oxygenases [12,15,28,29]. Similar to most 2-OG dependent oxygenases, IPNS binds to $Fe^{(II)}$ via a 2-histidine-1-carboxilate facial triad, involving His_{214}, His_{270}, and Asp_{216}. The overall structures of IPNS and DAOCS are similar as shown in Figure 1.5.

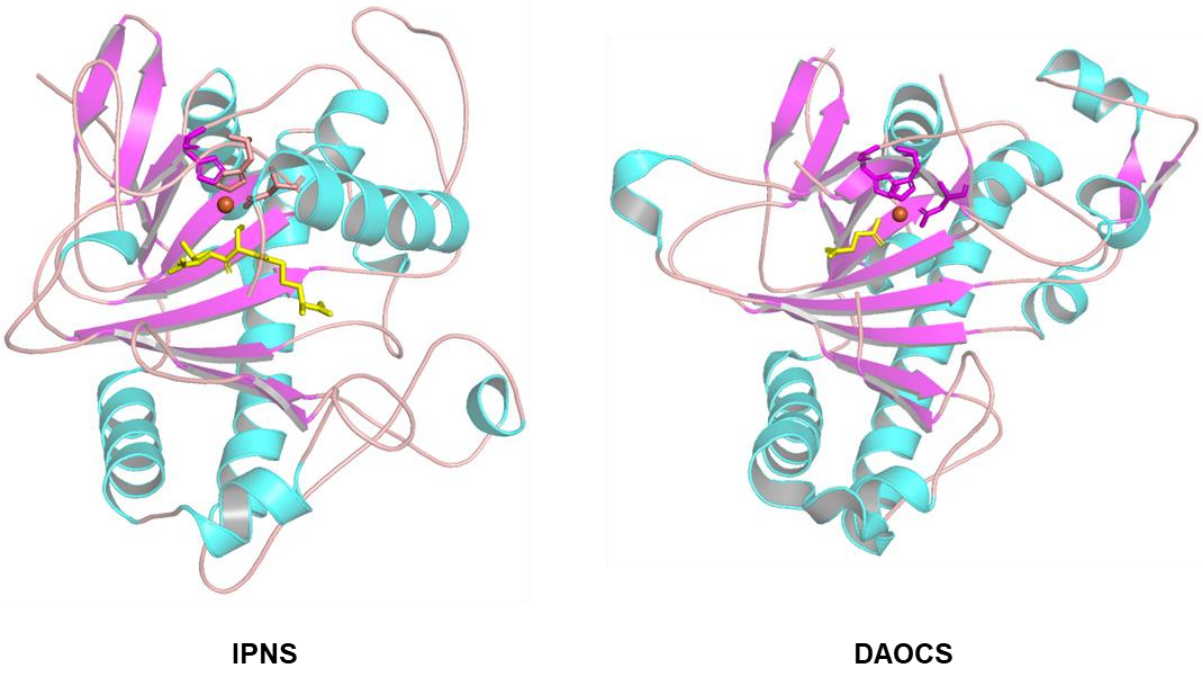


Figure 1.5: Global structural views of IPNS (from IPNS:$Fe^{(II)}$:ACV:NO complex, PDB ID : 1BLZ) and DAOCS (from DAOCS:$Fe^{(II)}$:Succinate complex, PDB ID : 1UO9). Cα backbone RMSD: 2.50 $Å^2$.

The IPNS core jelly-roll fold is comprised of 8 β-strands forming two structurally twisted β-sheets each containing four anti parallel β-strands (Figure 1.6) [12,15,30]. The IPNS active site lies in between two β-sheet layers with the Fe bound via coordination of His_{214}, His_{270}, and Asp_{216} (Figure 1.6). The rest of IPNS structure includes surface α-

helices covering the jelly-roll core, with the C-terminal α-helix lying between two jelly-roll layers [12,15,30].

When IPNS is in its resting state, the C-terminal α-helix interacts with the metal via Gln_{330} coordination, as shown in in the crystal structure of the IPNS:$Mn^{(II)}$ complex (Figure 1.6 a). Binding of the substrate, ACV, displaces Gln_{330} (and, in part, the C-terminal α-helix) and the ACV cysteinyl thiol coordinates the metal; as shown in the anaerobic crystal structure of the IPNS:$Fe^{(II)}$:ACV complex (Figure 1.6 b). In the presence of ACV, the C-terminal α-helix is bound to the active site including via a H-bond interaction of the Thr_{331} side chain hydroxyl with two bridging H_2O molecules which interact with the ACV L-α-aminoadipoyl carbonyl group via a H-bond (Figure 1.6 c). This water bridging interaction may stabilize the C-terminal α-helix in a position close to the active site. It is proposed that the C-terminus thus hinders the approach of other ACV molecules into the active site leading to formation of dimeric ACV during catalysis [31].

The ACV binding mode observed in the crystal structure of anaerobic IPNS:$Fe^{(II)}$:ACV complex (PDB ID: 6ZAE) is shown in Figure 1.7. The metal is coordinated by two histidine residues, one aspartate residue, the ACV thiol and one water molecule forming a square-pyramidal coordination geometry (Figure 1.7). The ACV valine isopropyl group is close to the sixth coordination site, which is where the dioxygen binds. It was observed that reaction with O_2 results in movement of the ACV isopropyl group to enable O_2 binding [30].

Recent comprehensive time-resolved crystallographic and NMR studies have shown that conformational changes involving ACV oxidation during catalysis correlate with motions extending through large parts of the IPNS structure [30,32]. The ACV valine carboxylate is positioned to form two H-bonds with Ser_{281} and Tyr_{189}, and a H_2O molecule is positioned to form bridging H-bond interactions with the ACV valine carboxylate, Arg_{279}, and Asn_{230}. The L-α-aminoadipoyl (LAAA) group is positioned to form H-bonds with Arg_{87} and Tyr_{91} and to make a hydrophobic interaction with Phe_{285} (Figure 1.7). A hydrophobic interaction between Leu_{223} and the ACV valine isopropyl group was observed. The aforementioned H-bond interactions along with the thiol coordination could, in part, be

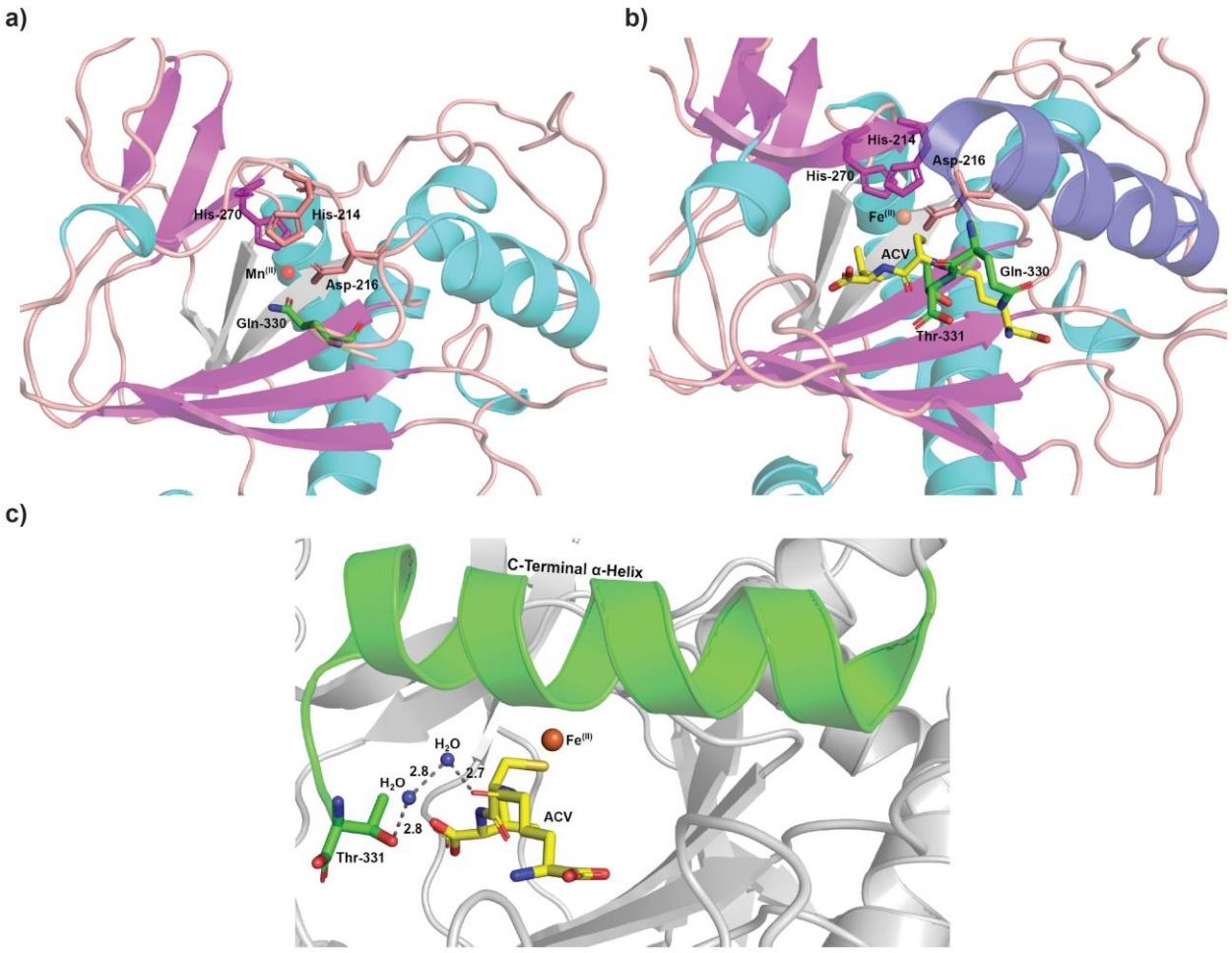


Figure 1.6: Views of the IPNS active site and the jelly-roll motif from: **(a)** a crystal structure of IPNS:$Mn^{(II)}$ complex (PDB ID: 1IPS), and **(b)** a crystal structure of the anaerobic IPNS:$Fe^{(II)}$:ACV complex (PDB ID: 6ZAE). The jelly-roll β-strands are in magenta. **(c)** The C-terminal α-helix in the structure of IPNS:$Fe^{(II)}$:ACV showing an interaction between Thr_{331} and ACV via a two-water bridge.

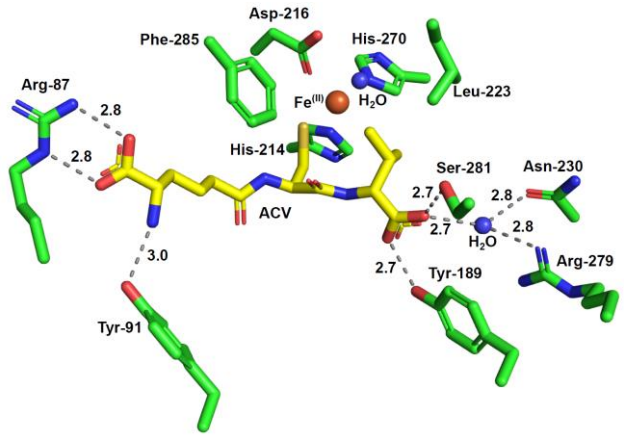


Figure 1.7: The metal coordination and ACV binding mode as observed in the anaerobic IPNS:$Fe^{(II)}$:ACV complex (PDB ID: 6ZAE), showing interactions with key residues of IPNS.

responsible for the extended conformation of ACV, which is essential for IPNS catalyzed oxidation to form IPN [33].

1.5: Reactions of Isopenicillin N Synthase with Substrate Analogues

There have been numerous studies studying on the reactions of ACV analogues with IPNS, a few of these which are relevant to the work described in Chapter 3 are described here. The ACV analogues can be classified as L-α-aminoadipoyl (LAAA), L-cysteinyl, and D-valine substitutes [15]. Substituting LAAA for a D-α-aminoadipoyl (DAAA) side chain led to the formation of penicillin N, an epimer of IPN (Figure 1.8 a) [34]. Other substitutions of the LAAA group showed similar reactions forming the penicillin core. The substitutions of the LAAA group with benzoyl and phenylacetyl side chains are shown examples (Figure 1.8 a), with the latter reaction formed penicillin G in a single step [34].

Studies using ACV selectively deuterated at the cysteinyl C-3 position have informed on the stereoselectivity of IPNS [34]; that is, only *pro-S* C-3 hydrogen of the ACV cysteine is removed during IPNS catalysis (Figure 1.8 b). Other pioneering mechanistic studies demonstrated that the ACV cysteinyl C3-H bond is cleaved before the valine C3-H bond, in support of a monocyclic intermediate being formed which subsequently converts into bicyclic IPN [35,36]. Thus, kinetic experiments in which the ACV cysteinyl C-β was doubly deuterated (L-α-aminoadipoyl-L-3,3-[D_2]-cysteinyl-D-valine) and ACV with valine C-β deuterated (L-α-aminoadipoyl-L-cysteinyl-D-3-[D]-valine) were conducted; the reaction was quenched and derivatized (via ester formation) [34]. The isolated reaction products of A[3-D_2]CV and AV[3-D]V were the penicilloate derivatives, likely due to hydrolysis during derivatization (Figure 1.8 c) [35]. A slower consumption rate for A[3-D_2]CV and similar consumption rate for AC[3-D]V depletion was observed compared to unlabelled ACV, indicating that cysteinyl oxidation and β-lactam ring formation occurs prior to ACV valine / thiazolidine ring formation in the IPNS reaction and that the cysteinyl CH cleavage step is rate-limiting [35]. Following the kinetic studies, a mechanism was proposed involving monocyclic intermediate formation during IPNS catalysis (Figure 1.8 d) [35].

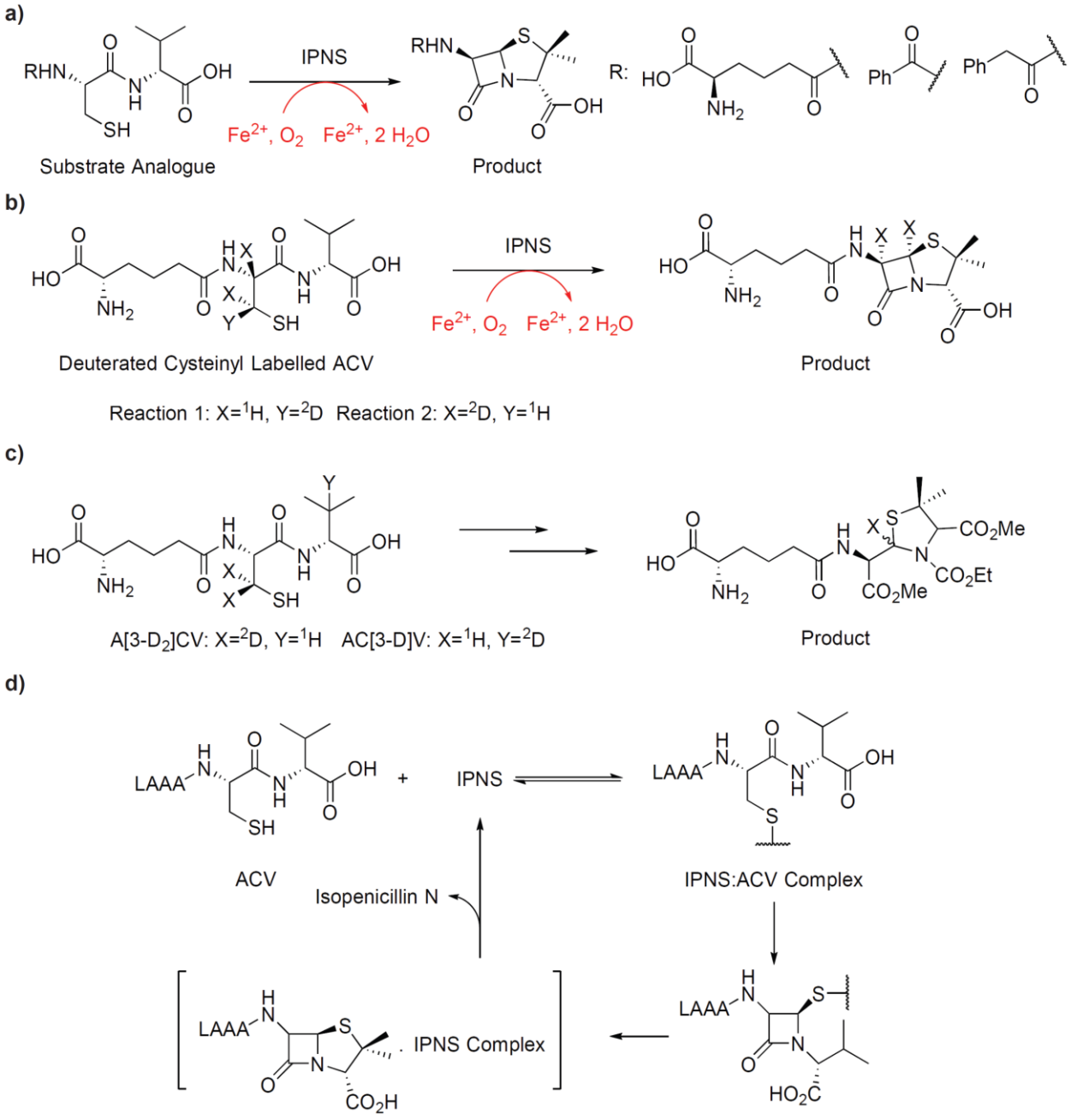


Figure 1.8: Reaction of IPNS with ACV analogues, including **(a)** L-α-aminoadipoyl modified, **(b)** cysteinyl deuterated at C-α and C-β positions, and **(c)** Cysteinyl and valinyl C-β deuterated [34,35]. **(d)** Early proposed mechanism of IPNS forming monocyclic intermediate, adopted from reference [35].

Many substrate analogue studies in which the ACV valine was replaced have been carried out. In one interesting study the ACV cysteinyl and valine residues were replaced with L-homocysteine and D-cysteine, respectively [37,38]. The reaction of L-α-aminoadipoyl-L-homocysteinyl-D-cysteine showed formation of γ-lactam ring fused to a five membered disulfide linked ring (Figure 1.9 a) [37,38]. Substitution of cysteinyl residue of ACV with L-3,3-difluorohomocysteine showed a different, but related 4-electron oxidation reaction with IPNS: no ring product was formed, but the difluorohomocysteine group was oxidized at C-4 position forming a thiocarboxylic acid (Figure 1.9 a) [37,39].

When the valine group of ACV was substituted with a D-cyclopropylalanine residue, reaction with IPNS showed formation of a bicyclic product with penicillin core and another bicyclic product with β-lactam ring fused to an unsaturated seven-membered ring (Figure 1.9 b) [37,40]. The latter experiment indicated the presence of an intermediate with free radical character on the ACV valine (or its substitutes) C-β during IPNS catalysis [40]. The free radical at D-cyclopropylalanine C-2 position can either interact with sulfur to form a penicillin product or can rearrange (cyclopropyl ring opening) and then react with the substrate sulfur to form the rearranged product [37,40].

Examining the results of turnover assays of valine variants of ACV with IPNS, namely ACG (L-α-aminoadipoyl-L-cysteinyl-glycine) and ACA (L-α-aminoadipoyl-L-3,3-[D_2]-cysteinyl-D-alanine), shows how subtle modifications can lead to different results [41]. The ACA substrate analogue was not observed to react, but ACG underwent a two-electron oxidation of its cysteinyl residue, interestingly leading to the formation an aldehyde product (Figure 1.9 c) [41].

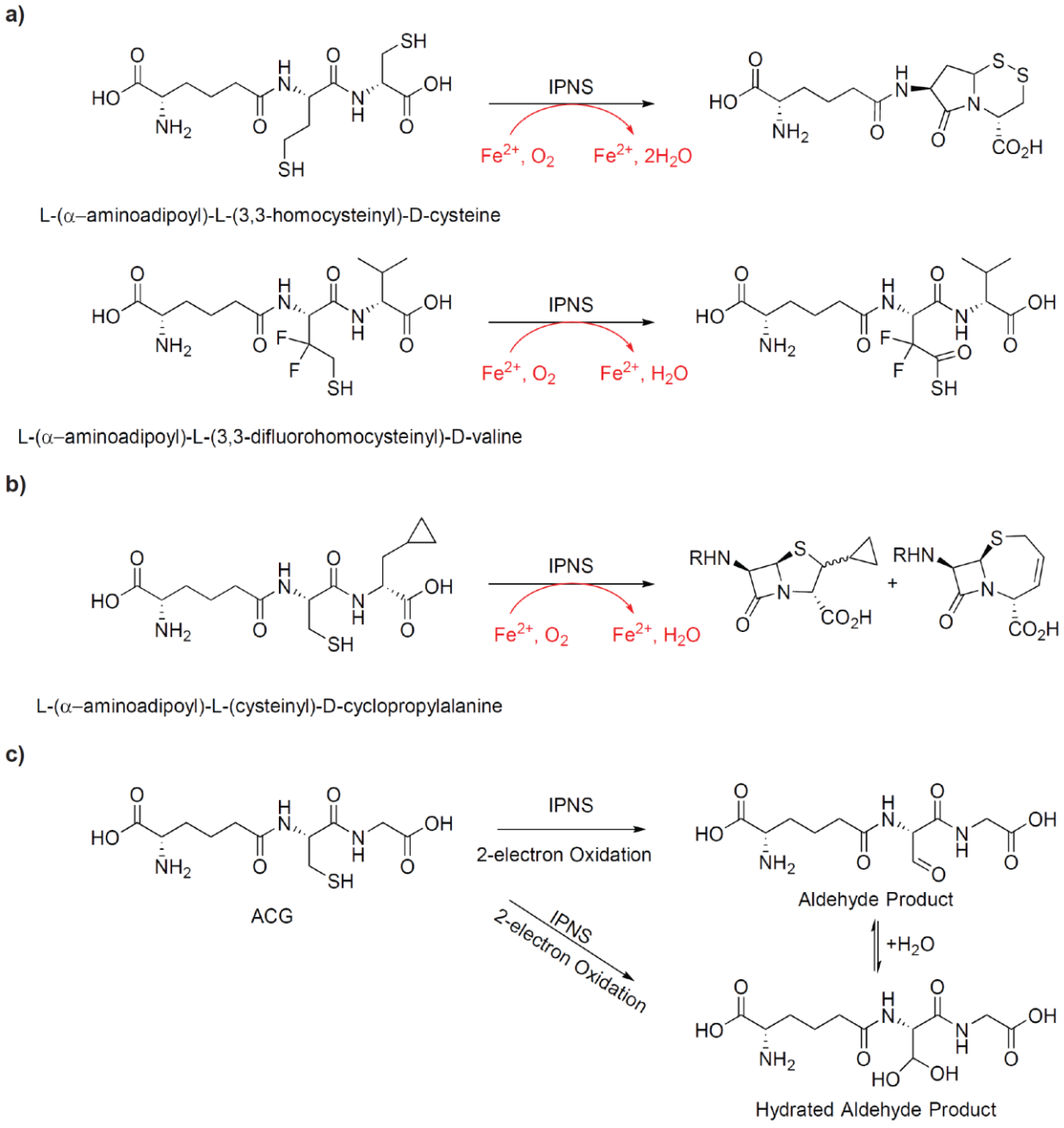


Figure 1.9: Turnover of IPNS with **(a)** L-α-aminoadipoyl-L-homocysteinyl-D-cysteine and L-α-aminoadipoyl-L-3,3-difluorohomocysteinyl-D-valine [37-39], **(b)** L-α-aminoadipoyl-L-cysteinyl-D-cyclopropylalanine [37,40], and **(c)** L-α-aminoadipoyl-L-cysteinyl-glycine [41].

1.6: Isopenicillin N Synthase Mechanism

The most recently proposed mechanism for the IPNS reaction is shown in Figure 1.10 (also described in Section 3.1.2): this was proposed on the basis of crystallographic, spectroscopic, computational and substrate analogue studies [15,34-44]. Initially, the ACV thiolate coordinates to $Fe^{(II)}$ in the position trans to His_{270} via substituting Gln_{330} and one water molecule (coordinated trans to Asp_{216}) leading to formation of penta-coordinated $Fe^{(II)}$. It was noted that binding of ACV to IPNS may promote O_2 binding, as ACV will make the active site more hydrophobic, and thiolate coordination decreases the $Fe^{(III)}/Fe^{(II)}$ reduction potential [41,42]. The latter is probably in part because the thiolate is a soft nucleophile, making $Fe^{(II)}$ more electron rich and hence, more likely to lose an electron [15,42]. O_2 then binds to the $Fe^{(II)}$ sixth coordination site forming an $Fe^{(III)}$-superoxide species, which displaces the ACV isopropyl group from its original position. Subsequently, the superoxide abstracts the pro-S hydrogen from the cysteinyl C-β position to form a peroxide and a free radical on the cysteinyl C-β position. The free radical on the cysteinyl C-β position forms a pi (л) bond with sulfur and one electron transfers from the sulfur to the $Fe^{(III)}$ to form $Fe^{(II)}$ and a thioaldehyde intermediate. The thioaldehyde can then undergo a two-step reaction; at the first step O-O bond cleaves via one proton abstraction from coordinated H_2O concomitantly converting the $Fe^{(II)}$-peroxide to an $Fe^{(IV)}$=O (ferroxo) species, and β-lactam ring forms at the second step via H_2O-mediated ring closure [44]. Ferroxo species formation has been commonly observed in catalysis by 2OG dependent oxygenases following oxidative reaction of 2OG into succinate and CO_2 [45]. A hydrogen is abstracted from ACV isopropyl group by the $Fe^{(IV)}$=O species to form a free radical and $Fe^{(III)}$ hydroxide, and the resulting free radical reacts with the sulfur to form the second (thiazolidine) ring. Simultaneously one electron from sulfur transfers into $Fe^{(III)}$ to form $Fe^{(II)}$, and the synthesized IPN is released from the active site, leaving IPNS in its resting state. The second ring formation step requires rotation of the ACV valine isopropyl group to face the valine β proton to the $Fe^{(IV)}$=O species [46,47]. According to the observed deuterium kinetic isotope effects, both C-H bond cleavage steps in IPNS mechanism are rate-limiting [48].

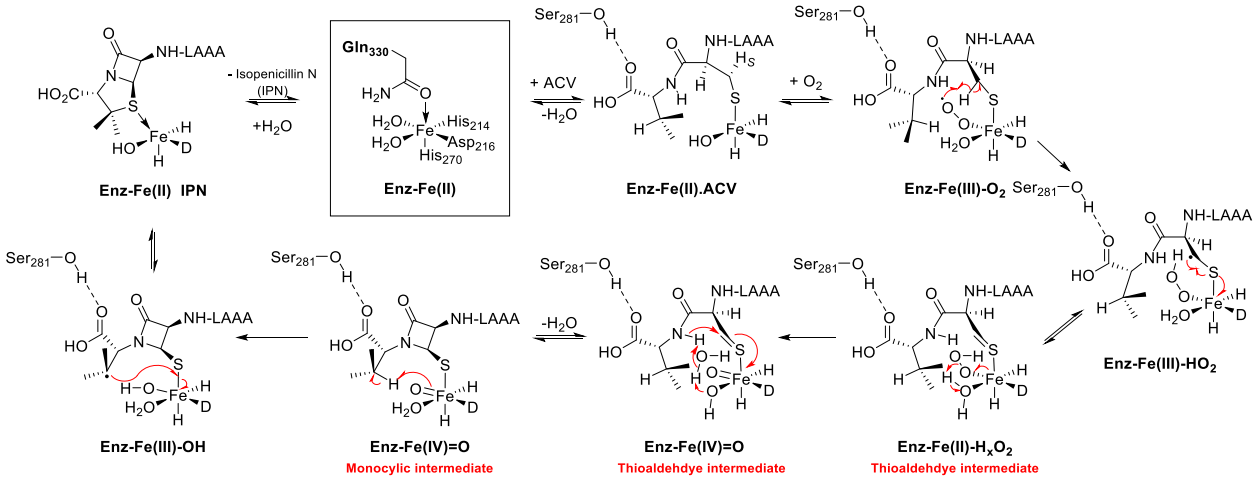


Figure 1.10: Proposed mechanism of WT_IPNS showing formation of IPN from ACV and O_2. Ser_{281} residue is also shown, which forms H-bond with the substrate valinyl carboxylate and may play role in the substrate's cysteinyl conformation. The mechanism was adapted from that given in reference [44].

1.7: Isopenicillin N Synthase from Different Species

Studies have shown that the gene sequences of IPNS from different Gram-negative and Gram-positive bacteria and fungi share a high level of similarity [49]. A subsequent study showed evidence for an IPNS encoding gene in the soil-living animal (*Folsomia candida*); the animal penicillin biosynthesis gene cluster also showed other relevant genes enabling IPN to be produced [50,51]. Evidence was presented that the F*c* IPNS was catalytically active [50]. The phylogenetic analysis led to the proposal that horizontal gene transfer between different species was the most possible mechanism for the presence of IPNS in *F. candida* due to the high similarity of the *F. candida* IPNS to IPNS sequences of different species [49-51]. In particular, the comparison of the protein sequence of IPNS from different fungi and bacteria showed a high level of conservation in the residues coordinating the metal (His_{214}, Asp_{216}, and His_{270}) and the residues interacting with ACV (Ser_{281}, Tyr_{189}, Tyr_{91}, Arg_{87}, Arg_{279}, Phe_{285}, Leu_{223}, Asn_{230}, Thr_{331}) [30]. Figure 1.11 shows a protein sequence alignment of IPNSs from different sources, the metal coordinating and substrate binding residues are coloured blue and red, respectively. Their observed high conservation level reflects the importance of such residues in IPNS function.

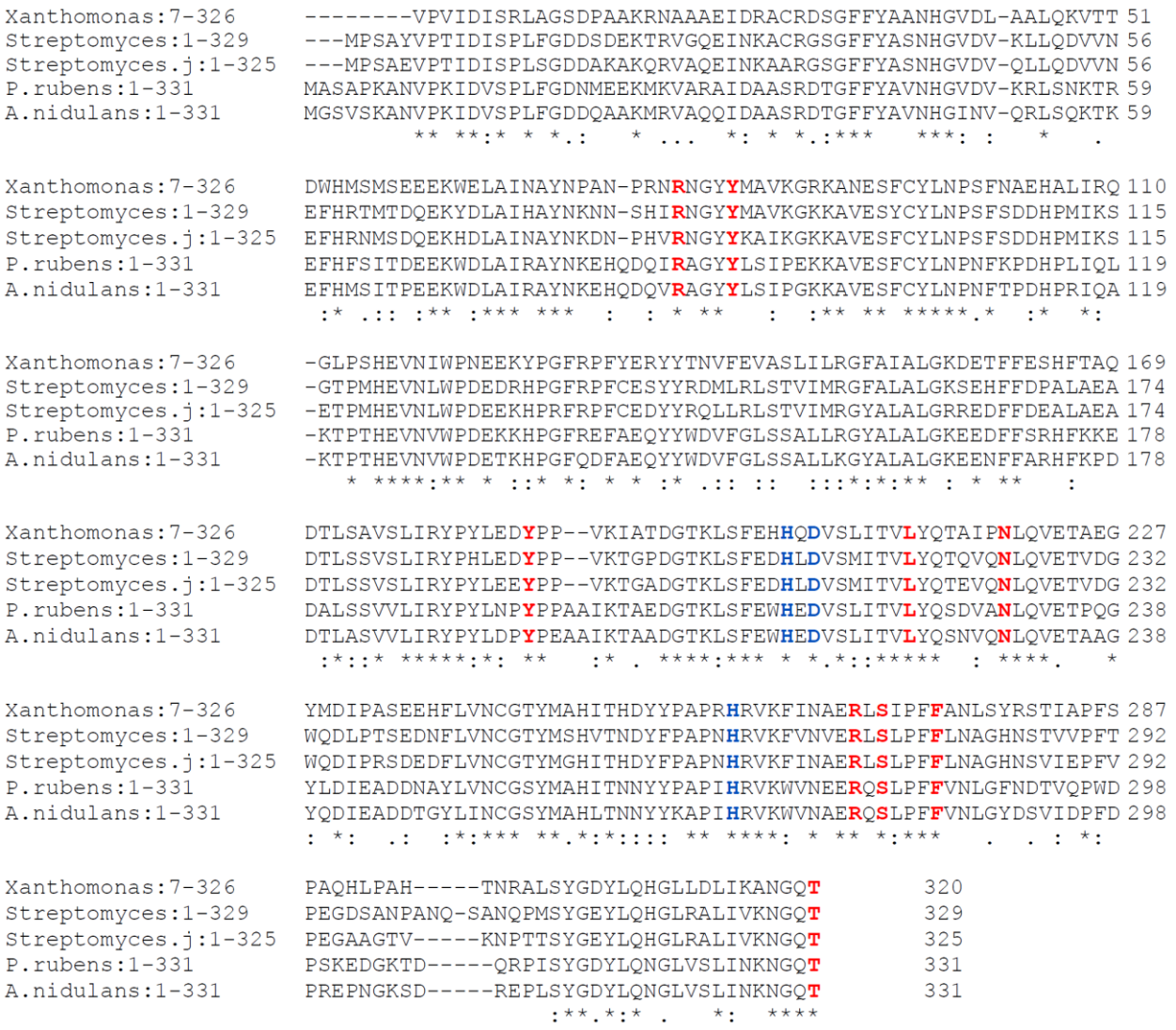


Figure 1.11: Multiple sequence alignment of IPNS from different fungi and bacteria. The metal coordinating and substrate binding residues are coloured blue and red, respectively. The alignment was made using BLAST search in NIH online server.

1.8: L-Carnitine Biosynthesis by γ-Butyrobetaine Hydroxylase (BBOX)

L-Carnitine (CAR) is essential for long-chain fatty acid β-oxidation in mitochondria of animals, plants, and many other eukaryotes [52-55]. Humans obtain CAR from their diet and produce it by biosynthesis in cells. As shown in Figure 1.12, the biosynthesis of CAR in animals (and humans) begins with degradation of lysine N-methylated proteins, leading to formation of N^{ε}-trimethyllysine (TML) [56]. Subsequently, a 2OG dependent oxygenase (TMLH) hydroxylates TML to form N^{ε}-hydroxy-trimethyllysine (HTML, Figure 1.12). The next step involves a retro-aldol reaction, fragmenting HTML into glycine and

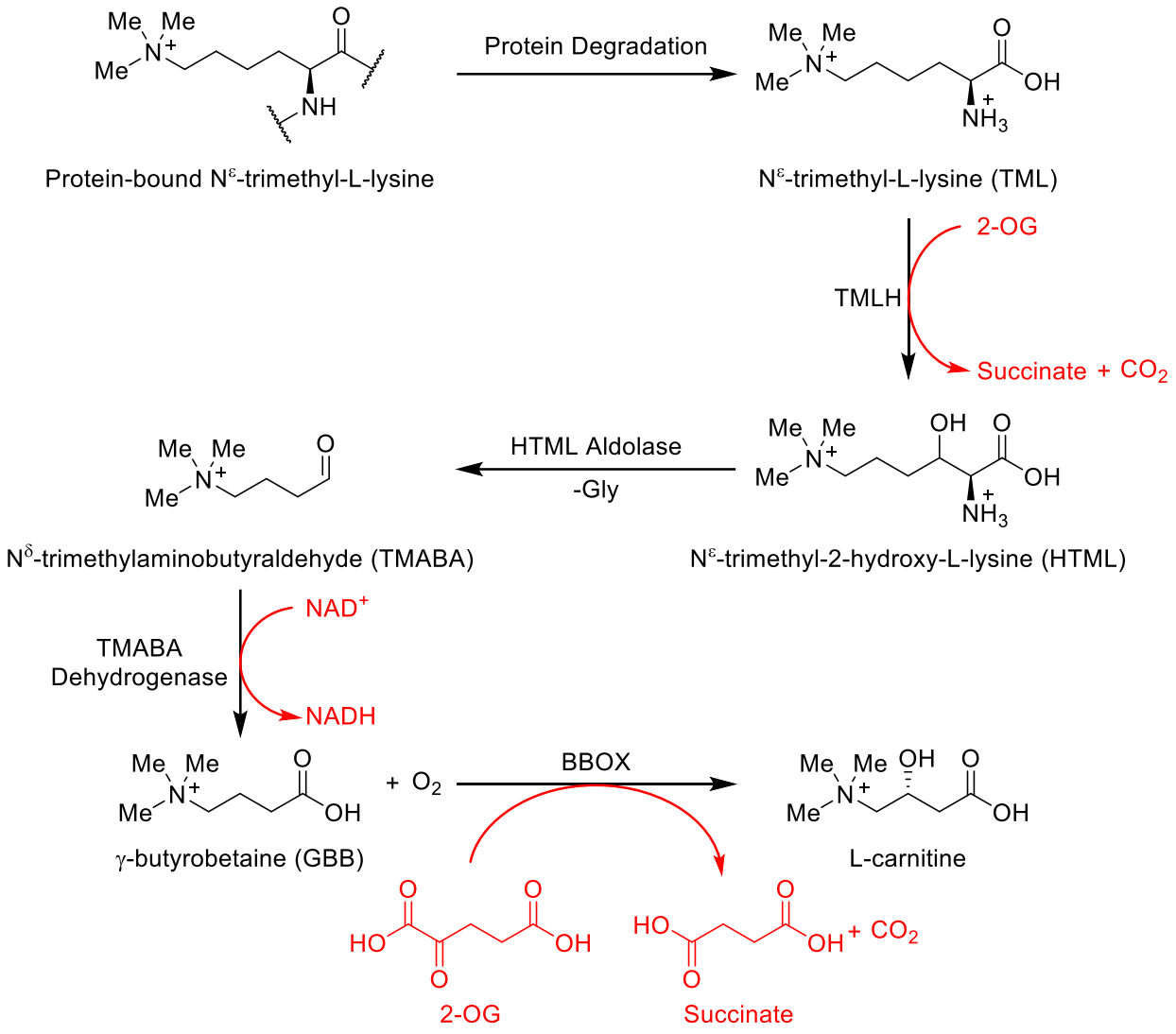


Figure 1.12: The L-carnitine biosynthesis pathway in human and other animals: BBOX catalyzes conversion of γ-butyrobetaine (GBB) to give L-carnitine. The scheme was adapted from reference [56].

N^{δ}-trimethylaminobutyraldehyde (TMABA) [56]. The latter intermediate is then oxidized into γ-butyrobetaine (GBB) by an NAD^+/NADH-dependent enzyme, TMABA dehydrogenase [56]. The last step in biosynthesis of CAR is the stereospecific hydroxylation of the GBB C-3 position, as catalyzed by γ-butyrobetaine hydroxylase (BBOX, Figure 1.12) [56,57]. BBOX is a 2OG dependent oxygenase which uses dioxygen, O_2, for the 2-electron oxidations of both GBB and 2OG.

Fatty acid oxidation produces ATP in mitochondria, a major source of energy, in addition to glucose oxidation [58]. It has been demonstrated that CAR plays a key role in

modulating the energy sources in cells by regulating levels of fatty acid oxidation: lower CAR levels decrease the contribution of fatty acid metabolism so indirectly upregulating glycolysis [58]. Glycolysis is less oxygen-demanding compared to fatty acid oxidation.

A high CAR level shifts energy supply towards more fatty acid oxidation and less glycolysis, something that can disturb the oxygen supply-demand balance in myocardial cells [58]. BBOX is a drug target for myocardial infarction treatment as it is involved in the last step of CAR biosynthesis, with one BBOX inhibiting drug (mildronate) being given after myocardial infarction in parts of the world [58,59].

1.9: Other Human 2OG Dependent Oxygenases

There are numerous types of 2OG dependent oxygenases catalyzing various pivotal oxidative reactions in many organisms, including humans and other animals [60]. One common reaction theme across 2OG dependent oxygenases is hydroxylation reactions, as well as N-methyl demethylations proceeding via initial methyl group hydroxylation. Some 2OG oxygenases are known to catalyze oxidations other than hydroxylation, including halogenation and ring modification reactions. Whereas in humans and animals, 2OG dependent oxygenases are known to catalyze hydroxylation and demethylation reactions [60]; the latter resulting from methyl hydroxylation.

Up to 70 2OG dependent oxygenases are found in humans; the majority of them modify proteins via hydroxylation / demethylation; most of the remainder modify other biological macromolecules, i.e. lipids and nucleic acids (Figure 1.13) [60]. The protein hydroxylase / demethylase group of human 2OG oxygenases can be subdivided into different groups, i.e. the proline-lysine hydroxylases, collagen hydroxylases, and the hypoxia-inducible factor (HIF) hydroxylases [60]. Hydroxylation of HIF-α at an asparagine residue by FIH is shown as an example in Figure 1.13 a. One of the largest sub-groups of protein hydroxylases / demethylases are the JmjC lysine demethylases (JmjC KDMs), which catalyze hydroxylation of N-methyl groups of trimethyl lysines in histones, leading to demethylation (Figure 1.13 b) [60].

Another group of 2OG oxygenases which modify nucleic acids and includes the Ten-Eleven Translocation subfamily (TET), which are known to initiate a multi-step

reaction to remove 5-methylcytosine (5mc) from DNA [60]. That is, 5mc is converted into the unmodified cytosine as a result of 5mc methyl group hydroxylation, which can undergo two further oxidations to the carboxylic acid, as catalyzed by the TET enzymes (Figure 1.13 c) [60]. The AlkB family are also DNA modifying 2OG dependent oxygenases of which there are nine human members [60]. Amongst the human AlkB family, ALKBH2 and ALKBH3 are known to remove cytotoxic methylated DNA bases; whereas ALKBH5 and FTO are enzymes that modify mRNA molecule [60].

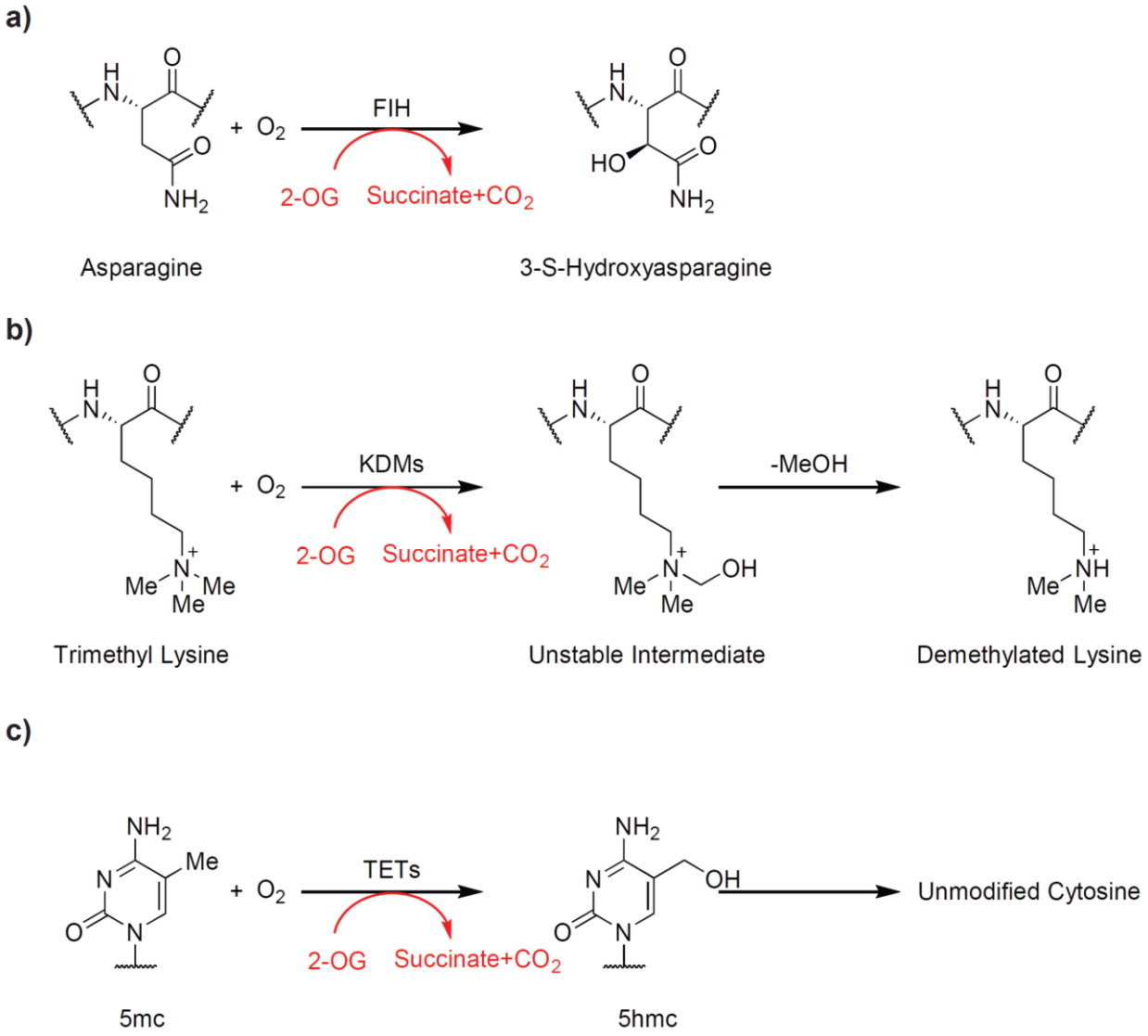


Figure 1.13: Main oxidative reactions catalyzed by human 2OG dependent oxygenases. The reactions include **(a)** protein hydroxylation by FIH, **(b)** histone trimethyl lysine demethylation by KDMs, and **(c)** conversion of 5-methylcytsine into unmodified cytosine by TETs. The scheme was adapted from [60].

1.10: Mechanism of 2OG Dependent Oxygenases

As described above, 2OG dependent oxygenases catalyze substrate oxidation coupled with oxidation of co-substrate, 2OG, to succinate and CO_2. Figure 1.14 shows the mechanism of 2OG oxygenases hydroxylating their substrate (shown as R'H) [61]. When the enzyme is at the resting state, $Fe^{(II)}$ has octahedral geometry bound to two histidine and one aspartate (or glutamate) residues, known as a facial triad, other coordination sites are occupied by water molecules [61]. The 2-oxoglutarate (2OG) chelates metal via substituting two H_2O molecules, with its ketone group trans to aspartate (or glutamate) and its carboxylate trans to histidine. The substrate (R'H) displaces the third water molecule via occupying the sixth coordination site. Subsequently, O_2 binds to the $Fe^{(II)}$ which simultaneously forms an $Fe^{(III)}$ superoxide species. The superoxide distal oxygen then reacts with the 2OG C-2 ketone group forming a tetrahedral intermediate at the C-2 position; simultaneously the $Fe^{(III)}$ is oxidized into $Fe^{(IV)}$. The so formed intermediate then loses a CO_2 via oxidative decarboxylation which cleaves the O-O bond and forms an $Fe^{(IV)}$=O intermediate, known as ferroxo species; a ferroxo species is commonly observed in the catalysis by oxygenases (and oxidases) and a ferroxo species is formed during the IPNS mechanism. The ferroxo species abstracts a hydrogen from the substrate, R'H, forming a free radical in the substrate and an $Fe^{(III)}$ hydroxide species. The free radical in the R' group then binds to the $Fe^{(III)}$OH forming the hydroxylated product (R'OH) with reduction of $Fe^{(III)}$ back to $Fe^{(II)}$. The succinate and product then leave the active site and binding of three water molecules converts the enzyme back to its resting state [61].

The mechanism of 2OG dependent oxygenases catalyzing reactions other than hydroxylation is generally thought to be similar to the scheme shown in Figure 1.14, up to the point of 2OG oxidative decarboxylation and $Fe^{(IV)}$=O formation (though there are exceptions). Instead of hydroxylation, the substrate can undergo different reactions / rearrangements following hydrogen abstraction by the ferroxo species. The mechanism of DAOCS is an example of mechanistic variation as described in Section 1.3 (Figure 1.4).

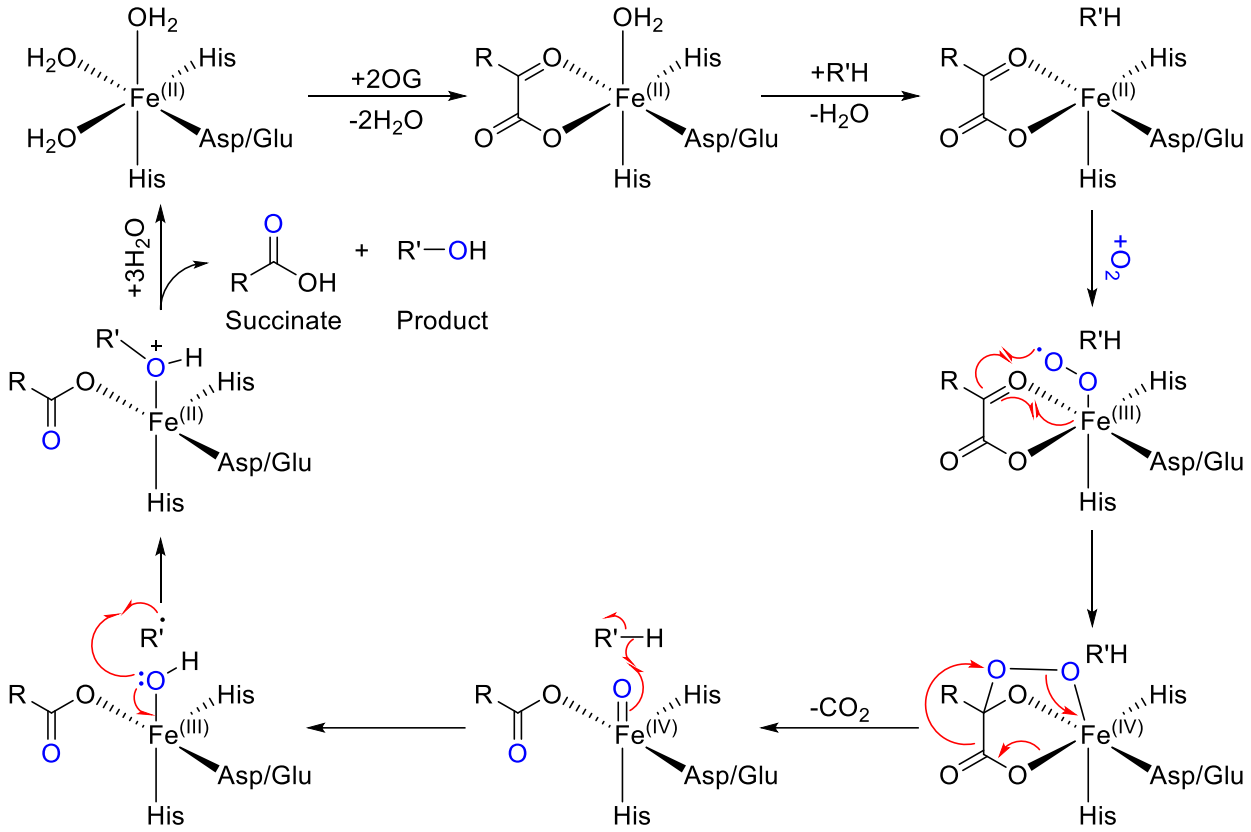


Figure 1.14: Proposed mechanism of 2OG dependent oxygenase catalyzed hydroxylation reactions. The dioxygen is coloured blue to highlight its path into the products. The figure was adapted from reference [61].

1.11: Importance of Second Shell Residues in Oxygenases

Computational studies have been carried out on 2OG dependent oxygenases to examine the role of second shell residues, relatively distant from the active site, in catalysis [62,63]. One example of such studies is human asparaginyl / aspartatyl hydroxylase (AspH) which is a 2OG dependent oxygenase catalyzing hydroxylation of epidermal growth factor-like domain proteins with the stoichiometry shown in Figure 1.13 a [62]. A modelling study using a combination of molecular dynamics and quantum mechanics (QM-MM) simulations has shown the significance of second shell residues in AspH [62]. It was observed that the R735W, R735Q, R688Q, and G434V mutants in the ferric superoxo and ferryl complexes have different substrate and 2OG binding and interactions compared to WT AspH [62]. Additionally, the correlated motions and the flexibility observed in the WT enzyme in the $Fe^{(III)}$ superoxide complex were diminished in all the studied mutants [62]. Importantly, the AspH mutations were shown

to affect the O-O activation (in 2OG decarboxylation) and hydrogen transfer (in substrate hydroxylation) steps during catalysis [62]. The peroxide bond cleavage energy barriers were affected in the mutants with the intermediates and transition states in the 2OG decarboxylation step showing different structures and energies in the mutants compared to the wildtype [62]. The modelling study also showed different substrate and 2OG coordination in the AspH $Fe^{(IV)}$=O complex with the mutants [62]. The latter is important as substrate positioning can play a role in the rate of the hydrogen abstraction step [62]. The energy barriers in the substrate hydroxylation step in R735Q and G434V mutants were calculated to be higher than the WT enzyme, leading to slowed hydroxylation [62].

1.12: Objectives of the Work Described in this Thesis

The work described in this thesis concerns mechanistic studies on IPNS and studies on γ-butyrobetaine hydroxylase inhibitor analysis. The studies on IPNS were designed to investigate the role of conformational changes involving residues in the second shell and beyond during catalysis. As summarized above, time-resolved crystallography and protein ^{19}F NMR studies on IPNS have revealed the importance of residues in second shell which connect ACV valine carboxylate to the enzyme α-helix 3 in surface [30,32]. The residues include Gln_{280}, Ser_{281}, and Leu_{282} on the enzyme β-11 strand, as well as Leu_{54} and Ser_{55} on α-helix 3 [30]. As these residues correlate active site dynamics with the motions on the IPNS surface, it was envisaged that substitutions on them may affect/alter the course of IPNS catalysis [30]. Following studies optimising IPNS production (Chapter 2), studies to probe this proposal are described in Chapter 3. Chapter 4 describes studies on a second investigation line involving the mode of action of inhibitors of BBOX.

The key activities were as follows:

1. Chapter 2 describes studies optimizing the expression of isopenicillin N synthase (IPNS) in 2YT and autoinduction media. IPNS expression was then examined in unlabelled minimal M9 media, and the conditions were further used for protein isotope labelling. The ^{15}N labelled M9 medium was used for preparation of ^{15}N labelled IPNS. Subsequently, the ^{15}N labelled IPNS was per-deuterated via expression in ^{2}H, ^{15}N labelled M9 medium. 2D ^{1}H-^{15}N HSQC spectra of labelled IPNS were examined.

2. Chapter 3 of this thesis describes work focusing on catalysis of IPNS mutants designed to explore the role of conformational changes during catalysis. Mutations of key residues involved in correlating ACV motions to the surface located α-helix 3 [30] were prepared using the polymerase chain reaction. The mutants were then expressed and purified using the conditions developed in Chapter 2 and were tested for turnover using NMR and LC-MS methods. A new thiazole ring containing four-electron oxidised product formed by S281A_IPNS was purified using HPLC and analyzed by NMR and LC-MS. The S281A, S281C, and Q280A_L282A mutants were crystallized. Two mechanisms were proposed for the formation of the new product on the basis of the solution and crystallographic data.

3. Chapter 4 describes NMR experiments on γ-butyrobetaine (BBOX) inhibitors. Recently synthesized potent inhibitors of BBOX (by Dr. S. Basak) were tested for turnover assays and for their binding affinities towards BBOX. Subsequently, the binding mode of a potent 2OG analogue inhibitor was examined using competitive binding assays.

1.13: References

[1] M. Nozaki, Y. Ishimura. Chapter 16, Oxygenases. Microbial Iron Metabolism. *Ed.* J. B. Neilands. *Academic Press* **1974** 417-444.

[2] J. B. van Beilen, and E. G. Funhoff. Expanding the alkane oxygenase toolbox: new enzymes and applications. *Curr. Opin. Biotechnol.* **2005** 16, 308-314.

[3] S. Martinez, and R. P. Hausinger. Catalytic Mechanisms of Fe(II)- and 2-Oxoglutarate-dependent Oxygenases. *J. Biol. Chem.* **2015** 290, 20702-20711.

[4] C. Loenarz, R. Chowdhury, C. J. Schofield, and E. Flashman. Oxygenases for oxygen sensing. *Pure Appl. Chem.* **2008** 80, 1837-1847.

[5] M. L. Neidig *et al.* CD and MCD of CytC3 and Taurine Dioxygenase: Role of the Facial Triad in α-KG-Dependent Oxygenases. *J. Am. Chem. Soc.* **2007** 129, 14224-14231.

[6] E. L. Hegg, and L. Jr. Que. The 2-His-1-carboxylate facial triad: an emerging structural motif in mononuclear non-heme iron(II) enzymes. *Eur. J. Biochem.* **1997** 250, 625-629.

[7] I. Pfeffer, L. Brewitz, T. Krojer, S. A. Jensen, G. T. Kochan, N. J. Kershaw, *et al.* Aspartate/asparagine-β-hydroxylase crystal structures reveal an unexpected epidermal growth factor-like domain substrate disulfide pattern. *Nat. Commun.* **2019** 10, 1-16.

[8] W. Aik, M. A. McDonough, A. Thalhammer, R. Chowdhury, and C. J. Schofield. Role of the jelly-roll fold in substrate binding by 2-oxoglutarate oxygenases. *Curr. Opin. Struct. Biol.* **2012** 22, 691-700.

[9] I. J. Clifton, M. A. McDonough, D. Ehrismann, N. J. Kershaw, N. Granatino, and C. J. Schofield. Structural studies on 2-oxoglutarate oxygenases and related double-stranded β-helix fold proteins. *J. Inorg. Biochem.* **2006** 100, 644-669.

[10] L. Brewitz, Y. Nakashima, C. J. Schofield. Synthesis of 2-oxoglutarate derivatives and their evaluation as cosubstrates and inhibitors of human aspartate/asparagine-β hydroxylase. *Chem. Sci.* **2020** 12, 1327-1342.

[11] C. J. Schofield, J. E. Baldwin, M. F. Byford, I. Clifton, J. Hajdu, C. Hensgens, and P. Roach. Proteins of the penicillin biosynthesis pathway. *Curr. Opin. Struct. Biol.* **1997** 7, 857-864.

[12] P. L. Roach, I. J. Clifton, V. Fülöp, K. Harlos, G. J. Barton, J. Hajdu, I. Andersson, C. J. Schofield, and J. E. Baldwin. Crystal structure of isopenicillin N synthase is the first from a new structural family of enzymes. *Nature* **1995** 375, 700-704.

[13] K. I. Kivirikko, and D. J. Prockop. Enzymatic Hydroxylation of Proline and Lysine in Protocollagen. *Proc. Natl. Acad. Sci.* **1967** 57, 782-789.

[14] C. Q. Herr, and R. P. Hausinger. Amazing diversity in biochemical roles of Fe(II)/2-oxoglutarate oxygenases. *Trends Biochem. Sci.* **2018** 43, 517-532.

[15] R. B. Hamed, J. R. Gomez-Castellanos, L. Henry, C. Ducho, M. A. McDonough, and C. J. Schofield. The enzymes of β-lactam biosynthesis. *Nat. Prod. Rep.* **2013** 30, 21-107.

[16] D. J. Waxman, J. L. Strominger. Penicillin-binding proteins and the mechanism of action of beta-lactam antibiotics. *Annu. Rev. Biochem.* **1983** 52, 825-869.

[17] E. Sauvage, F. Kerff, M. Terrak, J. A. Ayala, P. Charlier. The penicillin-binding proteins: structure and role in peptidoglycan biosynthesis. *FEMS Microbiol. Rev.* **2008** 32, 234-258.

[18] D. J. Tipper, J. L. Strominger. Mechanism of action of penicillins: a proposal based on their structural similarity to acyl-D-alanyl-D-alanine. *Proc. Natl. Acad. Sci.* **1965** 54, 1133-1141.

[19] N. J. Westwood, T. D. W. Claridge, P. N. Edwards, and C. J. Schofield. Reversible acylation of elastase by γ-lactam analogues of β-lactam inhibitors. *Bioorg. Med. Chem. Lett.* **1997** 7, 2973-2978.

[20] P. Taylor, V. Anderson, M. D. Walkinshaw, J. Dowden, S. L. Flitsch, N. J. Turner, K. Loughran. Novel Mechanism of Inhibition of Elastase by β-Lactams Is Defined by Two Inhibitor Crystal Complexes. *J. Biol. Chem.* **1999** 274, 24901-24905.

[21] C. R. Pitts, and T. Lectka. Chemical Synthesis of β-Lactams: Asymmetric Catalysis and Other Recent Advances. *Chem. Rev.* **2014** 114, 7930-7953.

[22] R. P. Elander. Industrial production of beta-lactam antibiotics. *Appl. Microbiol. Biotechnol.* **2003** 61, 385-392.

[23] T. R. van der Lende, M. van de Kamp, M. V. D. Berg, K. Sjollema, R. A. L. Bovenberg, M. Veenhuis, W. N. Konings, and A. J. M. Driessen. δ-(L-α-Aminoadipyl)-L-cysteinyl-D-valine synthetase, that mediates the first committed step in penicillin biosynthesis, is a cytosolic enzyme. *Fungal Genet. Biol.* **2002** 37, 49-55.

[24] M. F. Byford, J. E. Baldwin, C. Y. Shiau, and C. J. Schofield. The Mechanism of ACV Synthetase. *Chem. Rev.* **1997** 97, 2631-2650.

[25] J. E. Baldwin, R. M. Adlington, J. B. Coates, M. J. Crabbe, N. P. Crouch, J. W. Keeping, G. C. Knight, C. J. Schofield, H. H. Ting, C. A. Vallejo, M. Thorniley, and E. P. Abraham. Purification and initial characterization of an enzyme with deacetoxycephalosporin C synthetase and hydroxylase activities. *Biochem. J.* **1987** 245, 831-841.

[26] H. Tarhonskaya, A. Szöllössi, I. K. H. Leung, J. T. Bush, L. Henry, R. Chowdhury, A. Iqbal, T. D. W. Claridge, C. J. Schofield, and E. Flashman. Studies on Deacetoxycephalosporin C Synthase Support a Consensus Mechanism for 2-Oxoglutarate Dependent Oxygenases. *Biochemistry* **2014** 53, 2483-2493.

[27] D. Perry, E. P. Abraham, and J. E. Baldwin. Factors affecting the isopenicillin N synthetase reaction. *Biochem. J.* **1988** 255, 345-351.

[28] C. J. Schofield, and Z. H. Zhang. Structural and mechanistic studies on 2-oxoglutarate-dependent oxygenases and related enzymes. *Curr. Opin. Struct. Biol.* **1999** 9, 722-731.

[29] P. L. Roach, I. J. Clifton, C. M. H. Hensgens, N. Shibata, C. J. Schofield, J. Hajdu, and J. E. Baldwin. Structure of isopenicillinN synthase complexed with substrate and the mechanism of penicillin formation. *Nature* **1997** 387, 827-830.

[30] P. Rabe *et al.*, X-ray free-electron laser studies reveal correlated motion during isopenicillin N synthase catalysis. *Sci. Adv.* **2021** 7, eabh0250.

[31] L. A. McNeill, T. J. N. Brown, M. Sami, I. J. Clifton, N. I. Burzlaff, T. D. W. Claridge, R. M. Adlington, J. E. Baldwin, P. J. Rutledge, and C. J. Schofield. Terminally Truncated Isopenicillin N Synthase Generates a Dithioester Product: Evidence for a Thioaldehyde Intermediate during Catalysis and a New Mode of Reaction for Non-Heme Iron Oxidases. *Chem. Eur. J.* **2017** 23, 12815-12824.

[32] P. Rabe, C. C. Walla, N. K. Goodyear, J. Welsh, R. Southwart, I. Clifton, J. D. S. Linyard, A. Tumber, T. D. W. Claridge, W. K. Myers, and C. J. Schofield. Spectroscopic studies reveal details of substrate-induced conformational changes distant from the active site in isopenicillin N synthase. *J. Biol. Chem.* **2022** 298, 102249.

[33] C. D. Brown-Marshall, A. R. Diebold, E. I. Solomon. Reaction Coordinate of Isopenicillin N Synthase: Oxidase Versus Oxygenase Activity. *Biochemistry* **2010** 49, 1176-1182.

[34] J. E. Baldwin, and M. Bradley. Isopenicillin N Synthase: Mechanistic Studies. *Chem. Rev.* **1990** 90, 1079-1088.

[35] J. E. Baldwin, R. M. Adlington, S. E. Moroney, L. D. Field, and H.-H. Ting. Stepwise Ring Closure in Penicillin Biosynthesis. Initial β-Lactam Formation. *J. Chem. Soc. Chem. Commun.* **1984** 15, 984-986.

[36] E. Tamanaha *et al.* Spectroscopic Evidence for the Two C−H-Cleaving Intermediates of Aspergillus nidulans Isopenicillin N Synthase. *J. Am. Chem. Soc.* **2016** 138, 8862-8874.

[37] P. Rabe, J. J. A. G. Kamps, C. J. Schofield, and C. T. Lohans. Roles of 2-oxoglutarate oxygenases and isopenicillin N synthase in β-lactam biosynthesis. *Nat. Prod. Rep.* **2018** 35, 735-756.

[38] A. Daruzzaman, I. J. Clifton, R. M. Adlington, J. E. Baldwin, and P. J. Rutledge. The Interaction of Isopenicillin N Synthase with Homologated Substrate Analogues δ-(L-α-

Aminoadipoyl)-L-homocysteinyl-D-Xaa Characterised by Protein Crystallography. *ChemBioChem* **2013** 14, 599-606.

[39] J. E. Baldwin, G. P. Lynch, and C. J. Schofield. Isopenicillin N Synthase: A New Mode Of Reactivity. *Tetrahedron* **1992** 48, 9085-90100.

[40] J. E. Baldwin, R. M. Adlington, B. P. Domayne-Hayman, G. Knight, and H.-H. Ting. Use of the Cyclopropylcarbinyl Test to detect a Radical-like Intermediate in Penicillin Biosynthesis. *J. Chem. Soc., Chem. Commun.* **1987** 1661-1663.

[41] A. J. Long, I. J. Clifton, P. L. Roach, J. E. Baldwin, P. J. Rutledge, and C. J. Schofield. Structural Studies on the Reaction of Isopenicillin N Synthase with the Truncated Substrate Analogues δ-(L-α-aminoadipoyl)-L-cysteinyl-glycine and δ-(L-α-aminoadipoyl)-L-cysteinyl-D-alanine. *Biochemistry* **2005** 44, 6619-6628.

[42] M. Lundberg, P. E. M. Siegbahn, and K. Morokuma. The Mechanism for Isopenicillin N Synthase from Density-Functional Modeling Highlights the Similarities with Other Enzymes in the 2-His-1-carboxylate Family. *Biochemistry* **2008** 47, 1031-1042.

[43] P. J. Rutledge, 2-Oxoglutarate-Dependent Oxygenases. ed. C. J. Schofield and R. Hausinger. *R. Soc. Chem.* **2015** 20, 414-424.

[44] N. C. Chapman, and P. J. Rutledge. Isopenicillin N Synthase: Crystallographic Studies. *ChemBioChem* **2021** 22, 1687-1705.

[45] M. Costas, M. P. Mehn, M. P. Jensen, and L. Que Jr. Dioxygen activation at mononuclear nonheme iron active sites: enzymes, models, and intermediates. *Chem. Rev.* **2004** 104, 939-986.

[46] L. Que Jr, and R. Y. N. Ho Dioxygen Activation by Enzymes with Mononuclear Non-Heme Iron Active Sites. *Chem. Rev.* **1996** 96, 2607-2624.

[47] J. E. Baldwin, R. M. Adlington, D. G. Marquess, A. R. Pitt, M. J. Porter, and A. T. Russell. Evidence for an insertion-homolysis mechanism for carbon-sulfur bond formation in penicillin biosynthesis; 1. Synthesis of tripeptide probes. *Tetrahedron* **1996** 52, 2515-2536.

[48] J. E. Baldwin, and E. Abraham. The biosynthesis of penicillins and cephalosporins. *Nat. Prod. Rep.* **1988** 5, 129-145.

[49] G. Landan, G. Cohen, Y. Aharonowitz, Y. Shuali, D. Graur, and D. Shiffman. Evolution of Isopenicillin N Synthase Genes May Have Involved Horizontal Gene Transfer. *Mol. Biol. Evol.* **1990** 7, 399-406.

[50] D. Roelofs *et al.* A Functional Isopenicillin N Synthase in an Animal Genome. *Mol. Biol. Evol.* **2012** 30, 541-548.

[51] W. Suring *et al.* Evolutionary ecology of beta-lactam gene clusters in animals. *Mol. Ecol.* **2017** 26, 3217-3229.

[52] F. M. Vaz, and R. J. A. Wanders. Carnitine biosynthesis in mammals. *Biochem. J.* **2002** 361, 417-429.

[53] G. S. N. Naidu, I. Y. Lee, E. G. Lee, G. H. Kang, and Y. H. Park. Microbial and enzymatic production of L-carnitine. *Bioprocess Biosyst. Eng.* **2000** 23, 627–635.

[54] E. P. Brass, C. L. Hoppel, and W. R. Hiatt. Effect of intravenous L-carnitine on carnitine homeostasis and fuel metabolism during exercise in humans. *Clin. Pharmacol. Ther.* **1994** 55, 681–692.

[55] P. S. Shekhawat, S. Sonne, A. L. Carter, D. Matern, and V. Ganapathy. Enzymes involved in L-carnitine biosynthesis are expressed by small intestinal enterocytes in mice: Implications for gut health. *J. Crohns Colitis.* **2013** 7, 197-205.

[56] I. K.H. Leung, T. J. Krojer, G. T. Kochan, L. Henry, F. von Delft, T. D.W. Claridge, U. Oppermann, M. A. McDonough, and C. J. Schofield. Structural and Mechanistic Studies on γ-Butyrobetaine Hydroxylase. *Chem. Biol.* **2010** 17, 1316-1324.

[57] S. Englard, J. S. Blanchard, and C. F. Midelfort. γ-Butyrobetaine hydroxylase: stereochemical course of the hydroxylation reaction. *Biochemistry* **1985** 24, 1110-1116.

[58] M. Dambrova, E. Liepinsh, and I. Kalvinsh. Mildronate: cardioprotective action through carnitine-lowering effect. *Trends Cardiovasc. Med.* **2002** 12, 275-279.

[59] B. Z. Simkhovich, Z. V. Shutenko, D. V. Meirena, K. B. Khagi, R. J. Mezapuke, T. N. Molodchina, I. J. Kalvins, and E. Lukevics. 3-(2,2,2-Trimethylhydrazinium) propionate (THP)-a novel gamma-butyrobetaine hydroxylase inhibitor with cardioprotective properties. *Biochem. Pharmacol.* **1988** 37, 195-202.

[60] S. C. Fletcher, and M. L. Coleman. Human 2-oxoglutarate-dependent oxygenases: nutrient sensors, stress responders, and disease mediators. *Biochem. Soc. Trans.* **2020** 48, 1843-1858.

[61] S. Martinez, and R. P. Hausinger. Catalytic Mechanisms of Fe(II)- and 2-Oxoglutarate-dependent Oxygenases. *J. Biol. Chem.* **2015** 290, 20702-20711.

[62] A. Krishnan, S. O. Waheed, S. Melayikandy, C. LaRouche, M. Paik, C. J. Schofield, and T. G. Karabencheva-Christova. Effects of Clinical Mutations in the Second Coordination Sphere and Remote Regions on the Catalytic Mechanism of Non-Heme Fe(II)/2-Oxoglutarate-Dependent Aspartyl Hydroxylase AspH. *Chem. Phys. Chem.* **2024** 25, e202400303.

[63] M. G. Thomas, S. B. J. S. Rifayee, and C. Z. Christov. How Do Variants of Residues in the First Coordination Sphere, Second Coordination Sphere, and Remote Areas Influence the Catalytic Mechanism of Non-Heme Fe(II)/2-Oxoglutarate Dependent Ethylene-Forming Enzyme? *ACS Catal.* **2024** 14, 18550-18569.

Chapter 2: Expression of Labelled IPNS for NMR Spectra Peak Assignment

2.1: Introduction

2.1.1: Protein 2-D NMR Spectroscopy

NMR spectroscopy is a powerful tool to examine protein structure and dynamics in the solution state. Proteins have a large number of protons and normally diffuse and tumble slower than small molecules in solution due to their relatively large molecular weight [1,2]. The resulting 1-D ^{1}H NMR spectra of proteins therefore typically exhibit many overlapping broad peaks, making the interpretation of such spectra difficult. Two-dimensional NMR spectroscopy enables the assignment of peaks via spreading the resonances over two dimensions [1,3]. In particular, ^{1}H-^{15}N heteronuclear single quantum coherence spectroscopy (HSQC) can be used to correlate the chemical shifts of the protein amide protons and amide nitrogens [1,4,5]. Thus, in a ^{1}H-^{15}N HSQC spectrum of a protein sample, each cross peak represents the backbone NH of one amino acid. The chemical shifts in the proton and nitrogen dimensions of the cross peaks depend on the chemical environment of the corresponding backbone atoms [1,4,5]. Accordingly, the positions of the cross peaks in an ^{1}H-^{15}N HSQC spectrum represent the equilibrated structure of the protein backbone [1,4,5]. To obtain a protein ^{1}H-^{15}N HSQC spectrum, the protein needs to be uniformly ^{15}N labelled, in particular on its backbone NHs.

Some complications need to be considered in the analysis of a ^{1}H-^{15}N HSQC spectrum of a uniformly ^{15}N labelled protein. Amino acid residues with one or more nitrogens in their side chains (i.e. arginine-, lysine-, asparagine-, histidine- and glutamine residues) will also have ^{15}N-H bonds within their side chains. Therefore, there will be additional peaks in the ^{1}H-^{15}N HSQC spectrum corresponding to their side chain NH bonds [1]. These non-backbone resonances can be distinguished due to their different chemical shifts in both the proton and nitrogen dimensions. There is one exceptional natural amino acid, proline, which does not have backbone NH bond due to its cyclic structure; hence there are no cross peaks for prolines in ^{1}H-^{15}N HSQC spectra.

For larger proteins, due to their slower tumbling rate in solution, the ^{1}H transversal (T_2) relaxation rate will increase leading to NMR signal broadening [1,6]. Therefore, the

^{1}H-^{15}N HSQC spectra of large proteins will exhibit overlapping, broad peaks or low signal intensity due to losses during the INEPT (Insensitive Nuclei Enhancement by Polarization Transfer) transfer [1]. One well-known mechanism which increases the T_2 relaxation rate is dipole-dipole (DD) interactions between nuclei [1,6,7]. To compensate for the dipole-dipole interactions, protein per-deuteration coupled with uniform spin labelling (e.g. ^{15}N labelling) has been widely used [7]. When the non-exchangeable background protons of a uniformly ^{15}N-labelled protein are replaced with deuterons, the backbone ^{1}H-^{15}N bonds are surrounded by deuterons, which have a lower gyromagnetic ratio than protons [1]. Consequently, the dipole-dipole interactions between ^{1}H-^{15}N bonds and deuterons will be weaker, leading to enhanced resolution of the protein NMR spectra [7].

Another mechanism which is known to increase the T_2 relaxation rate depends on the difference between chemical shifts of the nuclei with different orientations in the magnetic field; this is known as chemical shift anisotropy (CSA) [1,6,7]. One established approach to suppress the T_2 relaxation rates in multi-dimensional NMR is transverse relaxation-optimized (TROSY) spectroscopy [1,6,7]. TROSY method is based on constructive cancellation of DD coupling and CSA mechanisms, leading to higher resolution in multidimensional NMR spectra of large proteins [1,6,7]. Therefore, obtaining a TROSY type spectra of per-deuterated ^{15}N labelled protein can give rise to a ^{1}H-^{15}N HSQC-like spectra with higher resolution, which is particularly useful in studying the structure and dynamics of lager proteins [6-8].

2.1.2: Preparation of Labelled Proteins Using Minimal Medium

One established method to prepare isotopically labelled proteins is to use a minimal medium [9,10]. Unlike conventional medium (e.g. 2YT), the minimal medium is designed to have, at least predominantly, only one source of carbon and nitrogen (i.e. glucose and NH_4Cl, respectively). The minimal medium is also enriched with essential metals and vitamins for bacterial growth [10]. It is possible to produce a labelled protein via expression of a recombinant protein in a minimal medium enriched with properly labelled carbon and/or nitrogen sources. However, due to the limited metabolites used in minimal media, cell growth in minimal media is significantly lower compared to the conventional nutrition-rich media. Additionally, isotope labelling (e.g. deuteration) can

make cell growth slower as it is difficult for bacteria to adapt to growth in D_2O [11]. Consequently, it is essential to optimize growth conditions in an unlabelled minimal media before production of labelled proteins.

Table 2.1: Recipe for preparation of minimal M9 media [10].

Minimal M9 Media Recipe	**Amount Per 1L Media**
$^{15}NH_4Cl/(NH_4)_2SO_4$	1 g
$Na_2HPO_4.2H_2O$	7.57 g
KH_2PO_4	3 g
NaCl	500 mg
^{13}C-glucose/glucose	4 g
EDTA	50 mg
$MnCl_2.4H_2O$	16 mg
$FeCl_3$	5 mg
$ZnCl_2$	50 μL 10 mg/mL stock
$CuCl_2$	10 μL 10 mg/mL stock
$CoCl_2$	10 μL 10 mg/mL stock
H_3BO_3	20 μL 5 mg/mL stock
d-Biotin	1 mL 1 mg/mL stock
Thiamine	1 mL 1 mg/mL stock
Na_2SO_4	42.6 mg
$MgSO_4$	120.4 mg
$CaCl_2.2H_2O$	65.7 mg
D_2O/H_2O	Dilute up to 1 L

The work described in this chapter initially focused on optimizing the growth conditions of recombinant isopenicillin N synthase (IPNS) in 2YT and in unlabelled minimal media. The minimal media used in the work was M9 media [10]. The recipe for

preparation of minimal M9 media is shown in Table 2.1. After examining recombinant IPNS production in *Escherichia coli* (BL21) in unlabelled minimal M9 media, ^{15}N labelled IPNS was produced in using minimal M9 media enriched with $^{15}NH_4Cl$ as the sole nitrogen source. Subsequently, per-deuterated ^{15}N labelled IPNS was produced using $^{15}NH_4Cl$ enriched minimal M9 media in D_2O. The optimized growth conditions in 2YT media were also used in the next chapter to produce IPNS mutants.

2.2: Results and Discussion

2.2.1: Optimizing Production of Recombinant IPNS

An isopenicillin N synthase (IPNS) pCOLD encoding vector (provided by Dr. P. Rabe) was transformed into *E. coli* BL21 strain (using the heat shock method [12]) for recombinant protein production. The IPNS vector was designed to encode for a kanamycin resistance gene and N-terminal hexa-histidine tagged (His-Tag) IPNS, with the His-Tag being employed for purification of IPNS. *E. coli* colonies containing the IPNS vector were picked to inoculate a starter culture then a large-scale culture.

To obtain an optimal yield of IPNS expression during large-scale growth, two different growth media conditions were examined. One medium was 2x yeast extract tryptone (2YT, for β-D-1-thiogalactopyranoside (IPTG) mediated expression) and the other was an autoinduction medium (Terrific Broth auto induction). After inoculation, both the large-scale growths were incubated at 37 °C; *E. coli* growth was monitored via measuring the culture optical density at 600 nm (OD_{600}). Once the OD_{600} has reached 0.6, the culture with the autoinduction medium was incubated at 18 °C for at least 18 hours to ensure expression of the IPNS gene. In the case of the 2YT medium, to induce IPNS expression, IPTG was added to the culture when the OD_{600} reached 0.6. To investigate the optimal concentration of IPTG, different concentrations of IPTG were added to the separate 2YT growth flasks (0-1000 μM). Similar to the autoinduction cultures, the 2YT cultures with various IPTG concentrations were incubated at 18 °C for at least 18 hours.

To examine the cellular growth and expression of IPNS in the aforementioned cultures, 10 mL of each culture was used for small scale purifications. As the recombinant IPNS proteins contain a N-terminal hexa-histidine tag (His-Tag), a nickel containing resin (NEBExpress Ni Resin) was used for small scale purification. The details of the small-scale purification method are discussed in Section 2.3.2. In brief, a 50 mL aliquot of cells from each culture was harvested via centrifugation (3000 g, 4 °C). The amounts of cell pellets obtained from 50 mL of each medium were measured (Table 2.2). The amount of cell pellet obtained from the 50 mL culture were similar for the autoinduction media and

for the 2YT media with IPTG; the use of 2YT medium without IPTG gave an increased amount of cell pellet (Table 2.2).

To isolate and purify expressed IPNS, the cell pellets were then dissolved (1:10 w/v ratio) in low imidazole buffer A (5 mM imidazole). The suspended cells were then lysed by sonification (details are given in Section 2.3.2). Subsequently, 1 mL of the cell lysates was treated with 200 μL of nickel resin (NEBExpress Ni Resin) that had been pre-equilibrated with buffer A. After allowing sufficient time (30 minutes) for the His-tagged IPNS protein to bind to the nickel ions ($Ni^{(II)}$), the resin was washed five times with 500 μL of buffer A. The five eluted fractions were collected separately (W1-W5). The nickel resins were then eluted twice with 500 μL of high imidazole buffer B (500 mM imidazole) and the fractions were collected (E1 and E2). The first eluted fraction (E1) from each media purification was examined for the presence of IPNS using SDS-PAGE gel analysis. The second eluted fractions (E2) did not contain protein, hence only the E1 fractions were analyzed. Figure 2.1 a shows SDS-PAGE gel image of E1 fractions from the different media investigated for recombinant IPNS production.

In Figure 2.1 a, the first four columns correspond to cells obtained from 2YT medium (with four different IPTG concentrations), and the last four columns correspond to cells grown in autoinduction medium (with four different medium concentrations ranging from 35 g/L to 95 g/L). In all conditions, the growth and IPNS expression temperatures were at 37 °C and 18 °C, respectively. The SDS-PAGE gel results showed that the IPNS expression in 2YT medium is preferred when induced using 500 μM IPTG and was similar to the expression level observed with the autoinduction medium (Figure 2.1 a). Therefore, an IPTG concentration of 500 μM was chosen for production of IPNS in 2YT medium. It is noteworthy that the higher level of IPTG (1000 μM) manifested decreased expression of IPNS, which might be due to the reported toxicity of IPTG at high concentrations [13].

After examining *E. coli* growth and recombinant IPNS expression in 2YT and autoinduction media, the minimal M9 medium was prepared using the recipe shown in Table 2.1. IPNS expressions were also examined in unlabelled minimal M9 media. After IPNS vector transformation into *E. coli* (using heat shock), one colony was picked to inoculate 100 mL of minimal M9 medium (starting culture). The grown starting culture was

used to inoculate three 100 mL minimal M9 medium for large-scale growth. When the OD_{600} reached 0.6, one growth was not treated with IPTG, and the other two growths were treated with 100 μM and 500 μM of IPTG. All media were then incubated at 18 °C for 18 hours shaking at 180 rpm. Similar to 2YT and autoinduction media, 50 mL aliquots of each minimal M9 medium were taken for IPNS purification as described above.

Table 2.2: List of media used for IPNS expression, the amount of harvested cells per 50 mL of each medium are shown.

Number	Medium Description	Pellet Amount Per 50 mL Culture
1	2YT, No IPTG	0.74 g
2	2YT, 100 μM IPTG	0.48 g
3	2YT, 500 μM IPTG	0.52 g
4	2YT, 1000 μM IPTG	0.48 g
5	Autoinduction (35 g/L)	0.53 g
6	Autoinduction (55 g/L)	0.43 g
7	Autoinduction (75 g/L)	0.50 g
8	Autoinduction (95 g/L)	0.45 g

Figure 2.1 b shows an SDS-PAGE gel image obtained from IPNS purification from three minimal M9 media with different IPTG contents. The IPNS was purified using nickel resin following the same protocol used for 2YT and autoinduction media (as described above). The cell lysate, first wash (W1), and elution fractions (E1, E2) were analyzed by SDS-PAGE gel for all three growth conditions (Figure 2.1 b). The condition with 500 μM IPTG showed the highest level of IPNS expression (Figure 2.1 b), and was consequently used for further expression studies in labelled minimal M9 media.

After the successful expression of IPNS in different media, a small amount of (120 mL) minimal M9 medium was prepared in D_2O. To obtain the maximum D_2O content, all stock solutions were also prepared in D_2O. As before the IPNS pCOLD vector was transformed into *E. coli* (BL21) and a colony was picked to inoculate 10 mL of D_2O medium (starting culture); the sufficiently grown culture (at 37 °C, overnight) was used to

inoculate 100 mL of medium in D_2O. The culture was subsequently treated with IPTG (500 μM final concentration) at OD_{600} 0.6, then was incubated at 18 °C for 18 hours. A 50 mL aliquot of the grown culture was taken to purify IPNS as described above. Figure 2.1 c shows an SDS-PAGE gel image of the wash (W1, W2) and eluted (E1, E2) fractions obtained from nickel resin purification. The eluted fractions showed a detectable amount of IPNS expression (Figure 2.1 c); however, at a lower level of IPNS expression compared to the unlabelled minimal M9 medium (Figure 2.1 b). It is known that *E. coli* cells struggle to adapt to a D_2O environment [13], consistent with the slower cellular growth and lower protein expression levels observed for IPNS.

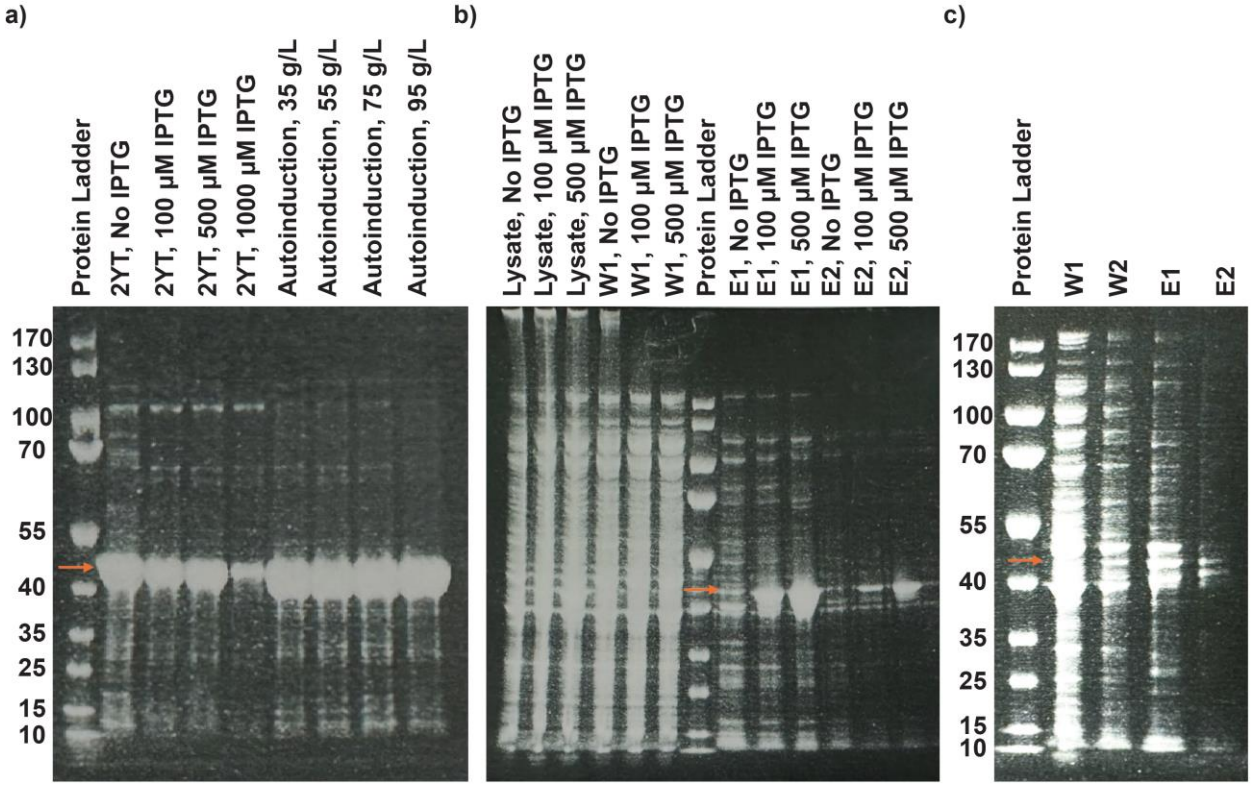


Figure 2.1: **(a)** Recombinant IPNS expression trials in 2YT media with different IPTG concentrations and in four autoinduction media with different concentrations. The SDS-PAGE gel image of E1 fractions obtained from nickel resin purification are shown. The IPNS band is marked with a red arrow. **(b)** Expression of IPNS in unlabelled minimal M9 media with different IPTG concentrations. The SDS-PAGE gel image of cell lysates, wash (W1), and elution (E1, E2) fractions obtained from nickel resin purification are shown. The IPNS band is marked with a red arrow. **(c)** Expression of IPNS in minimal M9 medium prepared in D_2O. The SDS-PAGE gel image of wash (W1, W2) and elution (E1, E2) fractions obtained from the nickel resin purification are shown. The expression level of IPNS in D_2O medium is lower than unlabelled minimal M9 medium. The IPNS band is marked with a red arrow.

2.2.2: Expression and Purification of ^{15}N Labelled IPNS

To obtain uniformly ^{15}N labelled IPNS, minimal M9 medium was prepared according to the recipe shown in Table 2.1; $^{15}NH_4Cl$ was used as the sole nitrogen source. The expression protocol was similar to the expression trials discussed in Section 2.2.1. In brief, 7.2 litre (12 separate 600 mL media) of ^{15}N labelled minimal M9 media was incubated at 37 ^oC until the OD_{600} reached 0.6, then the media were treated with IPTG (500 μM final concentration) and incubated at 18 ^oC. Subsequently, all cells were harvested by centrifugation (11000 g, 4 ^oC). The obtained cell pellets were used for purification of ^{15}N labelled IPNS.

Purified ^{15}N labelled IPNS was obtained from the cell pellets using two steps, with the details described in Section 2.3.3. The cell pellets from ^{15}N labelled medium were lysed and the cell extract was applied to a column enriched with $Ni^{(II)}$ ions (nickel His-Trap column). As the recombinant IPNS bears a N-terminal poly histidine tag (His-Tag), the IPNS will bind to the column $Ni^{(II)}$ ions; hence, the column was first washed with low imidazole buffer A (5 mM imidazole). The column was then eluted with high imidazole buffer B (500 mM imidazole) to remove the bound His-tagged IPNS. The buffer B percentage is shown in the nickel his-trap chromatogram (Figure 2.2). The fractions with UV absorption (280nm) were collected and their protein content was analyzed by SDS-PAGE gel (Figure 2.2). Subsequently, the fractions showing evidence for a substantial IPNS band (around 40 KDa) were combined and treated with the viral 3-C protease, which cleaves the N-terminal poly histidine tag [14].

After cleavage of the his-tag, the mixture was re-applied to the nickel His-trap column (reverse his-trap step). The column was washed five times with 20 mM imidazole buffer (W1-W5 fractions), then was eluted twice with buffer B (to give the E1, E2 fractions). As cleaved IPNS does not have strong interaction with $Ni^{(II)}$ ions, the protein could be collected in the former set of (W) fractions. According to SDS-PAGE gel analysis results (Figure 2.2), the W1 and W2 fractions were combined and were dialyzed using 10000 MW cutoff dialysis cassettes (Thermo Scientific) to remove metals, using buffer containing 5 mM 1,10-phenantroline and 50 mM EDTA.

The dialyzed mixture was applied to a size exclusion (SEC) column (Superdex 75, 300 mL, GE Healthcare, USA) to remove small molecules and contaminating proteins with different sizes to IPNS. The chromatogram obtained from the SEC purification is shown in Figure 2.2. The fractions showing UV absorbance at 280 nm were analyzed with SDS-PAGE and were found to contain relatively pure ^{15}N labelled IPNS (Figure 2.2). The identity of the protein was confirmed by mass spectrometry showing the expected mass (38206 Da) and confirmed mass (38202 Da) of labelled protein, difference should reveal 99 % of labelling. The obtained enzyme solutions were used for NMR studies.

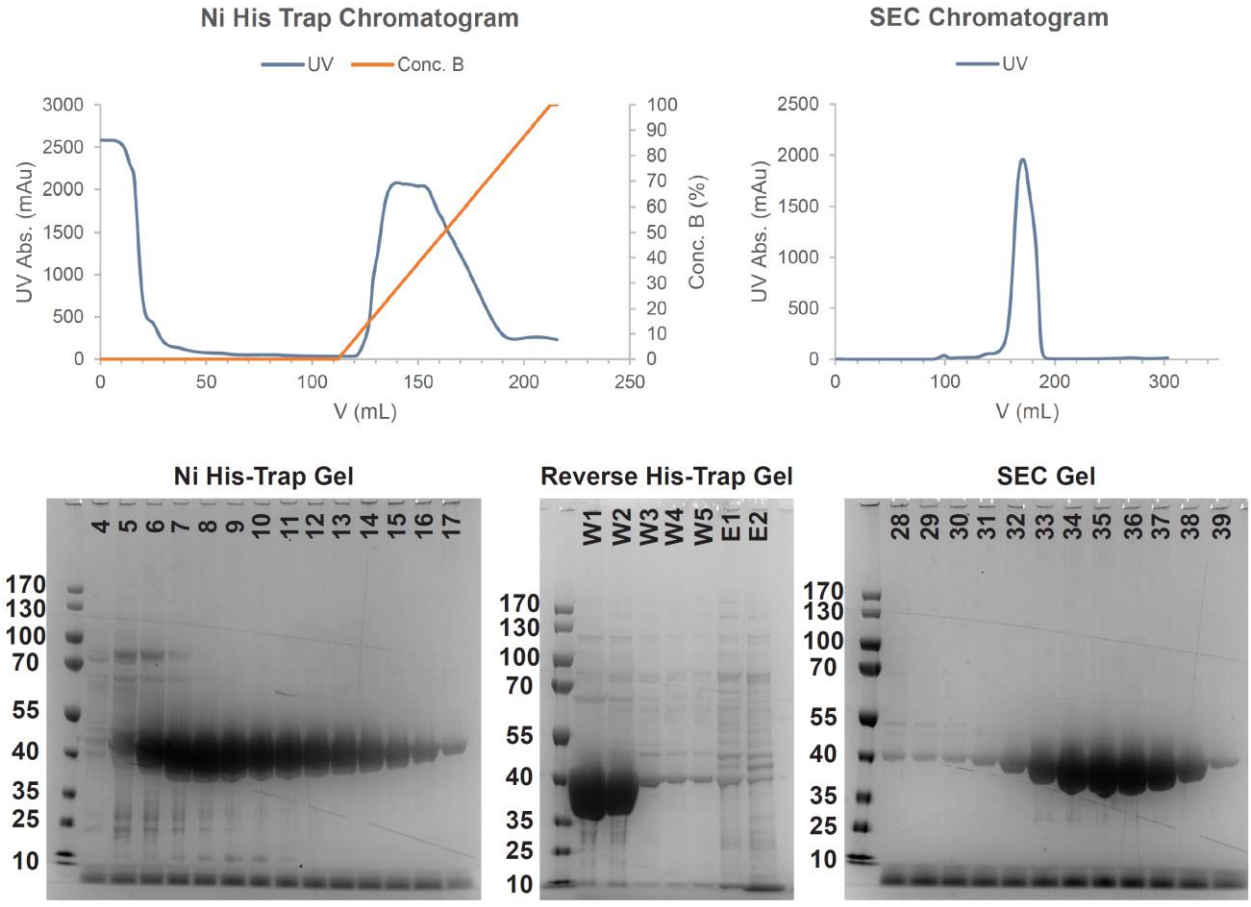


Figure 2.2: Purification of ^{15}N labelled IPNS using nickel his-trap and size exclusion (SEC) chromatography. The SDS-PAGE gel images of analyzed fractions are shown.

2.2.3: ^{1}H-^{15}N HSQC Spectra of IPNS

To examine whether the recombinant ^{15}N labelled IPNS was folded in solution, ^{1}H-^{15}N HSQC spectra were obtained. Cross peaks in ^{1}H-^{15}N HSQC spectra reflect the chemical environment of each amino acid residue NH and peak broadening depends on the tumbling rate of the protein molecules [6]. As the IPNS protein has a relatively slow tumbling rate in solution (compared to small molecules), relatively low sensitivity and resolution are observed in its NMR spectra due to decreased transversal relaxation time (T_2) [1,6-8]. Increasing the sample temperature increases molecular tumbling rates and can enhance NMR spectra resolution. However, higher temperatures can also increase the possibility of enzyme conformational changes, leading to broader peaks in NMR spectra. Additionally, higher temperatures could also destabilize/denature enzymes. Therefore, it was of interest to obtain ^{1}H-^{15}N HSQC spectra of IPNS at different temperatures.

To examine the structure of IPNS bound to its substrate, ACV, $Zn^{(II)}$ was used as a mimic for $Fe^{(II)}$. Since $Zn^{(II)}$ complexes are catalytically inert and have a similar radius to $Fe^{(II)}$, zinc has been widely used as iron mimic for NMR and crystallographic studies on $Fe^{(II)}$ using enzymes [15,16]. An advantage of $Zn^{(II)}$ is that it has a completely filled $3d^{10}$ electronic configuration. This results in no unpaired electrons, making $Zn^{(II)}$ diamagnetic, compared to $Fe^{(II)}$ which is usually paramagnetic. Therefore, IPNS:$Zn^{(II)}$:ACV complexes were prepared under normal (aerobic) conditions to examine their ^{1}H-^{15}N HSQC spectra. The NMR solution contained 100 μM apo ^{15}N labelled IPNS, 300 μM $ZnSO_4$, and 3.2 mM ACV at Tris-d_{11} buffer (at pH 6.50). It is crucial to have sample pH below 7.0 as higher pH will increase amide proton exchange rate causing NH resonance broadening in the spectra [17,18].

Figure 2.3 shows ^{1}H-^{15}N HSQC spectra of IPNS:$Zn^{(II)}$:ACV complex at temperatures ranging from 288 K to 308 K. The HSQC spectrum at 288 K showed poor sensitivity as peak intensities are close to the noise level, and the spectra obtained at 298 K, 303 K, and 308 K showed almost similar peak intensities (Figure 2.3). Looking at the spectrum at 298 K (and higher temperatures), it is notable that there are cross peaks overlapping in central region of the spectrum (Figures 2.3 c, 2.3 d, and 2.3 e). The

molecular weight of IPNS (~ 37.5 KDa) and relatively large number of (331) residues, has led to broad overlapping peaks in the ^{1}H-^{15}N HSQC spectra (Figure 2.3). Additionally, the HSQC spectra at 298 K (and higher temperatures) showed a number of peaks with low intensities (Figure 2.3). Observing peaks with lower intensities could correspond to oligomerized IPNS in the solution as their tumbling rate will be decreased compared to IPNS monomers and will have lower peak intensities. The latter may reflect the observation of unstable IPNS in the NMR samples with $Zn^{(II)}$ and ACV which caused IPNS to precipitate during NMR acquisition. The ^{1}H-^{15}N HSQC spectra of IPNS:$Zn^{(II)}$:ACV complex were obtained at 298 K for a second time (after the aforementioned temperature screening), and were superimposed with the first HSQC spectra at 289 K (Figure 2.4). Comparison of the HSQC spectra also showed a loss in peak intensities over time, potentially indicating a lower amount of monomeric IPNS in the solution (Figure 2.4). The latter was consistent with the observation that IPNS precipitated from the solution containing $Zn^{(II)}$ and ACV.

Since the ^{15}N labelled IPNS sample was unstable with $Zn^{(II)}$, the IPNS:$Fe^{(II)}$:ACV complex was examined for NMR studies. To prevent IPNS turnover in the presence of O_2 and oxidation of the $Fe^{(II)}$, the sample was prepared under anaerobic conditions. The NMR sample was prepared in an anaerobic chamber and contained 100 μM apo ^{15}N labelled IPNS, 300 μM $FeSO_4$, and 3.2 mM ACV in Tris-d_{11} buffer (at pH 6.50). The ^{1}H-^{15}N HSQC spectra of the IPNS:$Fe^{(II)}$:ACV complex were obtained at temperatures ranging from 293 K to 308 K (Figure 2.5). The peak intensities were comparable among different temperatures; the spectra showed broad overlapping peaks in the central region as IPNS is a relatively large molecule. Similar to the spectra obtained from the IPNS:$Zn^{(II)}$:ACV sample, the HSQC spectra of IPNS:$Fe^{(II)}$:ACV revealed peaks with smaller intensities manifesting unstable IPNS in the samples (Figure 2.5). As IPNS was unstable and precipitated with iron and zinc at 100 μM concentration, the thermal stability of apo IPNS was examined (described in Section 2.2.4); subsequently, another batch of ^{15}N labelled IPNS was freshly prepared.

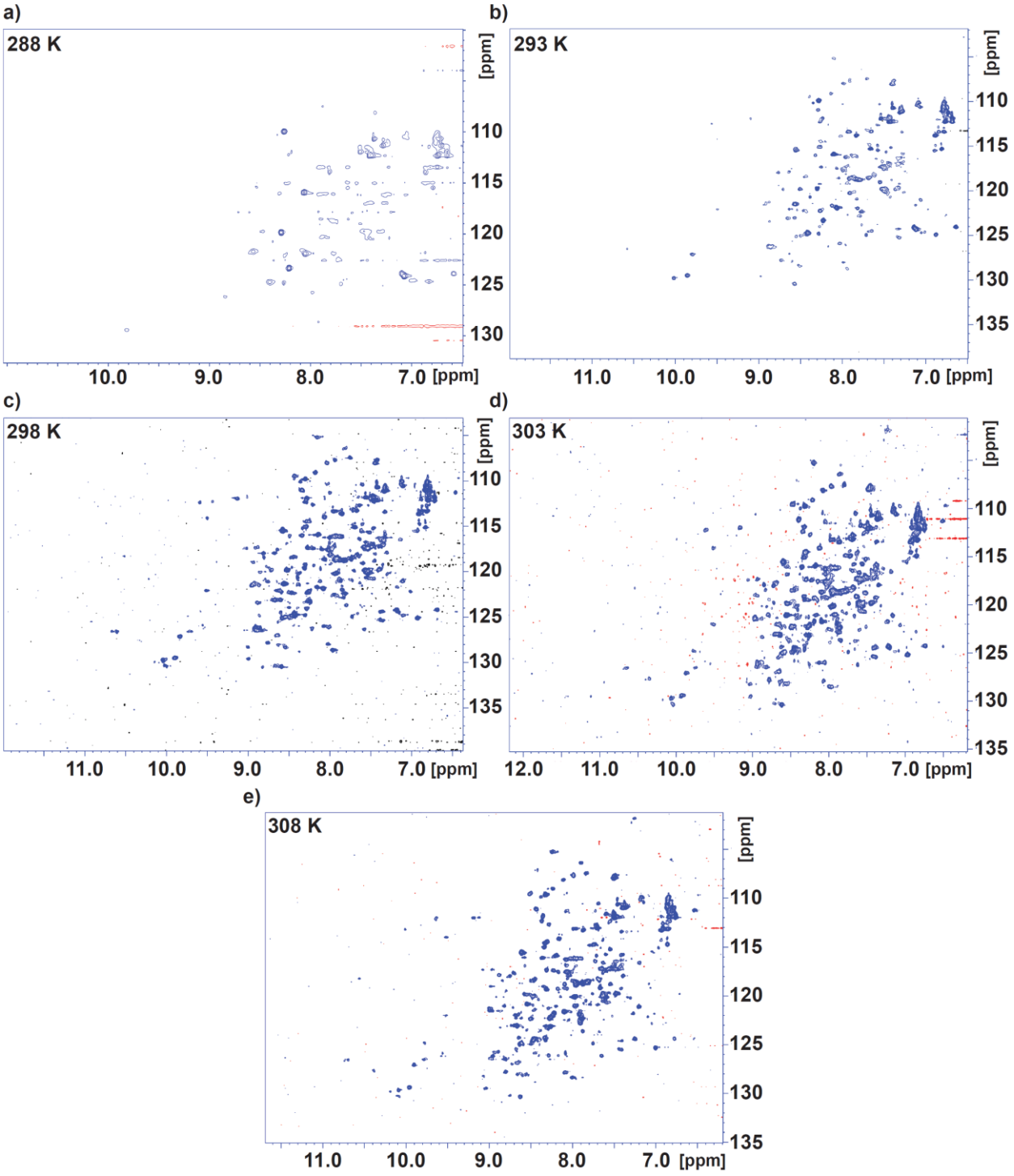


Figure 2.3: Obtained ^{1}H-^{15}N HSQC spectra of ^{15}N labelled IPNS:$Zn^{(II)}$:ACV complex at **(a)** 288 K, **(b)** 293 K, **(c)** 298 K, **(d)** 303 K, and **(e)** 308 K.

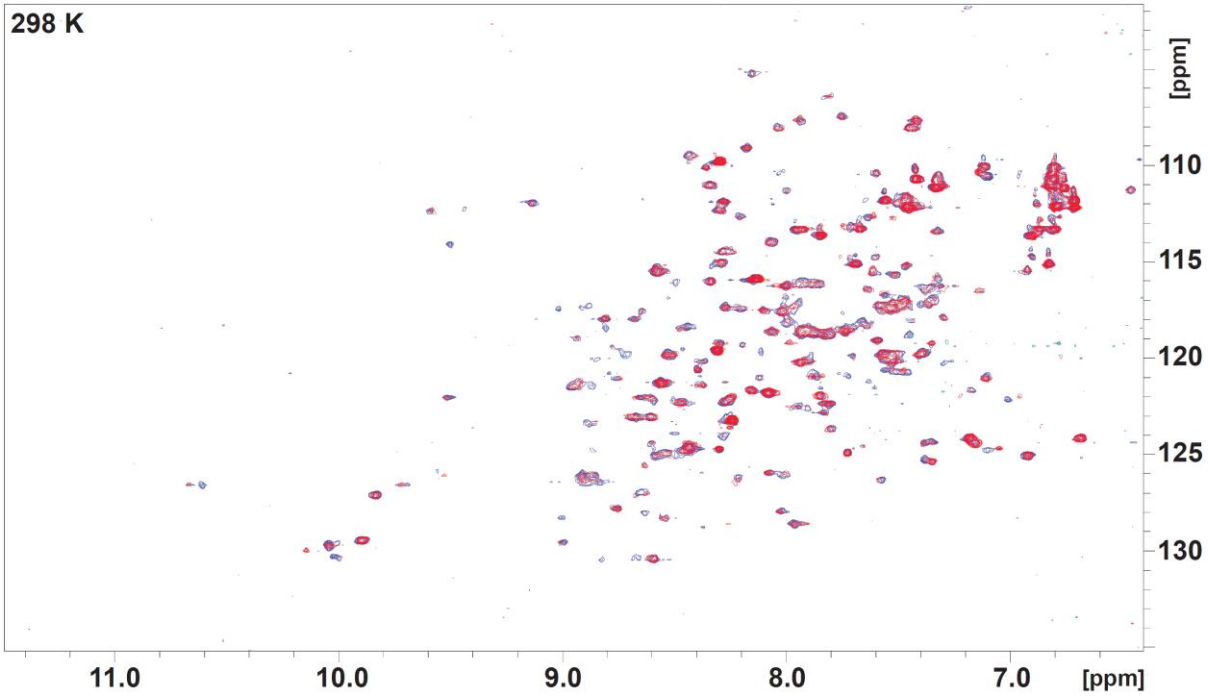


Figure 2.4: Obtained ^{1}H-^{15}N HSQC spectra of ^{15}N labelled IPNS:$Zn^{(II)}$:ACV complex at 298 K (blue) superimposed with the spectra recorded from the same sample at 298 K after temperature screening (red).

Comparison of HSQC spectra obtained from IPNS samples with zinc (aerobic) and iron (anaerobic) could indicate whether zinc is a suitable substitute for iron. A superimposition of the ^{1}H-^{15}N HSQC spectra of the IPNS:$Zn^{(II)}$:ACV and IPNS:$Fe^{(II)}$:ACV samples is shown in Figure 2.6. The peak positions and intensities were fairly similar in the IPNS samples with zinc and iron ions. The similarity of the HSQC spectra indicates that the substitution of iron with zinc does not significantly change the IPNS structure. Moreover, $Fe^{(II)}$ complexes may or may not be paramagnetic, depending on the coordination geometry and ligand field strength (e.g. energy gap between the metal 3d orbitals) [19]. The effects of paramagnetic metal ions bound to the enzymes have been widely studied by NMR; it has been observed that paramagnetic metals can broaden and shift NMR peaks [20]. The similarity of HSQC spectra of IPNS:$Zn^{(II)}$:ACV and IPNS:$Fe^{(II)}$:ACV samples support the proposal that $Fe^{(II)}$ is diamagnetic when is bound to IPNS and ACV under anaerobic conditions.

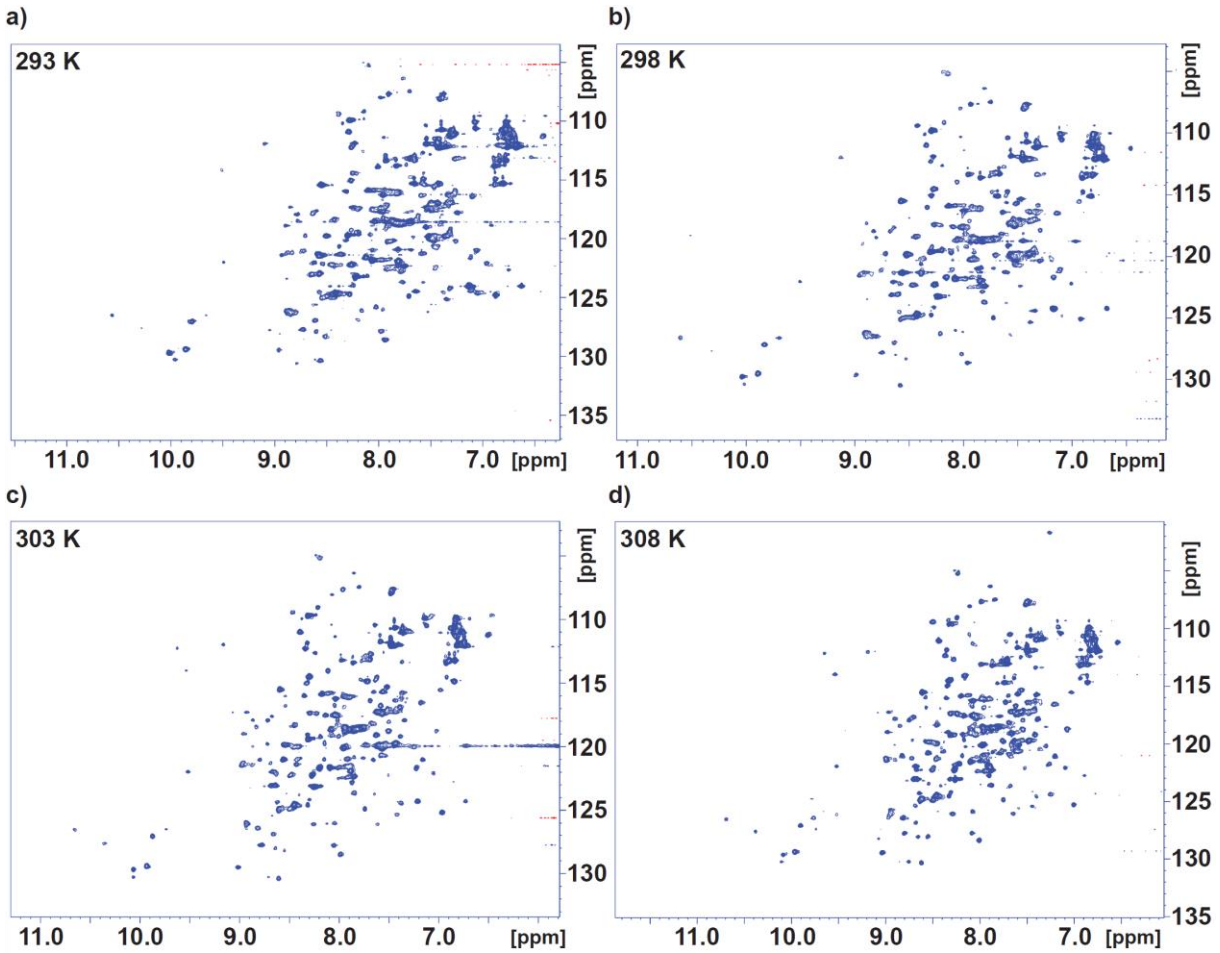


Figure 2.5: Obtained ^{1}H-^{15}N HSQC spectra of ^{15}N labelled IPNS:$Fe^{(II)}$:ACV complex samples under anaerobic conditions at **(a)** 293 K, **(b)** 298 K, **(c)** 303 K, and **(d)** 308 K.

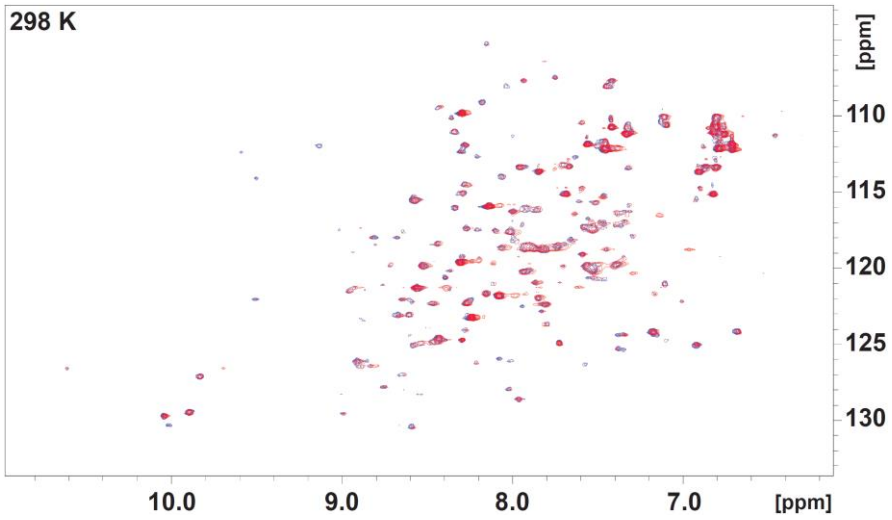


Figure 2.6: Superimposed ^{1}H-^{15}N HSQC spectra of ^{15}N labelled IPNS:$Zn^{(II)}$:ACV (blue, aerobic) and IPNS:$Fe^{(II)}$:ACV (red, anaerobic) samples obtained at 298 K.

2.2.4: Examining IPNS Melting Temperature (T_m)

The thermal stability of unlabelled IPNS was examined as the purified ^{15}N labelled IPNS with $Zn^{(II)}$ and $Fe^{(II)}$ appeared to be unstable and precipitated in NMR buffer at ambient temperatures (Section 2.2.3). One well known approach to examine an enzyme's thermal stability is to measure its melting temperature (T_m). At the melting temperature of a protein, there is considered to be equal populations of folded and unfolded proteins [21,22].

Thus, IPNS was treated with the SYPRO orange dye which has fluorescence emission in its planar conformation [21,22]. As the sample temperature increases and proteins become partially unfolded, the SYPRO orange molecules diffuse into / bind with the protein. Since SYPRO orange molecules have limited flexibility inside the protein, the planar conformation can be more favoured and hence, the fluorescence activity will increase [21,22]. Therefore, in the samples containing protein and SYPRO grange dye, monitoring the sample fluorescence (RFU at 600 nm) at different temperatures (typically from 20 ^oC to 95 ^oC) can result in a sigmoidal-shaped melt curve [21,22]. The mid-point of the melt curve is the melting temperature (T_m). Plotting the first derivative of the melt curve (-dRFU/dT) is useful to measure the protein T_m value [21,22].

In order to obtain IPNS melt curves with a measurable increase in fluorescence, it was necessary to optimize the ratio of dye to protein in the sample. Initially, different samples including 1 μM to 4 μM apo IPNS and SYPRO orange dye with 1x to 4x dilution factors were prepared. All the samples were in 50 mM Tris buffer at pH 6.50 (similar to the NMR conditions). The melt curves and the melt curve derivatives of samples with different concentrations of IPNS (2 μM, 4 μM) and dye (1x-4x dilution factors) are shown in Figure 2.7 a. All conditions with 2 μM IPNS did not reveal sufficient rise in fluorescence and the condition with 4 μM IPNS and 4x dye concentration showed the sharpest increase in fluorescence (Figure 2.7 a). As the obtained melt curve was sigmoidal-shaped with sufficient fluorescence rise for reliable measurement of protein melting temperature (T_m), the conditions with higher protein and dye concentrations were not examined. Therefore, the latter condition with 4 μM IPNS and 4x SYPRO orange concentrations were used for further thermal stability assays. The T_m values were almost similar among different

conditions and the sample with 4 μM IPNS and 4x dye concentration showed T_m value of 35.6 °C (Figure 2.7 a).

After optimizing the conditions for the T_m shift assay, samples with 4 μM apo IPNS and various concentrations of ACV (up to 40 eq.) and $Zn^{(II)}$ (up to 12 eq.) were analyzed. Similar to the NMR studies, $Zn^{(II)}$ was chosen as it does not react/bind with O_2 and is a mimic for $Fe^{(II)}$. The addition of ACV alone did not significantly shift the T_m value, whereas $Zn^{(II)}$ addition increased the IPNS T_m. Figure 2.7 b shows the melting curve and melt curve derivative diagrams of samples with 4 μM IPNS, 32 eq. ACV, and various ratios of $Zn^{(II)}$ (0-12 eq.). The T_m value of IPNS increased from 35.6 °C (apo enzyme) to 42.6 °C in the sample with 12 eq. $Zn^{(II)}$ and 32 eq. ACV (Figure 2.7 b).

The effects of other metals including $Ni^{(II)}$, $Mn^{(II)}$, $Co^{(II)}$, $Cu^{(II)}$, $Zn^{(II)}$, $Cd^{(II)}$, and $Fe^{(III)}$ on T_m value of IPNS were examined to determine which stabilizes IPNS. Figure 2.7 c shows the melting curves and melt curve derivatives of samples with 4 μM IPNS, 5 eq. metal, and 32 eq. ACV. Amongst the metals studied, $Ni^{(II)}$ revealed the highest T_m value (46 °C) which could, at least in part, be due to unspecific binding of $Ni^{(II)}$ to IPNS. The sample with $Cu^{(II)}$ did not show a sigmoid-shaped curve, and the sample with $Mn^{(II)}$ revealed the lowest T_m value (37.4 °C). The obtained T_m values of samples with $Co^{(II)}$, $Zn^{(II)}$, $Cd^{(II)}$, and $Fe^{(III)}$ were 41 °C, 40.8 °C, 40.6 °C, and 38.6 °C, respectively (Figure 2.7 c). Considering the obtained T_m values, the IPNS:$Zn^{(II)}$:ACV complex was chosen for further work as it appeared to be stable and manifested little denaturation at ambient temperatures.

The presence of L-arginine and L-glutamate in solution can increase protein stability [23]. In this regard, it has been observed that the protein solubility can increase in presence of L-arginine and L-glutamate, and the maximum solubility can be achieved when L-Arg and L-Glu are equimolar [23]. A computational study has shown that L-Arg and L-Glu can stabilize proteins via forming H-bonds and ionic interactions with the oppositely charged residues on protein surface; hence protein aggregation can be inhibited [24].

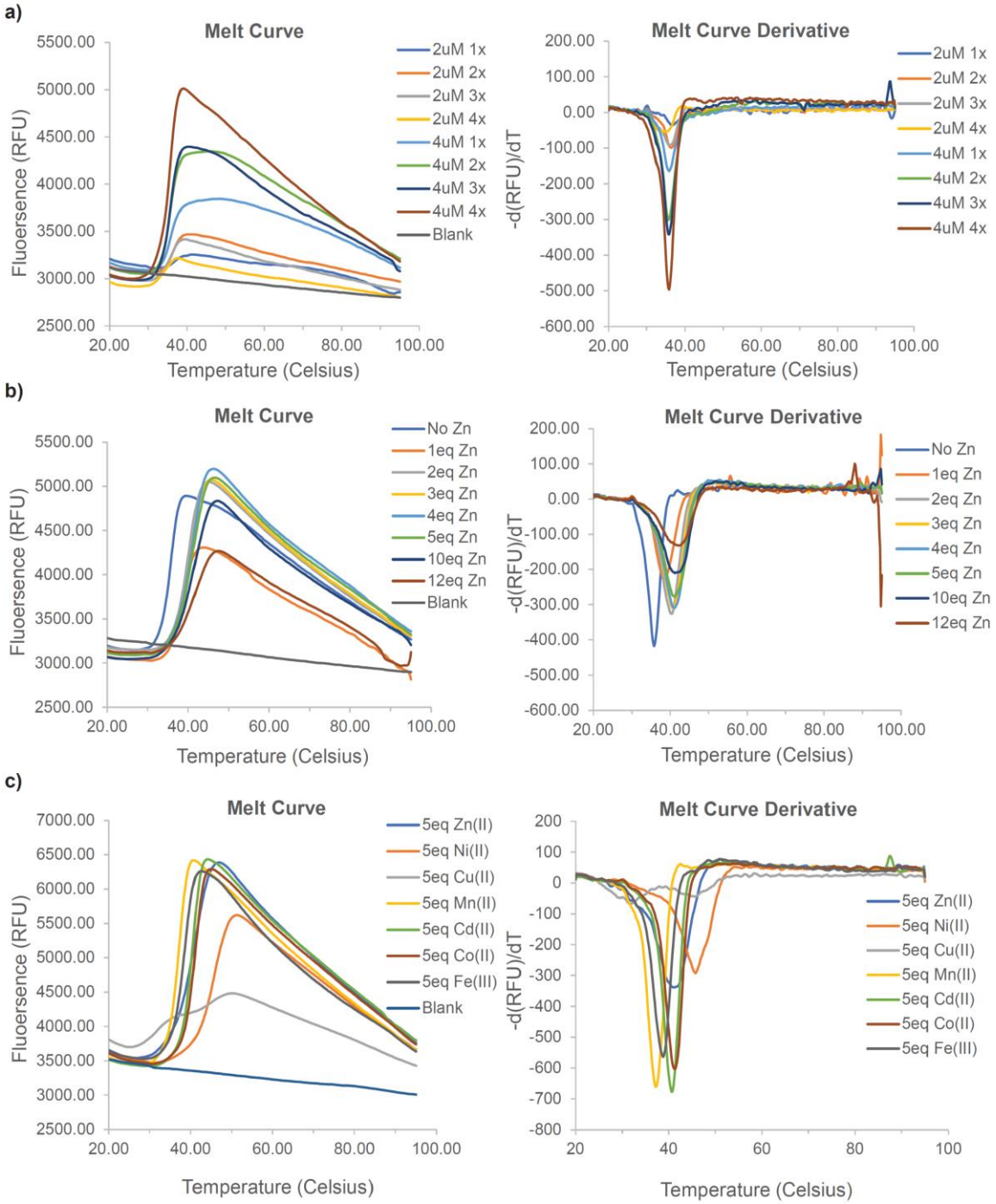


Figure 2.7: **(a)** melting curves and curve derivatives of samples with 2 μM and 4 μM apo IPNS and SYPRO orange dye with 1x to 4x dilution factors. A sample without protein and with 4x dye concentration was used as a control. **(b)** Obtained melting curves and melt curve derivatives of samples with 4 μM IPNS, 32 eq. ACV, and various concentrations of $ZnSO_4$ (up to 12 eq.). The sample without protein and with 4x dye concentration was chosen as blank. (c) Melting curves and melt curve derivatives of samples with 4 μM IPNS, 32 eq. ACV, and 5 eq. of metals including $Ni^{(II)}$, $Mn^{(II)}$, $Co^{(II)}$, $Cu^{(II)}$, $Zn^{(II)}$, $Cd^{(II)}$, and $Fe^{(III)}$. The sample without protein and with 4x dye concentration was chosen as blank.

In order to investigate whether L-arginine and L-glutamate increase the IPNS melting temperature, T_m values of IPNS in the presence of equimolar L-arginine and L-glutamate were measured. Figure 2.8 shows the melt curves and melt curve derivatives of samples including 4 μM IPNS, 5 eq. $Zn^{(II)}$, and 32 eq. ACV in presence of equimolar L-arginine and L-glutamate with various concentrations (1:1 molar ratio, up to 50 mM). The conditions with higher additive concentrations were not prepared due to the limited solubility of L-glutamate in water at ambient temperatures. According to the obtained T_m values, the IPNS melting temperatures increased from 41.2 °C (in absence of additives) to 43.2 °C in the sample with 50 mM L-arginine and 50 mM L-glutamate (Figure 2.8). Therefore, equimolar L-arginine and L-glutamate were added to the IPNS NMR samples to prevent protein precipitation during NMR studies.

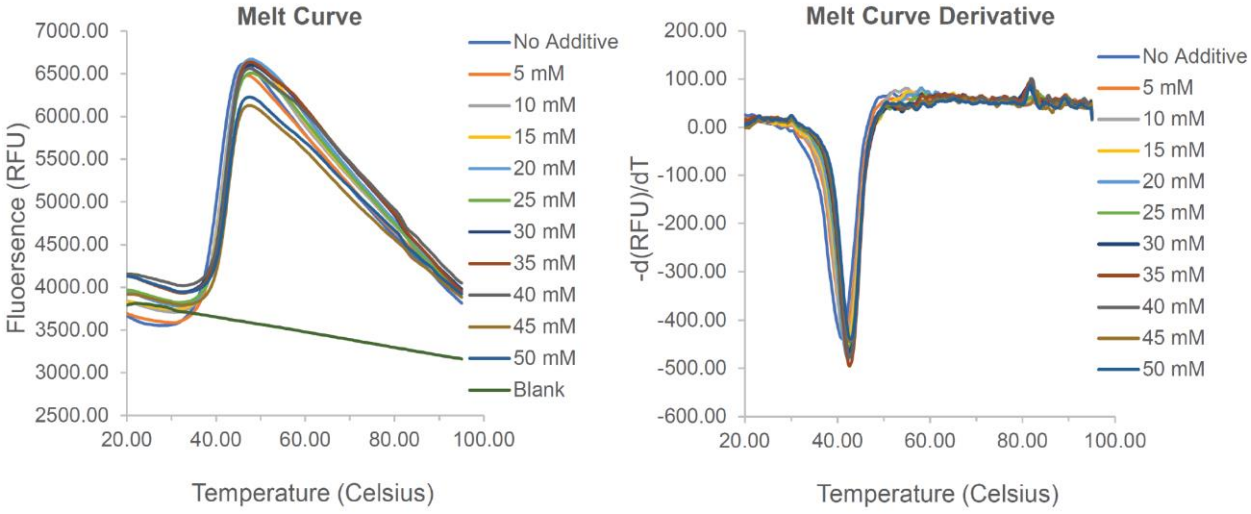


Figure 2.8: Obtained melting curves and melt curve derivatives of samples with 4 μM IPNS, 5 eq. $ZnSO_4$, and 32 eq. ACV with equimolar amounts of L-arginine and L-glutamate (1:1 molar ratio) with various concentrations (up to 50 mM). The sample without protein and with 4x dye concentration was used as a control.

2.2.5: Second Batch of ^{15}N Labelled IPNS ^{1}H-^{15}N HSQC Spectra

The first batch of ^{15}N labelled IPNS was unstable in NMR solution samples with precipitation being observed over time (Section 2.2.3). Therefore, a fresh batch of recombinant ^{15}N labelled IPNS was produced in *E. coli* using ^{15}N labelled minimal M9 medium and purified as described in Section 2.2.2. Because NMR sample pH should be at 6.50 (i.e. mildly acidic to prevent backbone NH exchanges), all buffers used for protein

purification were at pH 6.50 during NMR sample preparation. According to IPNS thermal stability assays, titration of $Zn^{(II)}$ into apo IPNS stabilized the protein, and the IPNS:$Zn^{(II)}$ complex is relatively stable compared to other metal ions in the presence of ACV (Figure 2.7). Therefore, the condition with IPNS, 3 eq. $ZnSO_4$, and 32 eq. ACV was chosen for NMR studies. Because L-arginine and L-glutamate can not only help to prevent protein aggregation [23,24] but also increased the IPNS:$Zn^{(II)}$:ACV T_m value (Figure 2.8), 50 mM L-arginine and 50 mM L-glutamate were also added to the NMR solution.

Figure 2.9 shows ^{1}H-^{15}N HSQC spectra obtained from the second batch of ^{15}N labelled IPNS in complex with $Zn^{(II)}$ and ACV at different temperatures. The NMR samples contained 100 μM apo ^{15}N labelled IPNS, 300 μM $ZnSO_4$, 3.2 mM ACV, 50 mM L-arginine, and 50 mM L-glutamate at 50 mM Tris-d_{11} buffer at pH 6.50. The peak intensities in the HSQC spectra were observed to slightly increase from 293 K to 298 K; whereas peak intensities remained stable from 298 K to 308 K (Figure 2.9). Furthermore, peak overlap in the central region of the HSQC spectra was observed (Figure 2.9), which is similar to the observed spectra of the first batch of ^{15}N labelled IPNS (Section 2.2.3). It is noteworthy that the cross peaks in the HSQC spectra of the second IPNS batch showed similar broadening and seemed to be uniform in size (Figure 2.9), which contrasts with the HSQC spectra from the first IPNS batch (Figure 2.3). The observed uniform peak broadening could indicate that the second IPNS batch was thermally stable in the NMR sample, that is no aggregation / oligomerization was occurring.

The second batch of ^{15}N labelled IPNS:$Zn^{(II)}$:ACV was apparently stable under NMR conditions for over a week with no precipitation being observed. The ^{1}H-^{15}N HSQC spectrum of IPNS:$Zn^{(II)}$:ACV at 298 K was obtained for second time after temperature screening, and the sample was stored at room temperature for one week and its ^{1}H-^{15}N HSQC spectrum was obtained for third time. The obtained first, second, and third ^{1}H-^{15}N HSQC spectra of IPNS:$Zn^{(II)}$:ACV at 298 K are shown in Figures 2.10 a, 2.10 b, and 2.10 c, respectively. The HSQC spectrum was found to be stable over time (up to one week), indicating that the IPNS:$Zn^{(II)}$:ACV complex is stable under NMR conditions at ambient temperature for a substantial time.

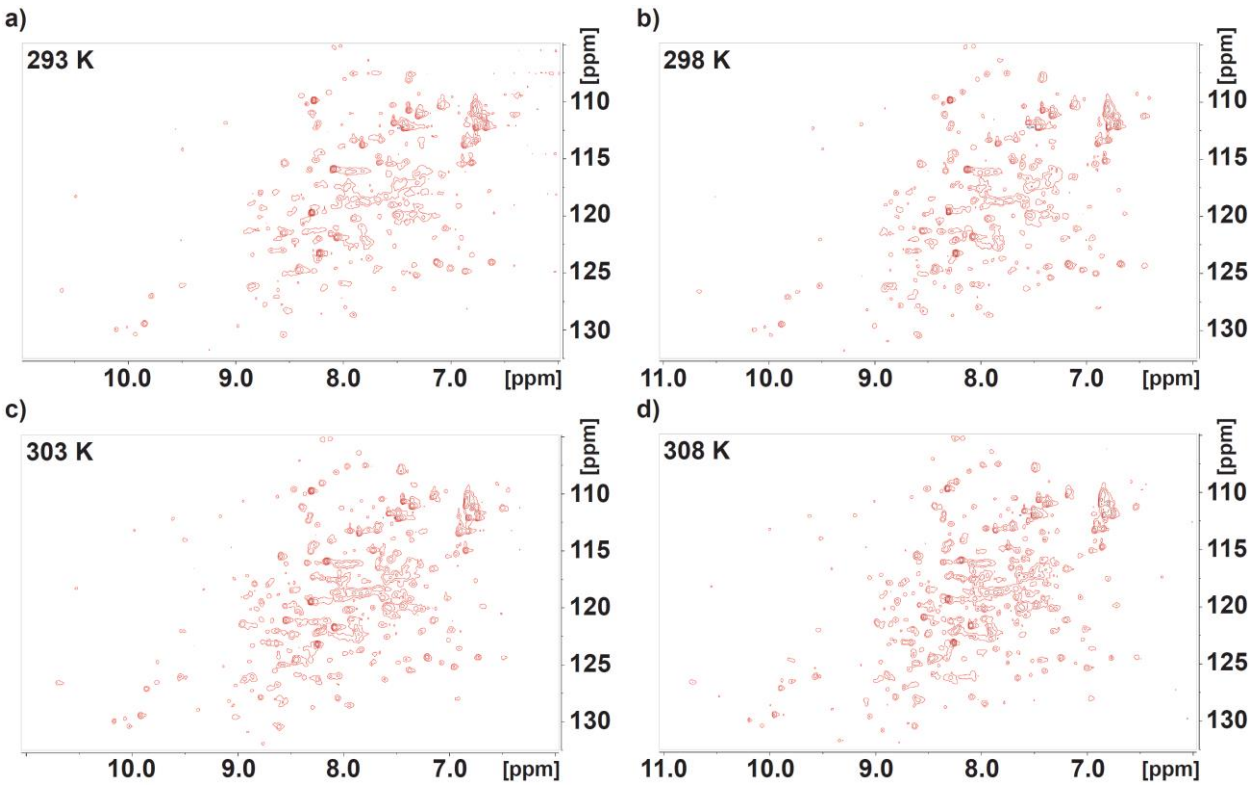


Figure 2.9: Obtained ^{1}H-^{15}N HSQC spectra of ^{15}N labelled (second batch) IPNS:$Zn^{(II)}$:ACV complex at **(a)** 293 K, **(b)** 298 K, **(c)** 303 K, and **(d)** 308 K.

It has been observed that the broad peaks with unusually low chemical shifts (below 0 ppm) in protein ^{1}H NMR spectra often correspond to side chain methyl groups which are in proximity of aromatic side groups, due to anisotropic effects of aromatic rings [25]. The mentioned methyl peak positions can be sensitive probes for local protein structure and dynamics [25]. Accordingly, the shielded region (below 0.0 ppm) of the ^{1}H NMR spectrum was also examined for IPNS:$Zn^{(II)}$:ACV sample (Figure 2.10 d). Comparison of the spectra obtained from the fresh sample, from the sample after temperature screening, and from the sample after one week showed similar ^{1}H NMR spectra in the shielded region (Figure 2.10 d). This observation indicates that the amount of monomeric IPNS:$Zn^{(II)}$:ACV in the solution did not change and the protein was not destabilized at ambient temperatures over a reasonable time. Therefore, it was proposed that labelled IPNS using similar conditions could be used for further NMR analysis.

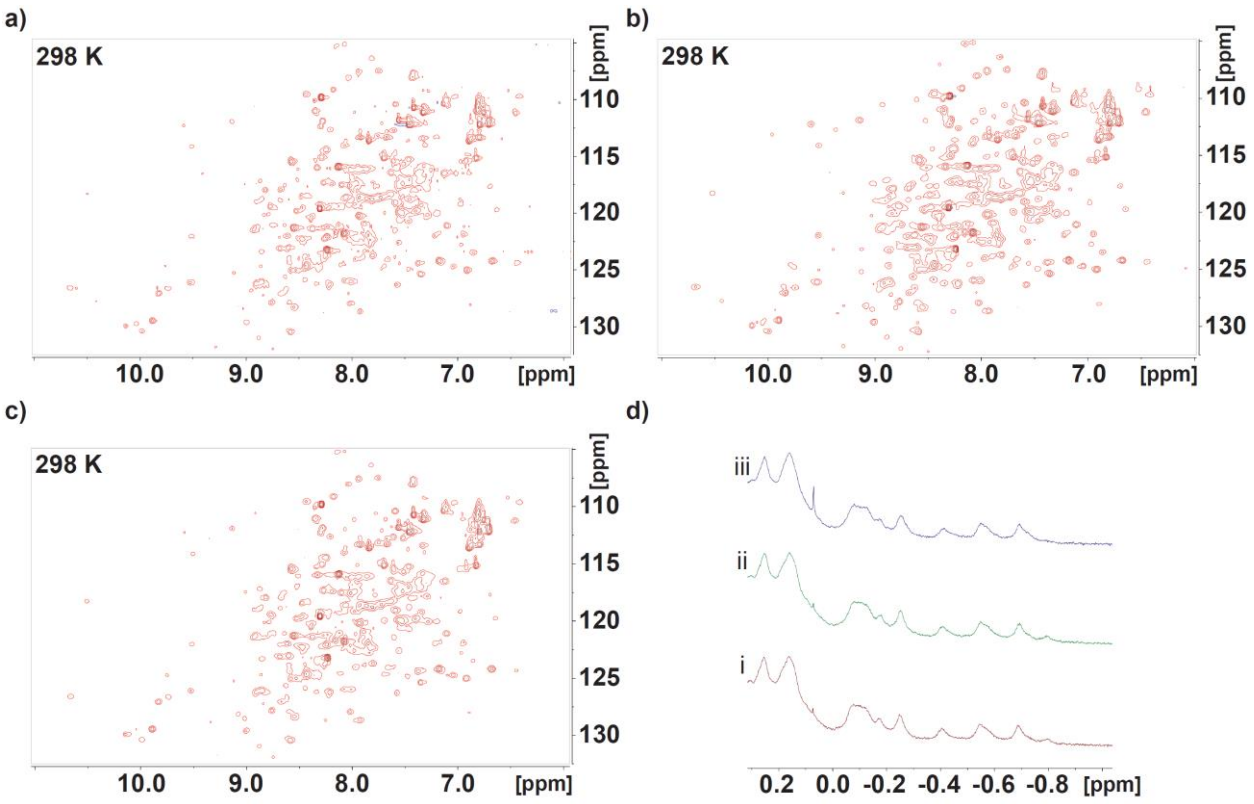


Figure 2.10: Spectra of ^{15}N labelled (second batch) IPNS:$Zn^{(II)}$:ACV complex obtained at 298 K. **(a)** The first ^{1}H-^{15}N HSQC spectrum obtained, **(b)** The second ^{1}H-^{15}N HSQC spectrum obtained after 3 hours, and **(c)** the third ^{1}H-^{15}N HSQC spectra obtained after one week, which showed similar peak intensities as in (a) and (b). **(d)** Comparison of ^{1}H NMR spectra in the shielded region obtained for first time (i), second time after 3 hours (ii), and the third time after one week (iii).

The HSQC spectra of ^{15}N labelled IPNS showed overlapping peaks. It has been demonstrated that TROSY 2D NMR spectra can enhance the resolution for larger proteins [6-8]. Therefore, a ^{1}H-^{15}N TROSY-HSQC spectrum of the IPNS:$Zn^{(II)}$:ACV sample was obtained and compared with its conventional HSQC spectrum (Figure 2.11). The TROSY-HSQC spectra showed fewer overlapping peaks in the central region of the spectra as peaks exhibited slightly less broadening in the ^{1}H dimension (Figure 2.11 a). The superimposed TROSY-HSQC and HSQC spectra of an IPNS:$Zn^{(II)}$:ACV sample also showed slightly better resolution in the TROSY-type spectrum (Figure 2.11 b). The peak intensities in the TROSY-HSQC spectrum are however less than those of the conventional HSQC spectrum (Figure 2.11 b). The latter observation is because peaks in TROSY-type spectra are one of four coupled peaks stemming from an HSQC spectrum without decoupling [7]. Moreover, all cross peaks are diagonally shifted in TROSY-type

spectra (with respect to the conventional HSQC), due to scalar ^{1}J (^{1}H,^{15}N) coupling (Figure 2.11 b) [7]. Although the TROSY-HSQC spectrum of ^{15}N labelled IPNS showed slightly better resolution, the spectrum still contained many overlapping peaks. Therefore, it was considered of interest, to examine TROSY-HSQC spectra of per-deuterated ^{15}N labelled IPNS, because a combination of TROSY analysis and per-deuteration should further enhance resolution as per-deuteration will minimize dipole-dipole (DD) interactions with protein NHs (discussed in Section 2.2.6) [6-8].

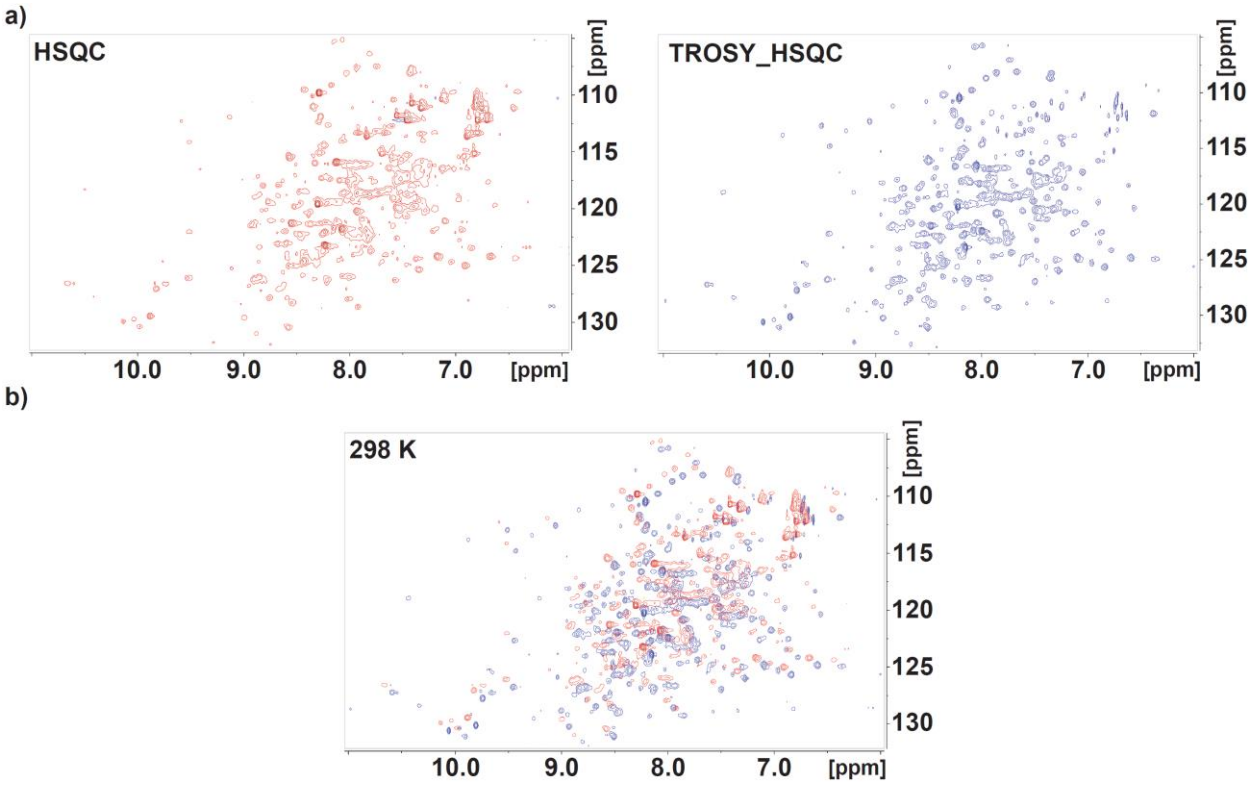


Figure 2.11: Spectra of ^{15}N labelled (second batch) IPNS:$Zn^{(II)}$:ACV complex at 298 K. **(a)** Conventional ^{1}H-^{15}N HSQC and TROSY-type ^{1}H-^{15}N HSQC spectra. **(b)** Superimposed HSQC (red) and TROSY-HSQC (blue) spectra at 298 K.

2.2.6: Expression and Purification of Per-deuterated ^{15}N Labelled IPNS

As shown in Section 2.2.5, the resulting ^{1}H-^{15}N HSQC spectra of ^{15}N labelled IPNS exhibited overlapping peaks, and the TROSY-type spectra slightly enhanced resolution. Therefore, per-deuterated ^{15}N labelled IPNS was produced to enhance the resolution in HSQC spectra via minimizing dipole-dipole interactions between ^{1}H nuclei [6]. To produce per-deuterated ^{15}N labelled IPNS, *E. coli* BL21 cell lines containing WT_IPNS vector were grown in a labelled minimal M9 medium. The M9 medium was prepared using the recipe

shown in Table 2.1, $^{15}NH_4Cl$ was used as sole nitrogen source and the medium ingredients were dissolved in D_2O. The labelled IPNS was produced in 1L of minimal M9 medium using the same protocol explained in Section 2.2.1. However, the cell growth and protein expression rates were slower than expressions in H_2O based M9 media.

The per-deuterated ^{15}N labelled IPNS was purified in one step with nickel resin using the gravity flow method (purification details given in Section 2.3.2). In brief, cell lysates were loaded onto the nickel resins pre-equilibrated with buffer A (5 mM imidazole); after allowing sufficient time (30 minutes), the flowthrough was collected (fraction W1). The nickel resin column was then washed four times with equal volumes (5 mL) of buffer A (giving fractions W2-W5). Subsequently, the nickel resin column was eluted with four buffers (1 CV) with 20 mM, 40 mM, 60 mM, and 500 mM imidazole concentrations; the fractions were collected at each step and labelled as E1, E2, E3, and E4, respectively. The SDS-PAGE gel image of W1-W5 and E1-E4 fractions showed relatively pure IPNS band in E4 fraction (Figure 2.12 a). The fraction containing IPNS was collected, concentrated and stored at -80 ^oC for NMR analysis. The amount of per-deuterated ^{15}N labelled IPNS obtained (approx. 1.5 mg) was sufficient for a few NMR samples.

The non-deuterated ^{15}N labelled IPNS sample showed methyl peaks at low chemical shifts (below 0 ppm) in the ^1H NMR spectrum (Figure 2.10 d). Observing the shielded region in ^1H NMR spectrum of per-deuterated ^{15}N labelled IPNS may inform on whether the non-exchangeable protons (e.g. methyl groups) are replaced with deuterons. Figure 2.12 b shows the shielded region in ^1H NMR spectrum of samples containing 100 μM non-deuterated and per-deuterated ^{15}N labelled IPNS (both in complex with $Zn^{(II)}$ and ACV). The ^1H NMR spectrum of per-deuterated ^{15}N labelled IPNS sample showed no peaks in the shielded methyl region, whereas the methyl peaks are observable in the non-deuterated IPNS sample. These observations confirm that the side chain protons were replaced with deuterons in the per-deuterated IPNS (Figure 2.12 b).

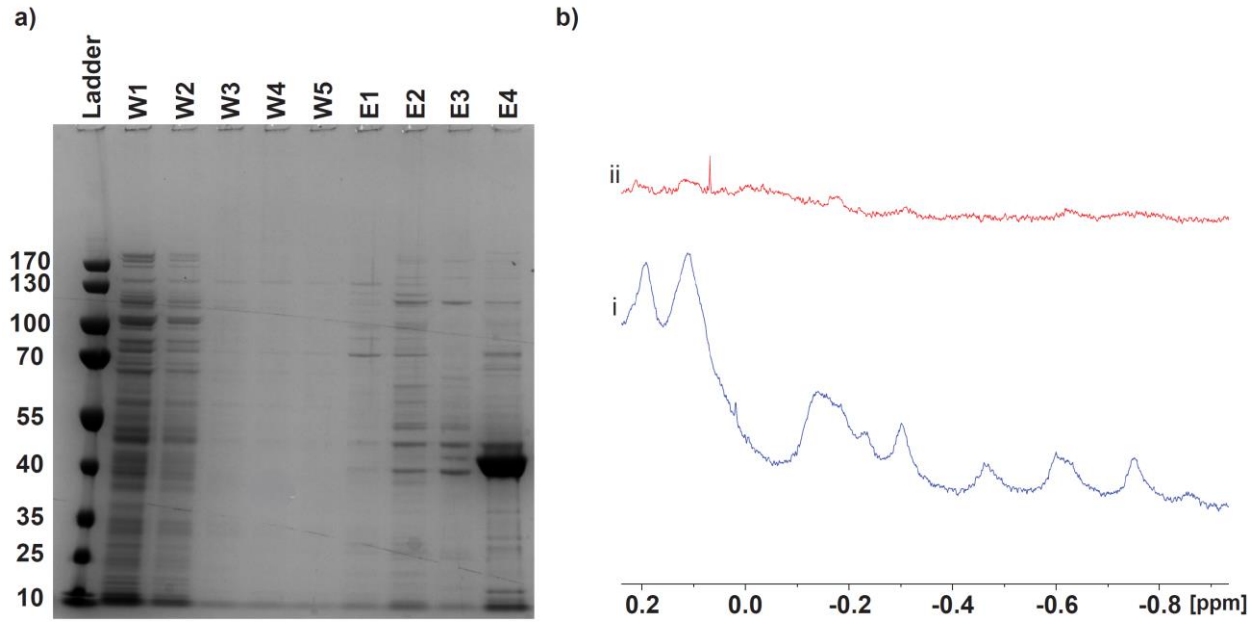


Figure 2.12: **(a)** Purification of per-deuterated ^{15}N labelled IPNS with nickel resins using a gravity flow method. The SDS-PAGE gel image of W1-W5 and E1-E4 fractions is shown. **(b)** Comparison of the shielded methyl region in the ^{1}H NMR spectra obtained from non-deuterated (i) and per-deuterated (ii) ^{15}N labelled IPNS samples. Both samples contained 100 μM IPNS, 300 μM $ZnSO_4$, and 3.2 mM ACV.

2.2.7: Effect of IPNS Per-deuteration on TROSY-Type ^{1}H-^{15}N HSQC Spectra

In order to examine whether per-deuteration can enhance the quality of IPNS HSQC spectra, conventional and TROSY-type ^{1}H-^{15}N HSQC spectra of the per-deuterated ^{15}N labelled IPNS were obtained (Figure 2.13). The NMR samples contained 100 μM ^{15}N labelled IPNS (for both non-deuterated and per-deuterated enzymes), 300 μM $ZnSO_4$, 3.2 mM ACV, 50 mM L-Arg, 50 mM L-Glu, and 50 mM Tris-d_{11} at pH 6.50.

The conventional ^{1}H-^{15}N HSQC spectrum of the per-deuterated IPNS sample showed slightly better resolution, however some peaks were still overlapping (Figure 2.13 a). In addition, compared to the non-deuterated IPNS, some peaks were missing in the HSQC spectrum of the per-deuterated IPNS (Figure 2.13 a). The latter observation is because some of the main chain NHs in the protein core were still deuterated and were

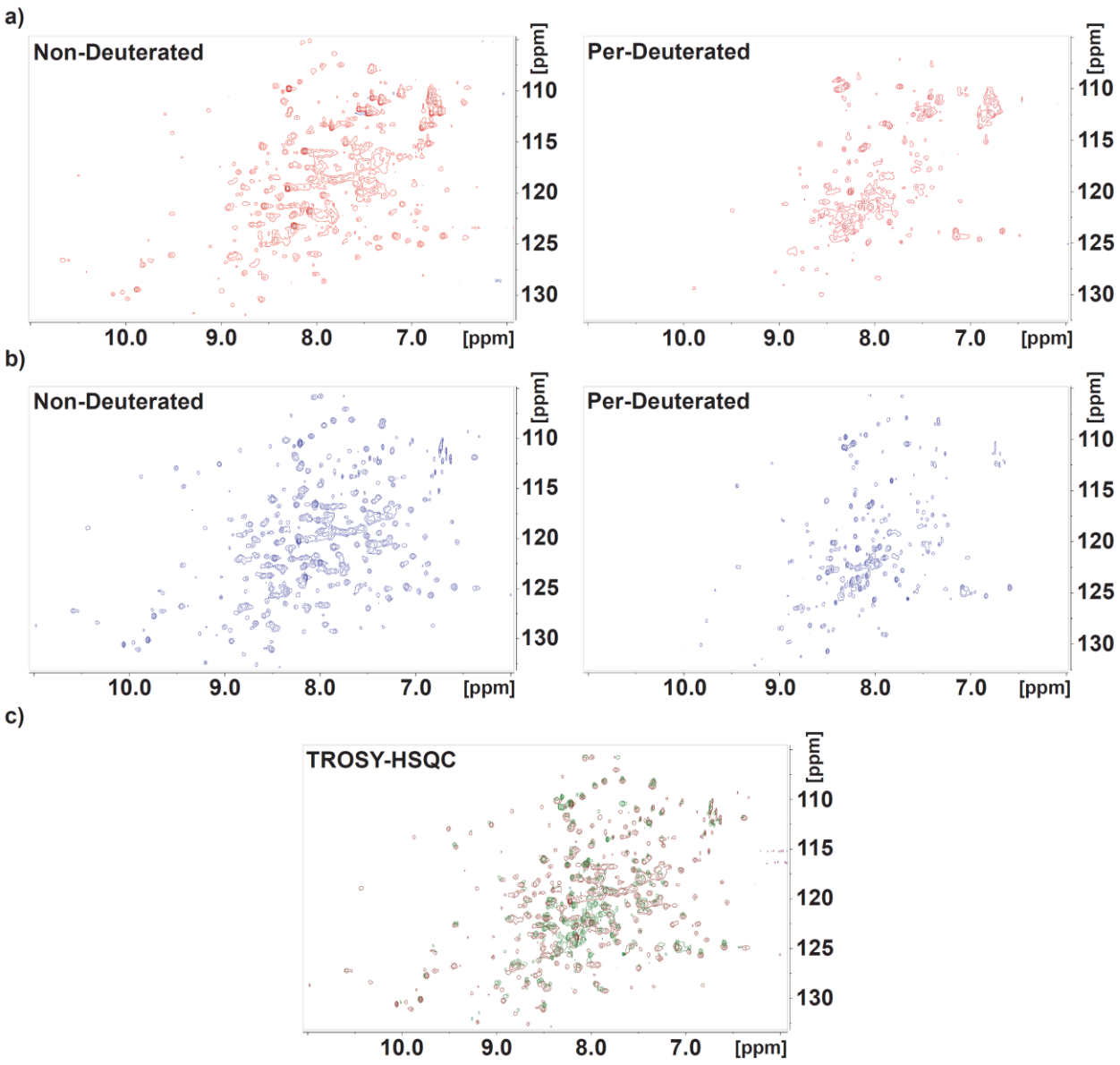


Figure 2.13: **(a)** Conventional ^{1}H-^{15}N HSQC spectra obtained from non-deuterated and per-deuterated IPNS samples in complex with $Zn^{(II)}$ and ACV. **(b)** TROSY-type ^{1}H-^{15}N HSQC spectra obtained from non-deuterated and per-deuterated IPNS samples in complex with $Zn^{(II)}$ and ACV. **(c)** Superimposed TROSY-type ^{1}H-^{15}N HSQC spectra of the non-deuterated (red) and per-deuterated (green) IPNS samples.

not exchanged with H_2O protons. Comparing the TROSY-type spectra between non-deuterated and per-deuterated IPNS also showed better resolution in the per-deuterated sample (Figure 2.13 b). In particular, the central region of the ^{1}H-^{15}N TROSY-HSQC spectrum of the per-deuterated IPNS showed a lower number of overlapping peaks (Figure 2.13 b). The superimposed ^{1}H-^{15}N TROSY-HSQC spectra of the non-deuterated

and per-deuterated IPNS samples also revealed better resolution (Figure 2.13 c). Accordingly, to overcome poor resolution in IPNS ^{1}H-^{15}N HSQC spectrum, a combination of per-deuteration and TROSY effect may be used to enhance resolution. On the other hand, some resonances were missing in the spectra of per-deuterated IPNS, possibly due to incomplete proton exchange between backbone NHs and H_2O. To obtain a better proton exchange in future work, the labelled IPNS may be purified using buffers with higher pH (e.g. pH 7.50) with subsequent exchange into an NMR buffer with pH 6.50. Alternatively, denaturing and subsequent refolding of the protein in H_2O may facilitate sufficient proton exchange with the backbone NHs.

2.2.8: Production of Per-deuterated ^{13}C-^{15}N Labelled IPNS

After examining IPNS expression trials in unlabelled, ^{15}N labelled, and ^{2}H-^{15}N doubly labelled minimal M9 media, triple labelled M9 medium was prepared. The M9 medium was prepared using the recipe shown in Table 2.1; $^{15}NH_4Cl$ and ^{13}C-glucose-D_7 were used as nitrogen and carbon sources, respectively. Subsequently, the M9 medium ingredients were dissolved in D_2O. After transforming the WT_IPNS vector into the *E. coli* BL21 cell line (using heat shock), cells were grown in the triple labelled minimal M9 medium using the protocol explained in Section 2.2.2; 3L of the resultant growth was used for large-scale production. After treatment of the culture with IPTG (500 μM final concentration), the culture was incubated at 18 ^{o}C for 48 hours. The cells exhibited extremely slow growth, with the OD_{600} only reaching 0.6 after 48 hours. Despite allocating seemingly sufficient time for growth and protein expression phases, the amounts of harvested cells were substantially lower than those previously obtained (~0.5 g cell pellets were obtained).

Prior to purification of the triple labelled IPNS (per-deuterated ^{13}C-^{15}N labelled), fractions of the cell culture (in triple labelled M9 medium) were aliquoted. The aliquoted culture was used for small-scale purification with nickel resins using the method described in Section 2.2.1. Figure 2.14 a shows an SDS-PAGE gel image of the wash (W1-W5) and elution (E1, and E2) fractions in the resin-based purification. The E1 fraction showed a relatively low level band indicating that IPNS has been produced; however, the production level was low (Figure 2.14 a).

The per-deuterated ^{13}C-^{15}N labelled IPNS (triple labelled IPNS) was purified using the method described in Section 2.2.2. The cell pellets (~ 0.5 g) were dissolved in binding buffer A (5 mM imidazole), and the cell lysate was applied onto the 5 mL nickel His-Trap column pre-equilibrated with buffer A. Subsequently, the column was washed with buffer A, then IPNS was eluted using a gradient from buffer A to buffer B (500 mM imidazole). Figure 2.14 b shows SDS-PAGE gel image of cell lysate, and fractions 4 to 12 from nickel his-trap chromatography. There were only low protein levels in the collected fractions, and the cell lysates showed no detectable evidence for IPNS protein. Therefore, IPNS was not expressed, at least to a substantial level, in the triple labelled minimal M9 medium.

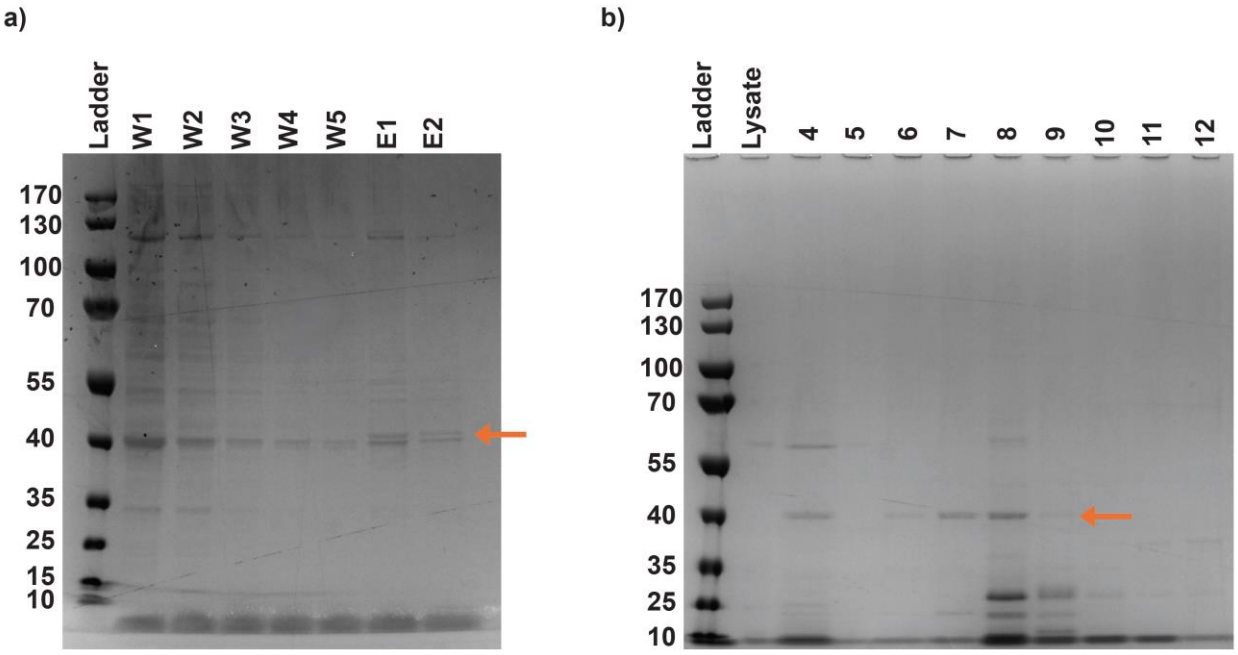


Figure 2.14: **(a)** Small-scale purification trial of per-deuterated ^{13}C-^{15}N labelled IPNS using nickel resins. SDS-PAGE gel image of wash (W1-W5) and elution (E1, and E2) are shown. IPNS band is marked with red arrow. **(b)** Purification of triple labelled IPNS using 5 mL nickel his-trap column. The SDS-PAGE gel image includes cell lysate, and fractions 4 to 12 from the nickel His-trap purification step. The IPNS band is marked with red arrow.

2.2.9: Conclusion

This chapter describes *E. coli* cell growth and expression conditions for production of recombinant WT_IPNS optimized first in 2YT and autoinduction media (TB), then

subsequently in unlabelled minimal M9 media. The optimized growth conditions in 2YT medium were further used, as described in the next chapter, to produce IPNS mutants.

After optimising the cellular growth and IPNS expression levels in unlabelled minimal M9 medium, it was shown that growth in single and double labelled (^{15}N and ^{2}D) minimal M9 medium provided sufficient amounts of IPNS for NMR analysis. It was then observed that per-deuteration and obtaining TROSY-type spectra of ^{15}N labelled IPNS enhanced the spectroscopic resolution. The production of triple labelled IPNS (per-deuterated, ^{13}C-^{15}N labelled) did not give sufficient amount of IPNS for spectroscopic analysis. To maximize the IPNS deuteration level, ^{13}C labelled glucose in the minimal M9 medium was also deuterated, which could decrease the rate of glucose metabolism in *E. coli* cell. The latter could be a reason why expression was less than in the previous expression trials using M9 media with normal (unlabelled) glucose.

Therefore, in future work, use of ^{13}C-glucose (without deuteration) could increase the cell growth rate in minimal M9 medium. Although using ^{13}C-glucose (without deuteration) will decrease the IPNS deuteration level, the resulting IPNS should be sufficiently deuterated as long as the M9 medium is in D_2O. Further, the phosphate buffers used in the M9 medium can make stable complexes with the essential metals used in the medium (Table 2.1); hence using another minimal medium with non-phosphate buffer (e.g. Tris) could potentially increase the yield. However, small quantities of phosphate are still needed as a precursor for the nucleic acids in the minimal media.

Overall, the work will enable future detailed studies on IPNS employing NMR as a tool to study conformational changes during catalysis. These were not pursued in my work due to time constraints and the pursuit of an alternative related line as described in the next chapter, involving mutants prepared by the procedures described in this chapter.

2.3: Methods

2.3.1: Expression Trials of IPNS in Different Media

The plasmid DNA used for wildtype IPNS expression was pCOLD I (Addgene, UK) encompassing Sal I and Not I restriction sites and a kanamycin resistant gene (provided by Dr. P. Rabe). The WT_IPNS DNA sequence was codon-optimized for expression in *E. coli* (using GeneArt, Thermo Fisher Schientific, UK) containing *N*-terminal hexa-histidine tag (His-Tag) bearing an *N*-terminal C human rhinovirus protease cleavage site [26].

The pCOLD plasmid of WT_IPNS was transformed into *E. Coli* BL21 cell line using the heat shock method. Initially, 2 μL of the IPNS vector solution (~50 ng/μL) was mixed with 20 μL of *E. coli* (BL21) solution, and the mixture was left on ice for 20 minutes. The mixture of *E. coli* and plasmid was then shocked at 42 ^{o}C for 15 seconds (heat shock). After the heat shock, the cell mixture was kept on ice for two minutes, when 200 μL of nutrient rich SOC medium (New England Biolabs, USA) was added. Subsequently, the cell mixture was incubated at 37 ^{o}C for 45-60 minutes to initiate pCOLD vector expression. The cell mixture was then spread over a 2YT (2x yeast extract tryptone) agar plate containing 50 mg/L kanamycin, and the plate was incubated at 37 ^{o}C overnight.

The 2YT medium for IPNS expression was prepared by dissolving 121 g 2x yeast extract tryptone powder into 1L Milli-Q water followed by autoclave sterilization. Four different TB autoinduction media were prepared by dissolving 35 g, 55 g, 75 g, and 95 g of the TB medium (Terrific Broth auto induction) in 1L Milli-Q water followed by autoclave sterilization. The unlabelled and labelled minimal M9 media were prepared using the recipe shown in Table 2.1. Some ingredients of the M9 medium including glucose, vitamins, and additives including $ZnCl_2$, $CuCl_2$, $CoCl_2$, and H_3BO_3 are unstable at autoclave temperatures. Therefore, stock solutions of these additives were syringe sterilized using 0.2 μM filter and added to the autoclaved M9 media (Table 2.1). For the minimal M9 media in D_2O, all stock solid powders and the stock solutions were prepared in D_2O (99.9 atom % D, Sigma-Aldrich). The $^{15}NH_4Cl$ and ^{13}C-glucose-d_6 (provided by Dr. P. Rabe) were used for ^{15}N and ^{13}C labelling, respectively.

To produce recombinant IPNS, single colonies from grown 2YT agar plates were picked to inoculate 100 mL (unless mentioned otherwise) of starting culture. The types of media used are explained in Sections 2.21 and 2.2.2. The starting culture was then incubated overnight at 37 ^{o}C shaking at 180 rpm. The grown starting culture was then diluted into the larger scale medium (with 1:10 v/v ratio) for large-scale growth. Kanamycin was added to all media (50 mg/L final concentration) prior to each inoculation step. The large-scale media were incubated at 37 ^{o}C and the cell growth was checked via measuring optical density at 600 nm (OD_{600}). Once OD_{600} reached 0.6, β-D-1-thiogalactopyranoside (IPTG) was added to the media to give a final concentration of 500 μM (and other concentrations as described in Section 2.2.1). For autoinduction media expression trials, no IPTG was added. Subsequently, the cell cultures were incubated at 18 ^{o}C for at least 18 hours, shaking at 180 rpm. The cells were harvested via centrifugation (11000 g, 8 min, 4 ^{o}C) and the collected pellets were stored at -80 ^{o}C.

2.3.2: Small-Scale IPNS Purification

To purify IPNS from small amounts of cell pellets (for expression trials), the cell pellets were resuspended in binding buffer A (1:10 w/v ratio) containing 50 mM Tris, 200 mM NaCl, and 5 mM imidazole at pH 6.5. Nickel resin (NEBExpress Ni Resin, New England Biolabs) was used to purify histidine-tagged IPNS. The nickel resin was washed three times with binding buffer A. The resuspended cells were lysed via sonification (60% amplitude, 9.9 s pulse on, 9.9 s pulse off, 6 minutes total time, Sonics-Vibra Cell). The lysed cell debris was sedimented via centrifugation (3000 g, 20 min, 4 ^{o}C). Subsequently, 1 mL of the lysate was mixed with 200 μL of nickel resin that has been pre-equilibrated with buffer A and the mixture was left on ice for 30 minutes. The mixture was centrifuged at 3000g for 2 minutes to sediment the nickel resins, and the top solution was separated with pipetting (W1 fraction). The resin was then washed via adding 500 μL of buffer A followed by centrifugation (3000 g, 2 min) and separation of the top solution. The latter step was repeated four times and fractions (W2-W5) were collected. The resins were then mixed with 500 μL of elution buffer B, including 50 mM Tris, 200 mM NaCl, and 500 mM imidazole at pH 6.5. The mixture was centrifuged (3000 g, 2 min) and the top solution was separated to isolate first eluted (E1) fraction. The last step was repeated to isolate

the second eluted (E2) fraction. The wash (W) and eluted (E) fractions were analyzed using SDS polyacrylamide gel electrophoresis (PAGE, Figure 2.1).

To purify the per-deuterated ^{15}N labelled IPNS (Section 2.2.5), the gravity-flow method with nickel resins was applied. As mentioned above, 0.5 g of cell pellets were resuspended in 5 mL binding buffer A (1:10 w/v ratio) and sonification was applied (60% amplitude, 9.9 s pulse on, 9.9 s pulse off, 6 minutes total time). The nickel resin (5 mL) was loaded onto a column, and after removing the resin solvent, the column was washed three times with 5 mL of binding buffer A. The lysed resuspended cells were centrifuged (3000 g, 20 min, 4 ^{o}C) and the supernatant was loaded onto a nickel resin column pre-equilibrated with buffer A. The nickel resin and cell lysate mixture were incubated for 30 minutes at 4 ^{o}C and the flowthrough was collected (W1 fraction). The column was then washed four times with 5 mL of binding buffer A followed by collecting the flowthrough (W2-W5 fractions). To elute the recombinant IPNS bound to the $Ni^{(II)}$ ions, the imidazole concentration was increased stepwise. That is, four different elution buffers including 50 mM Tris, 200 mM NaCl, and variable concentrations of imidazole (pH 6.5) were prepared. The column was eluted four times with buffers containing 20 mM, 40 mM, 60 mM, and 500 mM imidazole to provide E1, E2, E3, and E4 fractions, respectively. The wash (W) and eluted (E) fractions were analyzed using SDS-PAGE (Figure 2.12 a).

2.3.3: Large-Scale Purification of ^{15}N Labelled IPNS

A sufficient amount of cell pellets (15 g -25 g) was resuspended in binding buffer A (1:5 w/v ratio), and small quantities of DNAase I, phenylmethylsulfonyl fluoride, and lysozyme were added to the resuspended cell mixture. The cell mixture was then stirred for 20 minutes at room temperature and 20 minutes at 4 ^{o}C. Subsequently, cells were lysed via sonification (60% amplitude, 9.9 s pulse on, 9.9 s pulse off, 16 minutes total time). For the pellets obtained from labelled minimal M9 media; to maximize cell lysis yield, a French Press was used (20 Kpsi pressure) rather than sonification. The lysed cells were centrifuged (58000 g, 30 min, 4 ^{o}C) to remove the cell debris and the supernatant was passed through a 0.45 μM filter to remove all particles.

The filtered cell lysate was loaded onto the nickel His-Trap column (5 mL HisTrap HP, GE Healthcare, USA) pre-equilibrated with 25 mL (5 CV) of binding buffer A.

Subsequently, the column was washed with 100 mL (20 CV) of binding buffer A to remove any unbound proteins and small molecules from the lysate. Then IPNS was collected via eluting the column with a linear gradient from buffer A to 100% buffer B (in 20 CV). The fractions showing UV absorption at 280 nm in the nickel his-trap chromatogram were analyzed by SDS-PAGE (Figure 2.2). The fractions showing ~40 KDa molecular weight proteins (corresponding to IPNS) were collected and concentrated using 10000 molecular weight cut-off (MWCO) spin concentrators (Merck Millipore, USA) at 3000 g and 4 ^{o}C. To reduce the imidazole concentration in the protein sample, the solution was spin-concentrated down to ~3 mL volume. The concentrated protein sample was then diluted to 15 mL with binding buffer A. The mixture was spin-concentrated to ~7 mL and topped up with buffer A to 15 mL. The final mixture was treated with 3C protease (1:100 w/w ratio, provided by Dr. P. Rabe) overnight at 4 ^{o}C to cleave the N-terminal hexa-histidine tag.

The 3C protease (which contains a histidine tag) and the cleaved hexa-histidine tag were separated from the untagged IPNS using reverse his-trap step. The protein was applied to the nickel affinity column (5 mL HisTrap HP, GE Healthcare, USA) pre-equilibrated with buffer C (50 mM Tris, 200 mM NaCl, and 20 mM imidazole at pH 6.5) and the flowthrough was collected (W1). The column was then washed four times (1CV each step) with buffer C and W4-W5 fractions were collected. The column was then eluted twice (1 CV each step) with elution buffer B and the eluted fractions (E1, and E2) were collected. All fractions were analyzed by SDS-PAGE; showing relatively pure IPNS bands in W1 and W2 fractions (Figure 2.2). The W1 and W2 fractions were collected and spin concentrated via centrifugation (10000 MWCO, Merck Millipore, USA) at 3000 g and 4 ^{o}C to reach ~4 mL volume. The concentrated protein solution was loaded into the dialysis cassette (4-12 mL capacity, 10000 MWCO, Thermo Scientific) pre-saturated with buffer D (50 mM Tris, 200 mM NaCl, 50 mM EDTA, and 5 mM 1,10-phenantroline at pH 6.5). The dialysis cassette filled with the protein solution was stirred in 400 mL of buffer D at 4 ^{o}C for two hours.

To purify IPNS using size-exclusion chromatography (SEC), the dialyzed protein mixture was spin-concentrated to reach 1.8 mL-2 mL volume and then was injected into the Superdex 75 column (300 mL, GE Healthcare, USA) pre-equilibrated with buffer E

(50 mM Tris, and 200 mM NaCl at pH 6.5). The Superdex 75 column was eluted with 300 mL of buffer E, and the fractions showing UV absorption at 280 nM in the SEC chromatogram were analyzed by SDS-PAGE (Figure 2.2). The fractions containing a band corresponding to apparently highly purified IPNS were collected and concentrated to ~50 mg/mL using a spin-concentrator (10000 MWCO, Merck Millipore, USA) via centrifugation at 3000 g and 4 ^{o}C. The purified IPNS solution was then aliquoted and stored at -80 ^{o}C for NMR studies.

2.3.4: IPNS NMR Studies

All NMR studies on labelled IPNS were conducted using Bruker Avance III 700 MHz equipped with a 5 mm $^{1}H(^{13}C/^{15}N)$ inverse TCI cryoprobe. Standard 3 mm NMR tubes (Bruker, Germany) were used for NMR samples. All NMR samples were at 50 mM Tris-d_{11} buffer at pH 6.5 and 10% (v/v) D_2O for field frequency lock, and the sample volume was 160 μL. Unless mentioned otherwise, the IPNS:$Zn^{(II)}$:ACV samples contained 100 μM apo ^{15}N labelled IPNS, 300 μM $ZnSO_4$, and 3.2 mM ACV; the IPNS:$Fe^{(II)}$:ACV samples contained 100 μM apo ^{15}N labelled IPNS, 300 μM $FeSO_4$, and 3.2 mM ACV. The anaerobic IPNS:$Fe^{(II)}$:ACV sample was prepared in anaerobic chamber (Belle Technology, UK). The liquids (Tris-d_{11} buffer, D_2O, and IPNS stock solution) and powders (ACV and $FeSO_4$) were transferred into the anaerobic chamber and equilibrated for 16 hours prior to sample preparation. The Bruker 3mm NMR tube and J Young valve NMR tubes (5mm, Norell, USA) were also pre-equilibrated inside the anaerobic chamber prior to use. The anaerobic IPNS:$Fe^{(II)}$:ACV sample was then prepared (160 μL volume) inside the chamber, transferred into the 3mm NMR tube, and the tube was placed inside the J Young valve NMR tube.

The hsqcetfpf3gpsi with flip-back pulse sequence was used with 8 number of scans (F2 dimension) to obtain 2D ^{1}H-^{15}N HSQC spectra of the samples. The spectra acquisition time was 0.0918 s, with 1 s relaxation delay. The ^{15}N trosyetf3gpsi with flip-back pulse sequence was used with 64 number of scans (F2 dimension) to obtain the TROSY-HSQC spectra. The spectra acquisition time was 0.1835 s, with 1 s relaxation delay. In all 2D NMR spectra, the spectra widths were 15.4 ppm and 40.0 ppm for ^{1}H and ^{15}N dimensions, respectively. The 1D ^{1}H NMR spectra were obtained using zgesgp pulse

sequence containing water suppression using excitation sculpting with gradients. All 2D NMR spectra were processed via a square cosine window function, and the 1D ^{1}H NMR spectra were processed via an exponential window function (line broadening was set at 0.3). All NMR spectra were analyzed via Bruker topspin 3.6.5 (Bruker, Germany, www.bruker.com) and MestReNova 15.0.0 (MestReLabs, Spain, www.mestrelab.com).

2.3.5: IPNS Thermal Stability Assays

Thermal stability assays were performed using unlabelled apo IPNS. For protein-dye optimization, stock solutions of the apo IPNS (40.1 mg/mL, 1.069 mM) and SYPRO orange dye (5000x dilution factor, Thermo Fisher Scientific) were diluted with buffer F (50 mM Tris at pH 6.50) to the final concentrations of 10 μM and 20x dilution factor, respectively. Subsequently, to make different ratios of dye and IPNS, different volumes of the IPNS (10 μM) and SYPRO orange dye (20X) stock solutions were mixed in a 96-well plate with a final volume of 20 μL. For the $Zn^{(II)}$ concentration screening and metal screening experiments, a master mix containing 8 μM apo IPNS and 8x SYPRO orange dye was prepared in buffer F. The appropriate volumes of 50 mM ACV and 200 μM metal stock solutions were added to 10 μL of the master mix, and the mixtures were topped up with buffer F to 20 μL volume (to reach 4 μM IPNS and 4x dye concentrations). For L-arginine and L-glutamate screening, buffers including 50 mM Tris (pH 6.50) and various concentrations of L-arginine and L-glutamate (up to 50 mM, 1:1 molar ratio) were prepared. The stock solutions of apo IPNS (1.069 mM), SYPRO orange dye (20 x), ACV (50 mM), and $ZnSO_4$ (100 mM) were diluted in the aforementioned buffers to prepare samples with various concentrations of L-arginine and L-glutamate. For all experiments, the sample fluorescence intensity at 600 nm was measured using a thermal cycler (CFX96 C100, Biorad) at temperatures ranging from 20 ºC to 95 ºC. The fluorescence intensity at 600 nm was (RFU) plotted versus temperature to obtain the melt curve, and the first derivative (-dRFU/dT) of the melt curve was plotted to obtain the melting temperature (T_m). The data was analyzed using CFX Maestro (V 2.3, BioRad) and Excel.

2.4: References

[1] T. D. W. Claridge. High-Resolution NMR Techniques in Organic Chemistry. 3rd edition *Elsevier* **2016**.

[2] K. H. Gardner, and L. E. Kay. Production and Incorporation of ^{15}N, ^{13}C, ^{2}H (^{1}H-δ1 Methyl) Isoleucine into Proteins for Multidimensional NMR Studies. *J. Am. Chem. Soc.* **1997** 119, 7599–7600.

[3] K. Ivanov, P. K. Madhu, G. Rajalakshmi, G. Two-Dimensional (2D) NMR Methods. 1st edition *Wiley* **2023**.

[4] A. J. Storaska, R. R. Neubig. Chapter Eight - NMR Methods for Detection of Small Molecule Binding to RGS4. *Method Enzymol.* **2013** 522, 133-152.

[5] E. R. P. Zuiderweg. Insights into Protein Dynamics from ^{15}N-^{1}H HSQC. *Magn. Reson. Discuss.* **2021** 2021-2030.

[6] D. P. Frueh. Practical aspects of NMR signal assignment in larger and challenging proteins. *Prog. Nucl. Magn. Reason. Spectrosc.* **2014** 78, 47-75.

[7] K. Pervushin, R. Riek, G. Wider, and K. Wüthrich. Attenuated T_2 relaxation by mutual cancellation of dipole–dipole coupling and chemical shift anisotropy indicates an avenue to NMR structures of very large biological macromolecules in solution. *Proc. Natl. Acad. Sci.* **1997** 94, 12366-12371.

[8] V. Tugarinov, P. M. Hwang, and L. E. Kay. Nuclear magnetic resonance spectroscopy of high-molecular-weight proteins. *Annu. Rev. Biochem.* **2004** 73, 107–146.

[9] J. Li, and R. A. Byrd. A simple protocol for the production of highly deuterated proteins for biophysical studies. *J. Biol. Chem.* **2022** 298, 102253.

[10] M. Cai, Y. Huang, R. Yang, R. Craigie, G. M. Clore. A simple and robust protocol for high-yield expression of perdeuterated proteins in Escherichia coli grown in shaker flasks. *J. Biomol. NMR* **2016** 66, 85-91.

[11] E. S. O'Brien, D. W. Lin, B. Fuglestad, M. A. Stetz, T. Gosse, C. Tommos, *et al.* Improving yields of deuterated, methyl labelled protein by growing in H_2O. *J. Biomol. NMR* **2018** 71, 263–273.

[12] A. Froger, J. E. Hall. Transformation of Plasmid DNA into E. coli Using the Heat Shock Method. *JoVE* **2007** e253.

[13] P. R. Rizkiaa *et al.* Effect of Isopropyl-β-D-thiogalactopyranoside concentration on prethrombin-2 recombinan gene expression in *Escherichia coli* ER2566. *Procedia Chem.* **2015** 17, 118-124.

[14] E. H. Abdelkader, G. Otting. NT*-HRV3CP: An optimized construct of human rhinovirus 14 3C protease for high-yield expression and fast affinity-tag cleavage. *J. Biotech.* **2021** 325, 145-151.

[15] S. C. Fletcher, M. L. Coleman. Human 2-oxoglutarate-dependent oxygenases: nutrient sensors, stress responders, and disease mediators. *Biochem. Soc. Trans.* **2020** 48, 1843-1858.

[16] I. J. Clifton, M. A. McDonough, D. Ehrismann, N. J. Kershaw, N. Granatino, C. J. Schofield. Structural studies on 2-oxoglutarate oxygenases and related double-stranded β-helix fold proteins. *J. Inorg. Biochem.* **2006** 100, 644-669.

[17] J. B. Matthew, and F. M. Richards. The pH Dependence of Hydrogen Exchange in Protein. *J. Biol. Chem.* **1982** 258, 3039-3044.

[18] M. A. L. Eriksson, T. Härd, and L. Nilsson. On the pH Dependence of Amide Proton Exchange Rates in Proteins. *Biophys. J.* **1995** 69, 329-339.

[19] Q. Miao, C. Nitsche, H. Orton, M. Overhand, G. Otting, M. Ubbink. Paramagnetic Chemical Probes for Studying Biological Macromolecules. *Chem. Rev.* **2022** 122, 9571-9642.

[20] Paramagnetism in Experimental Biomolecular NMR. C. Luchinat, G. Parigi, E. Ravera, Eds. *R. Soc. Chem., Camb.* **2018** 1-316.

[21] F. H. Niesen, H. Berglund, and M. Vedadi. The use of differential scanning fluorimetry to detect ligand interactions that promote protein stability. *Nat. Protoc.* **2007** 2, 2212-2221.

[22] K. Huynh, and C. L. Partch. Current Protocols in Protein Science: Analysis of protein stability and ligand interactions by thermal shift assay. *Curr. Protoc. Protein Sci.* **2016** 79, 28.9.1–28.9.14.

[23] A. P. Golovanov, G. M. Hautbergue, S. A. Wilson, L. Y. Lian. A simple method for improving protein solubility and long-term stability. *J. Am. Chem. Soc.* **2004** 126, 8933-8939.

[24] D. Shukla, and B. L. Trout. Understanding the Synergistic Effect of Arginine and Glutamic Acid Mixtures on Protein Solubility. *J. Phys. Chem. B* **2011** 115, 11831-11839.

[25] A. Beier *et al.* Probing Protein−Ligand Methyl−π Interaction Geometries through Chemical Shift Measurements of Selectively Labelled Methyl Groups. *J. Med. Chem.* **2024** 67, 13187-13196.

[26] I. Pettinati, P. Grzechnik, C. Ribeiro de Almeida, J. Brem, M. A. McDonough, S. Dhir, N. J. Proudfoot, C. J. Schofield. Biosynthesis of histone messenger RNA employs a specific 3′ end endonuclease. *eLife* **2018** 7, e39865.

Chapter 3: Isopenicillin N Synthase (IPNS) – A New Mode of Reactivity

3.1: Introduction

3.1.1: Key Interactions in the IPNS Active Site

In a similar manner to other structurally related oxygenases, ferrous iron coordination in IPNS employs two histidine derived imidazole rings and one aspartate derived carboxylate ligand arranged in a facial orientation, often referred to the facial triad of Fe-ligands [1-3]. $His_{214,}$ $Asp_{216,}$ and His_{270} coordinate to the metal in the case of IPNS from *A. nidulans* (Figure 3.1). The substrate, ACV, binds through coordination of its thiol sulfur to the metal centre, in a manner apparently displacing the C-terminal Gln_{330} residue, which has been observed to bind the metal in the absence of ACV [4]. As observed in a crystal structure of the anaerobic IPNS:$Fe^{(II)}$:ACV complex (PDB ID: 6ZAE), the substrate thiol ligates *trans* to His_{270}; ACV binding is stabilized via electrostatic, H-bond and hydrophobic interactions with the active site residues (Figure 3.1). Tyr_{189} and Ser_{281} are positioned to form H-bonds with the ACV valine carboxylate and likely are involved in controlling the ACV valine conformation. One water molecule is bridged between ACV valine carboxylate, Asn_{230} and Arg_{279} and the valine isopropyl group showed hydrophobic interaction with Leu_{223} (Figure 3.1). The binding mode of the L-α-aminoadipoyl (L-AAA) ACV residue is stabilized via interactions with Arg_{87}, Tyr_{91}, and Phe_{285}.

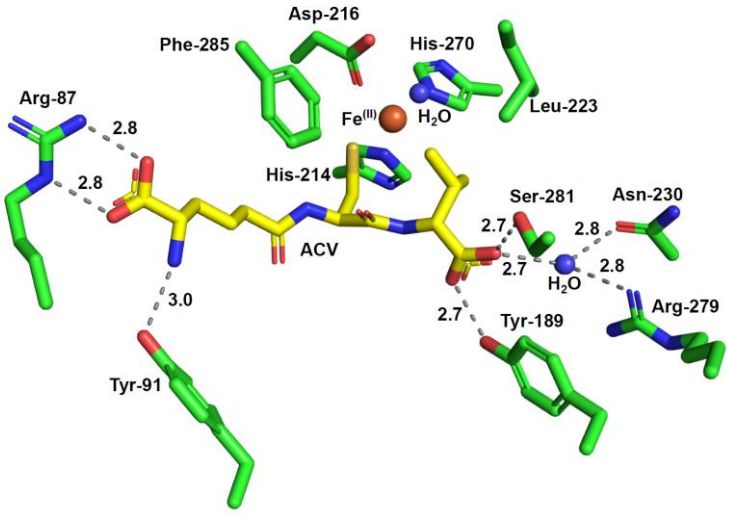


Figure 3.1: Active site view of IPNS bound to $Fe^{(II)}$ and ACV, under anaerobic conditions showing the metal coordinating residues and key residues interacting with the substrate (PDB ID: 6ZAE).

3.1.2: Role of Ser_{281} in IPNS Mechanism

The vital role of WT_IPNS in β-lactam antibiotic formation are described in Chapter 1 Section 1.3. The most recently proposed mechanism for IPNS catalyzed oxidation of ACV to give isopenicillin N (IPN) is shown in Figure 3.2 [5]. The ACV thiol(ate) binds to the metal centre trans His_{270} residue, displacing Gln_{330} residue from the same position [5]. Subsequently, dioxygen reacts with the $Fe^{(II)}$ forming an $Fe^{(III)}$ superoxide species. The superoxide abstracts the pro-S hydrogen from the cysteinyl C-β position leading to the formation of a peroxide and a cysteinyl free radical in the substrate. The resulting intermediate reacts to form a thioaldehyde with concomitant conversion of the $Fe^{(III)}$ to $Fe^{(II)}$. The peroxide distal oxygen abstracts a proton from coordinated H_2O after O-O bond cleavage, concomitantly forming the $Fe^{(IV)}$=O species. The thioaldehyde intermediate then undergoes ring closure forming a β-lactam, which is mediated by the distal water after peroxide cleavage (Figure 3.2) [5,6]. In this step, a (near) co-planar conformation is required for the atoms that form the β-lactam [7]. Ser_{281} interacts with ACV valine carboxylate (Figure 3.1) and may play a role in stabilizing the aforementioned co-planar conformation. The valine isopropyl group of the resulting monocyclic intermediate reacts with the $Fe^{(IV)}$=O species (ferryl intermediate) to form a second free radical intermediate which reacts with cysteinyl sulfur giving the second formed thiazolidine ring of IPN.

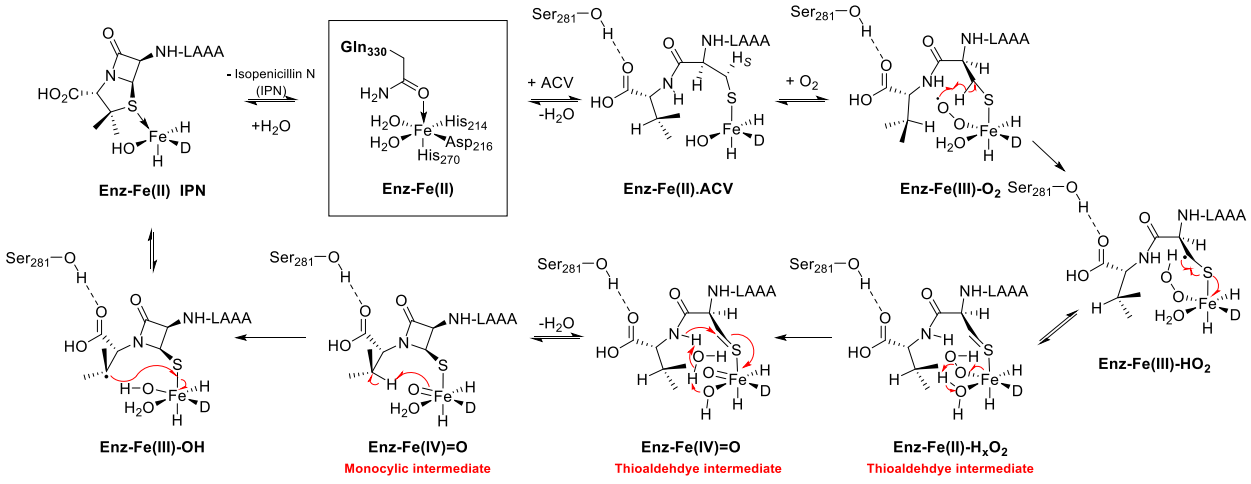


Figure 3.2: Proposed mechanism of WT_IPNS showing formation of IPN from ACV and O_2. The Ser_{281} residue is also shown, which forms an H-bond with the substrate valinyl carboxylate and may play a role in the substrate's cysteinyl conformation. The mechanism was adapted from that proposed in reference [5].

3.1.3: Observed Correlated Motions Through IPNS Structure in Catalysis

In a recently reported and detailed study on IPNS structure and dynamics using time-resolved crystallography, it was observed that conformational changes at the active site during catalysis correlate with conformational changes in α-helix 3 [8]. O_2 binding to the metal centre also correlated a change in the position of the ACV valinyl side chain (Figure 3.2). This conformational change appeared to be transferred through β-strand 11 to α-helix 3, which is located on the enzyme surface [8]. Specific residues were shown to connect the conformational changes at the active site with the motions at the protein surface [8]. These residues and the important structural motifs are labelled in Figure 3.3.

The aim of the work described in this chapter was to substitute these residues and to examine potential catalysis by the resulting mutants. It was envisaged that mutations of Ser_{281} would affect interactions between the substrate and β-strand 11, and that mutations of Gln_{280} and Leu_{282} would alter change interactions between β-strand 11 and α-helix 3.

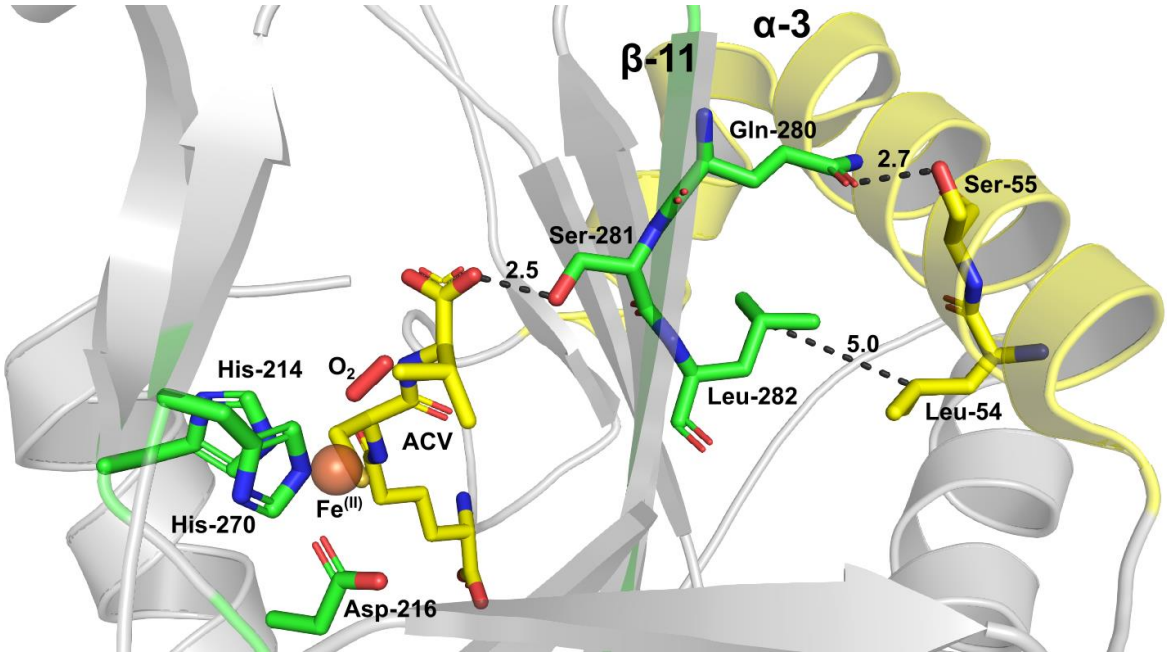


Figure 3.3: Crystal structure derived view of the IPNS:$Fe^{(II)}$:ACV complex after exposure to dioxygen (PDB ID: 6ZAP) [8]. Proposed key residues connecting active site dynamics to motions of β-strand 11 and α-helix 3 are labelled.

3.2: Results and Discussion

3.2.1: Mutations of Key Residues Involved in IPNS Dynamics

To investigate the roles of key residues involved in IPNS dynamics during catalysis [8], WT_IPNS was modified using side-directed mutagenesis (the primers used are given in Table 3.1). As stated above, it was envisaged that mutations of Ser_{281} would modulate interactions between the ACV valine carboxylate and the edge of active site, and mutations of Glu_{280} and Leu_{282} would modulate interactions between β-strand 11 and the surface located α-helix 3 (Figure 3.3).

The mutants were prepared via site directed mutagenesis procedures and the resultant proteins were prepared as described in Section 3.2.2. The plasmids used are given in Table 3.1. The S281A, S281C, and L282V mutants were successfully prepared on the first attempt using the Q5 and Phusion DNA polymerases (Figure 3.4 A). After optimizing the primer sequences based on melting temperatures, the S281T, Q280A and L282A PCR mutations were prepared. For each of the mutants, up to three different primers with various lengths were used (Figures 3.4 b and 3.4 c). The procedure for preparing the Q280A_L282A double mutant did not initially work when using the WT_IPNS template DNA. For preparation of the Q280A_L282A double mutant, the Q280A and L282A plasmids were successfully used as DNA templates in separate reactions (Figure 3.4 d). To confirm that the PCR reactions had enabled successful mutation of the original plasmid, all successful reactions were digested with DPN 1 and the resulting mixture was transferred to the *E. coli* (XL10 Gold) cell line. The replicated plasmids were isolated and sent for sequencing (by Eurofins), the results of which confirmed the presence of the desired mutations. The recombinant proteins were produced and purified as described in Section 3.2.2.

3.2.2: Expression and Purification of IPNS Mutants

After confirming the isolated plasmids sequences for each IPNS mutant, the plasmids were transformed into an *E. coli* cell line (BL21) for recombinant protein production. For each mutant, a bacterial culture was grown in 2YT media (details for

expression methods are discussed in Section 3.3.3). The obtained bacterial pellets were used for extraction and purification of the expressed protein.

Details of the protein purification procedures used for IPNS mutants are provided in Section 3.3.3 - a two-step method was used. In brief all the constructs produced proteins with an N-terminal poly-histidine tag (His-Tag). The extracted cell lysates were applied to a column enriched with $Ni^{(II)}$ ions (Ni His-Tag column). After washing unbound proteins with low imidazole buffer (buffer A), the bound IPNS mutants were eluted and collected using a buffer with high imidazole concentration (buffer B). The percentage of buffer B is shown in His-Trap chromatograms in Figure 3.5. The collected fractions were combined and treated with a 3-C protease, which cleaves the poly histidine tag from the proteins.

Table 3.1: Primers used to generate IPNS mutants.

Primer	**Sequence**
S281A fwd	CAAAAAACGG CAGGGCCTGA CGTTC
S281A rev	GAACGTCAGG CCCTGCCGTT TTTTG
S281C fwd	CGGCAGGCAT TGACGTTCTG C
S281C rev	GCAGAACGTC AGTGTCTGCC GTTTTTTG
S281T fwd	CCAGATTCACAAAA AACGGCAGGG TCTGACGTTC TGC
S281T rev	GCAG AACGTCAGAC CCTGCCGTTT TTTGTGAATCTGG
L282V fwd	CAAAAAACGG CACGCTCTGA CGTTCTGC
L282V rev	GAACGTCAGA GCGTGCCGTT TTTTGTGAAT CTG
L282A fwd	CAAAAAACGG CGCGCTCTGA CGTTCTGCATTAACCC
L282A rev	GGGTTAATGCAGAACGTCAGAGCG CGCCGTTTTT TG
Q280A fwd	CAAAAAACGGCAGGCTCGCACGTTCTGCATTAACCC
Q280A rev	GGGTTAATGCAGAACGTGCGAGCCTGCCGTTTTTTG
Q280A_L282A fwd	CAAAAAACGGCGCGCTCGCACGTTCTGCATTAACCC
Q280A_L282A rev	GGGTTAATGCAGAACGTGCGAGCGCGCCGTTTTTTG

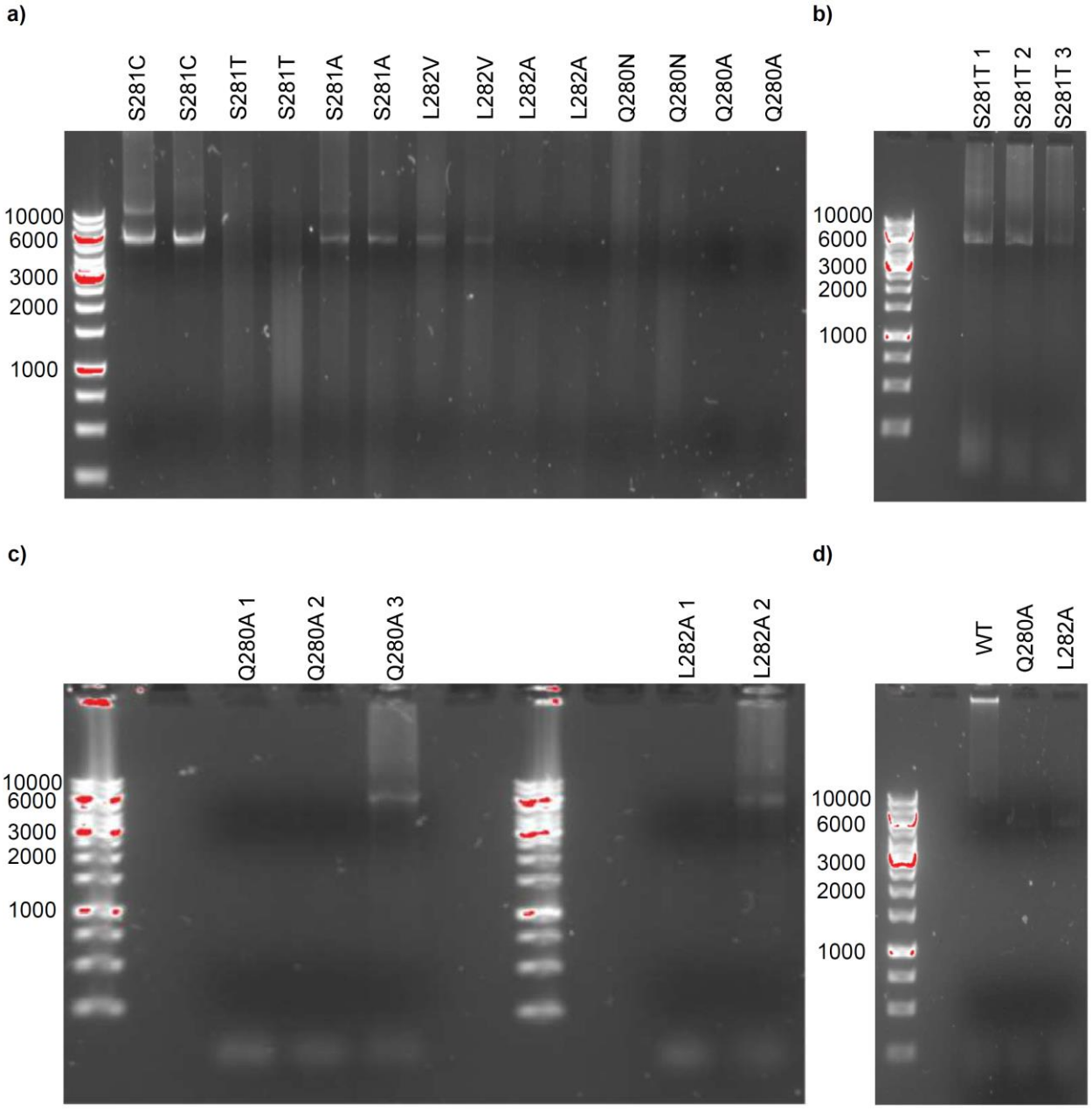
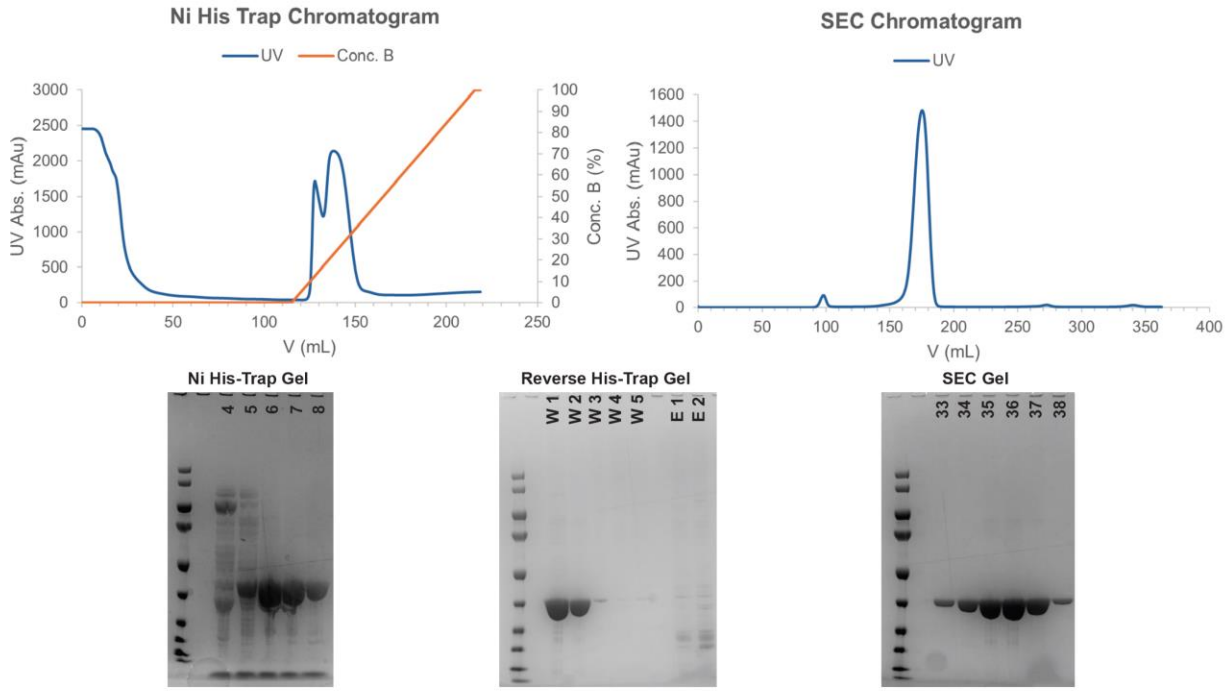
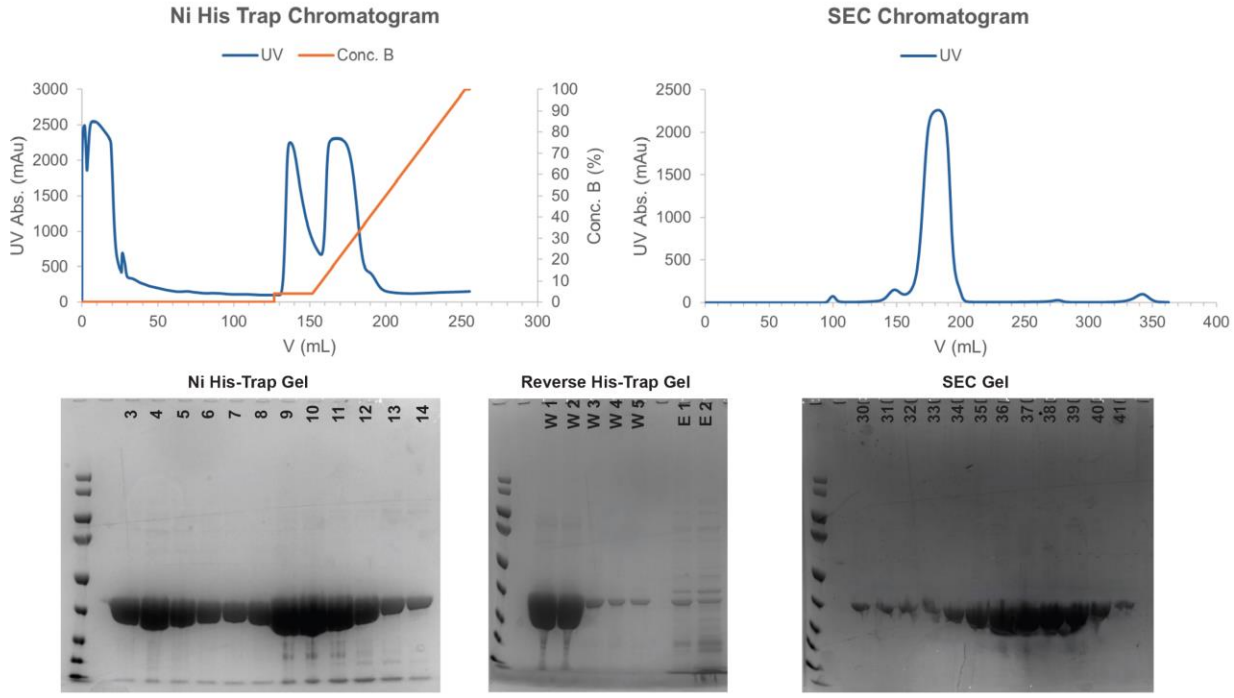


Figure 3.4: DNA gel images of PCR reaction products for IPNS mutants. **(a)** Phusion PCR reaction of originally designed primers for IPNS mutations. For each mutation, two annealing temperatures, at 68 °C and 72 °C were used. **(b)** Q5 PCR reaction using three different primers for the S281T mutation at 72 °C annealing temperature. **(c)** Q5 PCR reaction using up to three different primer length for the Q280A and L282A single mutations at 72°C annealing temperature. **(d)** Q5 PCR reaction using WT_IPNS, Q280A_IPNS, and L282A_IPNS as DNA templates and the Q280A_L282A double mutant primer.

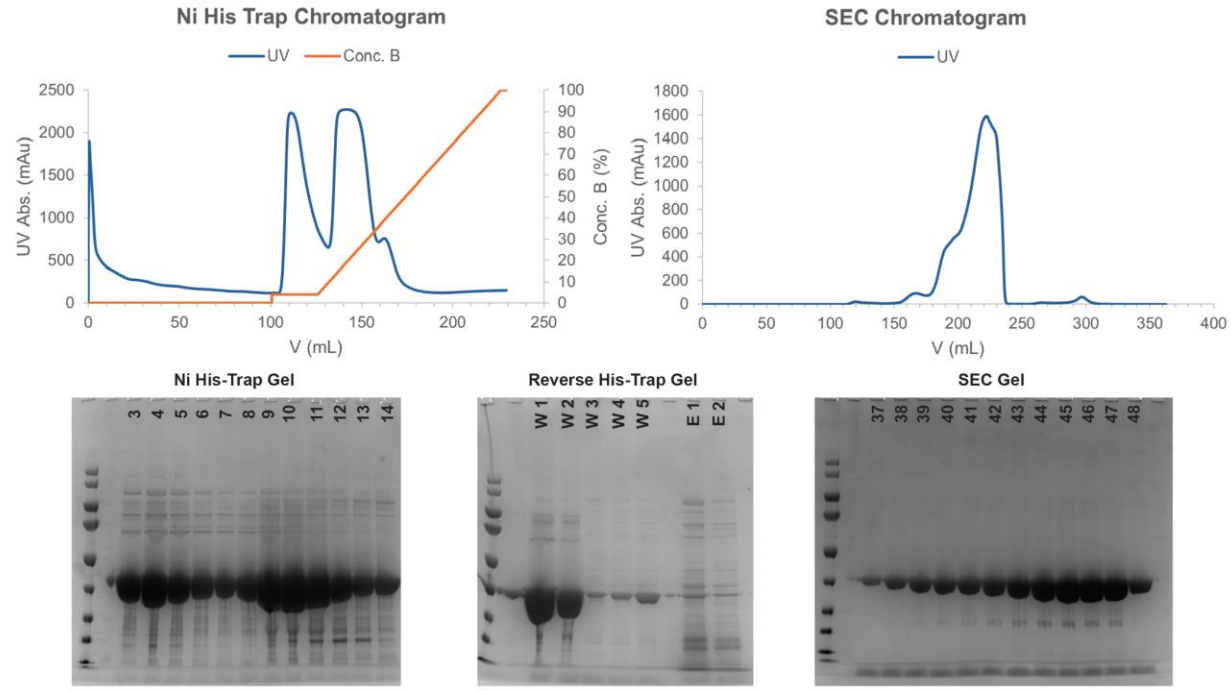
a)


Ni His Trap Chromatogram
UV
Conc. B
UV Abs. (mAu)
Conc. B (%)
V (mL)
SEC Chromatogram
UV
UV Abs. (mAu)
V (mL)
Ni His-Trap Gel
4 5 6 7 8
Reverse His-Trap Gel
W 1 W 2 W 3 W 4 W 5 E 1 E 2
SEC Gel
33 34 35 36 37 38

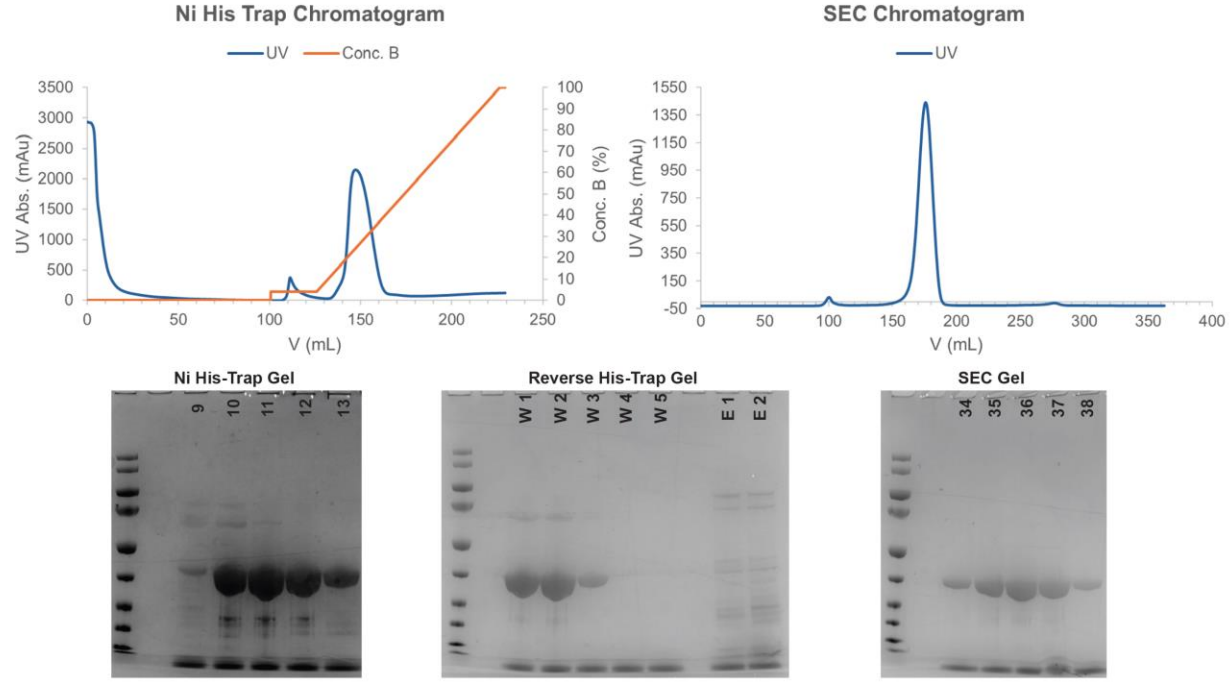
b)


Ni His Trap Chromatogram
UV
Conc. B
UV Abs. (mAu)
Conc. B (%)
V (mL)
SEC Chromatogram
UV
UV Abs. (mAu)
V (mL)
Ni His-Trap Gel
3 4 5 6 7 8 9 10 11 12 13 14
Reverse His-Trap Gel
W 1 W 2 W 3 W 4 W 5 E 1 E 2
SEC Gel

c)


Ni His Trap Chromatogram
UV
Conc. B
UV Abs. (mAu)
Conc. B (%)
V (mL)
SEC Chromatogram
UV
UV Abs. (mAu)
V (mL)
Ni His-Trap Gel
3 4 5 6 7 8 9 10 11 12 13 14
Reverse His-Trap Gel
W 1 W 2 W 3 W 4 W 5 E 1 E 2
SEC Gel
37 38 39 40 41 42 43 44 45 46 47 48

d)


Ni His Trap Chromatogram
UV
Conc. B
UV Abs. (mAu)
Conc. B (%)
V (mL)
SEC Chromatogram
UV
UV Abs. (mAu)
V (mL)
Ni His-Trap Gel
9 10 11 12 13
Reverse His-Trap Gel
W 1 W 2 W 3 W 4 W 5 E 1 E 2
SEC Gel
34 35 36 37 38

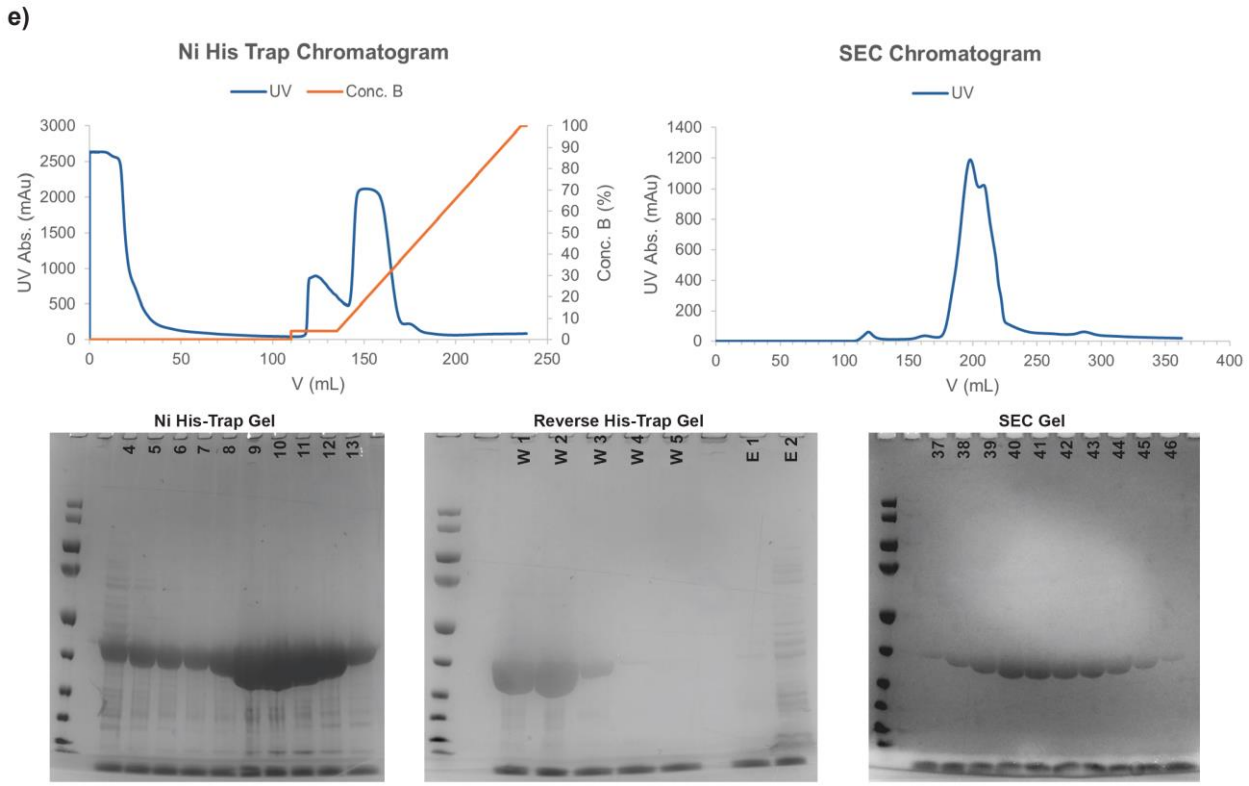


Figure 3.5: Purification of IPNS mutants including nickel his-trap, and size exclusion (SEC) chromatograms. The SDS page gel images of collected fractions are shown. The mutants shown include **(a)** S281A, **(b)** S281T, **(c)** Q280A_L282A, **(d)** Q280A, and **(e)** L282A.

After 3C-protease mediated cleavage, the mixture was re-applied to the His-Tag column and washed five times with low concentration imidazole buffer (this step is known as reverse His-Trap procedure) [8]. After each wash step, the flow through was collected (W1 to W5) and then the column was eluted twice with high concentration imidazole buffer (E1 and E2). In the reverse His-Trap procedure, the cleaved poly histidine tag as well as the 3C-protease (which has histidine tag) will bind to the column and the cleaved IPNS enzymes pass through the column [8].

According to the obtained SDS page gel from fractions from the reverse His-Trap step (Figure 3.5), the first two wash fractions were collected (W1 and W2). The collected wash fractions were dialyzed using a 10000 MW cutoff dialysis bag to remove the metals and then were applied to a size exclusion (SEC) column (Superdex 75, 300 mL, GE Healthcare, USA) to remove the small molecules as well as other proteins with different sizes. This step is also essential to remove any potential dimer/oligomer proteins. The

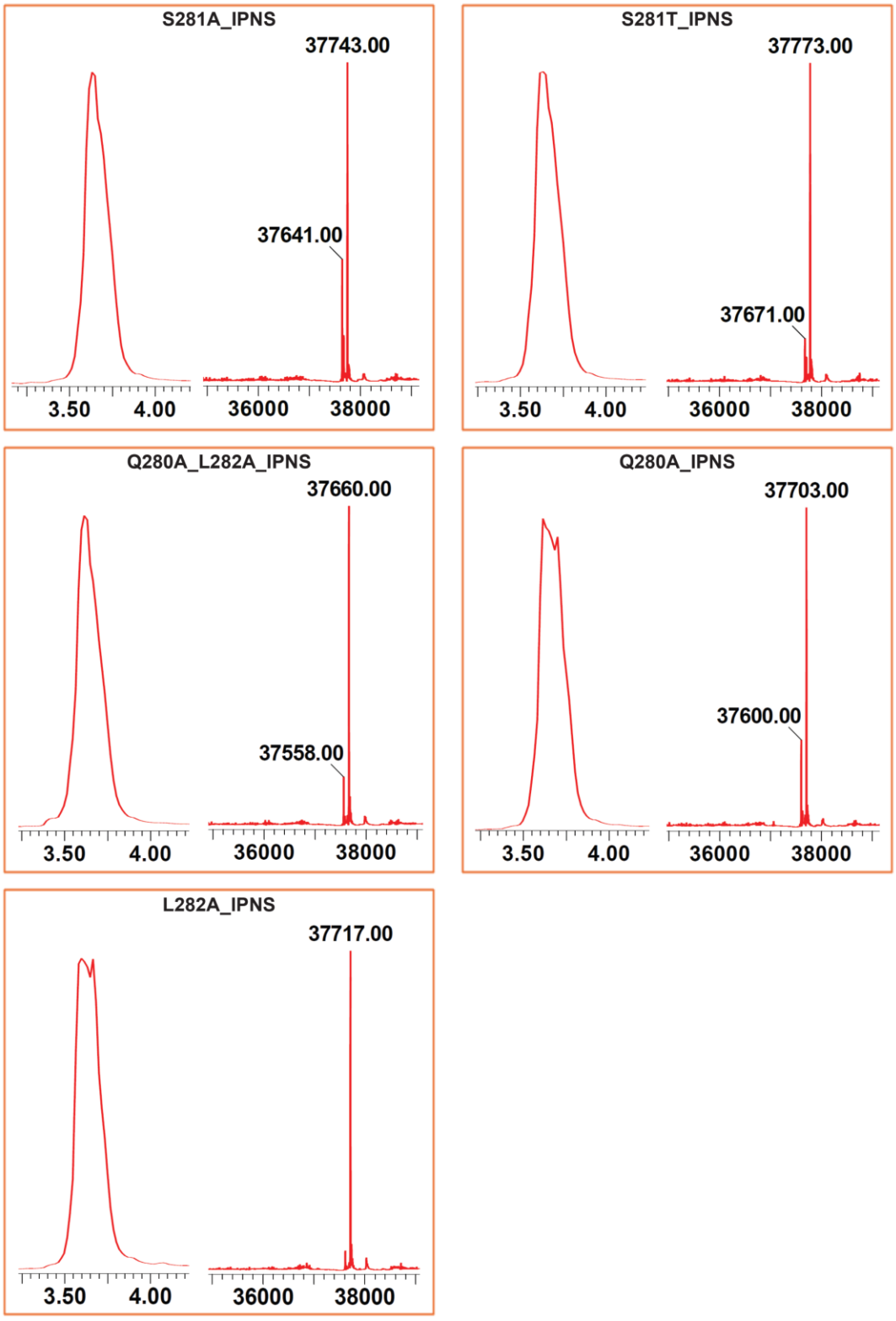


Figure 3.6: LC-MS spectra of the shown IPNS mutants after purification. The LC-MS analytical chromatogram and protein extracted masses are shown for each mutant.

resulting size exclusion (SEC) chromatograms for the IPNS mutants are shown in Figure 3.5. The SDS page gel images of collected fractions showed relatively pure bands for the IPNS mutants (Figure 3.5). The resulting enzyme solutions were used for turnover studies.

Considering the amount of 2YT media used to grow *E. coli* cells (BL21), the protein yields were similar for the IPNS mutants (c.a. 100 mg protein from 6L media). To confirm the purity of the obtained mutants, their obtained protein solutions were diluted (final concentration of 3 μM), then analyzed by LC-MS using a C-4 column (ACE Equivalence, ACT Ltd., UK). The resulting LC-MS chromatograms and combined protein masses are shown in Figure 3.6; the results support the purity of the samples. The protein masses also correspond with the expected masses of each mutant, confirming that the mutations were successful.

3.2.3: Monitoring Turnover of WT and S281A_IPNS Using ^{1}H NMR and LC-MS

The turnover of WT_IPNS was initially analyzed by ^{1}H NMR (700 MHz) as shown in Figure 3.5. Turnover can be followed by depletion of the ACV valine methyl group doublets and formation of the IPN singlet methyl peaks (1,1' methyl groups in Figure 3.7 b). The turnover mixture contained ACV, 1 equivalent of tris-(2carboxyethyl) phosphine (TCEP) (to hinder ACV disulfide bond formation), 0.4 equivalents of $Fe^{(II)}$, and 1 equivalent of sodium L-ascorbate, the latter to hinder iron oxidation.

WT IPNS was observed, by ^{1}H NMR (700 MHz), to fully convert ACV to IPN within 5 minutes. By contrast, under the same conditions S281A_IPNS had reduced activity, with ACV only being partially consumed within 2 hours after addition of 10 μM S281A_IPNS. Moreover, as shown in Figure 3.7 b, turnover of S281A_IPNS not only formed IPN, but also apparently formed a new product as evidenced by the appearance of singlets at around 1.18 ppm (labelled with blue asterisks in Figure 3.7 b). The new peaks had higher integrals compared to the IPN peaks. Therefore, S281A_IPNS appeared to form a major new product, with IPN being only a minor product.

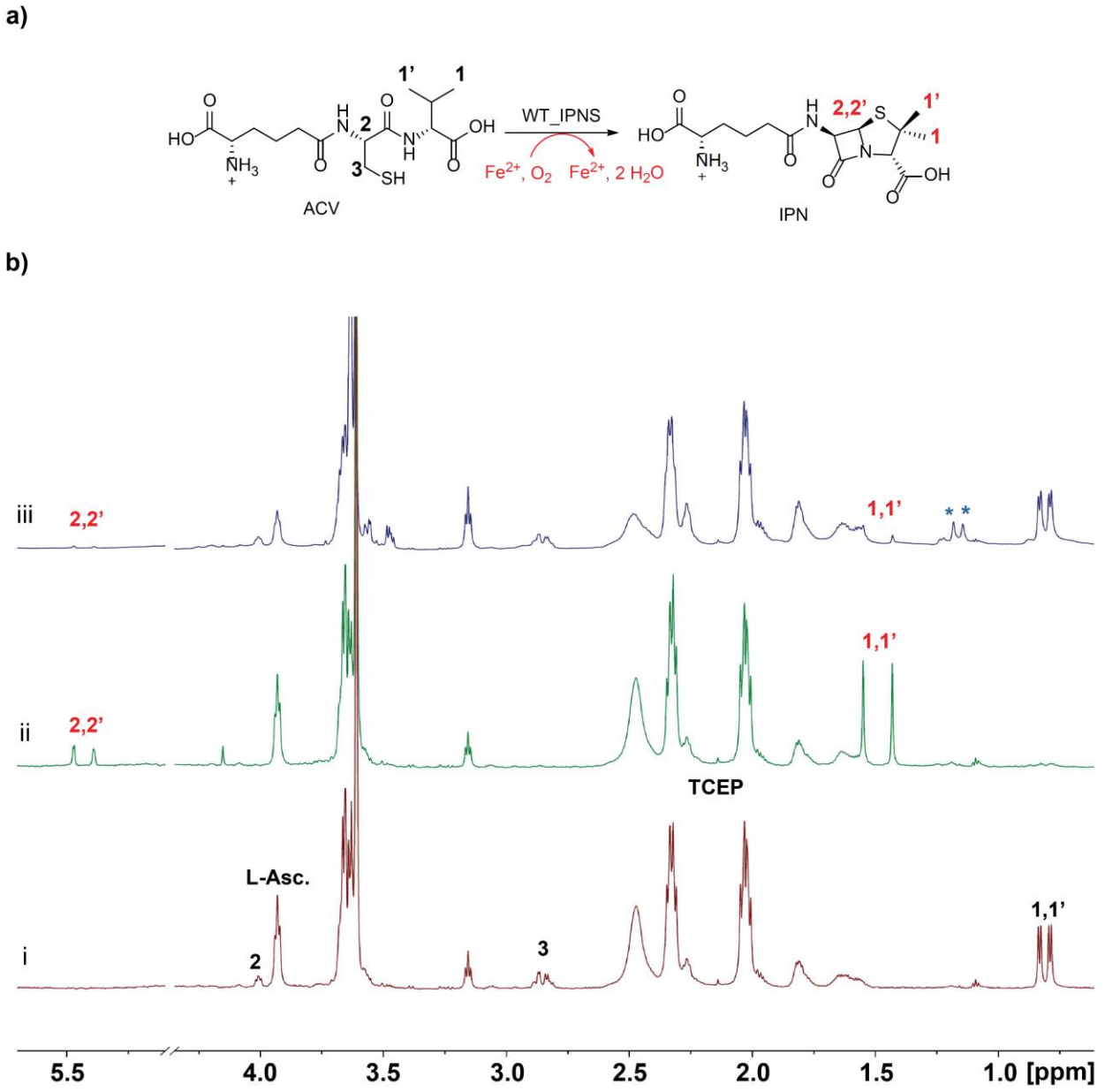


Figure 3.7: **(a)** Reaction of WT_IPNS turnover showing formation of isopenicillin N (IPN) **(b)** CPMG edited ^{1}H NMR spectra of WT and S281A IPNS turnover at 700 MHz. (i) IPNS reaction mixture without enzyme, (ii) 5 minutes after addition of 1 μM WT_IPNS to (i), and (iii) 2h after addition of 10 μM S281A_IPNS to (i).

An NMR time course of S281A_IPNS (Figure 3.8) demonstrated that the new peaks increased with incubation time. One initial possible explanation for the existence of the new peaks was that IPN was being hydrolyzed due to the presence of a

contaminating β-lactamase within the protein preparation (the Schofield group routinely makes recombinant β-lactamases and one is produced by wildtype *E. coli*).

In order to rule out the possibility of IPN hydrolysis with β-lactamase, the turnover assay was done in presence of different concentrations of a serine β-lactamase inhibitor, clavulanic acid [9,10] (Figure 3.8 b). The NMR spectra of S281A_IPNS turnover both with and without clavulanic acid were similar (Figure 3.8), indicating that the apparent new product does not result from serine β-lactamase activity. Moreover, when IPN produced by WT_IPNS turnover was treated with a β-lactamase (AmpC from *E. coli*) (Figure 3.9), the methyl peaks of the resultant hydrolyzed IPN had different chemical shifts compared to the apparent new product peaks. Therefore, the new product was proposed to be formed as a consequence of altered IPNS activity.

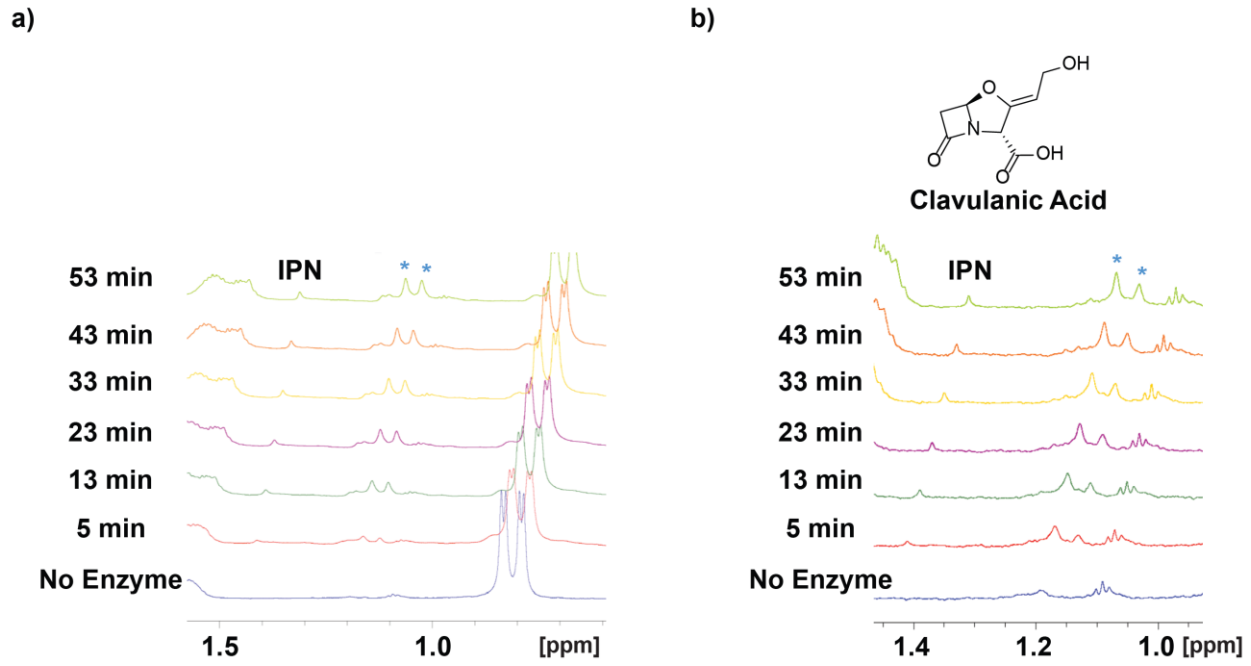


Figure 3.8: **(a)** Time course of S281A_IPNS turnover as analysed by ^{1}H NMR (700 MHz) which shows both IPN and the new product (blue asterisk) peaks rise over time. **(b)** Time course of S281A_IPNS turnover with 100 μM clavulanic acid showing similar spectra. The structure of clavulanic acid is shown; clavulanic acid is a potent inhibitor of serine β-lactamases [9,10].

To further investigate the turnover products of S281A_IPNS, LC-MS was used to analyze the masses of the new products. Since the positive ionization method was used

to ionize the molecules, the observed m/z values should be larger than the molecular masses by a mass of one proton. The turnover samples were prepared using different concentrations of S281A_IPNS (20 μM, 30 μM, and 40 μM) and examined by LC-MS (Figure 3.10 a and b). The two observed products are colour-coded; their corresponding MS profiles are shown in Figure 3.10 a. The first product peak shows an m/z value of 608.16 for its +1 ion and a peak with m/z 304.59, corresponding to the same molecule with a +2 charge (Figure 3.10 b). The second product peak which elutes after the first product peak shows an m/z value of 360.12, which is the same the expected mass for IPN. The second peak thus could correspond to IPN and/or a new product which is isomeric with IPN (Figure 3.10 b).

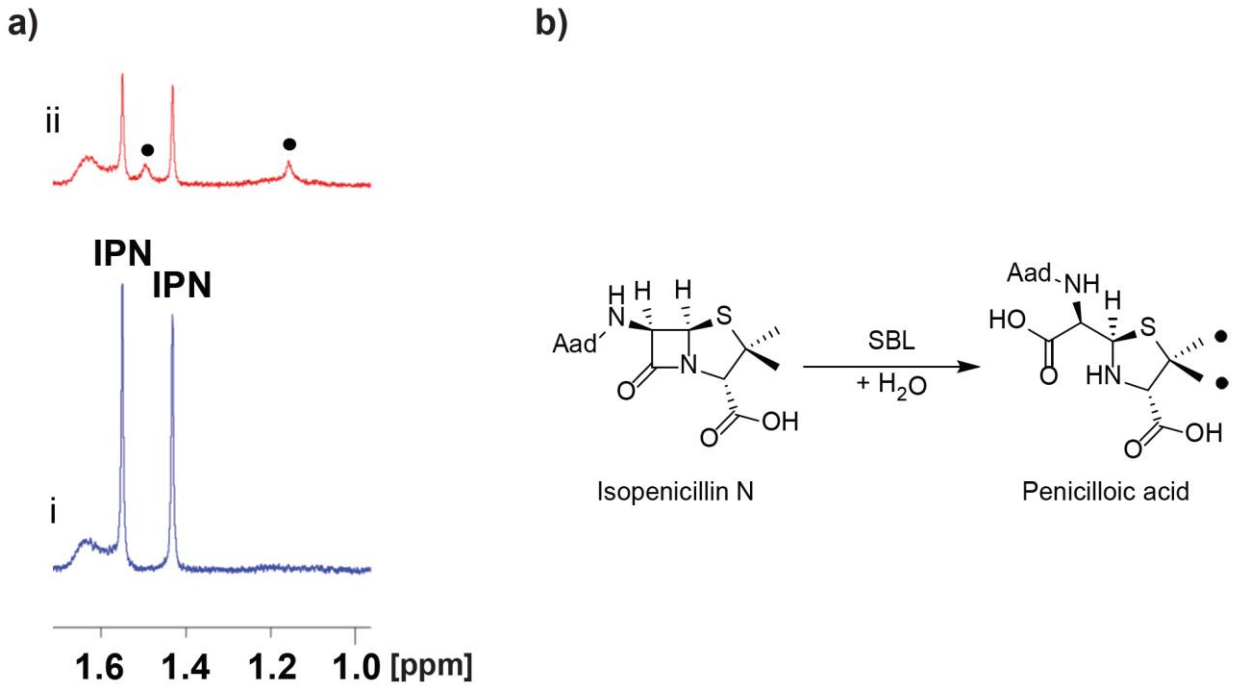


Figure 3.9: **(a)** Part of the CPMG edited ^{1}H spectrum of WT_IPNS turnover assay showing the IPN peaks (i) and the same sample after adding 10 nM of an SBL (AmpC from *E. coli*) showing hydrolyzed IPN (penicilloic acid) (ii). The penicilloic acid methyl peaks are labelled with black dots, which are different from observed new product peaks. **(b)** IPN hydrolysis reaction scheme.

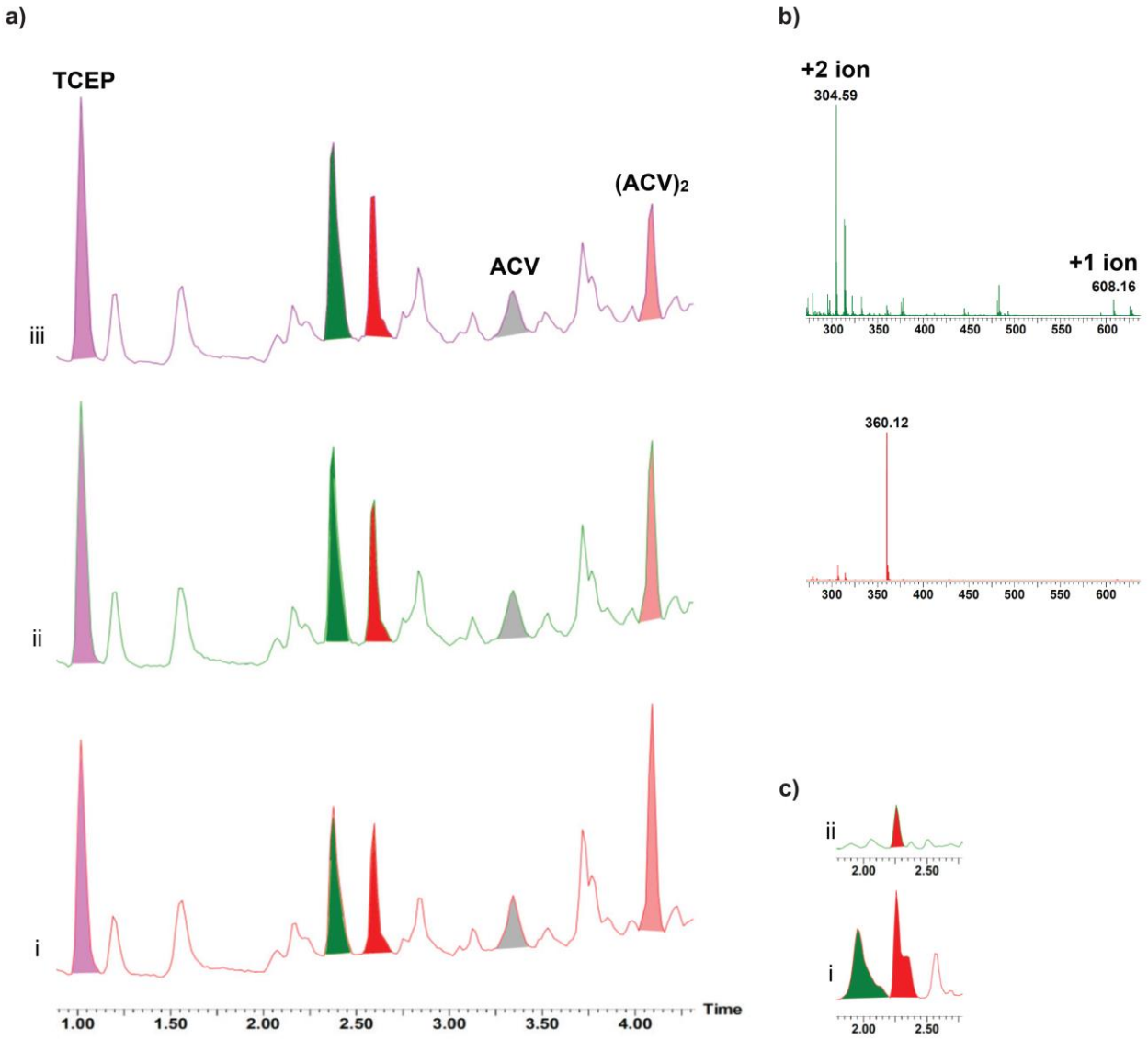


Figure 3.10: **(a)** LC-MS results of ACV reaction with 20 μM (i), 30 μM (ii), and 40 μM (iii) S281A_IPNS. **(b)** The extracted MS profiles of the turnover products eluting at 2.38 min and 2.60 min labelled green and red, respectively. **(c)** Chromatogram for S281A_IPNS turnover with (i) and without (ii) TCEP.

During the turnover time, the thiol form of ACV will oxidize to form the disulfide form $(ACV)_2$. Hence the amount of monomeric and dimeric ACV will vary depending on the amount of IPNS activity. The areas of both the green and red peaks in the LC-MS profile increase at higher S281A_IPNS concentrations; whereas the area of the dimeric ACV peak (eluting at 4 min) decreases (Figure 3.10 a). Therefore, both the green and red peaks likely correspond to turnover products. When the reaction was carried out without TCEP, the resulting chromatogram did not manifest the green product peak, and no

molecules with m/z = 608.16 were observed (Figure 3.10 c). These observations indicate that first peak with m/z = 608.16 likely represents an adduct between the ACV derived product and TCEP. Further evidence for this proposal is described in Section 3.2.4.

3.2.4: Purification of the S281A_IPNS Turnover Product with m/z=608.16

In order to better characterize the turnover products of S281A_IPNS, the reaction was carried out on a larger scale. The turnover conditions were 20 μM S281A_IPNS, 1 mM ACV, 1 mM TCEP and 0.2 mM $Fe^{(II)}$ at 50 mM Tris buffer and pH=7.5. Using HPLC, the products with m/z=608.16 and m/z=360.12 were isolated and purified.

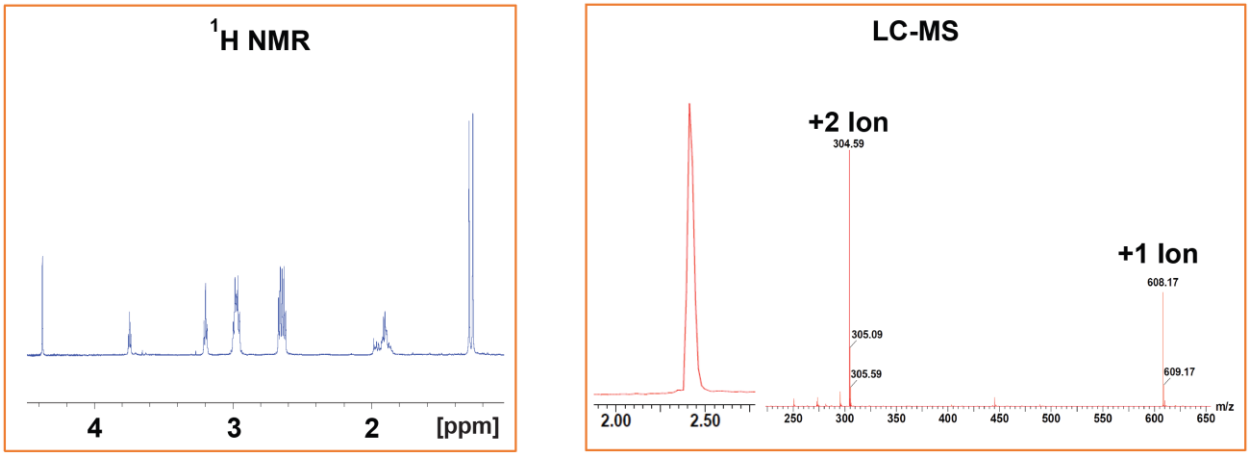


Figure 3.11: ^{1}H NMR (700 MHz) and LC-MS results of the first eluting product with m/z value of 608.17 from S281A_IPNS turnover with TCEP present.

Figure 3.11 shows the ^{1}H NMR and LC-MS spectra of the first eluting product. The chromatogram and NMR indicates that the product has been purified, and its extracted MS profile confirms it has m/z = 608.17. Note the m/z value of the peak with m/z = 304.59 increases by 0.5 units due to the ^{13}C isotope natural abundancy (Figure 3.11), confirming that the peak corresponds to the doubly charged ion molecule. To investigate the structure of the isolated product (m/z=608.17), 1-D and 2-D NMR spectra were obtained, including ^{1}H-^{13}C HSQC and HMBC spectra (Figure 3.12). After careful consideration of various possible structures, according to the obtained spectra and predicted mass (M+1 = 608.17), a structure was proposed for the product (Figure 3.12). In Figure 3.12, the protons are coded numerically corresponding to their NMR resonances.

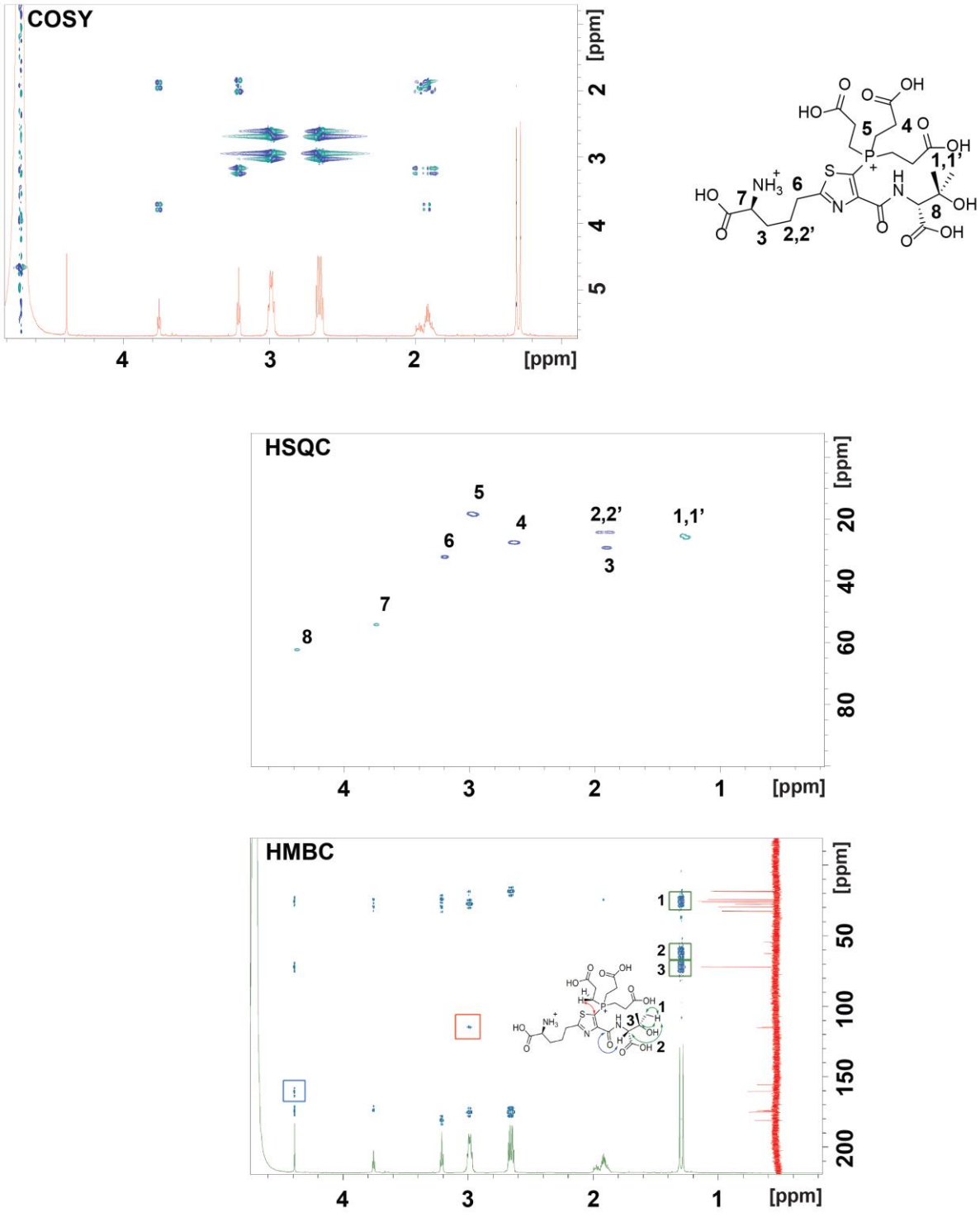


Figure 3.12: COSY, and ^{1}H-^{13}C HMBC and HSQC NMR spectra of the isolated product with m/z = 608.16. The most compatible structure based on NMR and its predicted mass are shown.

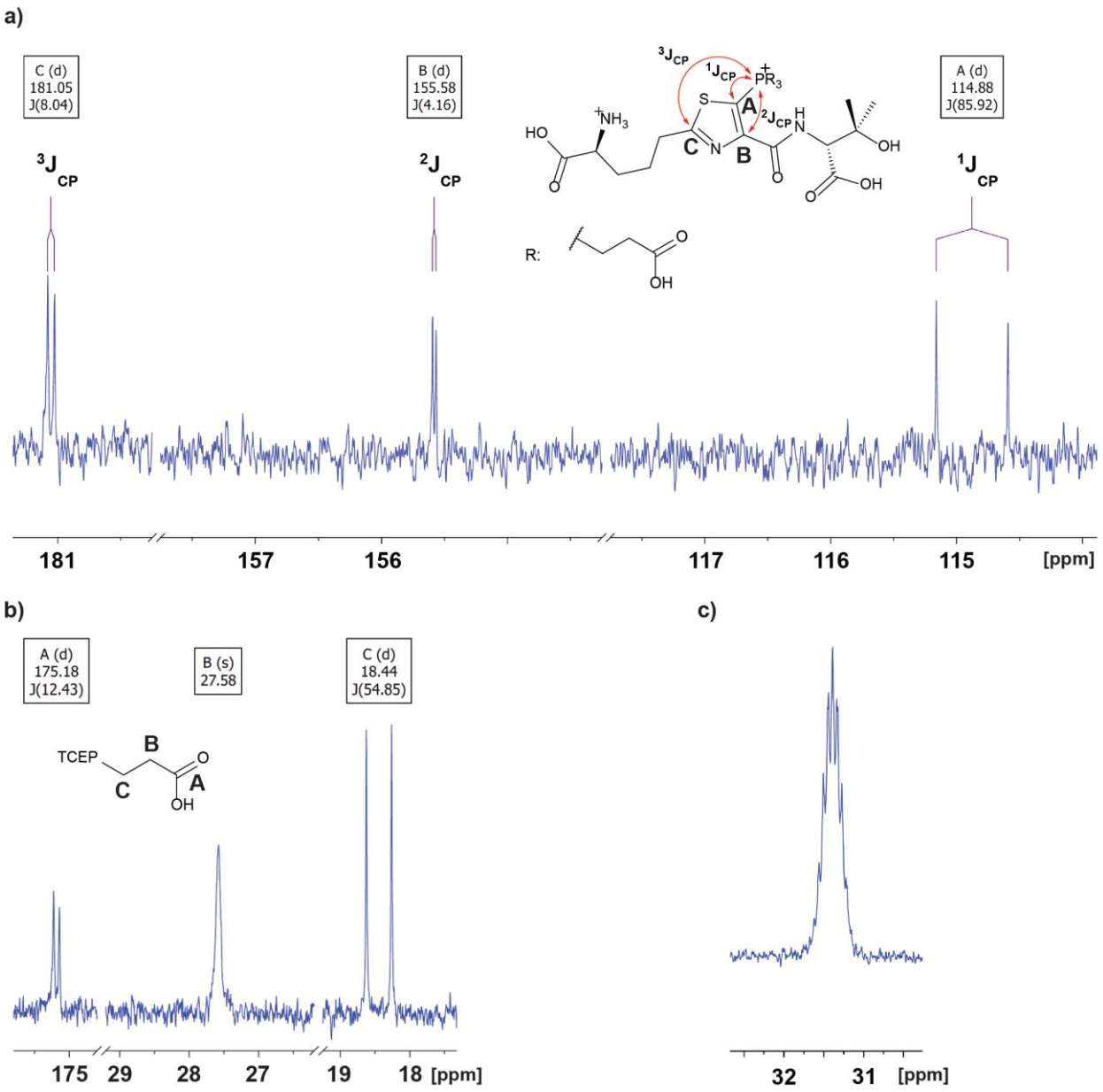


Figure 3.13: Observation of doublet peaks corresponding to the **(a)** thiazole ring and **(b)** TCEP moiety of the product with m/z = 608.16 in the proton-decoupled 1-D ^{13}C NMR spectrum (600 MHz). Coupling constants are shown within the boxes. **(c)** The observed ^{31}P NMR (600 MHz) resonance of the isolated product with m/z = 608.16.

Since the ^{31}P nucleus is NMR active and naturally abundant (I=1/2), some peaks in the 1-D ^{13}C NMR spectrum showed doublet peaks (Figure 3.13 a). The TCEP moiety of the product with m/z = 608.16 also showed doublet peaks in the ^{13}C NMR spectrum (Figure 3.13 b). Hence, the existence of carbon-phosphorus bond in the product is viable.

Moreover, a cross peak in ^{1}H-^{13}C HMBC spectra correlates a CH_2 group of TCEP with an aromatic carbon at 115 ppm (Figure 3.12). This observation supports the proposal that the product is an adduct formed between an ACV derived enzyme product and TCEP. Additionally, the 1-D ^{31}P NMR spectrum of the isolated product showed a multiplet at +31.4 ppm (Figure 3.13 c), which is similar to reported chemical shifts of tetrahedral phosphorus species [11]. In future experiments, existence of the carbon-phosphorus bond of the product with m/z = 608.16 can be evaluated by ^{31}P-^{13}C correlated NMR spectra.

In the HPLC chromatogram of the S281A_IPNS turnover mixture with TCEP, there was another peak next to the aforementioned product (m/z = 608.17) with m/z = 360.12. Although this peak has same m/z value as IPN, its ^{1}H NMR spectrum clearly manifested different peaks compared to IPN (Figure 3.14). Therefore, this product was proposed to be an isomer of IPN; notably, its ^{1}H NMR spectrum had similarity to that of the first eluting product with m/z = 608.17 (Figure 3.11). Comparison of the two spectra indicated that the product with m/z = 608.16 has an additional TCEP derived component compared to the product with m/z = 360.12 as their mass difference is 248.05 Da (equal to TCEP mass minus two protons).

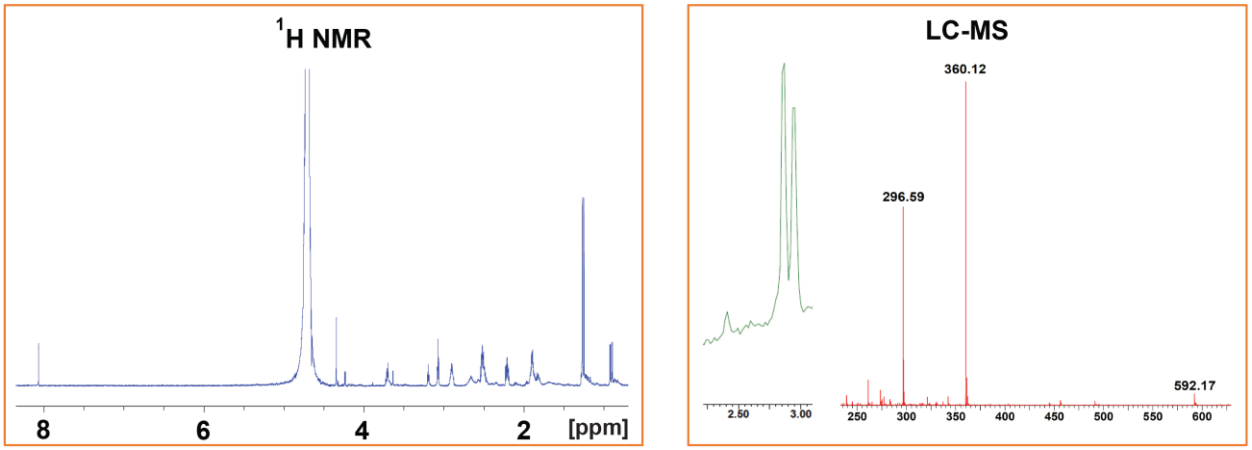


Figure 3.14: ^{1}H NMR (700 MHz) and LC-MS spectra of the second isolated product with m/z = 360.12 from S281A_IPNS turnover with TCEP present. Note this fraction with the second isolated product is less pure than the first fraction (Figure 3.11).

3.2.5: Purification of the S281A_IPNS Turnover Product with m/z=360.12

The second eluting peak was insufficiently pure for structural elucidation. Hence, a number of large-scale turnover reactions without TCEP were carried out. It was hoped that S281A_IPNS turnover without TCEP would only form the product with m/z = 360.12 (Figure 3.10 c), making its purification more feasible. However, the turnover yield was lower without TCEP, likely because of a lack of reducing agent to maintain ACV in the monomeric thiol form, (i.e. less product is produced due to ACV disulfide bond formation).

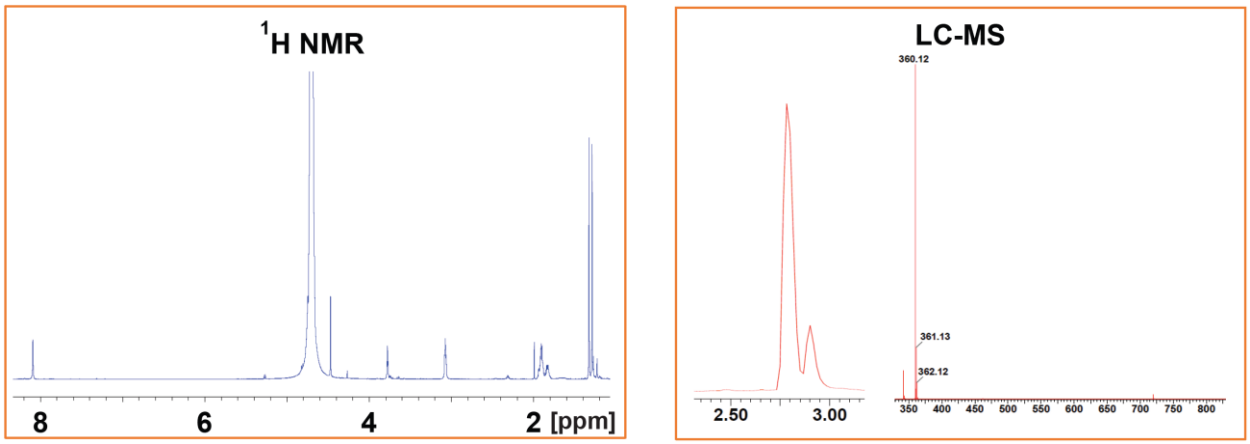


Figure 3.15: ^{1}H NMR (700 MHz) and LC-MS spectra of the isolated product with m/z = 360.12 from the S281A_IPNS turnover without TCEP.

After screening different conditions with various substrate and enzyme ratios, a 10 mL final volume reaction with 20 μM S281A_IPNS, 0.5 mM ACV and 0.2 mM $Fe^{(II)}$ at 50 mM Tris and pH 7.5 was set up. HPLC purification was done using a high-capacity C-18 column which resulted in higher purity of the product (m/z = 360.12). Its corresponding LC-MS and ^{1}H NMR spectra are shown in Figure 3.15.

The 2-D NMR spectra of the product and its most compatible structure are shown in Figure 3.16. The protons of the molecule are labelled numerically to correspond to chemical shift. It is notable that the ^{1}H NMR spectra of the product with m/z = 360.12 is similar to the spectra of the compound with m/z=608.12; the main differences being the lack of the TCEP derived CH_2 peaks and an additional peak in the aromatic region (8.07 ppm). The HMBC cross peaks are highlighted in the spectra (Figure 3.16).

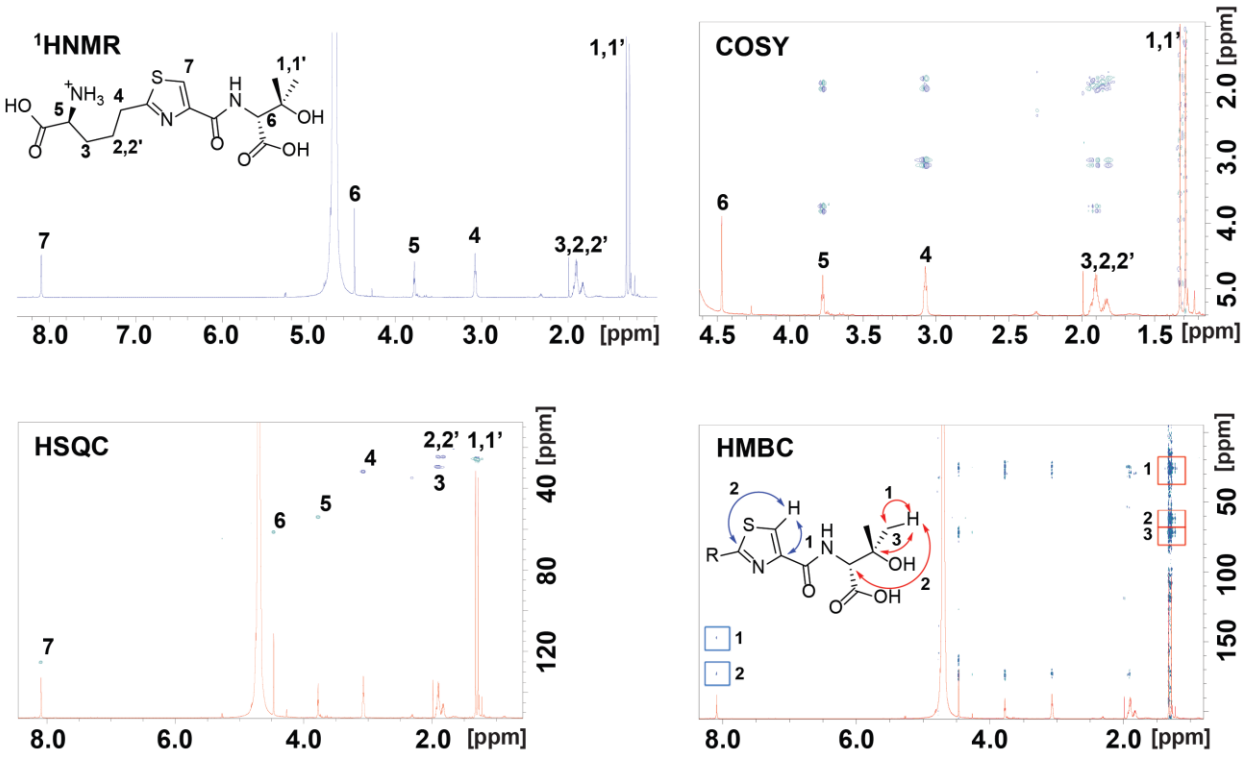


Figure 3.16: COSY, and ^{1}H-^{13}C HSQC and HMBC NMR spectra of the product with m/z = 360.12 obtained from S281A_IPNS turnover without TCEP. The proposed structure is shown, and its protons are labelled numerically to follow their resonances.

These analyses support the presence of a hydroxylated valine residue (red arrows in the HMBC spectrum, Figure 3.16) and thiazole ring formation (blue arrows, in the HMBC spectrum, Figure 3.16). Figure 3.17 shows four possible structures with m/z of 360.12; the predicted ^{1}H and ^{13}C chemical shifts (using ChemDraw software) are shown on the structures.

Table 3.2 presents the measured ^{1}H and ^{13}C chemical shifts of the assigned product structure according to COSY, HSQC and HMBC cross peaks. The experimental chemical shifts fit closely with the predicted values of the structure with the thiazole ring (Figure 3.17 b). Since the new product is isomeric with IPN, as with the conversion of ACV to IPN, its formation requires a 4-electron oxidation of ACV.

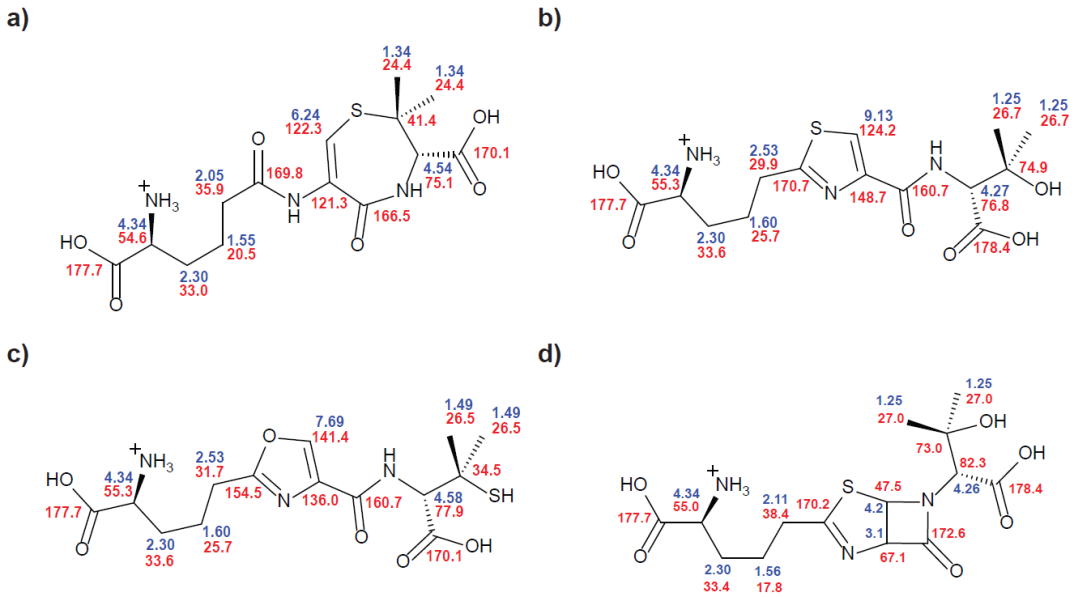


Figure 3.17: Four possible structures for the product with m/z=360.12 with predicted ^{13}C (red) and ^{1}H (blue) NMR chemical shifts. The chemical shifts were predicted using ChemDraw software.

Table 3.2: Observed ^{13}C and ^{1}H chemical shifts of the isolated product with m/z=360.12 according to the COSY, HSQC, and HMBC spectra.

Peak Number	δ(ppm)	COSY (ppm)	HSQC (ppm)	HMBC (ppm)
1	1.28	-	25.6	25.9, 61.5, 71.9
1’	1.32	-	25.9	25.6, 25.9, 61.5, 71.9
2	1.82	3.07	24.5	29.5
2’	1.90	3.07	24.5	29.5
3	1.90	3.71	29.5	24.5, 29.5, 172.8
4	3.07	1.82, 1.90	31.5	24.5, 29.5, 172.8
5	3.71	1.90	54.1	24.5, 29.5, 174.0
6	4.39	-	61.5	25.9, 71.9, 163.1, 174.0
7	8.07	-	125.3	147.2, 172.8

Regarding the product with m/z = 608.17, the structure with similar carbon skeleton to that of the product with m/z = 360.12 is proposed. Since there was no proton resonance in the aromatic region of the product with m/z = 608.17, it is proposed that TCEP would

be attached to the thiazole ring as shown in Figure 3.12. Moreover, the proton-decoupled ^{13}C NMR of the product with m/z = 608.17 shows three doublet peaks (Figure 3.13 a). In spectra of the product with m/z = 608.17 (Figure 3.12), the chemical shifts in both ^{1}H and ^{13}C dimensions are similar to those of the product with m/z = 360.12 (Figure 3.16). Interestingly, the formation of the product with m/z = 608.17 requires a 6-electron oxidation, contrary to the IPN and the product with m/z = 360.12 which involves a 4-electron oxidation. Full NMR characterization of the isolated products with m/z = 360.12 and m/z = 608.17 are shown in Table Appendix 3.I.

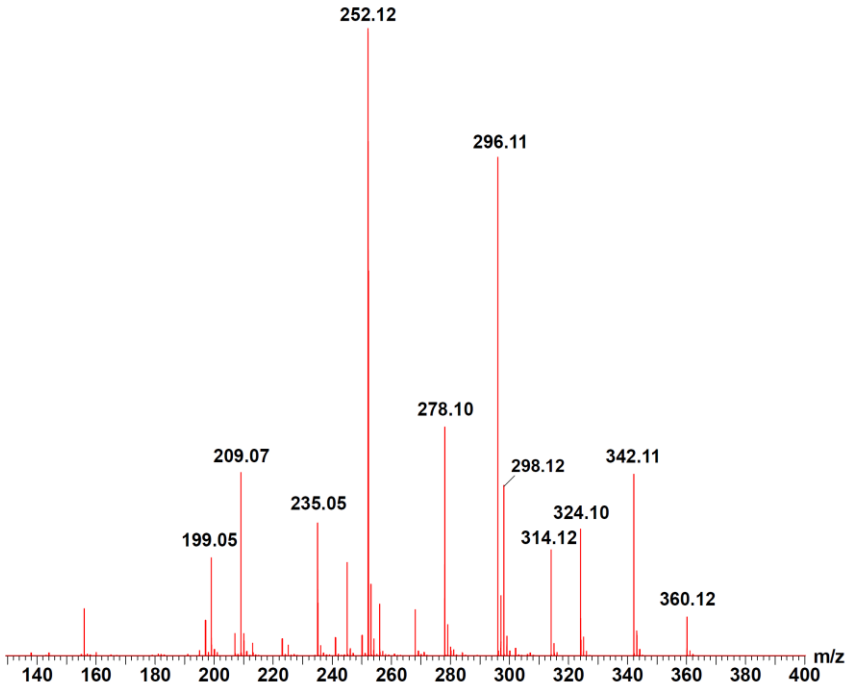


Figure 3.18: MS-MS fragmentation of the new product with m/z=360.12. The spectrum was obtained via locking at m/z = 360.12 and ionization potential was set at 20 volts.

In order to validate the proposed structure of the isolated product with m/z = 360.12, LC-MS-MS was utilized to study its fragmentation pattern. As a control, IPN was used. The MS-MS fragmentation of the new product is shown in Figure 3.18 and a possible fragmentation mechanism based on its structure is proposed in Figure 3.19. The positive ionization method was used, therefore fragmented ion molecules should have a positive charge. The proposed mechanism can account for some of the key peaks

observed in the MS-MS profile. The proposed ion molecules have a +1 charge; their calculated and observed m/z values are shown in Figure 3.19.

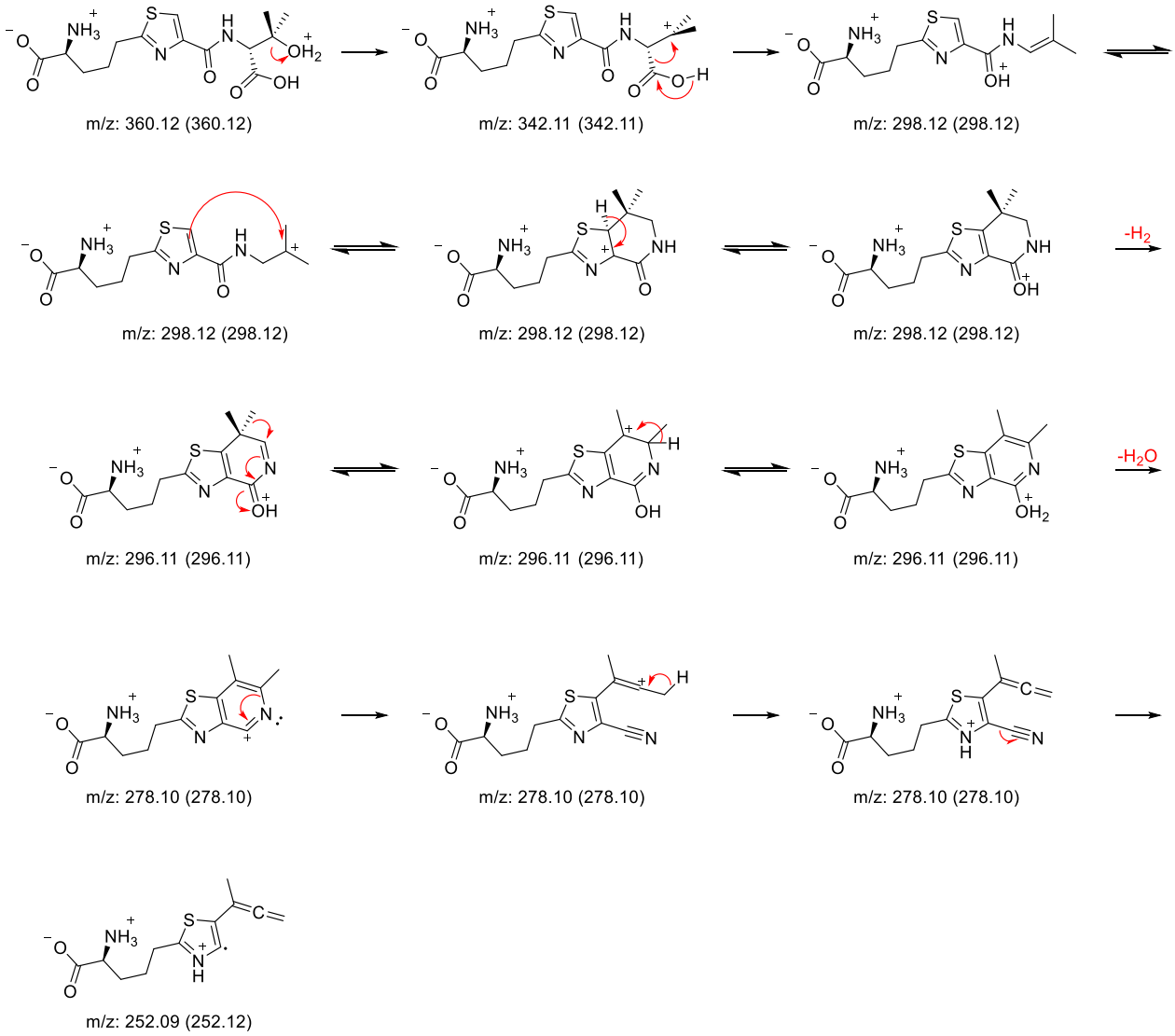


Figure 3.19: Proposed MS-MS fragmentation mechanism of the new product based on its structure. The predicted m/z values for fragment ions are shown with the observed m/z values in parentheses.

3.2.6: Turnover of Cysteinyl ^{13}C-^{15}N Labelled ACV with S281A_IPNS

To gain a better understanding of the new product with m/z = 360.12 formed by S281A_IPNS, the cysteinyl residue of ACV was ^{13}C and ^{15}N labelled (prepared by Dr. P. Rabe and Dr. S. Basak). The resulting labelled ACV was used for turnover assays and the crude mixture was analysed by NMR. The turnover was set up without TCEP, as with the TCEP present a mixture of both products (m/z = 360.12 and m/z = 608.17) were

formed, hence complicating analysis of the crude mixture. The spectrum of the reaction with S281A_IPNS is shown in Figure 3.20a; the ^{13}C and ^{15}N atoms are labelled with red and blue asterisks, respectively. To confirm that the same product was formed with the labelled ACV, ^{1}H CPMG spectra were obtained (Figure 3.20 b). An unlabelled ACV turnover mixture was used for comparison (Figure 3.20 b). The ACV and product methyl groups and NHs, and the product thiazole proton are labelled numerically; the spectrum of the labelled ACV turnover confirms that the same product was formed as with unlabelled ACV turnover. Due to the labelling, the product hydroxy valinyl NH and the thiazole proton manifested as doublets, supporting formation of the same product, consistent with the labelling scheme shown in Figure 3.20 a.

To confirm the carbon-carbon connections within the product, a 1-D proton-decoupled ^{13}C NMR spectrum of the labelled ACV turnover mixture was obtained and compared with ^{13}C NMR of purified unlabelled product (the deshielded region in Figure 3.21). The ^{13}C-NMR of labelled ACV was used as a reference (Figure 3.21). Two of the ^{13}C resonances in the product thiazole ring (carbon 1 and 2) and one in the product carbonyl (carbon 3) are multiplets (Figure 3.21). Figure 3.22 presents the splitting pattern of two of the mentioned carbon resonances which is compatible with the product labelling scheme proposed.

The product hydroxy valinyl carbonyl (marked C-3) shows a multiplet due to one bond and two bond ^{13}C-^{13}C and ^{13}C-^{15}N couplings (Figure 3.22). The product C-1 carbon in the thiazole ring shows a doublet of doublets due to one bond and two bond ^{13}C-^{13}C couplings (Figure 3.22). The coupling constants were extracted and are shown in Table 3.3.

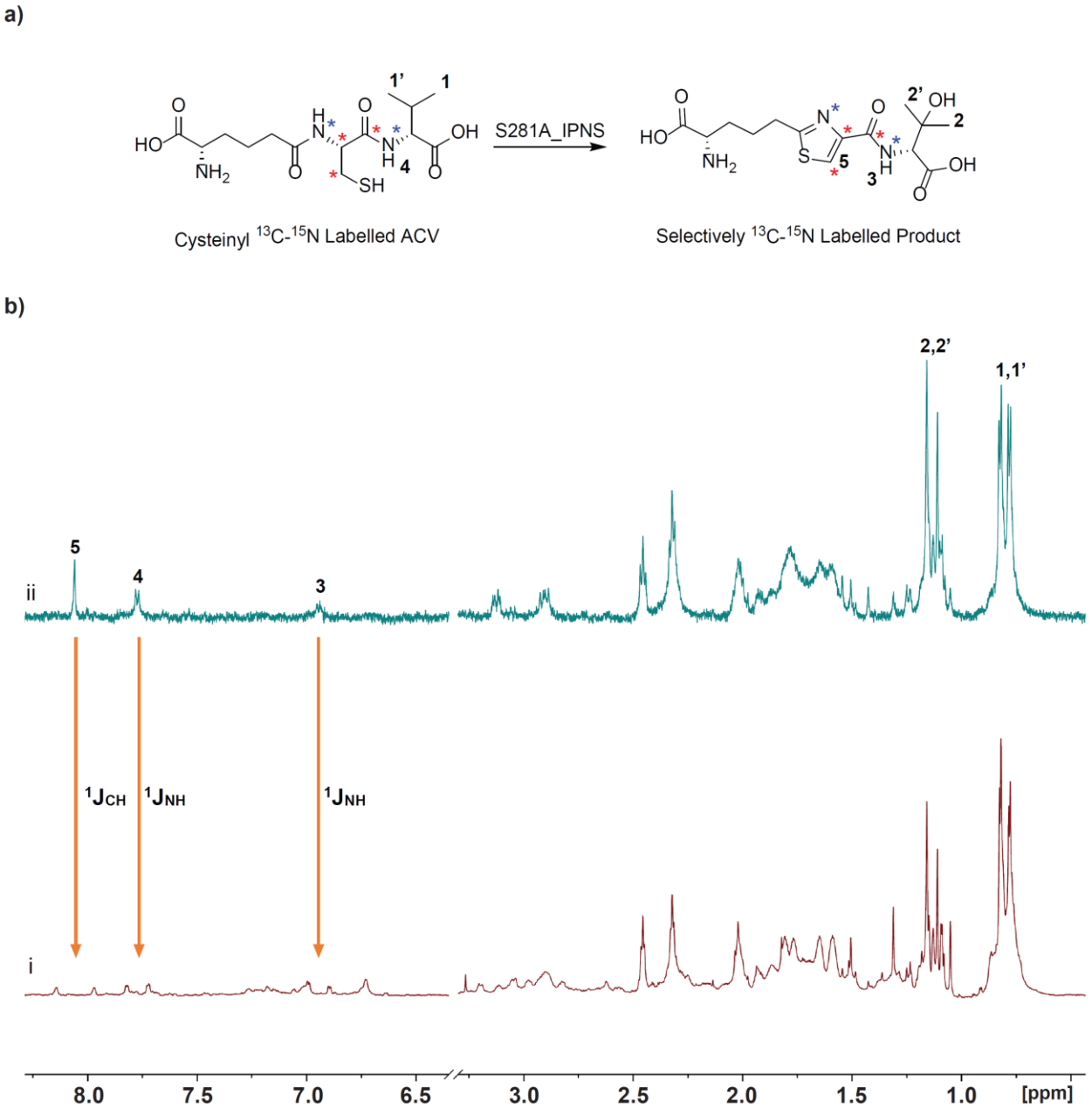


Figure 3.20: **(a)** Turnover of cysteinyl ^{13}C-^{15}N labelled ACV with S281A_IPNS. The ^{13}C and ^{15}N isotopes are labelled with red and blue asterisks, respectively. **(b)** ^{1}H CPMG spectrum of the labelled ACV turnover end point (i) showing formation of the new product. Endpoint of unlabelled ACV turnover with similar conditions was obtained as control (ii). The methyl, NH, and the thiazole protons are labelled numerically.

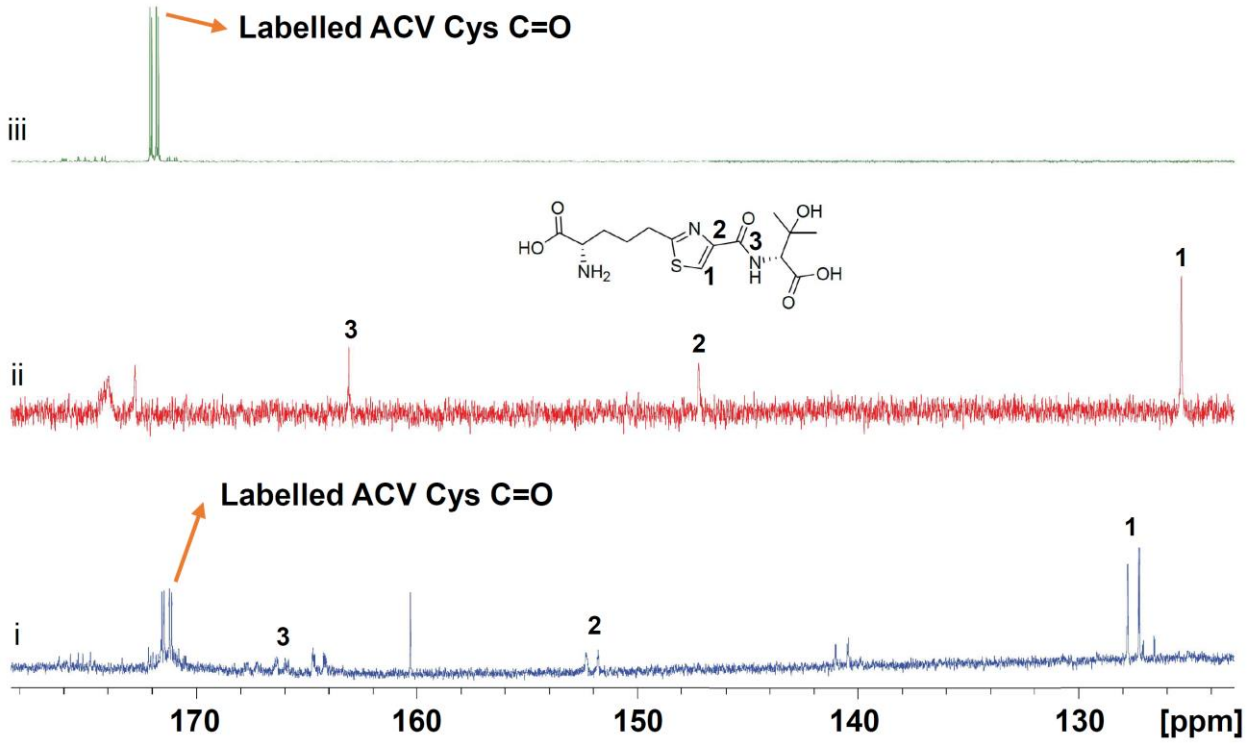


Figure 3.21: Deshielded region of the proton decoupled ^{13}C NMR spectrum obtained from the labelled ACV turnover endpoint mixture (i), the unlabelled purified new product (ii), and pure labelled ACV (iii).

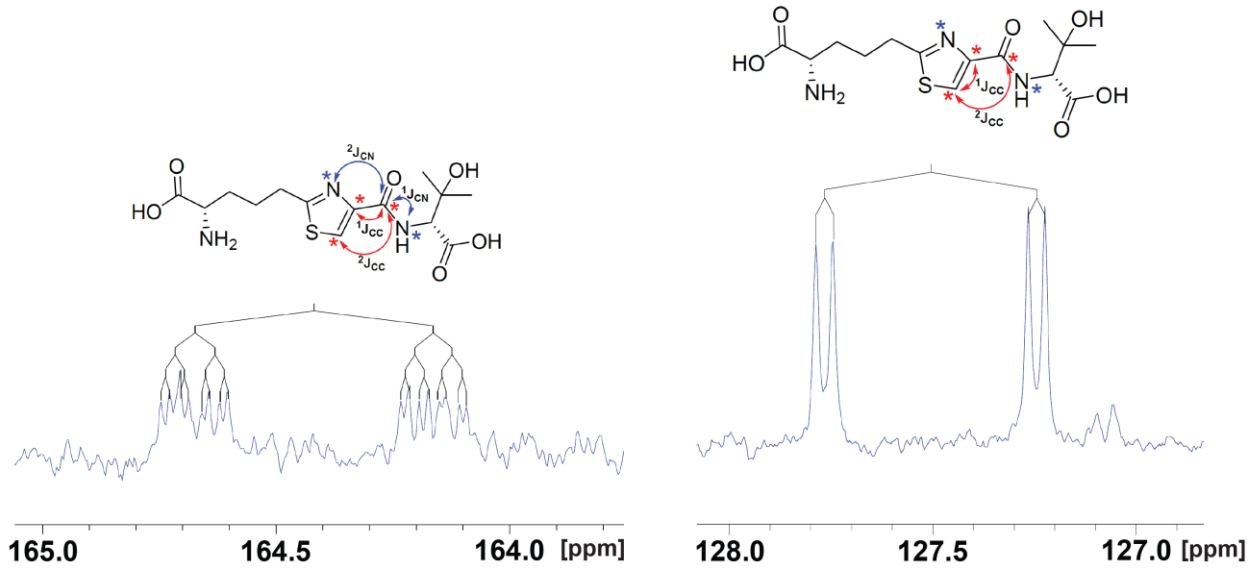


Figure 3.22: Splitting pattern of the product carbonyl (C-3) and the thiazole carbon (C-1) in 13C NMR spectrum of the labelled ACV turnover endpoint.

Table 3.3: One bond and two bond ^{13}C-^{13}C and ^{13}C-^{15}N coupling constants of the labelled ACV turnover product extracted from ^{13}C-NMR spectrum.

Coupling	Coupling Constant
$^{1}J_{CC}$ (C3)	77.0 Hz
$^{2}J_{CC}$ (C3)	6.2 Hz
$^{1}J_{CN}$ (C3)	12.5 Hz
$^{2}J_{CN}$ (C3)	2.7 Hz
$^{1}J_{CC}$ (C1)	78.7 Hz
$^{2}J_{CC}$ (C1)	6.3 Hz

To confirm the product's β-hydroxy valinyl moiety with its backbone chemical shifts, TROSY ^{1}H-^{15}N and TROSY HNCO spectra were obtained (Figure 3.23). Due to the nature of TROSY spectra, all cross peaks are shifted diagonally by half of the coupling constant between the coupled nuclei [12]. One cross peak in the ^{1}H-^{15}N spectrum showed a distinct position in both dimensions, with the nitrogen chemical shift at below 115 ppm and proton at 6.9 ppm. These chemical shifts are compatible with the presence of a hydroxylated valine in both dimensions; C3 hydroxylated amino acids such as serine and threonine exhibit similar chemical shifts [13]. Therefore, the NH of the product β-hydroxy valinyl moiety could be assigned to the mentioned peak (Figure 3.23 a). The other peaks in the spectrum correspond to ACV and dimerized ACV NHs which are present in the crude reaction mixture. In case of the TROSY HNCO spectrum, a plane with the amide proton and carbonyl carbon dimensions is shown and each cross peak corresponds to the NH coupled to its carbonyl (Figure 3.23 b). The cross peak at similar NH chemical shift (6.9 ppm) has a carbonyl chemical shift at 166 ppm which is labelled in Figure 3.23 b. Therefore, these ^{1}H-^{15}N-CO correlated data support the presence of hydroxylated valine residue.

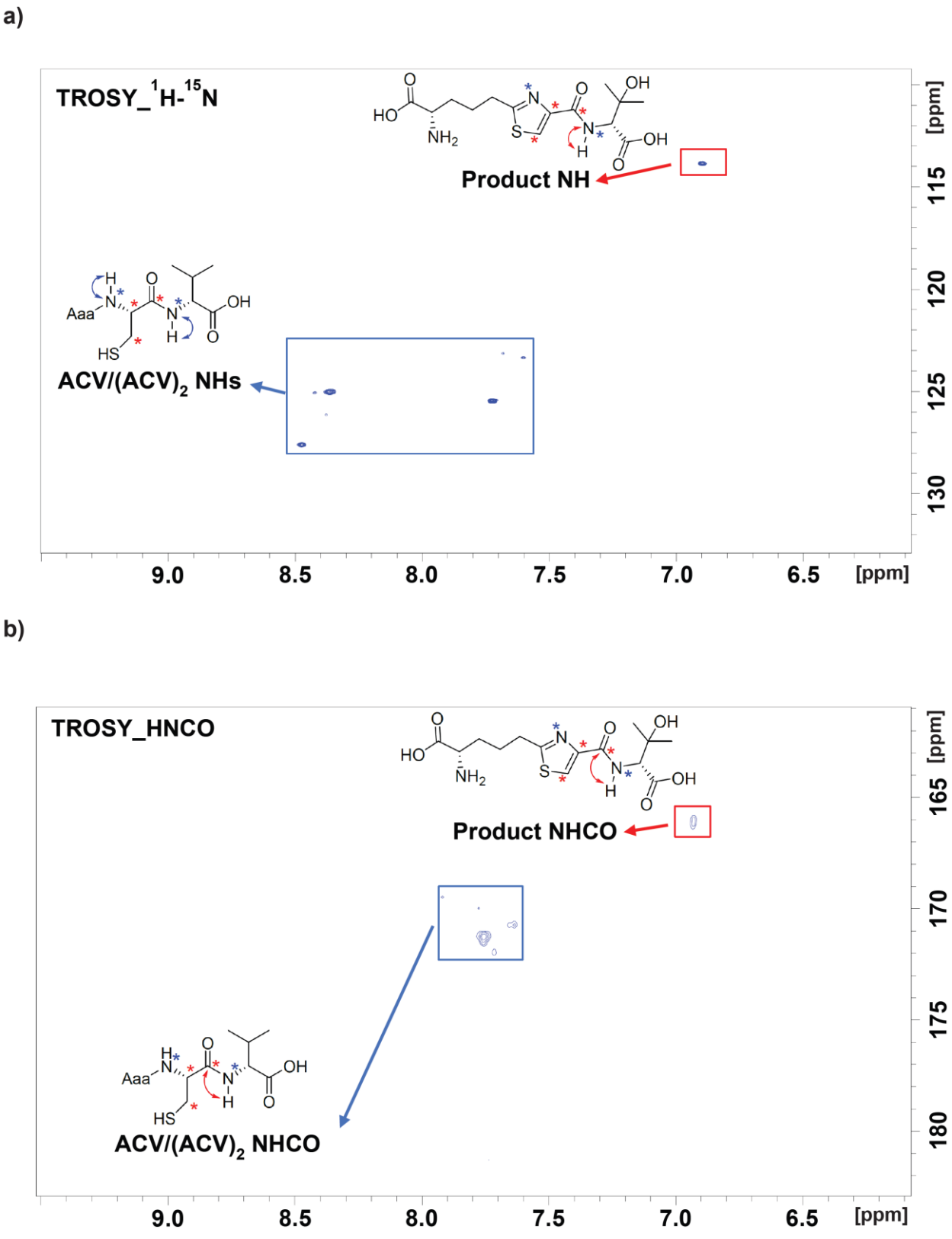


Figure 3.23: TROSY ^{1}H-^{15}N **(a)** and TROSY HNCO **(b)** spectra of the labelled ACV turnover crude mixture.

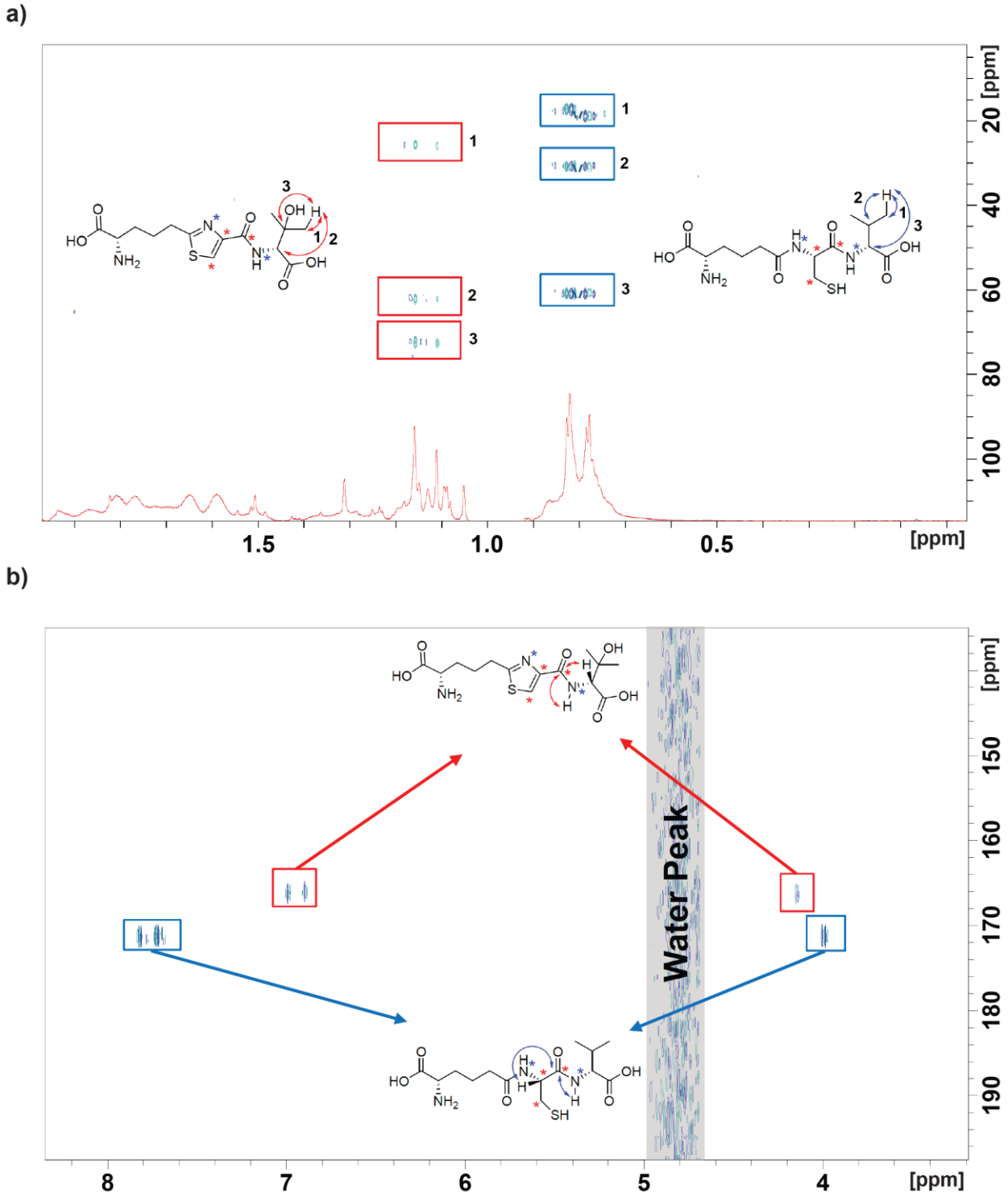


Figure 3.24: ^{1}H-^{13}C HMBC spectrum of the labelled ACV turnover at **(a)** methyl and **(b)** deshielded regions.

To obtain further evidence for the proposed product structure, a ^{1}H-^{13}C HMBC spectrum of the labelled ACV turnover product was obtained; the methyl and deshielded regions are shown in Figure 3.24. The methyl region of the labelled ACV turnover (Figure 3.24 a) is similar to that of the ^{1}H-^{13}C HMBC spectra of the unlabelled pure product (Figure 3.16) confirming that the same product is formed during catalysis. The deshielded region of the ^{1}H-^{13}C HMBC spectrum shows two cross peaks, one correlating with the product β-hydroxy valinyl NH and the other correlating with the product's β-hydroxy valinyl H-α to the carbonyl of the same moiety at 166 ppm (Figure 3.24 b). The appropriate cross peaks corresponding to the ACV and product NHs are doublets in the proton dimension due to ^{15}N labelling (Figure 3.24 b).

3.2.7: Turnover of S281A_IPNS Using ^{18}O Isotope

Since the S281A mutant produces different products compared to WT_IPNS, it is of interest to propose a mechanism to explain how this mutation affects the catalytic pathway. One useful experiment to support a proposed mechanism involves performing ^{18}O labelling studies [14,15]. By conducting the reaction with isotopically labelled $H_2{}^{18}O$ or $^{18}O_2$, and then monitoring the incorporation of the ^{18}O isotope into the reaction products, it may be possible to identify the origin of the different products and better understand the mutation's effect on the reaction mechanism [14,15].

In this regard, two separate experiments with different sources of ^{18}O were conducted. The first experiment was S281A_IPNS turnover under an $^{18}O_2$ atmosphere; the second experiment was turnover in $H_2{}^{18}O$. Since TCEP has shown to form an adduct with the new product, turnover mixtures with and without TCEP were prepared in both experiments. The reactions were quenched appropriately with acetonitrile and analysed by LC-MS to examine for ^{18}O isotope incorporation into the products.

In the turnover reactions exposed to $^{18}O_2$ (Figures 3.25 a and 3.25 b), the S281A_IPNS without TCEP formed an apparent product with m/z = 360.12, i.e. indicating a lack of ^{18}O isotope incorporation from $^{18}O_2$. An apparent product with m/z = 362.14 was also observed in the MS profile, but this may correspond to a different compound. This proposal is made because the ratio of the 360.12 and 362.14 ion peaks was different when the mass spectrum was obtained at slightly different retention times, indicating the

co-elution of two different species. Presently, it is not possible to say whether the m/z = 360.12 or the m/z = 362.14 species corresponds to the assigned product structure. It would be useful to repeat this experiment.

Turnover with TCEP manifested a product with m/z = 610.18 for its +1 ion; and no ion peak with an m/z = 608.17 was observed (Figure 3.25 a). Accordingly, full isotope incorporation of one ^{18}O atom from $^{18}O_2$ into the product with TCEP appears to occur.

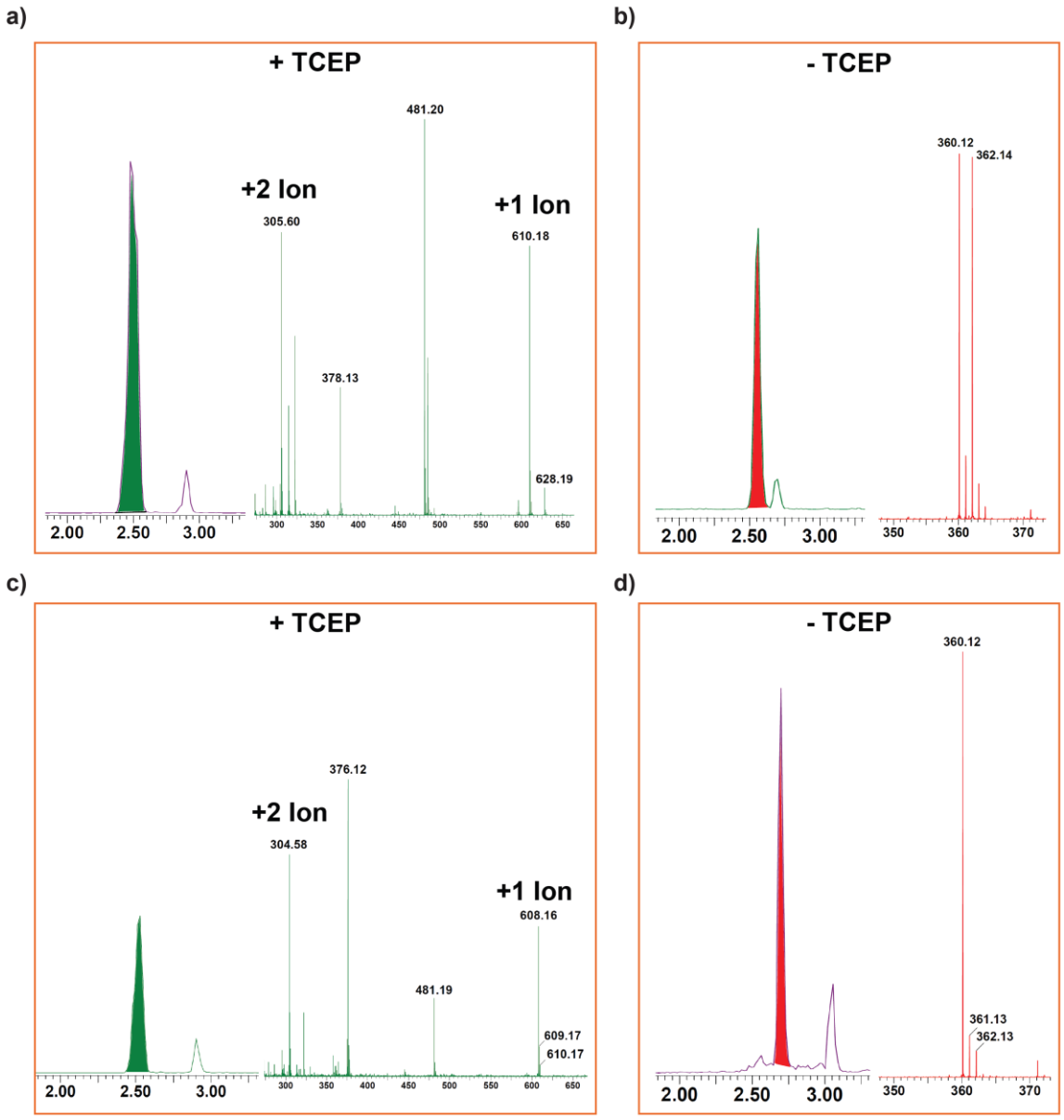


Figure 3.25: Obtained LC-MS results of the S281A_IPNS turnover exposed to $^{18}O_2$ with **(a)** and without **(b)** TCEP; and the same turnover at $H_2{}^{18}O$ water with **(c)** and without **(d)** TCEP.

In the turnover experiments in $H_2{}^{18}O$ water, neither the product with TCEP nor the product without TCEP showed any isotope incorporation (Figures 3.25 c and 3.25 d). Regarding the product with TCEP, it could be concluded that the new oxygen at the hydroxy valine residue is sourced from O_2. However, for the product obtained without TCEP (m/z = 360.12), more experiments are required to identify sources of the oxygen. However, given the lack of incorporation from $H_2{}^{18}O$ in the product obtained without TCEP, it would seem likely that O_2 is likely the source of the hydroxyl group in this case.

3.2.8: Other Mutants of IPNS Giving the New Product

Following studies on S281A_IPNS, other mutants of IPNS were examined for turnover. Unless mentioned otherwise, in all turnover assays the reaction conditions were: 10 μM enzyme, 500 μM ACV, 500 μM TCEP (for reactions with TCEP), and 200 μM $Fe^{(II)}$. The mutants involved Ser_{281}, which is located in the edge of the active site, and Gln_{280} and Leu_{282} which make connections between β-strand 11 and α-helix 3 (Figure 3.3).

The results of the S281T_IPNS ^1H CPMG time course with and without TCEP are shown in Figure 3.26 a. It was hypothesised that with the S281T mutant, where an additional methyl group present may cause a conformational change in its side chain leading to slightly alterations between the interaction between the ACV valinyl carboxylate and the edge of the active site. This altered interaction could alter the flexibility of the ACV valinyl group affecting the outcome of catalysis.

As shown in Figure 3.26 a, S281T_IPNS forms both IPN and the same new product(s) observed with S281A_IPNS turnover, both with and without TCEP. The key differences were lower level of the new product, and the overall faster reaction rate. The amounts of IPN and the new products were approximately equal in case of the S281T mutant. This observation emphasizes the importance of Ser_{281}, which forms an H-bond with the ACV valinyl carboxylate, in catalysis (Figure 3.3). The product without TCEP and the product with TCEP adduct could be followed by blue and black asterisks, respectively (Figure 3.26 a). The results of S281T_IPNS turnover based on proposed structures of the new products is shown in Figure 3.27. The new product methyl groups are labelled in accordance with the NMR data in Figure 3.26 a.

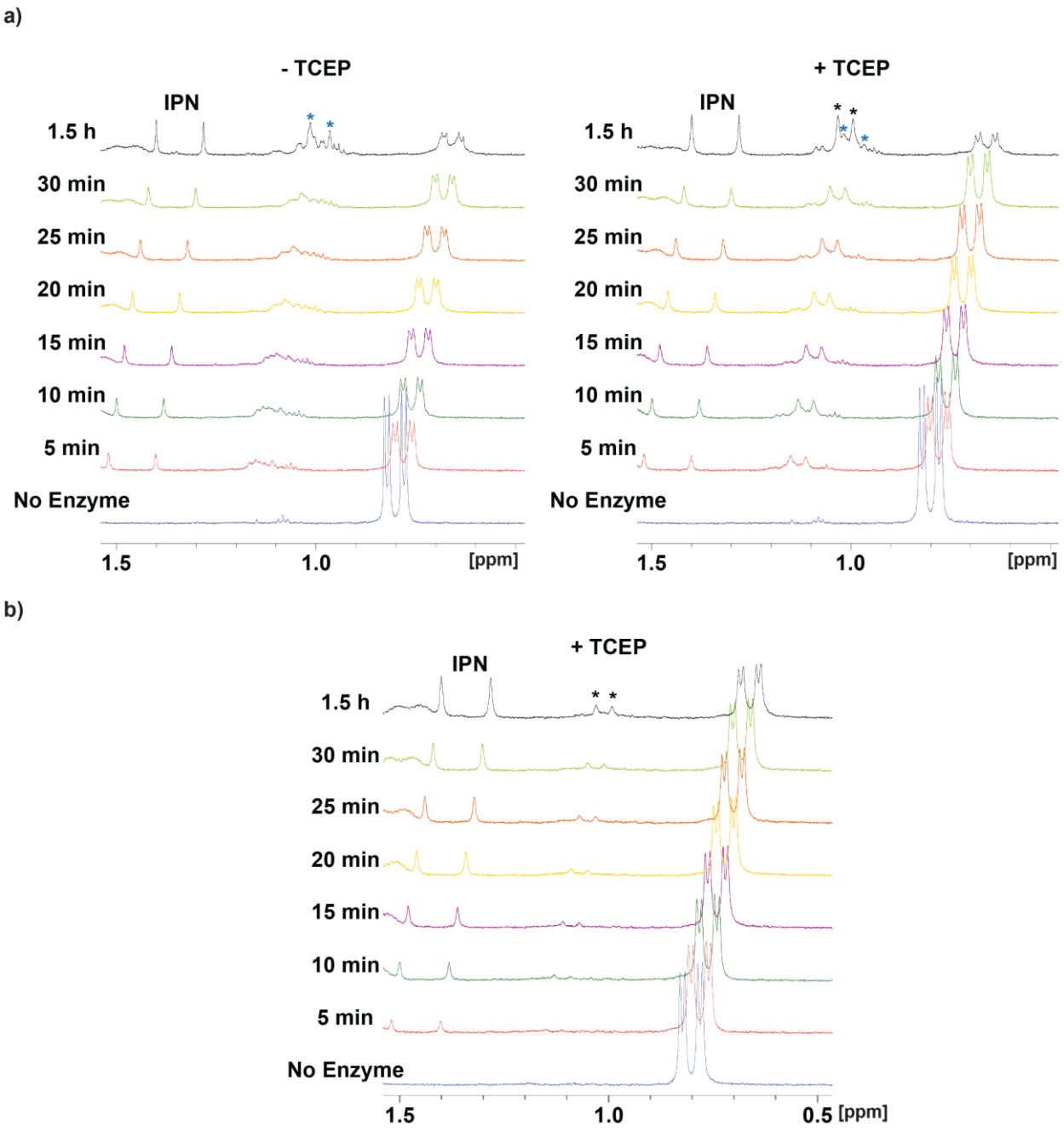


Figure 3.26: **(a)** S281T_IPNS time course with and without TCEP showing formation of both IPN and the new product with similar quantities. **(b)** S281C_IPNS time course with TCEP showing formation of IPN (major) and the new product (minor).

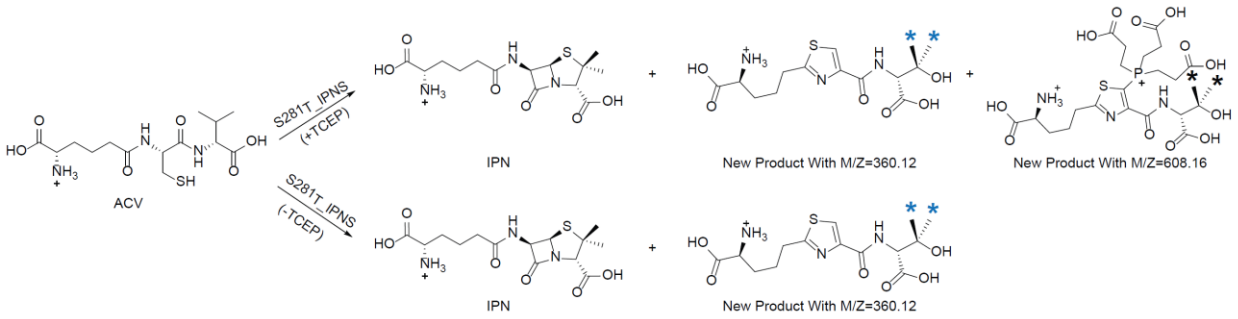


Figure 3.27: Reaction of S281T_IPNS with and without TCEP forming both IPN and the new products.

Another mutation of Ser_{281} subsequently prepared and examined for turnover assays was S281C_IPNS. For S281C_IPNS, a weaker interaction (compared to H-bond) between the ACV valinyl carboxylate and the Cys_{281} thiol was predicted. Due to the weaker interaction, a higher degree of flexibility in the ACV valinyl moiety may be expected, in turn causing formation of the new product.

As with S281T_IPNS, the ^{1}H CPMG spectrum of the S281C_IPNS time course revealed formation of both IPN and the new product (Figure 3.26 b). Moreover, the reaction rate was slower and the selectivity towards formation of the new product was lower than for the S281T mutant.

To examine the role of residues connecting the β-strand 11 to the α-helix 3 in IPNS, i.e. Gln_{280} and Leu_{282}, as shown in Figure 3.3, the Q280A_L282A double mutant as well as the Q280A and L282A single mutants were prepared, and their turnovers were analysed. In these mutations on residues located in the second shell of IPNS, the key residues interacting with ACV are intact. For the Q280A_L282A double mutant, due to lack of interaction between the β-strand 11 to the α-helix 3, higher flexibility of Ser_{281} (located in β-11) was predicted. This higher flexibility may then be transferred through a Ser_{281}-ACV H-bond to the ACV valine residue. Consequently, the Q280A_L282A mutant may exhibit altered catalysis.

The ^{1}H CPMG spectrum for Q280A_L282A IPNS reaction is shown in Figure 3.28 a; Q280A_L282A IPNS exhibited faster turnover, compared to the Ser_{281} IPNS mutants. Notably, despite the presence of intact Ser_{281}, the same new product was formed as a minor product during the turnover (labelled with an asterisk); IPN was the major observed

product. Although relatively small amounts of the new product were formed in Q280A_L282A IPNS turnover, its presence supports the proposal that increased flexibility in β-11 and consequently the ACV valine can alter IPNS catalysis to form the product with a thiazole ring.

In order to investigate which of the Gln_{280} or Leu_{282} residues have more impact on connecting the α-helix 3 to the β-strand 11, turnover of both the Q280A and L282A single mutants were analysed. The results of ^{1}H CPMG time course analyses of the L282A and Q280A mutants are shown in Figure 3.28 c and 3.28 c, respectively. The Q280A_IPNS variant only forms IPN, whereas L282A_IPNS forms minor amounts of the new product as well as IPN. Therefore, it appears that hydrophobic interactions between Leu_{282} and Leu_{54} have more impact on correlating motions of α-helix 3 to β-strand 11 and consequently, to the active site (Figure 3.3). On the other hand, the H-bond interaction between the Gln_{280} and Ser_{55} (Figure 3.3) apparently has less impact as the Q280A mutant only forms IPN. Furthermore, the Q280A_L282A IPNS mutant has higher selectivity for production of the new product compared to the L282A mutant, likely because of the weaker interaction between α-helix 3 and β-strand 11 in the case of the double mutant.

Another mutant aimed at disturbing the Gln_{280} and Ser_{55} H-bond was S55C_IPNS. To further perturb the mentioned interaction, the S55C mutant was further modified by adding small molecule tags to the Cys_{55} thiol group (the S55C_IPNS and its modified versions were provided by Dr. P. Rabe). These tags include 3-bromo-1,1,1-trifluoroacetone (BTFA), biotin (a larger molecule with biotin moiety was used), and 3-(2-Iodoacetamino)-PROXYL (used for EPR spin labelling [21]). Figure 3.29 presents the structures of these molecules.

The S55C_IPNS variant and its modified versions were examined in turnover assays (Figure 3.30). According to the obtained ^{1}H CPMG time course with S55C_IPNS, only IPN was formed, and the new product peaks were not observed. The time course also revealed two additional singlets which correspond to hydrolysed IPN. These peaks are similar to those observed in hydrolysed IPN spectra (Figure 3.9). Therefore, the catalysis of S55C_IPNS and the same enzyme with small molecule tags on the Cys_{55}

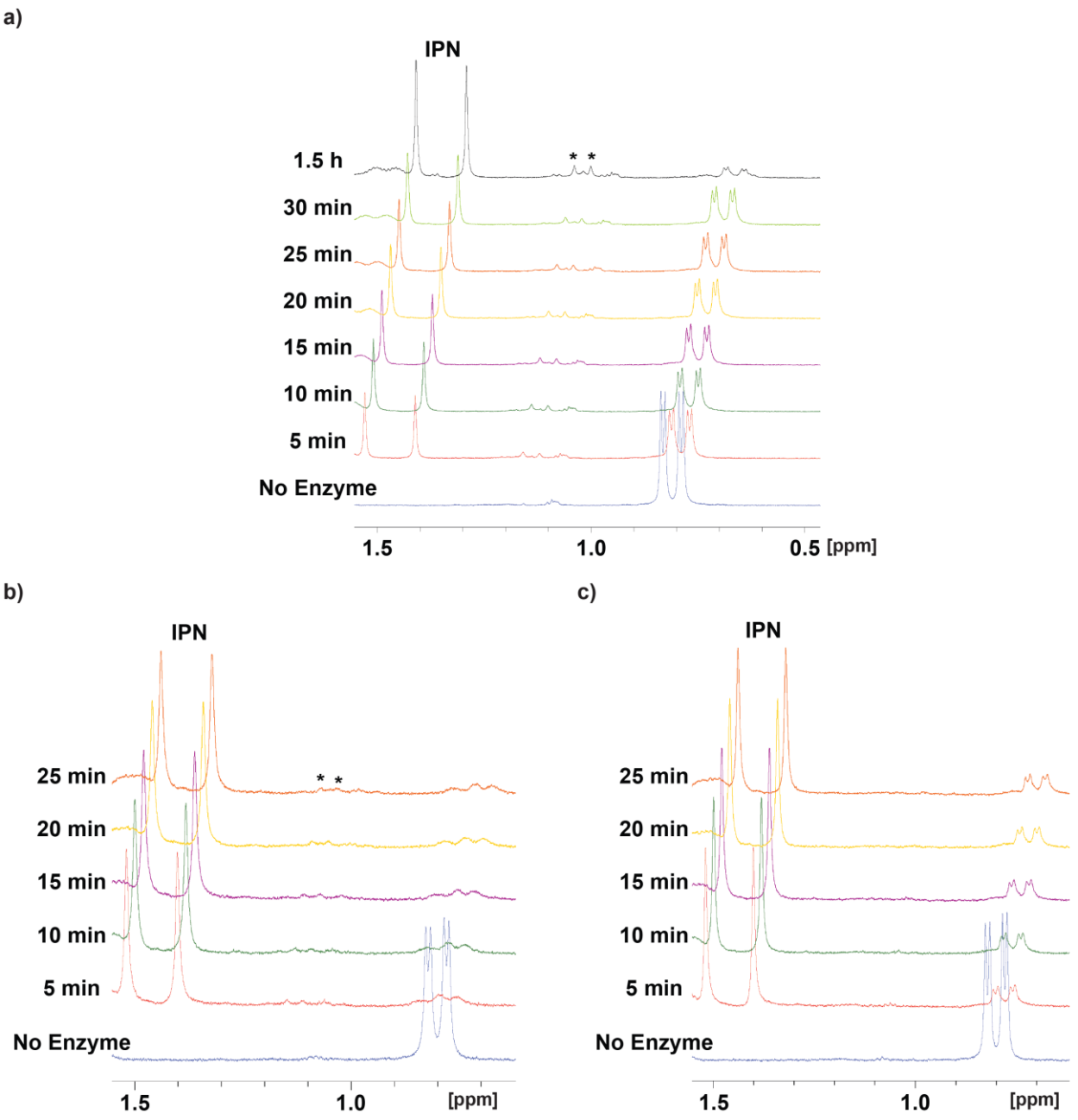
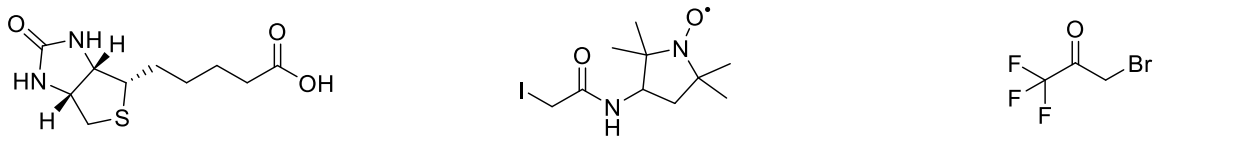


Figure 3.28: CPMG edited ^{1}H spectra of time courses of Q280A_L282A double mutant **(a)**, and L282A **(b)** and Q280A **(c)** single mutants. All turnover conditions were with TCEP and the new product is marked with a black asterisk.



Biotin | 3-(2-Iodoacetamino)-PROXYL | 3-Bromo-1,1,1-trifluoroacetone

Figure 3.29: Structures of three small molecules with different sizes which were attached to the S55C_IPNS Cys_{55} thiol group.

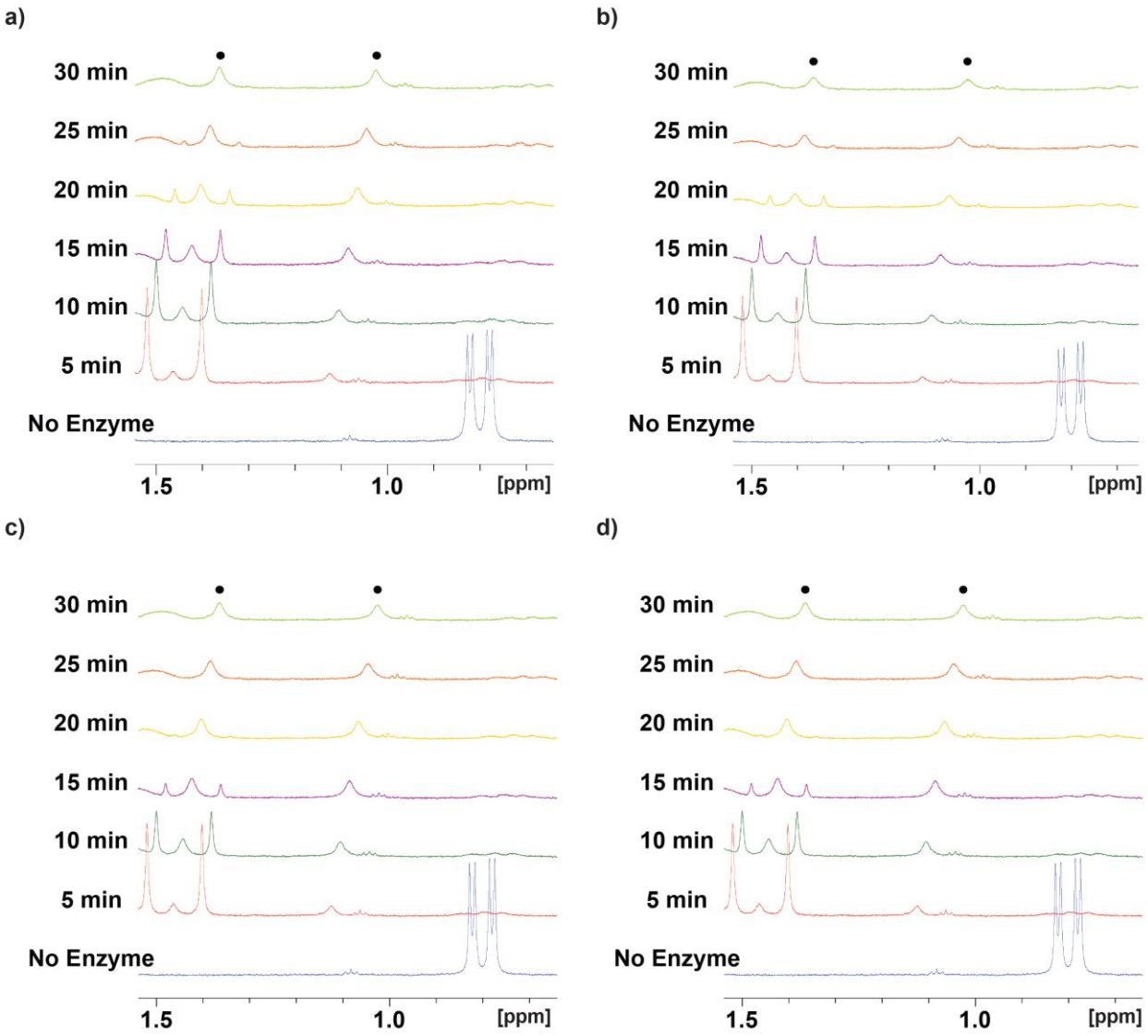


Figure 3.30: CPMG edited ^{1}H spectra of S55C_IPNS **(a)**, biotin tagged S55C_IPNS **(b)**, 3-(2-iodoacetamino)-PROXYL tagged S55C_IPNS **(c)**, and BTFA tagged S55C_IPNS **(d)**. All turnover conditions are with TCEP, and the hydrolysed IPN methyl peaks are labelled with black dots.

residue only forms IPN. The IPN hydrolysis could, at least in part, be due to β-lactamase impurities existed in the enzyme batches. This is in agreement with the Q280A_IPNS turnover experiment indicating that modifying the Gln_{280} and Ser_{55} H-bond does not affect the IPNS catalysis.

3.2.9: Examining S281T_IPNS Selectivity

Among the mutants of IPNS for which turnover was analysed, the S281T mutant showed almost equal amounts of IPN and the new products with and without TCEP (Figure 3.26 a). Therefore, the S281T mutant was further analysed to see how its selectivity changes under different conditions. It was envisioned that there should be a branch point in the catalysis which bifurcates, one forming IPN and the other enabling hydroxylation of the ACV substrate valine. The latter pathway eventually leads to formation of the new products. The selectivity in the mentioned step could depend on how rigid or flexible the ACV valine is, and this flexibility depends on type of the mutation. Proposed mechanisms are discussed in Section 3.2.14.

One experiment which could support the detailed proposed mechanism of enzymatic reaction, is to examine the IPNS mutant's activity and selectivity in D_2O [16,17]. In order to investigate whether D_2O changes the selectivity of S281T_IPNS, assays were conducted under the same conditions (with and without TCEP), one with near 100% D_2O and one with 10% v/v D_2O (small amount of D_2O is required for NMR external lock). The turnover of S281T_IPNS with TCEP shows different selectivity in near 100% D_2O (Figure 3.31 a). That is, in near 100% D_2O, a lower amount of the new product (TCEP adduct) was formed compared to IPN. However, the ^1H CPMG time course of S281T_IPNS without TCEP with 100% D_2O is similar to that of 10% v/v D_2O (Figure 3.31 b). Hence, the selectivity of S281T_IPNS turnover without TCEP does not change with D_2O.

Another turnover experiment with 50% D_2O was conducted to see if it shows a selectivity in between the other conditions. To better compare the selectivity of S281T_IPNS turnover (with TCEP), ^1H CPMG spectra at a specific time point (at 30 minutes) were examined. The ratio of IPN to all new products with hydroxylated valine

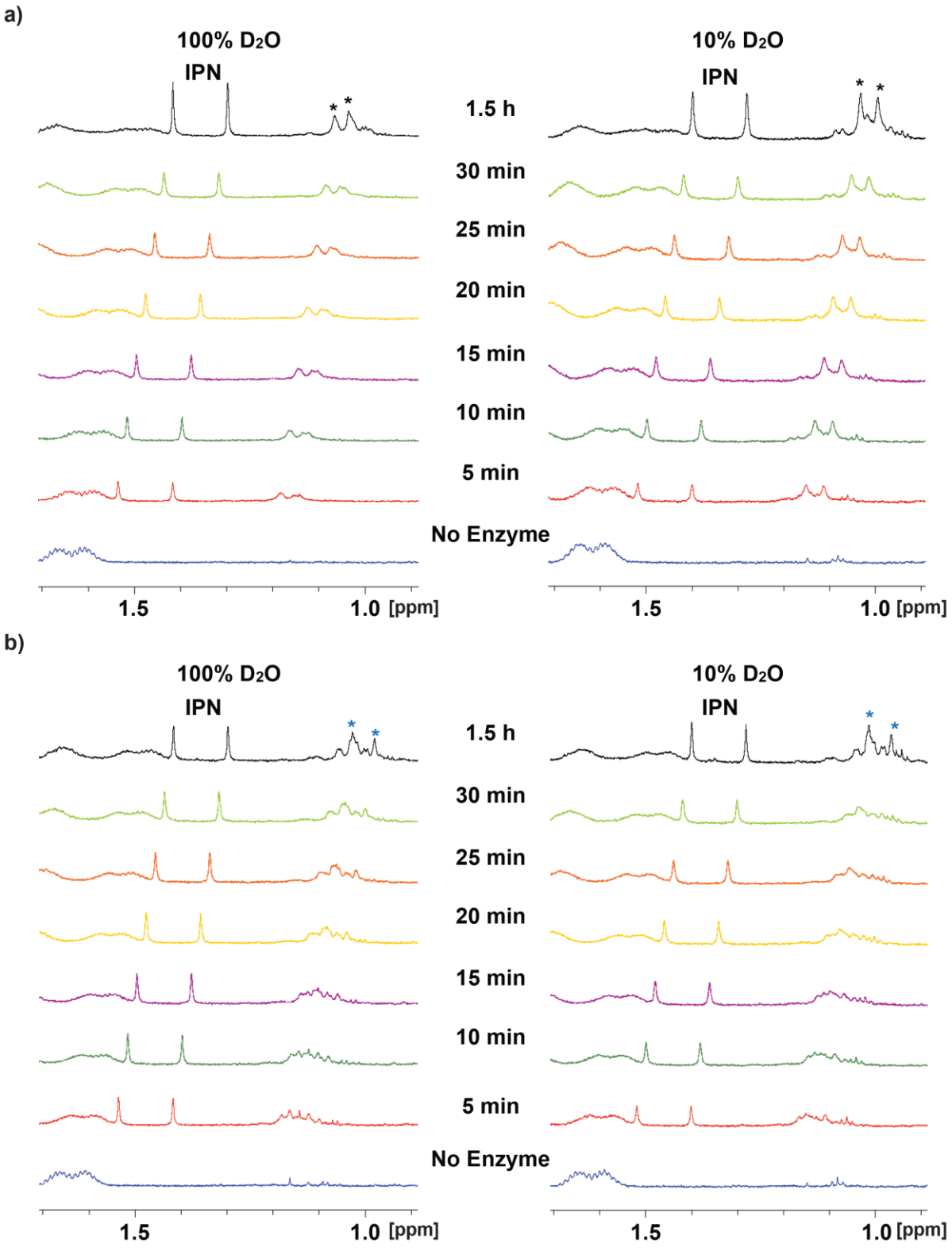


Figure 3.31: **(a)** CPMG edited ^{1}H NMR of S281T_IPNS time course with TCEP at full D_2O and 10% D_2O, the new product is marked with a black asterisk. **(b)** Time course of S281T_IPNS without TCEP at full D_2O and 10% D_2O, the new product is labelled with a blue asterisk.

was measured by their corresponding methyl peak integrals. This ratio was used to compare the selectivity with full D_2O, 50% D_2O, and 10% D_2O (Figure 3.32). The ratio of IPN to the new products increases as the D_2O content increases, indicating that formation of the product with TCEP is slower in D_2O. It is worth mentioning that the sample pH (or pD) increases at higher D_2O content [18]; the pH/pD of the buffers in 50% and 100 % D_2O (measured without correcting the solvent isotope effect) showed an increased value (Figure 3.32). This pH/pD change could have an effect on the S281T_IPNS selectivity.

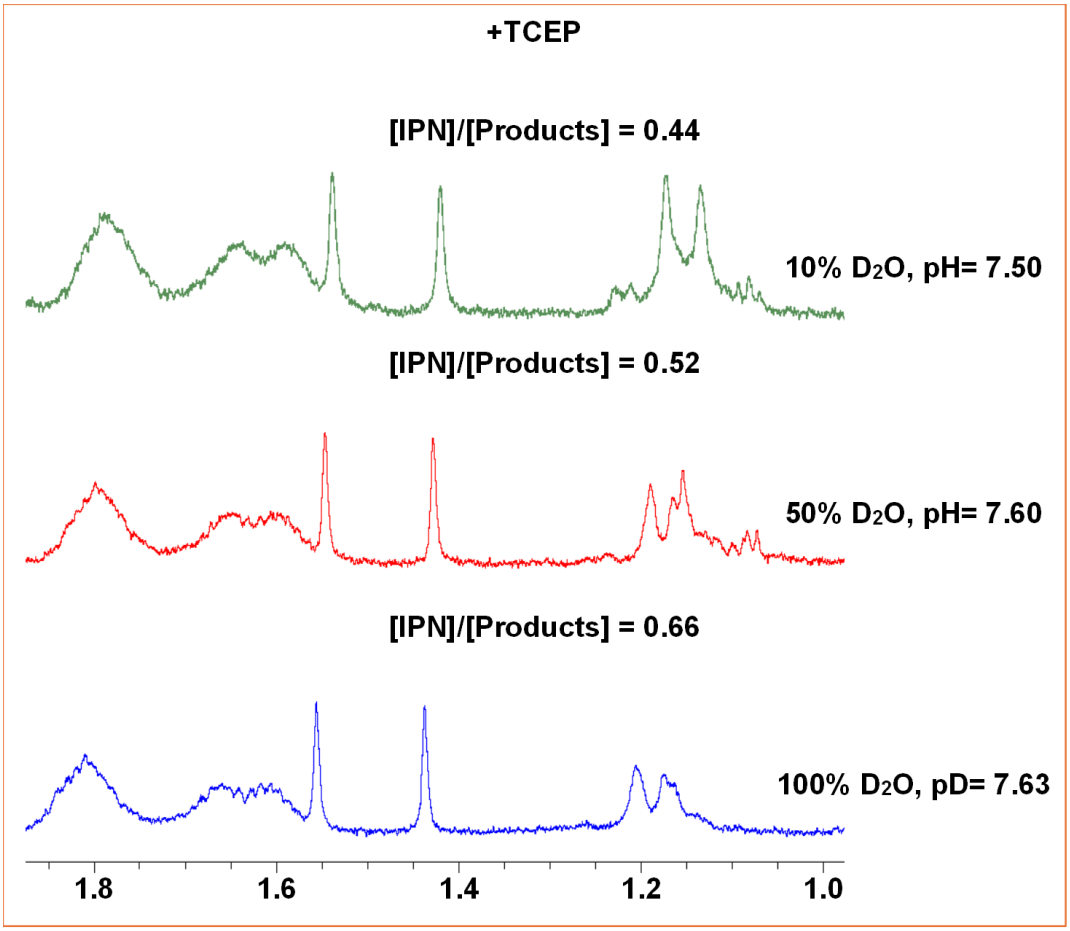


Figure 3.32: CPMG edited ^1H NMR spectra of S281T_IPNS turnover with TCEP after 30 minutes at 100%, 50%, and 10% D_2O. The change in ratio of IPN to the new products is shown. To better visualize the selectivity changes, spectra intensities are adjusted to have similar IPN methyl peak heights. The pH / pD values are shown without correcting the solvent isotope effect on pH.

Since the turnover samples dissolved in full or partial D_2O exhibits higher pH (or pD), the selectivity of the S281T_IPNS turnover at different pH values was analysed. Turnover samples of S281T_IPNS with and without TCEP at pH range from 7.0 to 8.0

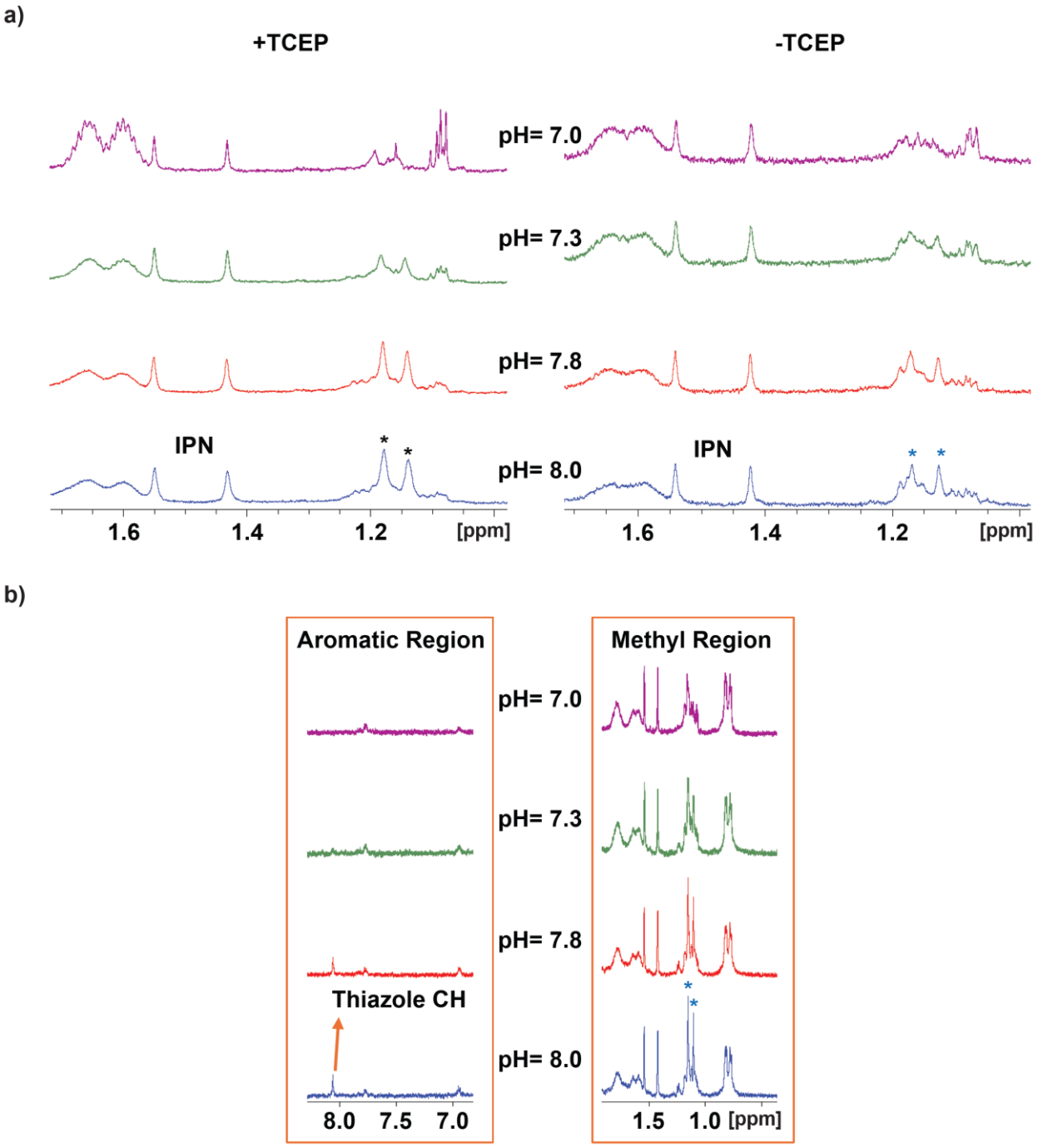


Figure 3.33: **(a)** CPMG edited ^{1}H NMR spectra of S281T_IPNS turnover after 5 minutes at different pH values with and without TCEP. The methyl resonances of the new products with and without TCEP are labelled with black and blue asterisks, respectively. **(b)** CPMG edited ^{1}H NMR spectra showing the methyl and aromatic region for the S281T_IPNS turnover without TCEP after 90 minutes at different pH values. The methyl resonances of the new product are labelled with a blue asterisk.

were prepared and their ^{1}H CPMG time courses were obtained. These experiments aimed to determine whether the observed selectivity change in D_2O for the turnover with TCEP is due to an isotope effect, rather than an artifact stemming from pH/pD changes.

The methyl regions in the spectra of S281T_IPNS turnover 5 minutes after start of the reaction at different pH values are shown in Figure 3.33 a. For both conditions with and without TCEP, the amount of the new product with respect to IPN is higher at higher pH values. This observation could be useful with respect to mechanistic proposals as more new products are formed under more basic conditions. To examine the formation of the thiazole ring in the turnover without TCEP, the aromatic proton at 8.07 ppm was monitored. In this regard, the endpoint of the S281T_IPNS turnover without TCEP (after 90 minutes) was examined at different pH values (Figure 3.33 b). Both methyl and the aromatic regions are shown at different pH values (Figure 3.33 b). By following the thiazole proton at 8.07 ppm (assigned in Section 3.2.5), it seems that the thiazole ring is formed faster at higher pH (Figure 3.33 b).

All in all, the S281T_IPNS turnover without TCEP did not show any significant change in rate of the new product formation in D_2O. However, turnover with TCEP showed evidence for slower formation of the new product with m/z = 608.17 (which is an adduct with TCEP) in D_2O. It was observed more basic conditions may increase the rate of formation of the product with TCEP (Figure 3.33 a), and D_2O buffers have slightly higher pD than pH of their equivalent H_2O buffer [18]. Therefore, in the turnover with TCEP, it is proposed that the slower rate of the new product (m/z = 608.17) formation in D_2O is due to a kinetic isotope effect. The formation of the new product (without TCEP) did not show any evidence for an isotope effect; hence it seems use of D_2O slows the rate of TCEP adduct formation. Overall, these findings imply that the isotope effect is only observed in the reaction with TCEP, therefore likely not involved in the enzyme catalysed reactions but only on the reaction of the small molecules.

3.2.10: Monitoring Possible Intermediates in S281T_IPNS Turnover

As described above, S281T_IPNS forms the same products as S281A_IPNS in turnover with or without TCEP. Time course studies to investigate the intermediates in S281T_IPNS catalysis were conducted. Turnover was analysed at similar timepoints by

NMR and LC-MS. The reason for choosing the S281T mutant for these studies was because it shows higher activity than the S281A_IPNS, hence it could be easier to track intermediates over a reasonable time (e.g. 90 minutes).

During the time course of S281T_IPNS without TCEP, the ^{1}H NMR spectra showed that the characteristic thiazole peak (at 8.07 ppm) appears to form at the later stages of turnover. That is, the methyl peaks at below 1.2 ppm, corresponding to the hydroxylated valine, appear at the beginning of the catalysis and the thiazole proton peak appears at a later stage (Figure 3.34 a). This observation indicates that the hydroxylation on the substrate valinyl moiety occurs first, and the thiazole ring forms subsequently (possibly in an enzyme independent process, although an active site reaction is also possible). Moreover, the methyl peaks in the ^{1}H NMR spectra at 5-minute time point and the peaks at 90-minute time point do not have same chemical shifts (grey lines in Figure 3.34 a). The methyl peaks at the 30-minute time point show small amounts of the intermediate peaks observed at 5 minutes as well as the final product peaks (Figure 3.34 a). Accordingly, there should be an intermediate with a hydroxylated valine moiety, which does not have a thiazole ring. This intermediate can eventually convert into the final isolated product via formation of the thiazole ring.

To better characterize the proposed intermediate, turnover was done without TCEP under similar conditions and the reaction was quenched at similar timepoints for analysis by LC-MS (Figure 3.34 b). As shown in Figure 3.34b, a peak eluting at 1.2 minutes with an m/z value of 378.13 is observed. This peak appears to form at the beginning of the time course and remains constant over time. This could correspond to the observed methyl peaks in the ^{1}H NMR spectrum at the beginning of the time course. A proposed intermediate with its predicted m/z (based on chemical ionization) is shown in Figure 3.35.

The proposed intermediate, bears a double bond at the cysteinyl and a hydroxyl group at the valinyl moieties of the substrate, and could be initially formed via substrate 4-electron oxidation. Subsequently, the proposed intermediate can convert into the product via losing one H_2O molecule (Figure 3.35). The LC-MS data in Figure 3.34 b also show an additional peak being formed overnight, which elutes slightly before the new product and the IPN peak. This peak (marked purple) could stem from IPN reaction with

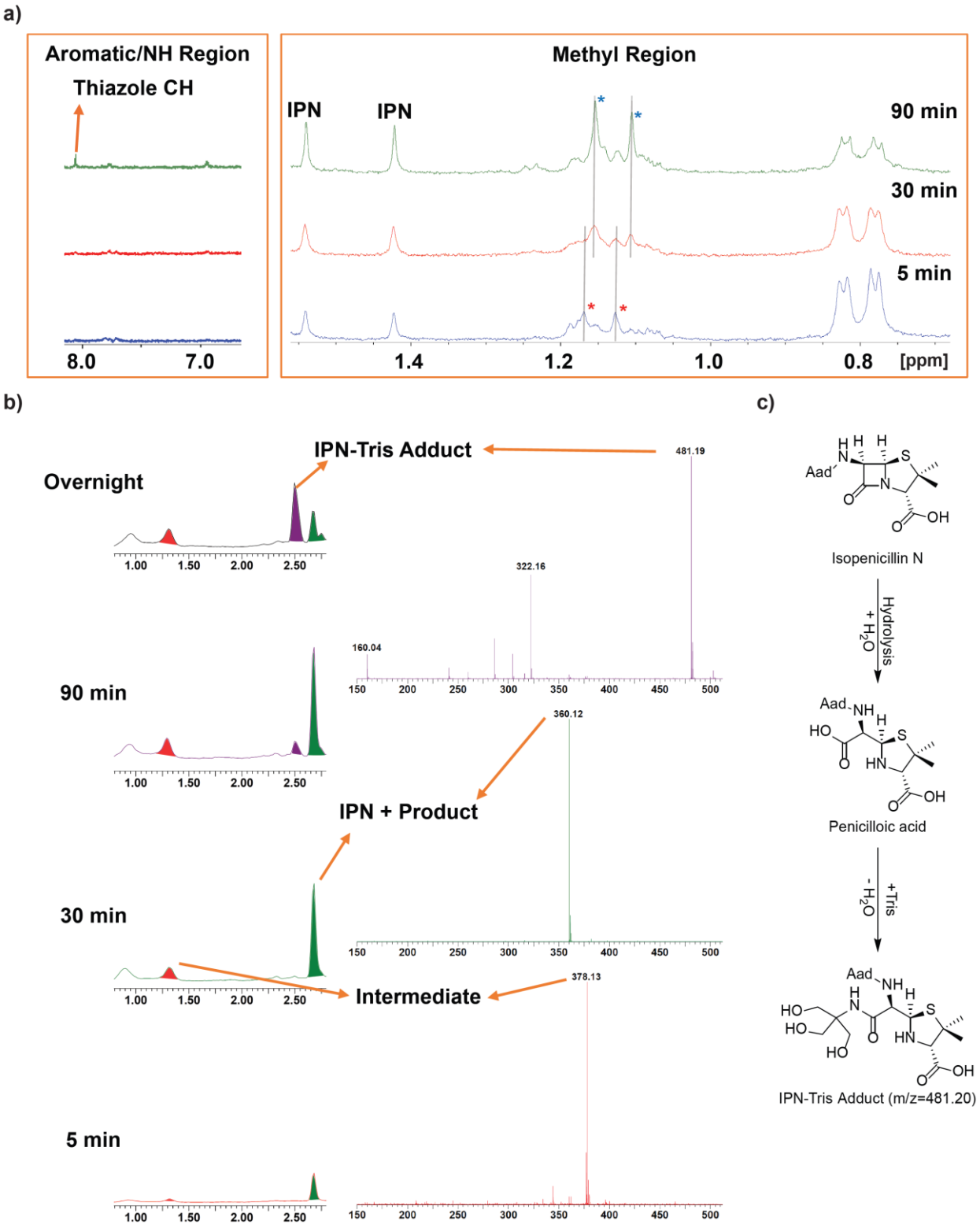


Figure 3.34: **(a)** CPMG edited ^{1}H NMR spectra of the S281T_IPNS turnover showing methyl and aromatic regions at different timepoints. **(b)** LC-MS spectra of the S281T_IPNS turnover quenched at specific

timepoints showing an intermediate with m/z=378.13. **(c)** Isopenicillin N hydrolysis followed by adduct formation with Tris buffer. The IPN-Tris adduct expected m/z value is shown in parentheses.

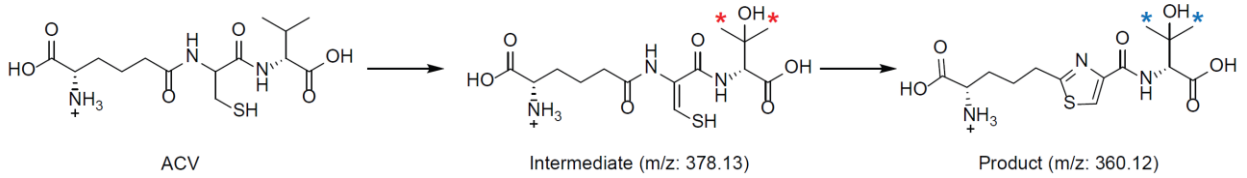


Figure 3.35: Proposed intermediate (which may or may not be enzyme bound) based on observed ^{1}H NMR and LC-MS data which converts into the product with m/z=360.12. The methyl groups are labelled in accordance with the spectra at Figure 3.34 a.

Tris buffer (Figure 3.34 c). Its experimental m/z value (481.19) fits with the expected m/z value of the adduct between IPN and Tris buffer (481.20).

To investigate how TCEP interacts with the S281T IPNS turnover, further experiments were conducted. In one experiment, an S281T_IPNS time course with TCEP present was examined by LC-MS, quenching at specific time points (similar to the experiment in Figure 3.34 b). According to the chromatograms obtained at different timepoints (Figure 3.36 a), there are two intermediate peaks with the same corresponding m/z value (628.19 for +1 charge and 314.6 for +2 charge). These peaks increase initially and then decrease at later timepoints; they could correspond to the same molecule with two different tautomeric/isomeric structures. As shown in Figure 3.36a, this molecule (red peaks) could be an intermediate which converts into the molecule with m/z=626.18 (grey peak) and eventually to the product with m/z=608.17 (green peak). Considering the proposed intermediate structure for the turnover without TCEP (Figure 3.35), a structure is proposed for the intermediate with m/z=628.19 (Figure 3.36 b). This structure could result from addition of TCEP to the intermediate with hydroxylated ene-thiol structure, whose predicted mass fits with the LC-MS data. Accordingly, another structure is proposed for the intermediate with m/z=626.18 which can result from further oxidation of the thiol group to form a double bond (Figure 3.36 b). The latter intermediate can convert into the product via forming a thiazole ring and loss of H_2O.

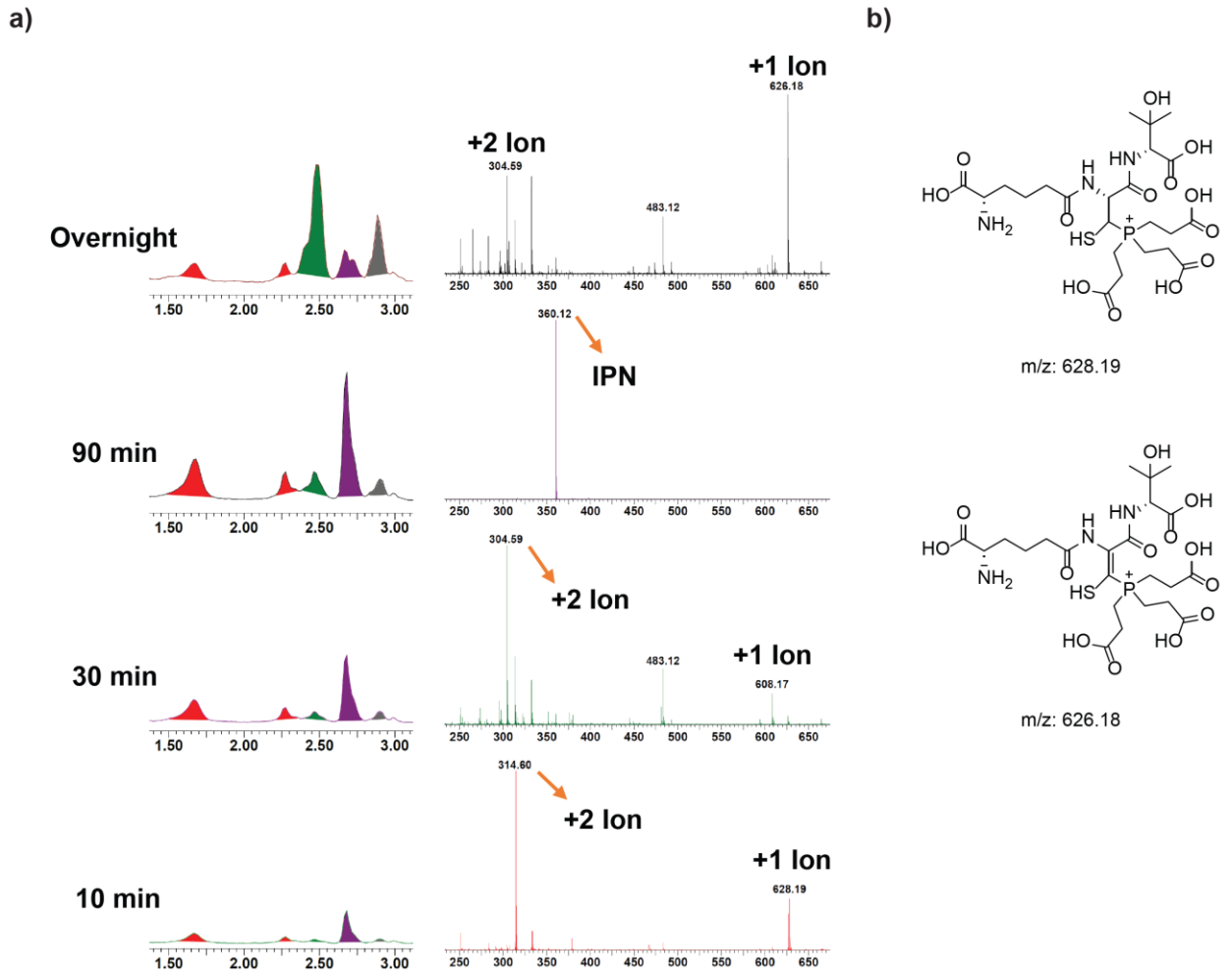


Figure 3.36: **(a)** Recorded LC-MS spectra of the S281T_IPNS turnover with TCEP quenched at specific timepoints showing intermediates with m/z values of 628.19 and 626.18 for their corresponding +1 charged ions. **(b)** Proposed intermediates for the turnover of S281T_IPNS with TCEP.

The combined evidence implies that TCEP interacts with a S281T_IPNS turnover product / intermediate through reaction of its phosphine with the proposed intermediate with m/z=378.13. As TCEP may be a stronger nucleophile at more basic pH, it can react faster and more TCEP adduct formation is expected at higher pH. This may explain why S281T_IPNS turnover with TCEP forms more new products (compared to IPN) at higher pH, which is shown in Figure 3.33 a (Section 3.2.9). Further studies on how TCEP interacts with turnover of S281T_IPNS (and other mutants forming the new product) are described in Sections 3.2.11 and 3.2.12.

3.2.11: Treatment of the Thiazole Product With TCEP

Since S281A_IPNS (and other mutants forming the new products) formed a different product with TCEP, it is interesting to understand how TCEP is involved in the catalysis. One possibility is the reaction between TCEP and the thiazole ring with the turnover final product. In addition to the time course studies described in Section 3.2.10, other experiments with TCEP were conducted. To investigate whether TCEP reacts with the thiazole ring in the product without TCEP (m/z = 360.12), the final product was treated with TCEP at different conditions. Under one set of conditions, TCEP was treated with the pure isolated product and under other conditions, the turnover crude mixture was present.

Figure 3.37 a shows the ^{1}H NMR spectrum of the isolated product from S281A_IPNS turnover with m/z value of 360.12 (from a batch without TCEP), which has been treated with TCEP. After addition of TCEP, the thiazole CH characteristic peak was not depleted over time, meaning that TCEP has not reacted with the thiazole ring (Figure 3.37 a). A small change in the product chemical shifts was observed due to the addition of TCEP (Figure 3.37 a). This change could arise from sample acidification as a high concentration of TCEP hydrochloride (TCEP.HCl) was added to the NMR tube.

In another experiment (Figure 3.37 b), a freshly prepared turnover crude mixture containing 20 μM S281A_IPNS, 500 μM TCEP, and 200 μM $Fe^{(II)}$ was used. The isolated product without TCEP (m/z = 360.12) was added to this turnover mixture rather than ACV. The goal of this experiment was to examine whether TCEP reacts with the product when fresh enzyme and iron(II) are present in solution. No change in the intensity of the thiazole CH peak was observed over a reasonable time (Figure 3.37 b). That is, the thiazole CH peak did not decrease meaning no adduct was formed. Therefore, the enzyme and ingredients in the turnover mixture do not facilitate the possible reaction of TCEP with the thiazole ring at the product with m/z = 360.12.

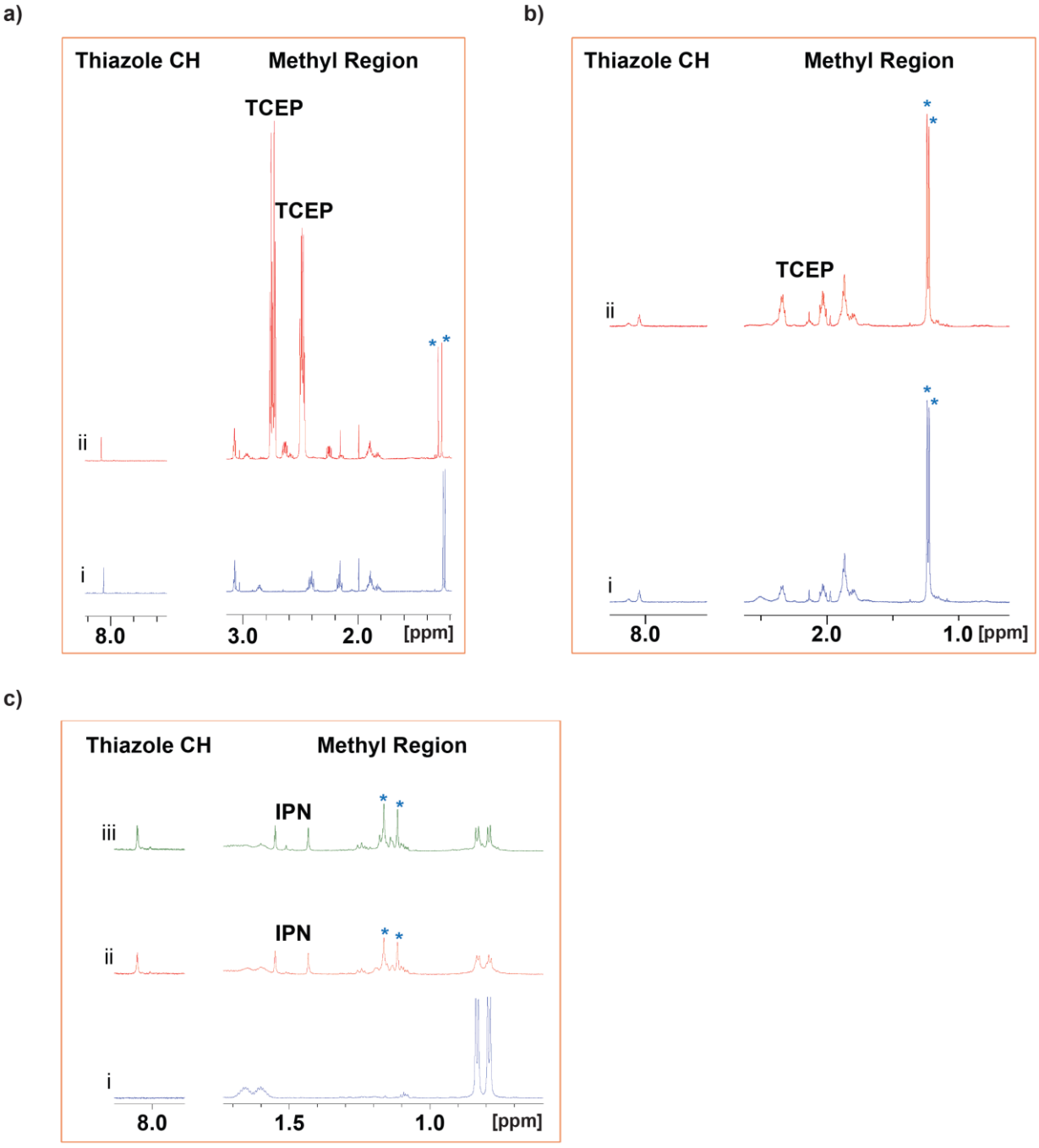


Figure 3.37: Treatment of the S281A/S281T_IPNS turnover product with m/z=360.12 with TCEP (methyl peaks are marked with blue asterisks). **(a)** ^{1}H NMR spectra of the isolated new product without TCEP (i) and 3 hours after addition of TCEP (ii). **(b)** CPMG edited ^{1}H NMR spectra of the turnover crude mix with TCEP and 10 μM S281A_IPNS at 5 minutes (i) and 6 hours (ii) after addition of the isolated new product. **(c)** Addition of TCEP to the S281T_IPNS turnover end point. The CPMG edited ^{1}H NMR spectra of the turnover mixture without enzyme (i), turnover end point at 90 minutes after addition of S281T_IPNS (ii), and 3 hours after addition of TCEP (1 eq.) to the turnover end point (iii) are shown.

A separate experiment was conducted to investigate whether or not TCEP reacts with the turnover product with m/z=360.12. In this experiment, a turnover sample with S281T_IPNS was prepared without TCEP to convert ACV into IPN and the new product. TCEP (1 eq.) was added when significant amounts of the new product were formed (after 90 minutes). As shown in Figure 3.37c, the thiazole CH peak did not show any change over time. Therefore, the reaction of TCEP with the product with m/z=360.12 does not seem to occur. It is more likely that TCEP adduct forms during the catalysis through reaction of the TCEP phosphine group with an intermediate, as discussed in Section 3.2.10.

3.2.12: Addition of TCEP to the Midpoint of S281T_IPNS Turnover

Another method was conducted to examine whether TCEP reacts with an intermediate in the catalysis of mutants forming the new product with the thiazole ring (e.g. S281A and S281T mutants). In this experiment, turnover of ACV with S281T_IPNS was initially done without TCEP. After a few minutes, according to the time course studies described in Section 3.2.10, there should be enough of the intermediate formed. This intermediate does not contain a thiazole ring but was shown to have a hydroxylated valinyl group in ^{1}H NMR spectra (Figure 3.34 a) and m/z value of 378.13 (Figure 3.34 b). Therefore, TCEP (1 eq.) was added to the turnover mixture 8 minutes after the start of the reaction, rather than starting the reaction with TCEP present.

Figure 3.38 shows the CPMG edited ^{1}H NMR spectra of S281T_IPNS turnover. The turnover initially started with 10 μM enzyme and without TCEP, and one equivalent of TCEP was added 8 minutes after the start of the reaction. As shown in the aromatic region of the spectra (Figure 3.38), the thiazole characteristic peak at 8.07 ppm was not observed over time. Additionally, two new methyl peaks around 1.15 ppm increase after addition of TCEP; these are compatible with a product having reacted with TCEP with m/z = 608.17 (black asterisks). The methyl peaks corresponding to the product not reacted with TCEP (m/z = 360.12) also appear with lower peak intensity (blue asterisks in Figure 3.38). According to the aforementioned data, addition of TCEP in the turnover midpoint has minimized formation of the product without TCEP and hence, TCEP reacts with an intermediate to form the adduct with m/z = 608.17.

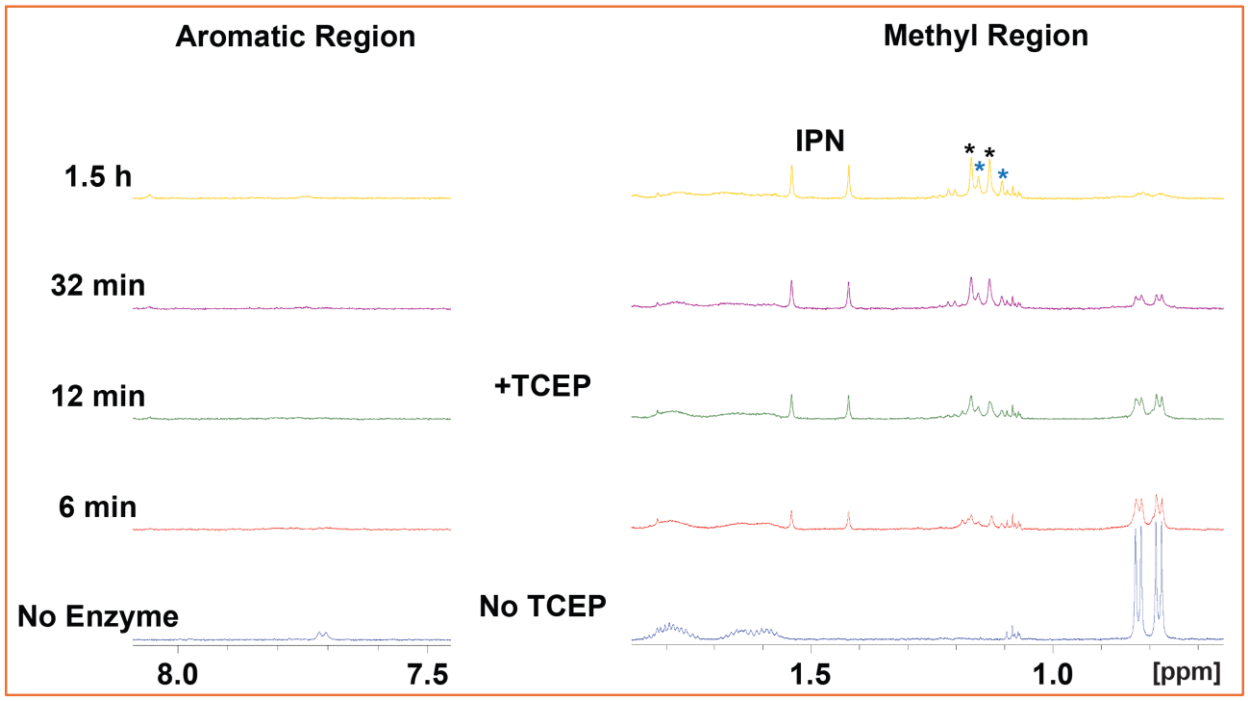


Figure 3.38: CPMG edited ^{1}H NMR spectra of S281T_IPNS turnover which was started without TCEP. Afterwards, 1 equivalent of TCEP was added to the turnover mixture 8 minutes after start of the reaction. The formation of the product with a free thiazole ring (blue asterisk) was minimized and the product with TCEP addition (black asterisk) was formed.

According to the afore-described data and the detected intermediates in the turnover of S281T_IPNS with TCEP (Section 3.2.10), it is possible that TCEP reacts with the intermediate containing an ene-thiol and a hydroxylated valine group (m/z=378.13). A scheme of potential steps in formation of the product adduct with TCEP is shown in Figure 3.39, which is based on proposed structures of the observed intermediates and their corresponding m/z values in time course studies.

It is noteworthy that the final TCEP derived product (m/z=608.17) is formed via a six-electron oxidation of ACV. That is, four-electron oxidation has occurred during enzymatic catalysis, and the additional two-electron oxidation has occurred during modification of the TCEP adduct with the ene-thiol intermediate.

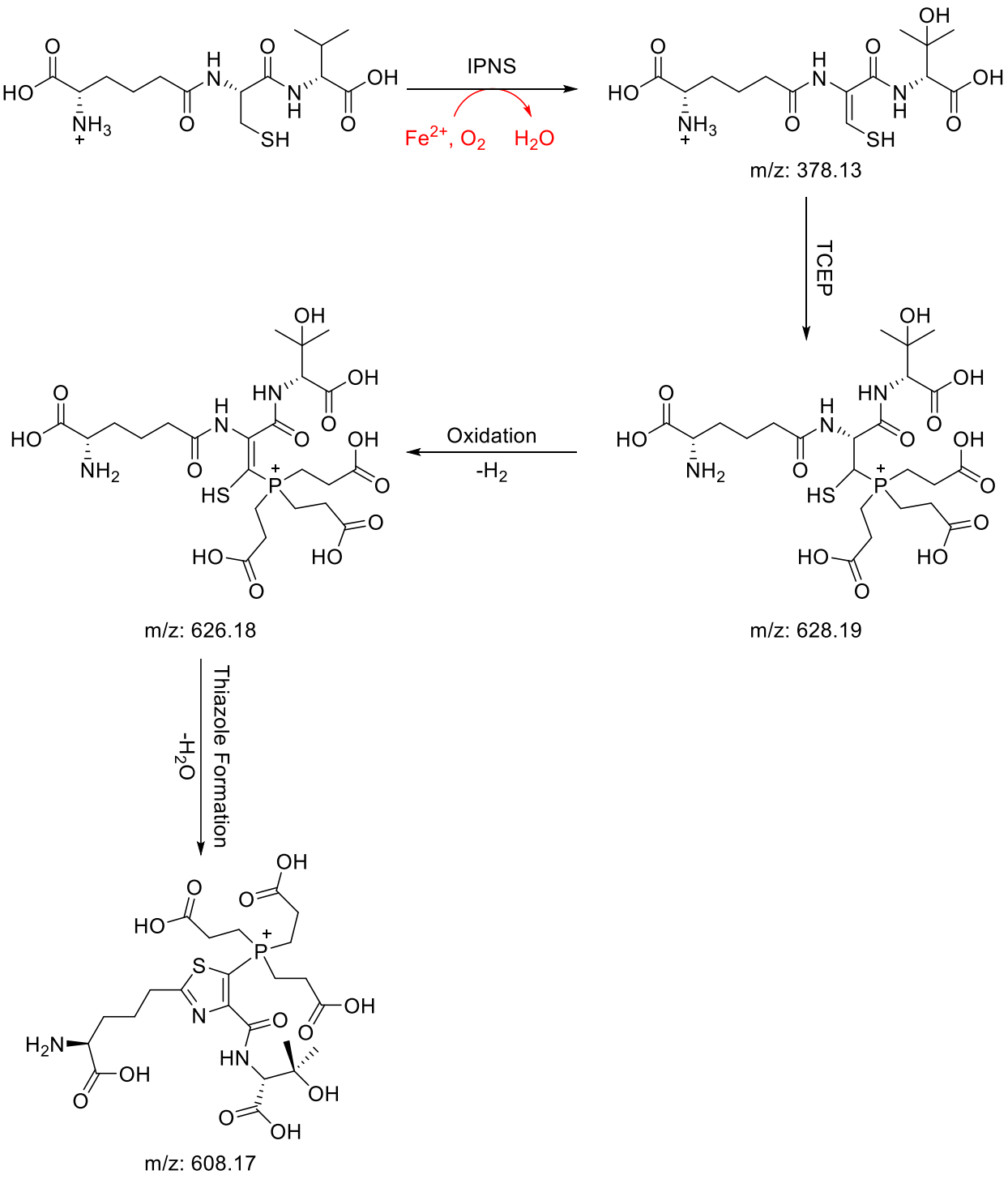


Figure 3.39: Proposed steps in formation of TCEP adduct with the product with thiazole ring.

3.2.13: Formation of Thiazole and Oxazole Rings in Biological Processes

Serine and cysteine residues in peptide-based natural products can undergo enzymatic cyclization during post-translational modification [19]. These reactions can eventually form heterocycles such as thiazole- and oxazole rings. Figure 3.40 shows two different pathways leading to formation of thiazole and oxazole rings with cysteine and serine residues, respectively [19]. These pathways include cyclodehydration and oxidation steps. Cyclodehydration occurs via nucleophilic attack of a cysteine thiol (or serine hydroxyl) group to an amide carbonyl followed by dehydration, leading to the formation of a five-membered heterocyclic ring. Oxidation occurs before or after cyclodehydration step, leading to the formation of an aromatic thiazole or oxazole ring [19].

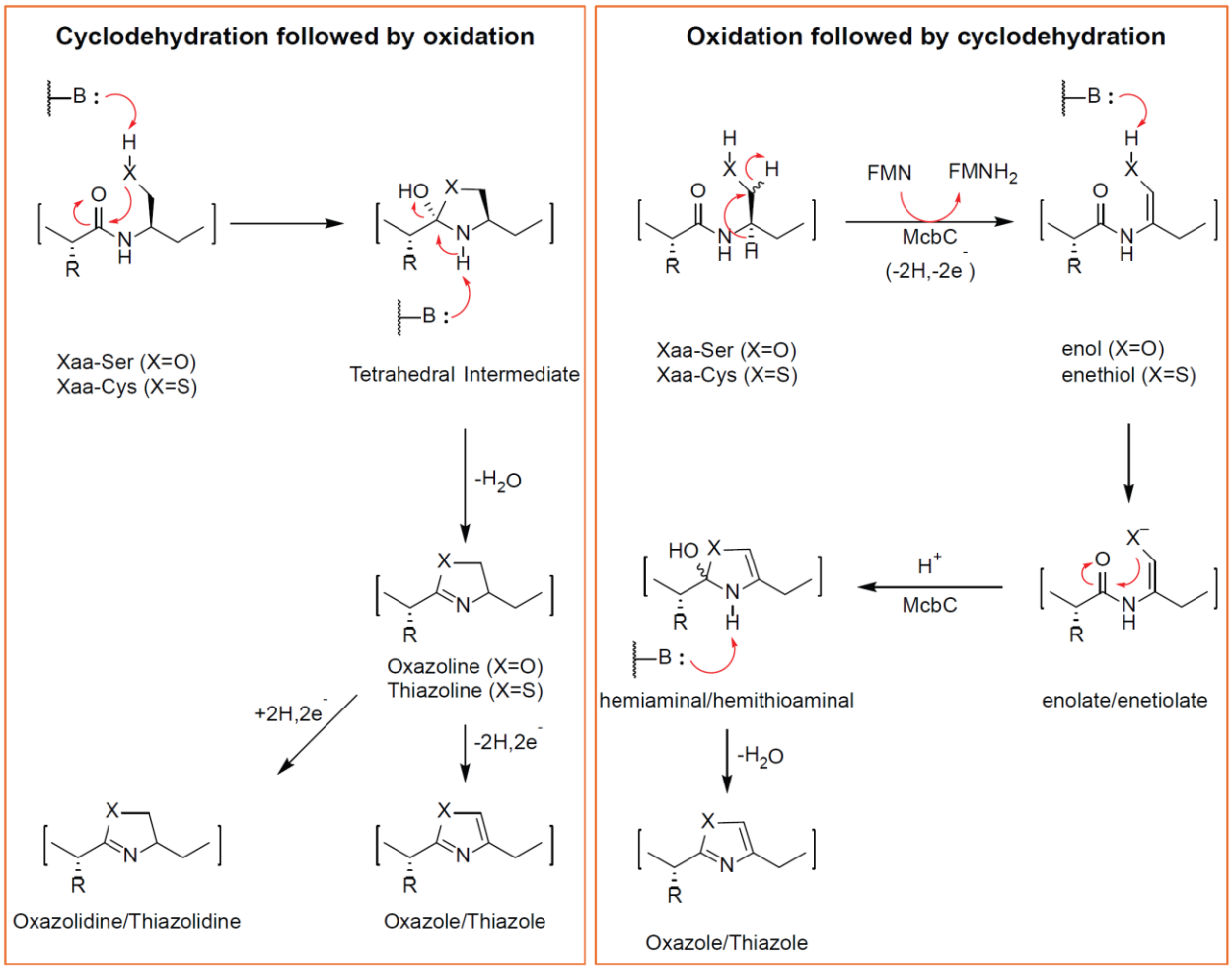


Figure 3.40: Formation of thiazole and oxazole rings involving post-translational modification of peptides with serine and cysteine residues, respectively [19].

Catalysis by S281A_IPNS and other mutants which form products with a thiazole ring has shown an intermediate with ene-thiol and hydroxylated valine groups which then form the thiazole ring through a cyclodehydration step. This intermediate is similar to the enethiolate intermediate shown in Figure 3.40. Therefore, the mechanism of the new product formation could be similar to observed mechanisms in other biological processes [19]. Section 3.2.14 explains a proposed mechanism for the IPNS mutants which form the new product with the thiazole ring.

3.2.14: Proposed Mechanism of Formation of the Product with a Thiazole Ring

A mechanism is proposed here for the new product formation taking into account the observed time course data and nature of the mutations leading to altered IPNS catalysis. As shown in Figure 3.41, the branch point in the mechanism is the thioaldehyde intermediate. To form the β-lactam ring, the cysteinyl residue in the thioaldehyde intermediate (shown with orange square) needs to have a co-planar conformation, which facilitates formation of the four-membered ring. The Ser_{281} residue, which is located on edge of the active site, can stabilize the substrate valinyl group via an H-bond with its carboxylate. However, in the S281A mutant this H-bond does not exist (and in the S281T mutant the H-bond interaction is weakened) which can increase the mobility of the ACV substrate valine group. This increased mobility will reduce the chance of having the co-planar arrangement and consequently, rate of monocyclic intermediate formation leading to IPN will decrease. Alternatively, the thioaldehyde intermediate can convert into an enethiol. The enethiol intermediate can react with the iron(IV) oxo ($Fe^{(IV)}$=O) species to hydroxylate the valine group and convert iron back to the Fe(II) state. The resulting intermediate which contains enethiol and hydroxylated valine eventually forms the product with a thiazole ring via cyclodehydration.

The suggested mechanism can also account for the observed changes in S281T_IPNS selectivity at different pH values (Section 3.2.9). As shown in Figure 3.33 a, S281T_IPNS forms the new product faster than IPN at higher pH values. Because thiazole ring formation occurs via nucleophilic attack of enethiol sulfur (Figure 3.41), reaction will likely be faster at higher pH as enethiol will be more deprotonated. Moreover, in the suggested mechanism during new product formation, the ACV valine hydroxylation

occurs first and thiazole ring forms later. This could explain why methyl peaks in the 1.15ppm region (corresponding to hydroxylated valine chemical shift range) appear at the beginning of time course, and the thiazole proton peak (at 8.07 ppm) forms later (time course NMR results are shown in Figure 3.34 a).

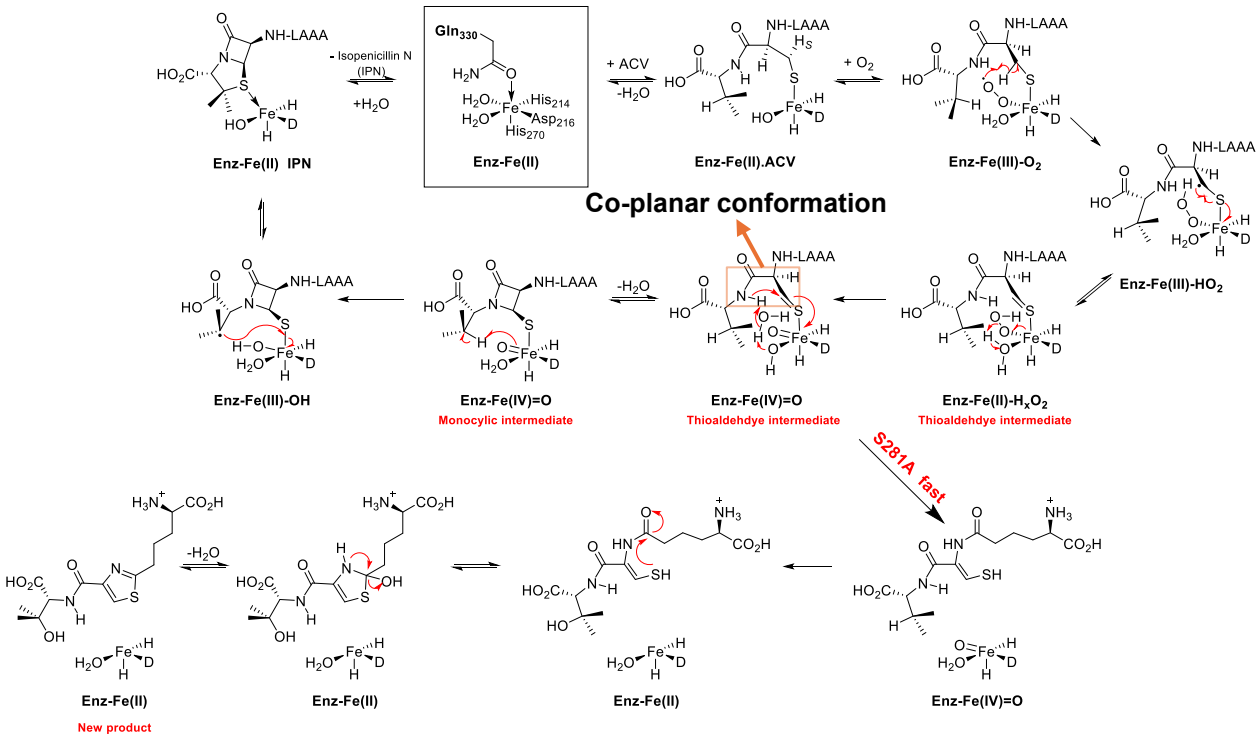


Figure 3.41: Proposed mechanism for formation of IPN and the new product in S281A_IPNS and related mutant turnover. Note in the new product formation, the ACV thiol S may (re)ligate with the Fe to enable ACV valine hydroxylation.

An alternative mechanism for formation of the product with thiazole ring is proposed in Figure 3.42. The second proposed mechanism also has a branch point at the thioaldehyde intermediate. In this mechanism, the distal water molecule from peroxide cleavage attacks the thioaldehyde, rather than enabling β-lactam ring formation, forming the hydrated thioaldehyde intermediate. The valine C-β of the latter intermediate is hydroxylated by the $Fe^{(IV)}$=O species, concomitantly reducing iron back to $Fe^{(II)}$. The resulting intermediate then undergoes thiazoline ring formation in a cyclodehydration step. The intermediate with the thiazoline ring converts into the product with a thiazole ring via loss of one H_2O. In the second proposed mechanism, the intermediate with the

thiazoline ring and hydroxyvaline group showed an expected m/z value of 378.13, which could be an alternative structure for the observed intermediate in the time course studies (Section 3.2.10).

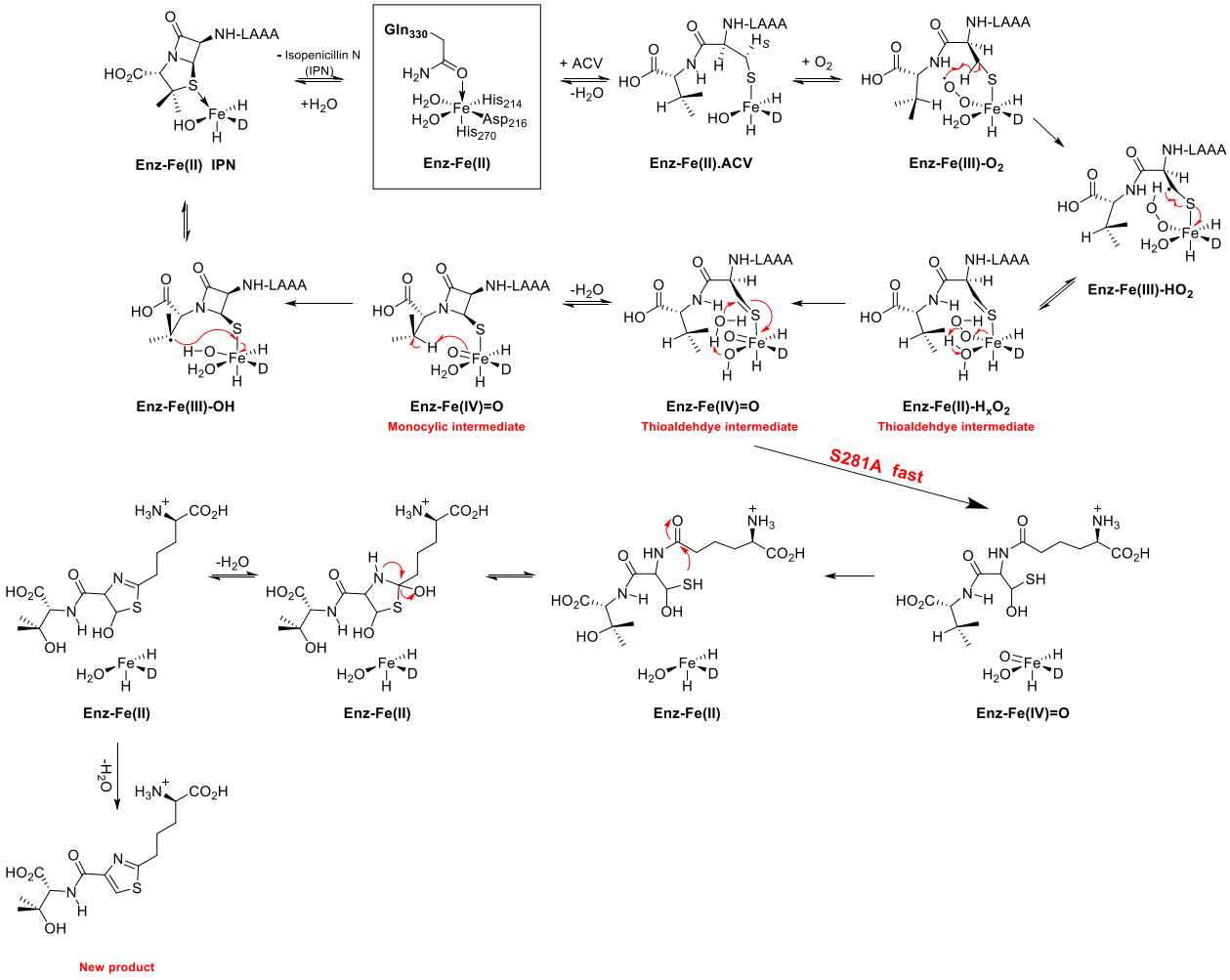


Figure 3.42: An alternative proposed mechanism for the formation of IPN and the new product in S281A_IPNS and related mutant turnover. Note in the new product formation, the ACV thiol S may (re)ligate with the Fe to enable ACV valine hydroxylation.

3.2.15: Antibiotic Activity Testing of the New Product

Since IPNS forms the precursor of the β-lactam antibiotics, it is worth checking whether or not the new product formed by S281A_IPNS shows any antibiotic activity. For this reason, the isolated product with m/z=360.12 was tested for antibiotic activity using an agar plate assay (carried out by Dr. K. Calvopina Tapia). In addition to the isolated new product (labelled as 360), isopenicillin N (IPN) and penicillin N (PenN) were used to see

if the products of IPNS and IPN epimerase exhibit any antibacterial activity. Ampicillin was used as a positive control. A suspension of *E. coli* ATCC25922 strain with OD_{600} = 0.1 was spread over two agar plates. In both plates, a drop of each of the compound stock solutions (360, IPN, PenN, and Ampicillin) were added. The stock solutions were at 10 mM and 1 mM concentrations. Both plates were incubated at 37°C overnight and the bacterial growth was examined afterwards as shown in Figure 3.43. The plate treated with 1 mM stock solution has not shown any antibiotic activity, and the one treated with 10 mM stock solution shown no growth on the ampicillin position (Figure 3.43). Therefore, none of the IPN, penN, and the new product showed any antibacterial activity. For the β-lactam compounds (IPN and penN), further steps are required to convert the molecules into a more potent antibiotic [20]. For the new product with a thiazole ring (360), similar modifications may convert the compound into an antibiotic.



O.D. 600 = 0.1, 1 mM **O.D. 600 = 0.1, 10 mM**

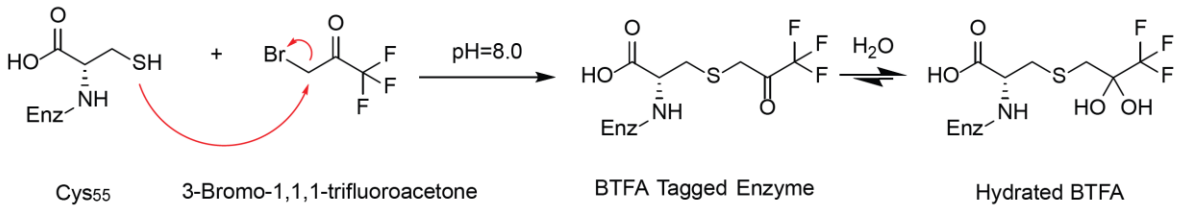
Figure 3.43: Antibiotic activity test of the new product with m/z=360.12 (labelled as 360), isopenicillin N (IPN), penicillin N (penN), and ampicillin as positive control (carried out by Dr. K. Calvopina Tapia).

3.2.16: Examining The Role of Q280A_L282A Mutation on Transforming Active Site Dynamics to the Surface α-3 Helix

Mutations on second shell residues of IPNS connecting β-strand 11 and α-helix 3 were examined for turnover assays (data shown in Section 3.2.8). The Q280A_L282A double mutant turnover assay showed minor amounts of new product formation. This mutation will likely decrease the interaction between β-strand 11 and α-helix 3 and hence,

β-strand 11 will have higher mobility. The Ser_{281} residue is located in β-strand 11, and its increased mobility will cause higher mobility in the substrate valinyl group. According to the proposed mechanism in Figure 3.41, the mentioned higher mobility may cause the thioaldehyde intermediate to undergo tautomerization and form the new product as a minor pathway.

a)



Cys_{55} 3-Bromo-1,1,1-trifluoroacetone BTFA Tagged Enzyme Hydrated BTFA

b)

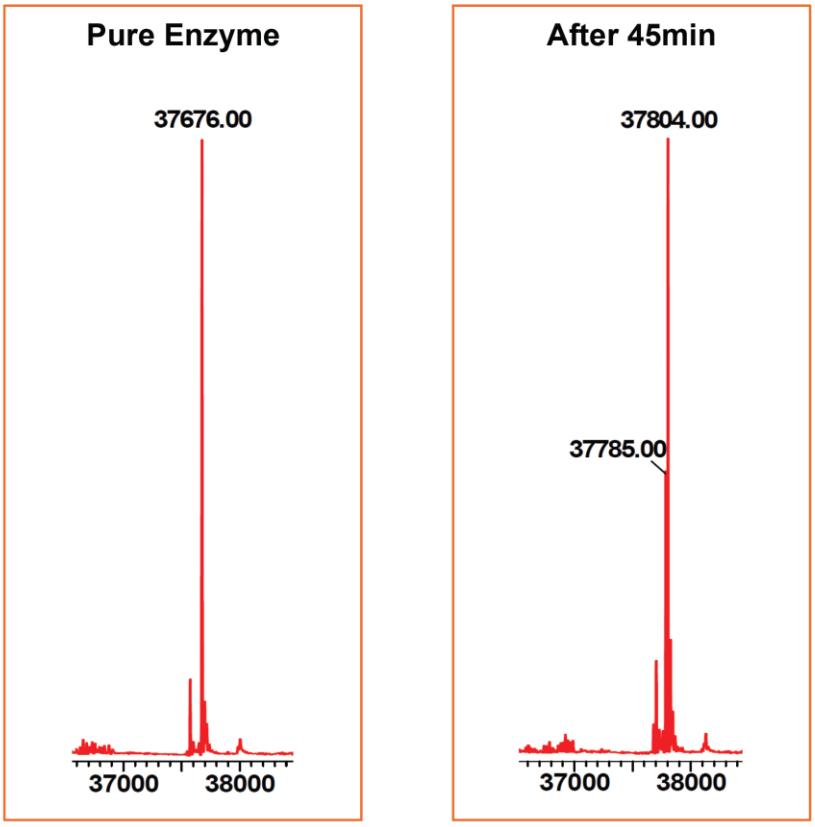


Figure 3.44: **(a)** Schematic diagram of S55C_Q280A_L282A IPNS reaction with BTFA. **(b)** Extracted protein mass from sample containing pure S55C_Q280A_L282A IPNS and the sample taken from BTFA reaction mixture after 45 minutes. The spectra show the enzyme is fully tagged and the mass difference is compatible with BTFA mass in its hydrated form (37804-37676=128 Da).

Using ^{19}F NMR spectroscopy of BTFA tagged S55C_IPNS, correlated motions of the enzyme active site and α-helix 3 were observed in solution state [8]. Ser_{55} is located in α-helix 3 and S55C mutation is required to have a fluorine tag on the α-helix 3. Similarly, the Q280A_L282A mutant was examined to see if motions of the active site is correlated with the α-helix 3 motions. For this purpose, the S55C_Q280A_L282A mutant was prepared, and the resulting enzyme was treated with BTFA (Figure 3.44 a). Reaction progress was monitored via observing protein mass using LC-MS (Figure 3.44 b). The pure untagged enzyme mass was compared with its mass 45 minutes after treating with BTFA which shows the enzyme is fully tagged, and the mass difference is 128 Da which is compatible with BTFA in its hydrated form (Figure 3.44).

In order to examine whether BTFA attached to the Cys_{55} residue can alter the enzymatic catalysis, turnover of S55C_Q280A_L282A IPNS was compared with that of BTFA tagged enzyme. In this mutant the interaction between β-strand 11 and α-helix 3 is disturbed (the interactions are shown in Figure 3.3) and addition of BTFA to the Cys_{55} residue may further weaken the mentioned interaction. As shown in Figure 3.45, CPMG edited ^{1}H NMR spectra of untagged and BTFA tagged S55C_Q280A_L282A IPNS reveals formation of IPN and minor amounts of the product with a thiazole ring (m/z = 608.17 for turnover with TCEP). Similar turnover was observed with the Q280A_L282A IPNS (Figure 3.28 a), and further modifications on Ser_{55} residue did not significantly change the reaction selectivity. Therefore, the BTFA tagged S55C_Q280A_L282A IPNS is active and could be used as a model for ^{19}F NMR studies.

The BTFA tagged S55C_Q280A_L282A IPNS (labelled as $IPNS^{*}$) was used for ^{19}F NMR studies. In this experiment, the fluorine peak position depends on the α-helix 3 conformation, and the peak broadening depends on the helix mobility [8,21]. The aim of this experiment was to compare the ^{19}F NMR spectra of the $IPNS^{*}$:$Fe^{(II)}$:ACV complex under anoxic conditions with the spectra of $IPNS^{*}$:$Fe^{(II)}$:ACV:NO complex. Nitric oxide acts as dioxygen mimic and binds to the iron, but it will not further react with the substrate [8,21]. Apo $IPNS^{*}$ and the $IPNS^{*}$:$Fe^{(II)}$ complex were used for reference spectra. In order

to observe how α-helix 3 dynamics depends on temperature, the spectra of all samples were recorded at temperatures ranging from 285 K to 313 K.

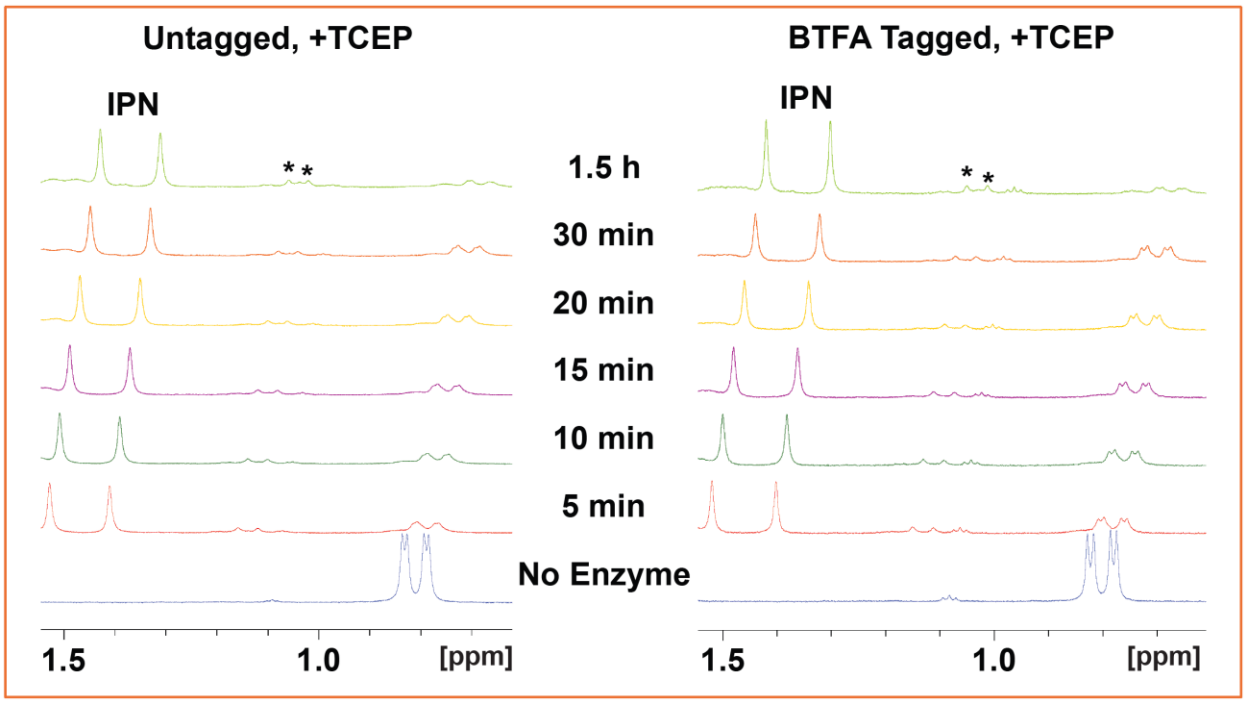


Figure 3.45: CPMG edited ^{1}H NMR spectra obtained from turnover of untagged (left) and BTFA tagged (right) S55C_Q280A_L282A IPNS with TCEP present. The turnover shows formation of IPN (major) and the new product bound to TCEP (minor, methyl peaks labelled with asterisks) in both samples. The thiazole CH peak was not detected as the new product was bound to the TCEP.

Figure 3.46 a shows ^{19}F NMR spectra of four different samples containing IPNS* at different temperatures (285 K to 313 K). The samples include IPNS*:Fe$^{(II)}$, IPNS*:Fe$^{(II)}$:ACV, IPNS*:Fe$^{(II)}$:NO, and IPNS*:Fe$^{(II)}$:ACV:NO. In all samples, 1,1,1-trifluoroacetone was used as internal standard, and the spectra at different temperatures were referenced via fitting the internal standard peaks. As shown in Figure 3.46 a, in all samples, the IPNS* fluorine peak slightly shifts to lower chemical shifts (with respect to the internal standard) at higher temperatures. The fluorine peak becomes sharper at higher temperatures. This contrasts with results of analogous experiments with BTFA tagged S55C IPNS (equivalent to WT_IPNS, labelled as WT_IPNS*) [8,21]. That is, in similar complexes of WT_IPNS*, the fluorine peak was shown to become broader at higher temperatures [8,21]. However, in case of the triple mutant (IPNS*), a lack of interactions between β-strand 11 and α-helix 3 will likely cause higher mobility in the

region. Hence, the helix which contains the BTFA group is expected to have a lower energy barrier between different conformations. Accordingly, the transition between conformations will be moderately fast at the lowest temperature (285 K), showing a broad peak. As the temperature rises, this exchange will become faster, and its corresponding peak will become sharper.

Figure 3.46b presents the overlayed spectra of different samples including IPNS* at 298 K, and the apo IPNS* was used as a reference. The apo IPNS* spectrum shows one minor peak with the same chemical shift as for IPNS*:$Fe^{(II)}$ (labelled with an asterisk in Figure 3.46 b). The latter fluorine peak could be due to possible iron(II) contamination in the apo sample. Exposing the sample containing IPNS*:$Fe^{(II)}$ to nitric oxide (NO) has shown no change in the fluorine peak, indicating no change in α-helix 3 conformation and dynamics. By contrast exposing the IPNS*:$Fe^{(II)}$:ACV complex to NO has revealed a change in the fluorine spectrum; the broad peak slightly decreases, and a new sharp fluorine peak occurs at lower chemical shift (Figure 3.46 b). This likely corresponds to a change in the α-helix 3 conformation, similar to those observed with WT_IPNS* [8,21]. By comparing spectra of IPNS*:$Fe^{(II)}$:ACV and IPNS*:$Fe^{(II)}$:ACV:NO samples, it is noticeable that both fluorine peaks are present in both samples, and their relative population changes upon addition of NO (Figure 3.46 b). The addition of NO to $Fe^{(II)}$ may cause a change in the ACV valinyl position which changes the conformation of β-strand 11 (due to the H-bond between valinyl carboxylate and Ser_{281} in the β-strand). Because there is a weaker interaction between β-strand 11 and α-helix 3, the conformational change of the α-helix is reversible. Therefore, both conformations of the α-helix are thermally accessible.

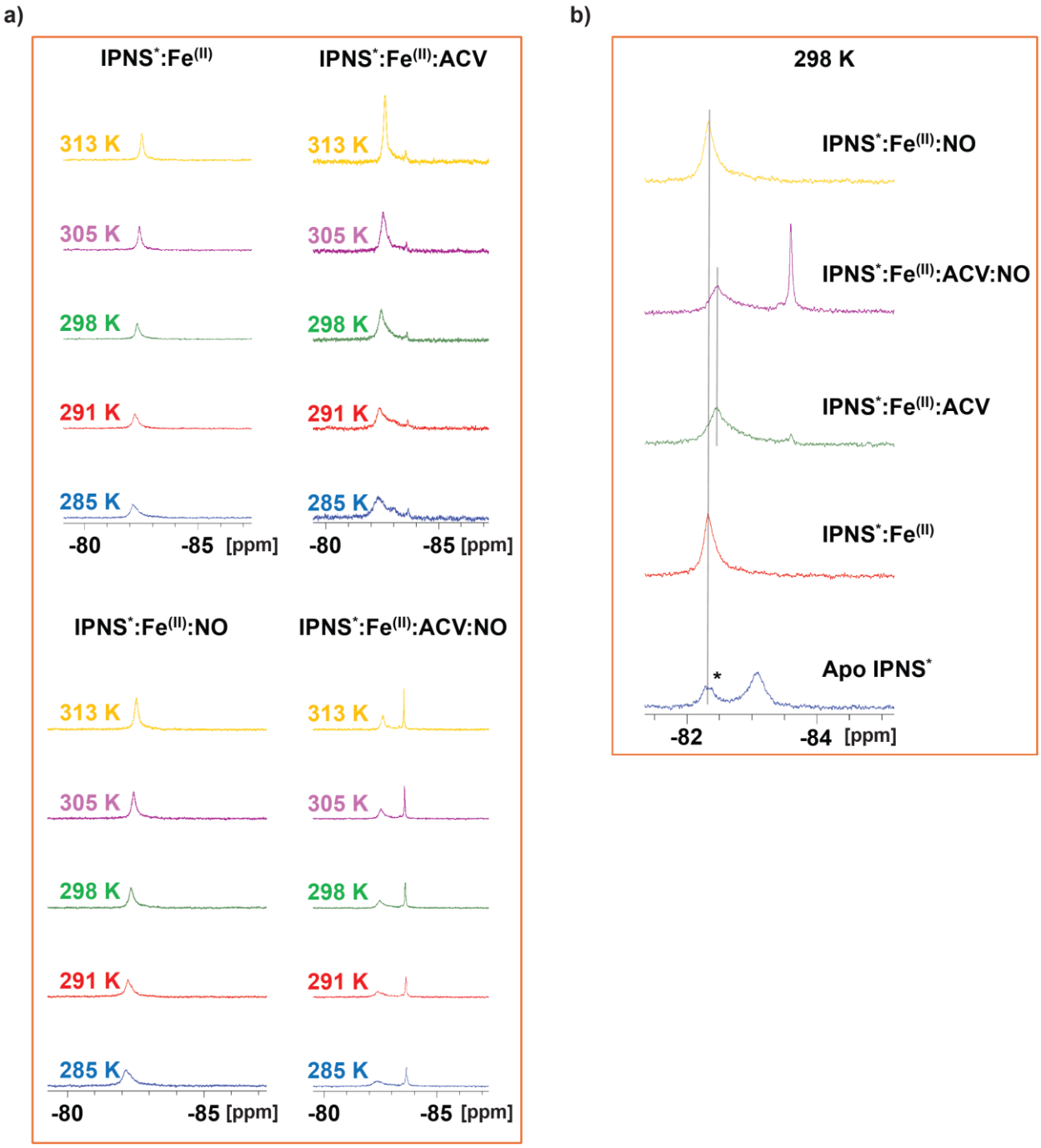


Figure 3.46: BTFA tagged S55C_Q280A_L282A IPNS (IPNS*) ^{19}F NMR spectroscopy with 1,1,1 trifluoroacetone as internal standard. **(a)** Spectra of IPNS* complexes with Fe(II) and ACV under anoxic conditions and nitric oxide (NO) exposed conditions. All spectra were recorded at different temperatures (285 K-313 K) and were referenced using the internal standard peak. **(b)** Comparison of room temperature (298 K) ^{19}F NMR spectra of different samples containing IPNS* under anoxic and NO exposed conditions.

3.2.17: Crystallography Studies on IPNS Mutants

In the current chapter, it has been observed that mutations on Gln_{280}, Ser_{281}, and Leu_{282} residues of IPNS can alter the catalytic pathway to form a new product with a thiazole ring. Therefore, to gain insight into the active site of IPNS mutants, three IPNS mutants were studied by X-ray crystallography. The IPNS mutants (S281A, S281C, and Q280A_L282A) were crystallized with $Fe^{(II)}$ and ACV under anaerobic conditions using the batch method with crystals seeds of WT enzyme. The obtained crystal structures of IPNS mutants (data analysis by Dr. P. Rabe) were compared with the WT_IPNS structure in complex with $Fe^{(II)}$ and ACV under anaerobic conditions (PDB ID: 6ZAE).

When looking at the overall structure it is apparent that the structures superimpose similarly (main chain RMSD comparison also shows the overall ribbon superimposed in Figure 3.47). The main chain RMSD values of S281A, S281C, and Q280A_L282A mutants were found to be 0.336 $Å^2$, 0.283 $Å^2$, and 0.353 $Å^2$, respectively. While most of the structures are identical there is a different conformation of the C-terminal region in IPNS mutants (Figure 3.47). Overall, the C-terminal region of WT_IPNS forms a helix, in the mutants structures the C-terminal region seems to be truncated (Figure 3.47). In the WT_IPNS structure, the C-terminal Thr_{331} interacts with L-α-aminoadipoyl carbonyl group of ACV through H-bond formation with two bridging H_2O molecules (Figure 3.47 a). This crucial interaction is likely to be the reason why the C-terminus in WT_IPNS is ordered. It is also described in the literature [22,23]. Thus, these residues are important for catalysis and substrate binding and product release. This seems to be different in the mutant structures likely due to the increased mobility of ACV in the IPNS mutants (S281A, S281C, and Q280A_L282A) resulting from the weaker interaction of the ACV carboxylate with the mutated amino acids. Consequently, in all IPNS mutants crystallized, poor electron density was observed in the C-terminal region which made it impossible to build the model for the last amino acids resulting in a deletion of these amino acids from the model (Figures 3.47 b, 3.47 c, and 3.47 d).

To have a better comparison with the WT_IPNS structure, the structures of S281A (green) and WT (cyan) IPNS were aligned, and different regions were compared (Figure 3.48). When looking at the active site these changes in the C-terminus can be explained

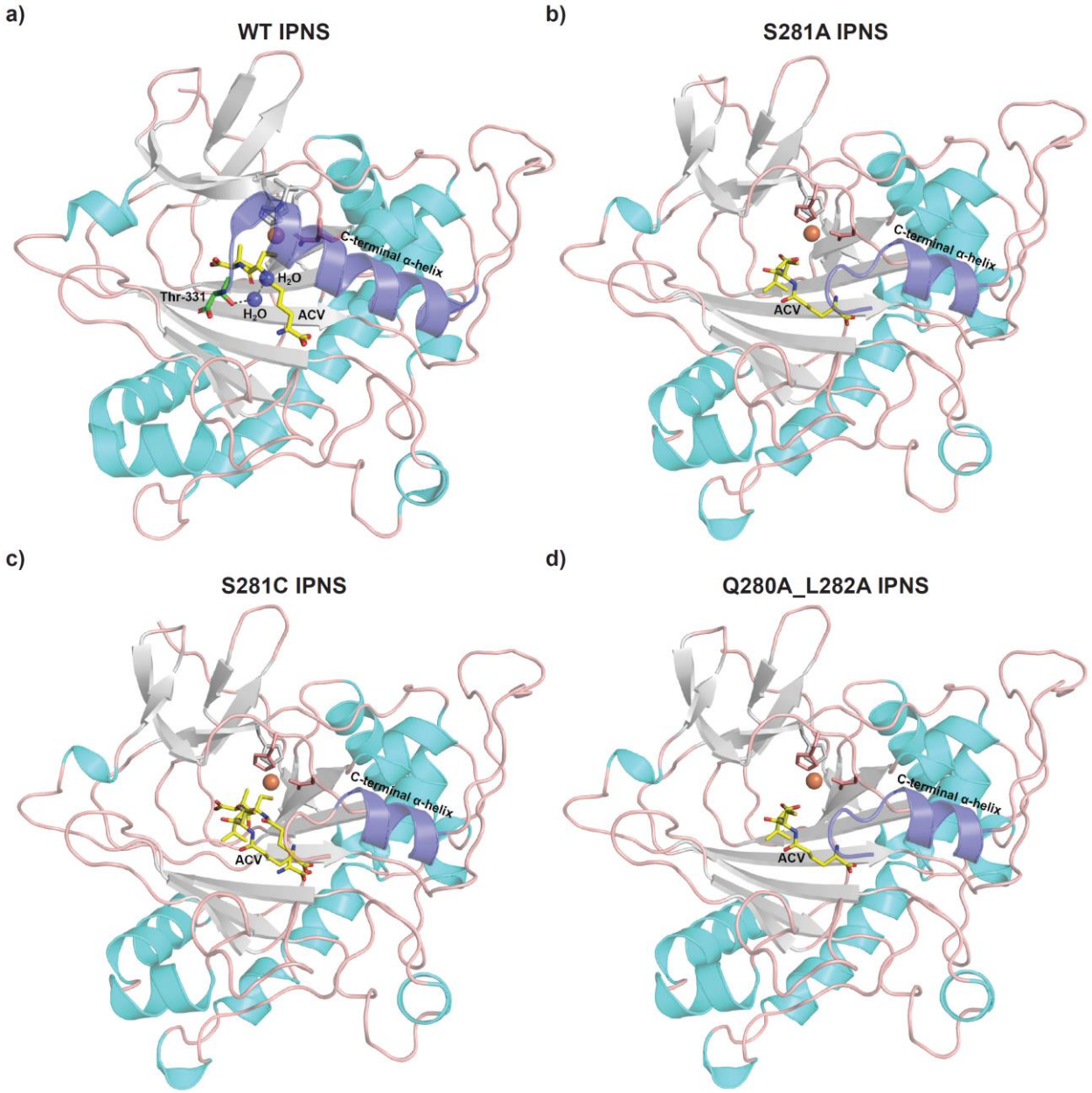


Figure 3.47: Global structures of **(a)** WT_IPNS (PDB ID: 6ZAE), **(b)** S281A_IPNS, **(c)** S281C_IPNS, and **(d)** Q280A_L282A IPNS. The C-terminal α-helix is highlighted and main chain RMSD values of S281A, S281C, and Q280A_L282A mutants are 0.336 Å^2, 0.283 Å^2, and 0.353 Å^2, respectively. In all structures, IPNS is bound to $Fe^{(II)}$ and ACV under anaerobic conditions. All IPNS mutant structures were obtained by Dr. P. Rabe.

due to an altered conformation of the ACV substrate. The crystal structure of S281A_IPNS:$Fe^{(II)}$:ACV complex revealed a different conformation of ACV in the active site and confirmed correct mutation on Ser_{281} (Figure 3.48). In the WT structure ACV is

usually coordinated through thiolate coordination to $Fe^{(II)}$, and is stabilized with direct H-bond interactions (Ser_{281},$Arg_{87,}$ Tyr_{189}, Tyr_{91}), indirect H-bond interactions through water bridging (Asn_{230}, Arg_{279}, Thr_{331}), and hydrophobic interactions (Leu_{223}, Phe_{285}) as shown in Figure 3.1. In the structure of S281A_IPNS this important interaction of Ser_{281} with the ACV carboxylate is interrupted, therefore ACV cannot bind in its actual coordination. It is also surprising that the ACV-S interaction with the Fe is not present anymore. The ACV is indeed flipped in the active site and the ACV-S seem to have no direct interactions with any other residue. ACV direct H-bond interactions with S281A_IPNS residues include the interactions of its L-α-aminoadipoyl carboxylate group with Arg_{87} and Ser_{183} residues (Figure 3.48 a). Indirect H-bond interactions between ACV and S281A_IPNS residues showed one H_2O bound to Ser_{323}, Tyr_{91}, and ACV LAAA carboxylate (Figure 3.48 a). Another H_2O was bridged between Ser_{102} and the ACV LAAA carbonyl group, and Tyr_{189} showed H-bond interaction (via water bridge) with the ACV valine carboxylate (Figure 3.48 a). The Ile_{187} and Val_{185} residues showed hydrophobic interactions with ACV valine isopropyl and L-α-aminoadipoyl methylene groups, respectively (Figure 3.48 a). The S281A_IPNS active site $Fe^{(II)}$ is coordinated through a glycerol (glycerol is added when cryo-cooling crystals for data collection preventing ice formation) (Figure 3.48 a). This may indicate the active site in S281A_IPNS could be more accessible by nucleophiles present in solution compared to WT_IPNS. In the S281A_IPNS structure, one water molecule is bridged between $Fe^{(II)}$ and ACV via coordinating to $Fe^{(II)}$ and forming an H-bond to ACV valine carboxylate. This latter interaction is not present in WT_IPNS, because the carboxylate is forming a hydrogen bond with the Ser_{281} residue, therefore in WT_IPNS the ACV valine isopropyl group is facing $Fe^{(II)}$ (Figure 3.48 a) preventing a direct coordination of another H_2O molecule (which would result in an octahedral $Fe^{(II)}$ coordination site) but allowing a vacant space for O_2 coordination promoting fast catalysis in WT_IPNS. The aligned structures of ACV bound to S281A, and WT IPNS showed different conformations. In particular, the substrate valine group showed different conformation due to lack of H-bond interaction with Ser_{281} in S281A_IPNS (Figure 3.48 b). However, the substrate L-α-aminoadipoyl (L-AAA) carboxylate has not shifted significantly due to the conserved interaction with Arg_{87} (Figure 3.48 b).

Due to the increased mobility of ACV in S281A_IPNS, the C-terminal α-helix exhibited higher dynamics as ACV is interacting with the C-terminal Thr_{331} through bridging H_2O molecules which has resulted in a lack of electron density in the C-terminal region (described above). Therefore, in the refined structure of S281A_IPNS, the C-terminal α-helix is truncated as aligned with WT_IPNS (Figure 3.48 c). Moreover, due to the increased mobility of Ala_{281} and β-strand 11 in S281_IPNS, the α-helix 3 has shown a shifted position with respect to WT_IPNS (Figure 3.48 d).

The ACV electron density map in the refined crystal structure of S281C_IPNS showed two possible conformations of ACV in the active site, labelled as conformations 1 and 2 (Figure 3.49 a). The structure also shows Cys_{281} in two different conformations (Figure 3.49 a). One of the ACV conformations (conf. 1) shows thiol coordination to $Fe^{(II)}$ as well as H-bond (like) interaction between the ACV valinyl carboxylate and Cys_{281} in its first conformation (Figure 3.49 a), whereas the second ACV conformation shows ACV valinyl carboxylate close to $Fe^{(II)}$, with its isopropyl group facing away from $Fe^{(II)}$ (Figure 3.49 a). The ACV in its second conformation shows no interaction with Cys_{281}, causing Cys_{281} to have different conformations (e.g. conf. 1 and 2 in Figure 3.49 a). The overlayed structures of S281C (green) and WT (cyan) IPNS in the active site region indicated that the first ACV conformation (conf. 1) shares a similar structure with ACV bound to WT_IPNS (Figure 3.49 b). Whereas the second ACV conformation (conf. 2) shows a different structure, which is similar to the ACV structure bound to S281A_IPNS (Figure 3.48). Similar to the ACV structure bound to S281A_IPNS, the second conformation of ACV bound to S281C_IPNS showed direct H-bonds with the Arg_{87} and Ser_{183} residues and indirect interactions (via water bridges) with Asn_{287}, Tyr_{91}, Ser_{102}, and Tyr_{189} (Figure 3.49 a). The second conformation of the ACV valine isopropyl showed hydrophobic interactions with Ile_{187} and Val_{185} (Figure 3.49 a). It is noteworthy that co-existence of both ACV conformations (one similar to WT and the other similar to S281A IPNS) could explain why S281C_IPNS forms both IPN and the new product with a thiazole ring in its catalysis (Figure 3.26 b). Comparison of S281C_IPNS structure in C-terminal region with WT_IPNS revealed a truncated C-terminal α-helix in S281C_IPNS (Figure 3.49 c). The latter is due to the lack of electron density in the C-terminal region of S281C_IPNS (similar to S281A_IPNS structure) reflecting higher dynamics of the C-terminal region.

Comparison of the α-helix 3 region in S281C and WT IPNS showed a shifted position of α-helix 3 (Figure 3.49 d). Similar to S281A_IPNS, the shifted position of α-helix 3 in S281C_IPNS could be due to the increased mobility of the β-strand 11, resulting from increased mobility of Cys_{281} (Figure 3.49 d).

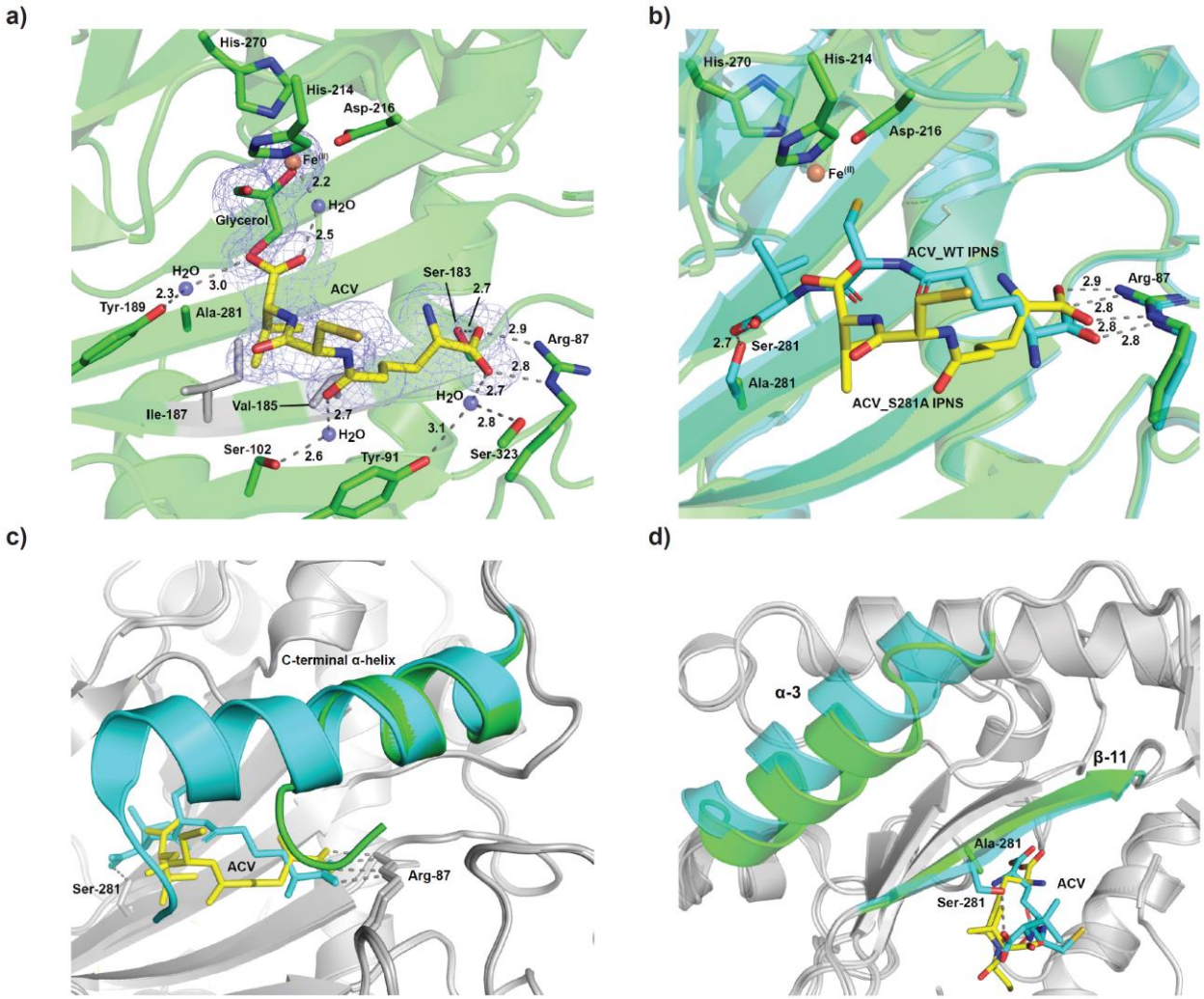


Figure 3.48: Obtained crystal structure of S281A_IPNS in complex with $Fe^{(II)}$ and ACV under anaerobic conditions (crystals and structure obtained by Dr. P. Rabe). WT_IPNS structure was under the same conditions (PDB ID: 6ZAE). **(a)** View of S281A_IPNS active site showing the substrate, $Fe^{(II)}$, and glycerol electron density map. **(b)** Overlayed structures of S281A (green) and WT (cyan) IPNS in the active site region, showing different ACV conformations. **(c)** Overlayed structures of S281A (green) and WT (cyan) IPNS in the C-terminal region. **(d)** Overlayed structures of S281A (green) and WT (cyan) IPNS in the α-helix 3 and β-strand 11 regions.

The refined crystal structure of Q280A_L282A IPNS showed ACV with a similar conformation as in S281A_IPNS (and conformation 2 in S281C_IPNS), and a Tris molecule coordinated to $Fe^{(II)}$ (Figure 3.50 a). The electron density map also confirmed correct mutations on the Gln_{280} and Leu_{282} residues (Figure 3.50 a). Observing the Tris molecule bound to $Fe^{(II)}$ may indicate that the active site in Q280A_L282A IPNS can be accessible by nucleophiles present in the solution. One water molecule is bridged between Tris and Ser_{281} via forming H-bonds and the water molecule coordinated to $Fe^{(II)}$ showed an H-bond with the ACV valine carboxylate (Figure 3.50 a). The ACV in Q280A_L282A IPNS structure showed direct H-bonds with Arg_{87} and Ser_{183} residues and indirect interactions (via water bridges) with Asn_{287}, Ser_{323}, and Ser_{102}; the ACV valine isopropyl showed hydrophobic interactions with Ile_{187} and Val_{185} (Figure 3.50 a). Overall, the ACV interactions with Q280A_L282A IPNS were similar to those observed with S281A and S281C (second conformation) mutants. The overlayed structures of Q280A_L282A (green) and WT (cyan) IPNS in the active site region also showed different ACV conformations (Figure 3.50 b). Unlike WT_IPNS, the ACV thiol group is not coordinated to $Fe^{(II)}$ and the ACV valine isopropyl group is facing away from $Fe^{(II)}$ (Figure 3.50 b). Comparison of the C-terminal α-helix structures of Q280A_L282A (green) and WT (cyan) IPNS showed that the C-terminal region is truncated in Q280A_L282A IPNS (Figure 3.50 c). The latter was also observed in S281A and S281C mutants, which results from a lack of electron density due to higher mobilities in the C-terminal region. The α-helix 3 is also slightly shifted in Q280A_L282A IPNS (Figure 3.50 d); however, the shift in α-helix 3 seems to be smaller compared to the S281A and S281C mutants (Figures 3.48 d and 3.49 d). Because one water molecule is bridged between Ser_{281} and Tris in the Q280A_L282A IPNS structure (Figure 3.50 a), Ser_{281} could be less dynamic and hence the β-strand 11 could have less mobility compared to the S281A and S281C mutants. Therefore, the extent of α-helix 3 shift in Q280A_L282A IPNS could be less than what was observed in S281A and S281C mutants. Another factor contributing to the α-helix 3 shift in Q280A_L282A IPNS could be weaker interactions between α-helix 3 and β-strand 11 as compared with WT_IPNS.

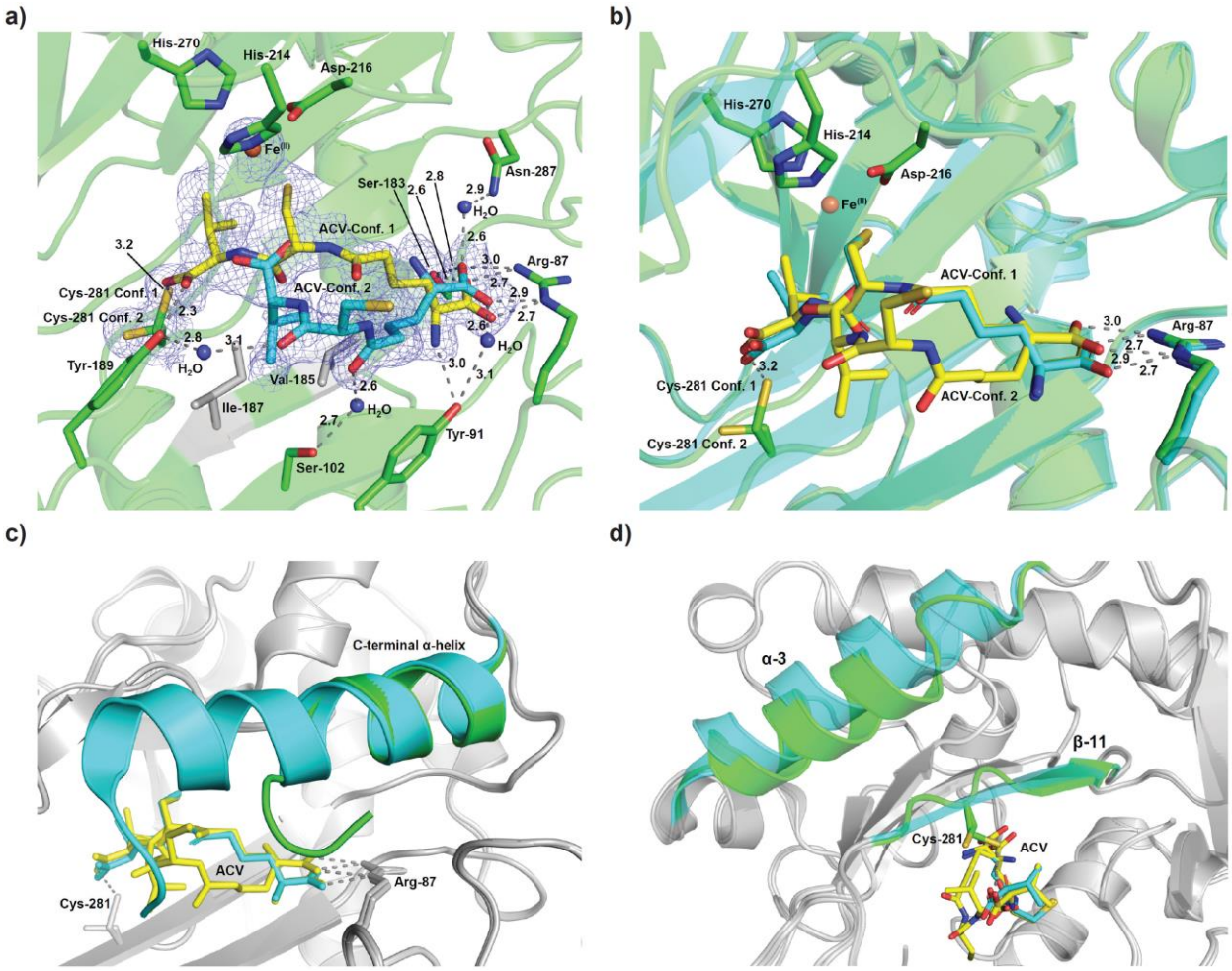


Figure 3.49: Obtained crystal structure of S281C_IPNS in complex with $Fe^{(II)}$ and ACV under anaerobic conditions (crystals and structure obtained by Dr. P. Rabe). WT_IPNS structure was under the same conditions (PDB ID: 6ZAE). **(a)** View of S281C_IPNS active site showing the substrate, $Fe^{(II)}$, and Cys_{281} electron density map, showing two conformations for ACV and Cys_{281} (conf. 1 and conf. 2). **(b)** Overlayed structures of S281C (green) and WT (cyan) IPNS in active site region, showing different ACV conformation. **(c)** Overlayed structures of S281A (green) and WT (cyan) IPNS in C-terminal region. **(d)** Overlayed structures of S281A (green) and WT (cyan) IPNS in the α-helix 3 and β-strand 11 regions.

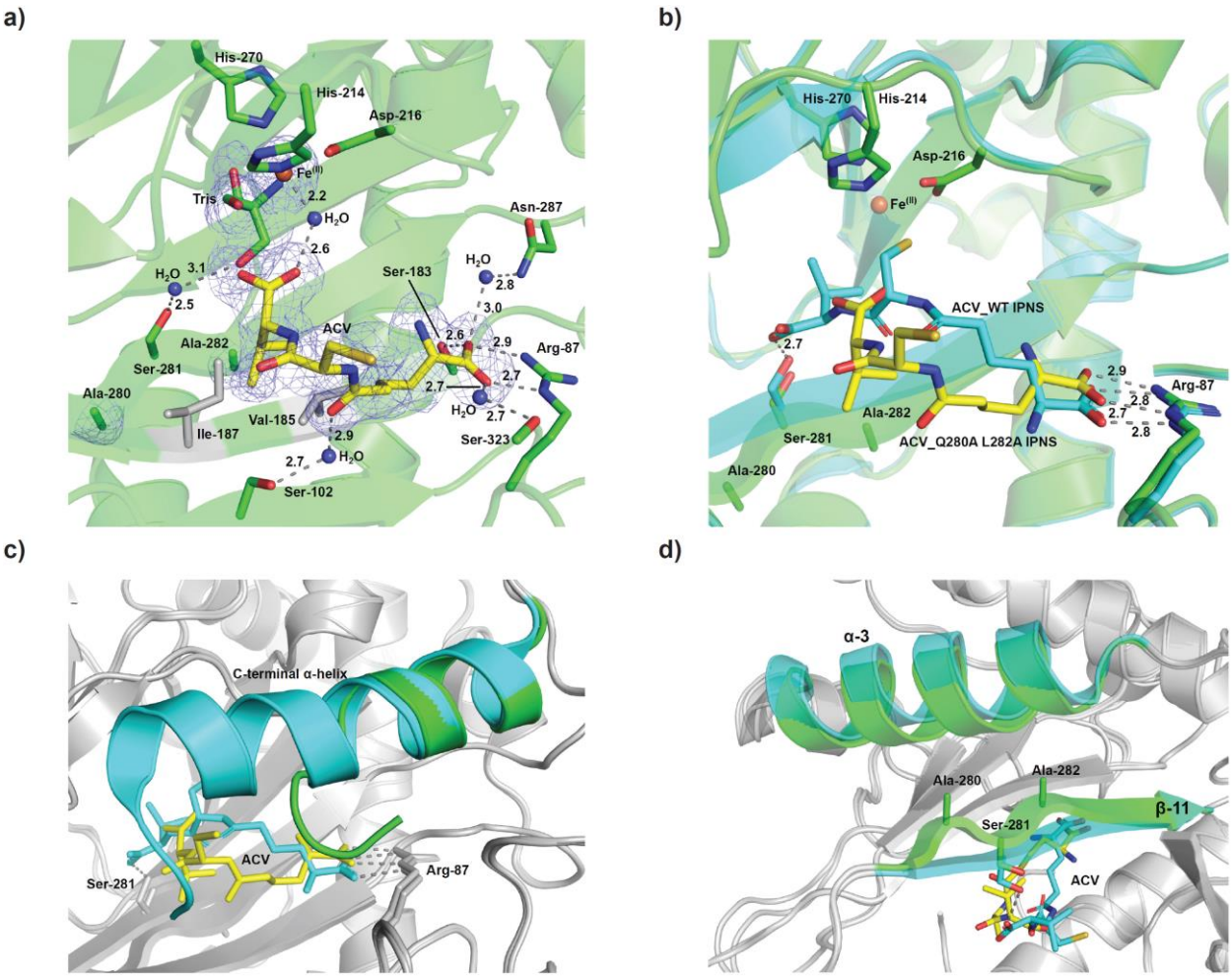


Figure 3.50: Obtained crystal structure of Q280A_L282A IPNS in complex with $Fe^{(II)}$ and ACV under anaerobic conditions (crystals and structure obtained by Dr. P. Rabe). WT_IPNS structure was under the same conditions (PDB ID: 6ZAE). **(a)** View of Q280A_L282A IPNS active site showing the substrate, $Fe^{(II)}$, and Tris electron density map. The electron density maps of Ala_{280} and Ala_{282} residues are shown. **(b)** Overlayed structures of Q280A_L282A (green) and WT (cyan) IPNS in the active site region, showing different ACV conformation. **(c)** Overlayed structures of Q280AL_L282A (green) and WT (cyan) IPNS in the C-terminal region. **(d)** Overlayed structures of Q280A_L282A (green) and WT (cyan) IPNS in the α-helix 3 and β-strand 11 regions.

3.2.18: Conclusion

In this chapter, the interactions between the IPNS active site and β-strand 11, and between β-strand 11 and α-helix 3 were altered via mutations on Gln_{280}, Ser_{281}, and Leu_{282} residues. It was observed that the S281A_IPNS, by removing the H-bond between ACV valine carboxylate and Ser_{281} hydroxyl groups, caused formation of an alternative product bearing a thiazole ring. The product was isomeric to IPN, and when the turnover was carried out in presence of TCEP, the major product was found to be an adduct between the thiazole ring and the TCEP. Both new products were purified for structure elucidation and full NMR characterization is shown in Table Appendix 3.I.

Turnover studies revealed that other mutants disrupting the H-bond interaction between the ACV valine carboxylate and the active site (S281T and S281C mutants) can form both IPN and the new product with a thiazole ring. Moreover, disrupting the interactions between β-strand 11 and α-helix 3 in IPNS (Q280A_L282A and L282A mutants) altered IPNS catalysis to form a minor amount of the new product bearing the thiazole ring. Overall, catalysis by other mutants indicated that increasing the mobility of ACV valine, either via altering the interactions of the valine carboxylate group or via increasing the mobility of β-strand 11, can alter IPNS catalysis. Time course studies of turnover without TCEP revealed that ACV valine hydroxylates prior to formation of the thiazole ring. Based on observed intermediates and the proposed idea that increased ACV valine mobility can form the altered product, two mechanisms were proposed for formation of the product with thiazole ring.

The S281A, S281C, and Q280A_L282A mutants were crystalized with $Fe^{(II)}$ and ACV under anaerobic conditions (by Dr. P. Rabe) to gain insight into IPNS active site and global structure. Structural analysis showed a different conformation of ACV, with its cysteine thiol away from $Fe^{(II)}$, and with different valine orientation as the isopropyl group was facing away from $Fe^{(II)}$. Interestingly, S281C IPNS showed one additional ACV conformation similar to the WT_IPNS structure, consistent with formation of both IPN and the altered product in S281C_IPNS turnover. Also, the C-terminal α-helix showed poor electron density in all mutants, which reflects its higher mobility. The latter could reflect the increased mobility of ACV which caused the C-terminal region to be more mobile.

3.3: Methods:

3.3.1: Preparation of ACV Substrate

The tripeptide ACV (from Dr. P. Rabe) which was dimerized via disulfide bond formation, marked as $(ACV)_2$, was used to prepare monomeric ACV. For this purpose, 300 mg $(ACV)_2$ powder was suspended in 5 mL 0.2 M TCEP solution and was vortexed at room temperature until the mixture was clear. The resulting mixture was purified using liquid chromatography (Biotage Selekt Chromatography system, Biotage), equipped with a C-18 column (Biotage Star Bio C-18) using a gradient of H_2O:CH_3CN from 0 to 18% CH_3CN in 25 column volumes (CV) and then from 18% to 100% CH_3CN in 3 CV. The collected fractions of monomeric ACV were collected and freeze-dried. The mobile phases used for the chromatography step were acidic (0.1% formic acid in water and acetonitrile); hence the collected ACV fractions were acidic and mixing the substrate with enzyme made the latter precipitate. Therefore, the ACV fractions were dissolved in 2 mL of 0.1 M TCEP solution and subsequently were applied to Shimadzu high-performance liquid chromatography (HPLC) system with a Sunfire semi-prep column (C-18, 5 μM, 150 mm length, 10 mm diameter) and the compound was purified applying a gradient of H_2O to CH_3CN from 1% to 30%. To neutralize and remove the acid contamination, the water mobile phase contained 10 mM NH_4HCO_3 (slightly basic). The ACV fractions were collected, freeze-dried, aliquoted into 2 mL fractions and stored at -80 ˚C for further use.

3.3.2: Mutation of pCOLD_IPNS

The original plasmid DNA of WT_IPNS was pCOLD I (Addgene, UK) including Sal I and Not I restriction sites (provided by Dr. P. Rabe). The DNA sequence of WT_IPNS was codon-optimized for expression in *E. coli* (using GeneArt, Thermo Fisher Schientific, UK) encompassing an N-terminal hexa-histidine tag with *N*-terminal C human rhinovirus protease cleavage site [24].

To prepare plasmids of IPNS mutants, as described in Section 3.2.1, the pCOLD vector of WT_IPNS was used as a template DNA for a Q5 site-directed mutagenesis kit (New England Biolabs, USA). The primers used to successfully prepare mutated plasmids are listed in Table 3.1. After successful PCR reaction as illustrated by agarose gel

electrophoresis (Figure 3.4), the DNA fragments were treated with DPN I at 37 ^{o}C for up to 3 hours. The digested mixtures were transformed into the *E. Coli* XL10 Gold cell line (Agilent Technologies, USA) by heat shock and were grown overnight at 37 ^{o}C on a 2YT agar plate containing 50 mg/L kanamycin. Up to four single colonies per mutant were picked and grown in liquid 2YT media at 37 ^{o}C while shaking at 180 rpm overnight. Subsequently, 5-10 mL of grown cultures were used to isolate the plasmid DNA using GeneJet Plasmid Miniprep kit (Thermo Fisher Scientific, USA). The isolated plasmids were sent for DNA sequencing (Eurofins, Germany) and the existence of the expected mutations was confirmed using APE by comparing to the WT sequence.

3.3.3: Expression and Purification of IPNS Mutants

The plasmids of pCOLD IPNS mutants were transformed into the *E. coli* BL21 cell line using heat shock and were grown overnight at 37 ^{o}C in 2YT agar plates containing 50 mg/L kanamycin. Single colonies were picked and used to inoculate 100 mL liquid 2YT media containing 50 mg/L kanamycin. The cultures were incubated at 37 ^{o}C shaking at 180 rpm overnight. Subsequently, 6 mL of resulting starting culture was transferred into 600 mL (1:100 v/v ratio) fresh 2YT media enriched with 50 mg/L kanamycin (large scale growth). The inoculated media were incubated (180 rpm, 37 ^{o}C) until their optical density at 600 nm (OD_{600}) reached 0.6. The protein expression was then induced via addition of β-D-1-thiogalactopyranoside (IPTG, 0.5 mM final concentration) and the media were incubated at 18 ^{o}C with shaking at 180 rpm overnight. The resulting cells were harvested via centrifuging (11000 g, 8 min, 4 ^{o}C) and stored at -80 ^{o}C.

For each mutant, a sufficient amount of cell pellets (up to 25 g) was resuspended in buffer A (1:5 w/v ratio) containing 50 mM Tris, 200 mM NaCl, and 5 mM imidazole at pH 7.5. Small quantities of DNAase I, phenylmethylsulfonyl fluoride, and lysozyme were added to the resuspended cell mixture and stirred for 20 minutes at room temperature and then 20 minutes at 4 ^{o}C. The cells were lysed via sonification (60% amplitude, 9.9 s pulse on, 9.9 s pulse off, 16 minutes total time, Sonics-Vibra Cell) and the lysed cell debris was removed via centrifugation (58000 g, 30 min, 4 ^{o}C). Subsequently, the supernatant was filtered via 0.45 μM filter to remove all particles.

The filtered supernatant was then loaded onto a nickel affinity column (5 mL HisTrap HP, GE Healthcare, USA), pre-equilibrated with 25 mL (5 CV) of buffer A. The column was washed with another 100 mL (20 CV) of buffer A to remove any other proteins and molecules in the lysate and then eluted with a linear gradient (20 CV) from 100% buffer A to 100% buffer B (50 mM Tris, 200 mM NaCl, and 500 mM imidazole at pH=7.5). The fractions showing a UV signal in the chromatogram were analyzed by SDS polyacrylamide gel electrophoresis (PAGE, Figure 3.5). The fractions showing a protein with the size of ~40 kDA suggesting IPNS production were collected and concentrated via centrifuging using 10000 molecular weigh cut-off (MWCO) spin concentrators (Merck Millipore, USA) at 3000 g and 4 ^{o}C. To reduce the imidazole concentration of protein solutions, all fractions were collected and concentrated to 3 mL volume. The concentrated protein solution was diluted with buffer A to 15 mL volume. The resulting mixture was concentrated again to 7 mL and diluted again with buffer A (to 15 mL). The protein solution was then treated with 3C protease with 1:100 w/w ratio overnight at 4 ^{o}C to cleave the N-terminal hexa-histidine tag.

To remove cleaved hexa-histidine tag and the 3C protease (which is histidine tagged) from the reaction mixture, the protein mixture was passed through the nickel affinity column (5 mL, HisTrap HP, GE Healthcare, USA) pre-equilibrated with buffer C (50 mM Tris, 200 mM NaCl, and 20 mM imidazole at pH=7.5). The column was then washed 4 times (1 CV) with buffer C and then eluted 2 times (1 CV) with buffer B. The wash and elution fractions were analyzed by SDS-PAGE (Reverse His-Trap gel, Figure 3.5). In all mutants, W1-W3 fractions were collected and concentrated with centrifuging with spin concentrators (10000 MWCO, Merck Millipore, USA) at 3000 g and 4 ^{o}C. The concentrated mixture (less than 4 mL) was injected into dialysis bags (4-12 mL capacity, 10000 MWCO, Thermo Scientific) pre-saturated with buffer D (50 mM Tris, 200 mM NaCl, 50 mM EDTA, and 5 mM 1,10-phenantroline at pH=7.5). The dialysis bag loaded with the protein solution was then immersed in 400 mL buffer D and stirred at 4 ^{o}C for two hours.

To further purify with size-exclusion (SEC) chromatography, the dialyzed protein solution was then concentrated to 1.8-2 mL and loaded onto the Superdex 75 column (300 mL, GE Healthcare, USA) pre-equilibrated with buffer E (50 mM Tris, and

200 mM NaCl at pH=7.5). Subsequently, the Superdex 75 column was eluted with buffer E (1 CV) and fractions showing UV absorption were examined via SDS-PAGE (SEC chromatogram and SEC gel, Figure 3.5). All fractions showing pure IPNS in the SDS-PAGE gel were collected and concentrated to ~50 mg/mL using centrifuge tubes (10000 MWCO, Merck Millipore, USA) at 3000 g and 4 ^{o}C. The concentrated pure protein solution was then aliquoted and stored at -80 ^{o}C.

The purity of IPNS mutants was also examined by protein LC-MS (QTOF Xevo G2-S, Waters, USA). The stock solutions of IPNS mutants were diluted in H_2O to the final concentration of 3 μM and were applied to the LC-MS. To elute the protein, H_2O:CH_3CN (both with 0.1% formic acid) gradient from 5% to 95% CH_3CN over 10 min was used. The resulting chromatograms of the IPNS mutants confirm the purity and the protein deconvoluted masses confirm the IPNS mutations were successful (Figure 3.6).

3.3.4: Preparation of BTFA Tagged S55C_Q280A_L282A IPNS

Similar to other mutants of IPNS, S55C_Q280A_L282A IPNS plasmid DNA was prepared using site-directed mutagenesis with S55C IPNS primers (from Dr. P. Rabe) and Q280A_L282A IPNS pCOLD plasmid as template DNA. The S55C_Q280A_L282A IPNS was subsequently expressed and purified as described above.

A 10 mL solution of purified apo S55C_Q280A_L282A IPNS in buffer F (25 mM Tris, and 100 mM NaCl at pH=8.0) with 10.7 mg/mL protein concentration (285 μM) was treated with 285 μM (1 eq) tris(2-carboxyethyl)phosphine and incubated for 5 minutes at 4 ^{o}C. Subsequently, 3-bromo-1,1,1-trifluoroacetone (BTFA) was added to the solution (15 eq) and the mixture was incubated at 4 ^{o}C for 45 minutes. The reaction of BTFA with the cysteine of S55C_Q280A_L282A IPNS was monitored using protein LC-MS (QTOF Xevo G2-S, Waters, USA) monitoring the covalent modification of the protein. The observed protein mass had changed from 37676 Da to 37804 Da confirming full alkylation and the mass difference, 128 Da, is compatible with BTFA ligand in its hydrated form (Figure 3.44) [8,21].

The protein mixture containing BTFA tagged S55C_Q280A_L282A IPNS (IPNS*) was concentrated to 1.8-2 mL using centrifuge tubes (10000 MWCO, Merck Millipore,

USA) and loaded onto Superdex 75 column (300 mL, GE Healthcare, USA) pre-equilibrated with buffer E (50 mM Tris, and 200 mM NaCl at pH=7.5). The fractions showing pure IPNS* bands in SDS-PAGE gel were collected, concentrated to 50 mg/mL, and stored at -80 ^{o}C.

3.3.5: NMR Studies on IPNS Mutants

All NMR experiments for unlabelled ACV turnover assays were carried out using Bruker Avance III 600 MHz equipped with a 5 mm BB-F/^{1}H Prodigy N_2 cryoprobe and Bruker Avance III 700 MHz equipped with a 5 mm ^{1}H(^{13}C/^{15}N) inverse TCI cryoprobe. For all turnover assays, the probe temperature was set at 298 K and 5 mm Bruker standard NMR tubes were used. Unless mentioned otherwise, all turnover samples were at 50 mM Tris-d11 buffer at pH=7.50 with 10% v/v D_2O to lock NMR signals; purified turnover products were dissolved at D_2O. For turnover experiments, the PROJECT – CPMG pulse sequence (includes replicative [t-180$^{o}_{y}$-t-90$^{o}_{y}$-t-180$^{o}_{y}$-t]$_n$ pulses) was used to suppress protein resonances [25]. The turnover conditions of IPNS mutants included 0.5 mM ACV, 0.5 mM tris(2-carboxyethyl)phosphine (for experiments with TCEP), 0.2 mM $Fe^{(II)}$ (from ferrous ammonium sulfate), and 0.5 mM sodium L-ascorbate. The reaction was started via addition of the enzyme and was monitored by recording of NMR spectra at fixed timepoints (using multizg command). The resulting spectra were processed via an exponential window function (line broadening was set at 0.3), and analyzed via Bruker topspin 3.6.5 (Bruker, Germany, www.bruker.com) and MestReNova 15.0.0 (MestReLabs, Spain, www.mestrelab.com).

For labelled ACV turnover experiments (Section 3.2.6), a Bruker Avance III HD 950 MHz spectrometer equipped with high sensitivity 5mm TCI cryoprobe for ^{1}H/^{13}C/^{15}N detection was used (with support from Prof. C. Redfield). The ^{13}C NMR spectra of labelled ACV turnover was obtained using Bruker NEO 600 MHz spectrometer equipped with 5 mm BB-F/^{1}H helium-cooled cryoprobe optimized for multinuclear observation.

The ^{19}F-NMR spectra of BTFA tagged S55C_Q280A_L282A IPNS (IPNS*) were obtained using a Bruker Avance III 600 MHz spectrometer equipped with a 5 mm BB-F/^{1}H Prodigy N_2 cryoprobe. For all samples, CF_3COOH was used as internal standard (100 μM) and the obtained spectra were referenced according to the internal standard

peak at – 75.45 ppm. To make anoxic IPNS* samples, NMR buffer (50 mM Tris-d_{11}, pH=7.50), D_2O, stock solution of IPNS* (1.36 mM) and CF_3COOH (10 mM) were transferred into an anaerobic chamber (Belle Technology, UK). Powders of ACV and $FeSO_4$ were transferred into the anaerobic chamber to prepare their stock solutions (ACV 100 mM, $FeSO_4$ 10 mM). All liquids and powders were equilibrated in the anaerobic chamber for at least 16 hours before use. The sample volume was 450 μL including 10% v/v D_2O. The NMR samples were transferred into J Young valve NMR tubes (5mm, Norell, USA) inside the anaerobic chamber. The J Young valve tubes were also pre-equilibrated inside the chamber.

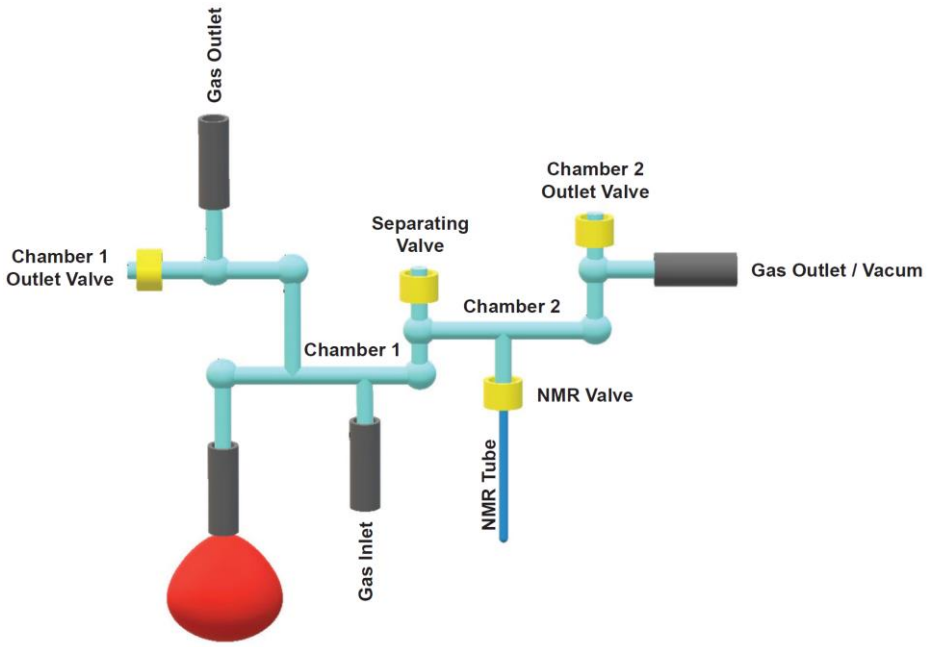


Figure 3.51: Apparatus used to expose J Young NMR samples to nitric oxide (scheme adopted from reference [8]).

The anoxic samples in J Young valve tubes were exposed to nitric oxide (NO) using glass apparatus shown in Figure 3.51. The NMR tube was connected to the glass apparatus with open separating valve and closed chamber 1 outlet (Figure 3.51). The air inside the apparatus was then removed under vacuum and subsequently the system was purged with argon through the gas inlet (Figure 3.51). The latter process was repeated twice to minimize oxygen content in the apparatus. After decreasing the pressure with a vacuum, the separating valve was closed and chamber 1 was filled with NO gas. Whilst

chamber 2 was under a low pressure, the NMR valve was opened and then the separating valve was opened to expose the NMR sample to NO. The sample was exposed to NO for 45 minutes and was mixed by inverting the tube three times. The NMR sample was held on ice as NO is corrosive and changes the pH over time. The NMR valve was then closed, and after purging the apparatus again with argon the J Young tube was removed.

3.3.6: LC-MS Studies on IPNS Mutants Catalysis

All LC-MS experiments were conducted using HPLC-MS (QTOF Xevo G2-S, Waters, USA) instrument equipped with HPLC column (ACE Equivalence 3, C-18, 50x2.1 mm, ACT Ltd., UK). A gradient of H_2O:CH_3CN (both in 0.1% formic acid) from 1% to 50% CH_3CN over 7 min was used to elute the samples. The MS unit was in positive ion mode forming ion molecules with +1 charge (M+1) and in some cases with +2 charge (M+2). The IPNS mutants turnover samples were set up similarly to the NMR conditions at 50 mM Tris buffer (pH=7.50). All LC-MS data were analyzed using Mass Lynx software (version 4.1).

3.3.7: Preparation and Isolation of S281A_IPNS Turnover Products

To purify the new products formed by S281A_IPNS catalysis, various large-scale (5-10 mL) turnover mixtures including 10-20 μM S281A_IPNS and 0.5-1.0 mM ACV with and without TCEP (1 eq.) were prepared at 50 mM Tris buffer (pH=7.50) and left overnight. The turnover mixture was then quenched with 10% v/v formic acid solution (with 1:10 v/v ratio) and the denatured enzyme was removed by centrifuging at 3000 g and 4 ^{o}C. The top solution was filtered using centrifuge tubes (10000 MWCO, Merck Millipore, USA) to remove enzymes in the mixture. The enzyme-free mixture was then freeze-dried and dissolved in 1-2 mL Milli-Q water. Subsequently, the mixture was loaded into Shimadzu high-performance liquid chromatography (HPLC) system connected to a Sunfire semi-prep column (C-18, 5 μM, 150 mm length, 10 mm diameter). The compounds were isolated using the solvents H_2O and CH_3CN (both containing 0.1% formic acid) starting with 1% CH_3CN for 5min followed by a gradient from 1% to 18% CH_3CN over 15 min. The fractions were collected separately, and the new product fractions were identified using LC-MS (QTOF Xevo G2-S, Waters, USA). The new product

fractions were freeze-dried and dissolved in D_2O (99.9 atom % D, Sigma-Aldrich) for NMR analysis (Sections 3.2.4 and 3.2.5).

3.3.8: Turnover Experiments in D_2O

To prepare turnover samples in full D_2O, 50 mM Tris buffer solutions at appropriate pH values (from 7.0 to 8.0) were prepared. A certain volume of the buffer solution (5 mL) was freeze-dried and then dissolved in the same volume of D_2O (99.9 atom % D, Sigma-Aldrich). The pD of the buffers in D_2O were then measured without correction of solvent isotope effect on pH/pD. Subsequently, S281T_IPNS stock solutions were buffer exchanged into the D_2O buffers using PD-10 columns (1.5 mL, PD-10 Desalting columns, Cytiva). The buffer exchanged samples were left on ice for 30 minutes. Meanwhile, H_2O molecules inside the enzyme core diffuse into the D_2O solutions. To minimize the H_2O content, S281T_IPNS samples were buffer exchanged again in D_2O buffers.

To set up turnover reactions in D_2O, the stock solutions of ACV, $Fe(NH_4)_2(SO_4)_2.6H_2O$, TCEP, and sodium L-ascorbate were prepared in D_2O (99.9 atom % D, Sigma-Aldrich). The turnover reactions were then prepared in D_2O buffers and monitored using NMR spectroscopy (as explained in Section 3.3.5).

3.3.9: ^{18}O Isotope Studies

For the experiments with $^{18}O_2$, the S281A_IPNS turnover samples were initially prepared in the anaerobic chamber (Belle Technology, UK). The turnover conditions were similar to the NMR and LC-MS studies with 50 mM Tris buffer. The powders including ACV, $Fe(NH_4)_2(SO_4)_2.6H_2O$, TCEP, and sodium L-ascorbate were transferred into the anaerobic chamber for 16 hours to equilibrate before making anaerobic stock solutions. The 50 mM Tris buffers at various pH values (6.5, 7.0, 7.5, 8.0, 8.5) and S281A_IPNS enzyme solution (1.4 mM) were also transferred to the anaerobic chamber and equilibrated for 16 hours. The anaerobic turnover mixtures including 20 μM S281A_IPNS and 0.5 mM ACV with and without TCEP (1 eq) were prepared in a plate at 5 different pH values (6.5 to 8.5) and transferred to a sealed box with a valve. The sealed box was then removed from the glove box and was connected to $^{18}O_2$ capsule ($^{18}O_2$, 97 ATOM-% ^{18}O, Merck, US) through the valve. The turnover was initiated with exposing the sealed box to

$^{18}O_2$ and the box was transferred back inside the glove box (to prevent potential $^{16}O_2$ contamination) and the samples were incubated overnight. The turnover reactions were quenched inside the anaerobic chamber using acetonitrile (pre-equilibrated in the anaerobic chamber) and were analyzed by LC-MS (QTOF Xevo G2-S, Waters, USA).

For the experiments with $H_2{}^{18}O$, stock solutions of ACV, $Fe(NH_4)_2(SO_4)_2.6H_2O$, TCEP, and sodium L-ascorbate were prepared in $H_2{}^{18}O$. The S281A_IPNS stock solution (1.4 mM) was buffer exchanged into 50 mM Tris buffer at $H_2{}^{18}O$ (pH=7.5) using PD-10 buffer exchange columns (1.5 mL, Cytiva) and the enzyme sample was left at 4 ^oC for 30 minutes. The enzyme-bound $H_2{}^{16}O$ will exchange into the solution during this step. To minimize the $H_2{}^{16}O$ content in the enzyme solution, the enzyme mixture was buffer exchanged into 50 mM Tris buffer at $H_2{}^{18}O$ (pH=7.5) one more time. Subsequently, two turnover reactions including 20 μM S281A_IPNS and 0.5 mM ACV with and without TCEP (1 eq) were prepared and left overnight. The turnover mixtures were quenched with acetonitrile and analyzed with LC-MS (QTOF Xevo G2-S, Waters, USA).

3.4: References

[1] I. Borovok, O. Landman, R. Kreisberg-Zakarin, Y. Aharonowitz and G. Cohen. Recent advances in the structure and function of isopenicillin N synthase. *Biochemistry* **1996** 35, 1981–1987.

[2] R. Kreisberg-Zakarin, I. Borovok, M. Yanko, F. Frolow, Y. Aharonowitz and G. Cohen. Isopenicillin-N Synthase. *Biophys. Chem.* **2000** 86, 109–118.

[3] T. S. Sim and P. Loke. Molecular Studies on Isopenicillin N Synthases. *Appl. Microbiol. Biotechnol.* **2000** 54, 1–8.

[4] P. L. Roach, I. J. Clifton, C. M. Hensgens, N. Shibata, C. J. Schofield, J. Hajdu, J. E. Baldwin. Structure of Isopenicillin N Synthase Complexed with Substrate and the Mechanism of Penicillin Formation. *Nature* **1997** 387, 827-830.

[5] N. C. Chapman, and P. J. Rutledge. Isopenicillin N Synthase: Crystallographic Studies. *ChemBioChem* **2021** 22, 1687-1705.

[6] E. Tamanaha *et al.*, Spectroscopic evidence for the two C-H-Cleaving Intermediates of Aspergillus nidulans Isopenicillin N Synthase. *J. Am. Chem. Soc.* **2016** 138, 8862–8874.

[7] C. D. Brown-Marshall, A. R. Diebold, E. I. Solomon. Reaction Coordinate of Isopenicillin N Synthase: Oxidase Versus Oxygenase Activity. *Biochemistry* **2010** 49, 1176-1182.

[8] P. Rabe *et al.*, X-ray free-electron laser studies reveal correlated motion during isopenicillin N synthase catalysis. *Sci. Adv.* **2021** 7, eabh0250.

[9] C. Reading, M. Cole. Clavulanic Acid: a Beta-Lactamase-Inhibiting Beta-Lactam from Streptomyces clavuligerus. *Antimicrob. Agents Chemother.* **1977** 11, 852-857.

[10] S. M. Drawz, R. A. Bonomo. Three Decades of β-Lactamase Inhibitors. *Clin. Microbiol. Rev.* **2010** 23, 160-201.

[11] T. A. Albright, W. J. Freeman, and E. E. Schweizer. Magnetic Resonance Studies. II. Investigation of Phosphonium Salts Containing Unsaturated Groups by ^{13}C and ^{31}P Nuclear Magnetic Resonance. *J. Am. Chem. Soc.* **1975** 97, 2946-2950.

[12] K. Pervushin, R. Riek, G. Wider, and K. Wüthrich. Attenuated T_2 relaxation by mutual cancellation of dipole–dipole coupling and chemical shift anisotropy indicates an avenue to NMR structures of very large biological macromolecules in solution. *Proc. Natl. Acad. Sci.* **1997** 94, 12366-12371.

[13] D. S. Wishart, C. G. Bigam, A. Holm *et al.*, ^{1}H, ^{13}C and ^{15}N random coil NMR chemical shifts of the common amino acids. I. Investigations of nearest-neighbor effects. *J. Biomol. NMR* **1995** 5, 67-81.

[14] J. E. Baldwin, R. M. Adlington, N. P. Crouch, and I. A. C. Pereira. Incorporation of ^{18}O-Labelled Water into Oxygenated Products Produced by the Enzyme Deacetoxy/deacetyl cephalosporin C Synthase. *Tetrahedron* **1993** 49, 7499-7518.

[15] K. D. McCarty, Dr. Y. Tateishi, T. Y. Hargrove, Prof. Dr. G. I. Lepesheva, Prof. Dr. F. P. Guengerich. Oxygen-18 Labeling Reveals a Mixed Fe−O Mechanism in the Last Step of Cytochrome P450 51 Sterol 14α-Demethylation. *Angew. Chem. Int. Ed.* **2024** 63, e202317711.

[16] C. M. Harris, L. Pollegioni, and S. Ghisla. pH and kinetic isotope effects in D-amino acid oxidase catalysis. Evidence for a concerted mechanism in substrate dehydrogenation via hydride transfer. *Eur. J. Biochem.* **2001** 21, 5504-5520.

[17] M. Bayrak *et al.* Correlating structure and activity of pepsin enzyme in H_2O and D_2O for the study of gastric digestion. *Food Chem. Adv.* **2024** 4,100638.

[18] K. A. Rubinson. Practical corrections for p(H,D) measurements in mixed H_2O/D_2O biological buffers. *Anal. Methods* **2017** 9, 2744-2750.

[19] R. S. Roy, A. M. Gehring, J. C. Milne, P. J. Belshaw, C. T. Walsh. Thiazole and oxazole peptides: biosynthesis and molecular Machinery. *Nat. Prod. Rep.* **1999** 16, 249–263.

[20] R. B. Hamed, J. R. Gomez-Castellanos, L. Henry, C. Ducho, M. A. McDonough, C. J. Schofield. The Enzymes of β-lactam Biosynthesis. *Nat. Prod. Rep.* **2013** 30, 21-37.

[21] P. Rabe *et al.* Spectroscopic studies reveal details of substrate-induced conformational changes distant from the active site in isopenicillin N synthase. *J. Biol. Chem.* **2022** 298, 102249.

[22] M. Sami, T. J. N. Brown, P. L. Roach, C. J. Schofield, J. E. Baldwin. Glutamine-330 is not essential for activity in isopenicillin N synthasefrom Aspergillus nidulans. *FEBS Lett.* **1997** 405, 191-194.

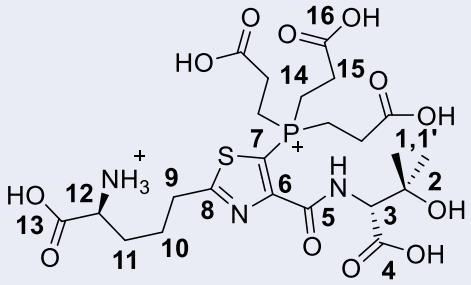
[23] L. A. McNeill, T. J. N. Brown, M. Sami, I. J. Clifton, N. I. Burzlaff, T. D. W. Claridge, R. M. Adlington, J. E. Baldwin, P. J. Rutledge, and C. J. Schofield. Terminally Truncated Isopenicillin N Synthase Generates a Dithioester Product: Evidence for a Thioaldehyde Intermediate during Catalysis and a New Mode of Reaction for Non-Heme Iron Oxidases. *Chem. Eur. J.* **2017** 23, 12815-12824.

[24] I. Pettinati, P. Grzechnik, C. Ribeiro de Almeida, J. Brem, M. A. McDonough, S. Dhir, N. J. Proudfoot, C. J. Schofield. Biosynthesis of histone messenger RNA employs a specific 3′ end endonuclease. *eLife* **2018** 7,e39865.

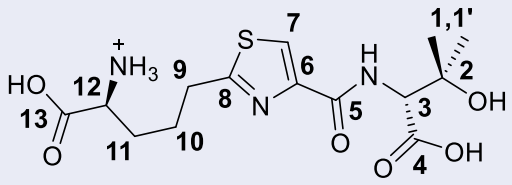
[25] J. A. Aguilar, M. Nilsson, G. Bodenhausen, and G. A. Morris. Spin echo NMR spectra without J modulation. *Chem. Commun.* **2012** 48, 811–813.

3.5: Appendix 3.I

Table Appendix 3.I: Observed ^{13}C and ^{1}H chemical shifts for the products with m/z = 608.16 and m/z = 360.12 according to the ^{1}H NMR, ^{13}C NMR, COSY, ^{1}H-^{13}C HSQC, and ^{1}H-^{13}C HMBC spectra.



New Product With m/z = 608.16



New Product With m/z = 360.12

Number	^{13}C δ (ppm)	^{1}H δ (ppm)	Number	^{13}C δ (ppm)	^{1}H δ (ppm)
1, 1’	25.4, 26.0	1.28, 1.31	1, 1’	25.6, 25.9	1.28, 1.32
2	72.1	-	2	71.9	-
3	62.3	4.39	3	61.5	4.39
4	174.3	-	4	174.0	-
5	160.6	-	5	163.1	-
6	155.6	-	6	147.2	-
7	114.9	-	7	125.3	8.07
8	181.1	-	8	172.8	-
9	32.25	3.21	9	31.5	3.07
10	24.3	1.88, 1.96	10	24.5	1.82, 1.90
11	29.4	1.92	11	29.5	1.90
12	54.3	3.75	12	54.1	3.71
13	174.0	-	13	174.0	-
14	18.4	2.98	-	-	-
15	27.6	2.65	-	-	-
16	175.2	-	-	-	-

Chapter 4: NMR Studies on γ-Butyrobetaine Hydroxylase

4.1: Introduction

4.1.1: γ-Butyrobetaine Hydroxylase

This chapter describes studies employing NMR that focused on an $Fe^{(II)}$ and 2-oxoglutarate (2OG) dependent oxygenase, γ-butyrobetaine hydroxylase (BBOX), which synthesizes L-carnitine (CAR) via catalyzing the stereospecific hydroxylation of γ-butyrobetaine (GBB) at the C-3 position (Figure 4.1) [1-4]. As in catalysis by many other oxygenases employing 2OG as co-substrate, BBOX-catalyzed hydroxylation is coupled with the two-electron oxidation of 2OG giving succinate and CO_2 (Figure 4.1). The synthesized L-carnitine plays a role in enabling fatty acid metabolism in animals, plants, and many eukaryotic microorganisms, by enabling fatty acid transport into mitochondria; BBOX is also present in many bacteria where its role is less clear [5-7]. In humans and other animals L-carnitine is both produced by BBOX catalysis and is obtained from food. The BBOX substrate γ-butyrobetaine is produced from N^{ε}-trimethyllysine, which is produced from trimethyllysine residues in proteins.

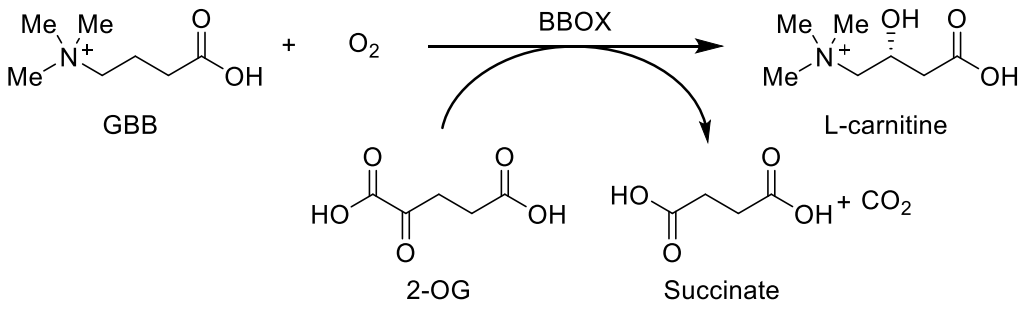


Figure 4.1: Reaction scheme for BBOX, which catalyzes conversion of γ-butyrobetaine (GBB), O_2, and 2-oxoglutarate (2OG) into L-carnitine, succinate, and CO_2.

Carnitine and hence the activity of BBOX has been linked with myocardial infarction therefore BBOX has become a drug target for heart disease [8,9]. BBOX has also been linked to cancer, in particular triple negative breast cancer [10], hence is of increasing interest as a drug target.

One well known inhibitor of BBOX, which is being used to suppress fatty acid metabolism and hence favour glycolysis is mildronate (Figure 4.2) [9]. Mildronate is a close structural analogue of GBB, but studies have shown that mildronate is not a simple GBB competing inhibitor, instead reacting with BBOX to give several smaller molecules, including malonic acid semi-aldehyde and formaldehyde, the latter of which is toxic [11,12]. It is therefore difficult to predict the biological effects of mildronate, which has also been used as a performance enhancing drug by athletes [13].

It is therefore of interest to develop BBOX inhibitors which react by a simpler mechanism than mildronate, i.e. which do not act as a substrate. Only a limited amount of work has been done towards this objective – studies in Oxford led to the identification of a moderately potent BBOX inhibitor, but in order for it to be effective in cells, a prodrug form was required [14]. In the current study, a library containing around 20 potent BBOX inhibitors (designed and synthesized by Dr. S. Basak) was tested against human BBOX (h-BBOX, provided by Dr. E. Salah) and bacterial BBOX, i.e. BBOX from *Pseudomonas sp. AK1* (ps-BBOX) to investigate their protein binding and reactivity properties. Ps-BBOX can be produced easily and is consequently a good model system for human BBOX which is more difficult to prepare [15,16]. Figure 4.2 shows the structures of some of the inhibitors investigated which included both derivatives of GBB and a new class of N-acyl sulfonamide BBOX inhibitors.

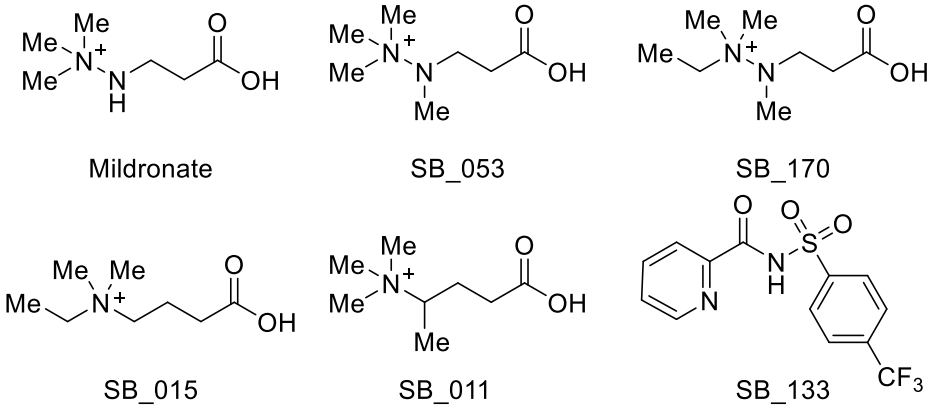


Figure 4.2: Structures of mildronate and some of the potent BBOX inhibitors (designed and synthesized by Dr. S. Basak). The inhibitors investigated included both derivatives of GBB / mildronate and a new class of N-acyl sulfonamide BBOX inhibitors, exemplified by SB_133.

4.1.2: Examining Protein-Ligand Binding Using NMR Spectroscopy

There are two general NMR based approaches that are widely used to examine the interactions of small molecule ligands with proteins [17,18]. One approach is to study the protein bound complex (the protein-observe method) in which changes of protein NMR peaks are monitored during ligand titration [17, 18]. Monitoring the protein peaks using ^{19}F NMR and ^{1}H-^{15}N HSQC spectroscopy upon ligand titration are examples for the protein-observed method [18]. The other approach is to study only the ligand (the ligand-observe method), in which the small molecule signal is monitored during protein titration [17,18]. The Carr–Purcell–Meiboom–Gill (CPMG), saturation transfer difference (STD), and water–ligand observed via gradient spectroscopy (waterLOGSY) are ligand-observed NMR assays which do not require deconvolution steps as ligand resonances are distinct [18]. Hence, the ligand-observed NMR assays can be useful for fast screening of the binding affinities of multiple ligands to a single protein [18].

The Carr-Purcell-Meiboom-Gill (CPMG) pulse sequence holds the sample magnetization vector in a transversal plane, leading to a decay in the magnetization vector and hence in the NMR signals [19]. Consequently, in CPMG-edited ^{1}H NMR spectra, signals of large molecules (proteins) will not be observed due to their slow tumbling rate, whereas the small molecule peaks will not fully decay [19]. Therefore, binding of small molecules can be measured via examining CPMG edited ^{1}H NMR spectra of the small molecule in solution with and without the target protein [18,20,21]. The small molecule will tumble slowly (as for the protein) if it binds to the protein and its CPMG NMR signal intensity will consequently decay if the ligand binds non-reversibly (with slow exchange rates) [18,20,21]. As described in this chapter, the CPMG method was used to examine the binding affinities of the inhibitors to BBOX because these experiments are practical for non-reversible binders, are not time-consuming, and do not require isotope labelling.

4.2: Results and Discussion

4.2.1: BBOX Inhibitor Turnover Studies

Prior to examining whether BBOX inhibitors can undergo oxidative reactions by the enzyme, the turnover of γ-butyrobetaine GBB with human BBOX (h-BBOX) was analyzed. Figure 4.3 a shows the obtained ^{1}H NMR spectra of the GBB reaction with h-BBOX at selected timepoints. The turnover sample contained 50 μM GBB, 400 μM 2OG, 50 μM $Fe^{(II)}$, and 0.5 mM L-ascorbate (to hinder $Fe^{(II)}$ oxidation). The NMR buffer for all turnover and binding assays contained 80 mM KCl, as it was observed that KCl can facilitate BBOX activity [3,11]. The reaction was initiated via addition of h-BBOX (50 nM final concentration) and was monitored via obtaining the ^{1}H NMR spectrum at specific time points. Reaction progress was monitored via integration of the NMe_3 peak integrals of CAR and GBB (Figure 4.3). GBB was observed to be almost completely converted to L-carnitine (CAR) in the presence of h-BBOX after one hour, as shown by a time course plot (Figure 4.3 b).

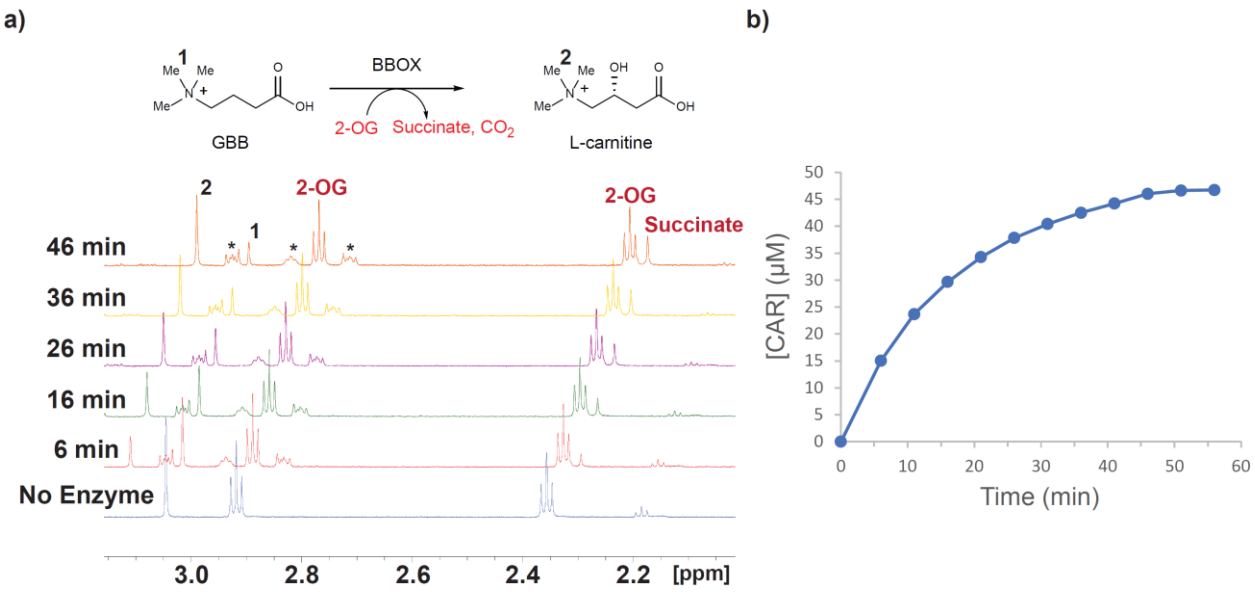


Figure 4.3: **(a)** The ^{1}H NMR spectra of GBB turnover with h-BBOX at specific timepoints. The turnover mixture contained 50 μM GBB, 400 μM 2OG, 50 μM Fe(II), and 0.5 mM L-ascorbate. The NMe_3 peaks of GBB (1) and L-carnitine (2) are labelled numerically. Impurities from h-BBOX batch are labelled with an asterisk. **(b)** The reaction progress versus time obtained from GBB (1) and L-carnitine (2) relative peak integrals.

After examining GBB turnover, the BBOX inhibitors shown in Figure 4.2 which were analogues of GBB, were analyzed by turnover assay with both human BBOX (h-BBOX) and *Pseudomonas sp. AK1* BBOX. Among the tested GBB analogues, SB_011 was observed to react with both h-BBOX and ps-BBOX; SB_015 reacted with ps-BBOX but not h-BBOX. The other analogues (SB_053 and SB_170) were not observed to react (the ^{1}H NMR spectra shown in Figure Appendix 4.I).

The ^{1}H NMR spectra obtained at selected time points of SB_011 turnover with h-BBOX showed depletion of the substrate NMe_3 peak (at 3.0 ppm) and formation of a singlet peak at 3.10 ppm corresponding to the product NMe_3 peak (Figure 4.4 a). The turnover sample with h-BBOX contained 50 μM SB_011, 400 μM 2OG, 50 μM $Fe^{(II)}$, and 0.5 mM L-ascorbate; the conversion rate of SB_011 was slower compared to GBB turnover with h-BBOX (Figure 4.4 a). Turnover was started by adding h-BBOX (50 nM final concentration). The structural similarity of SB_011 and GBB coupled with the observation of a ~0.1 ppm shift in the NMe_3 peak of SB_011 on BBOX treatment, suggests that SB_011 will undergo C-3 hydroxylation as for GBB (as shown in Figure 4.4 a). The sample with SB_011 and ps-BBOX also showed slow formation of the same peak at 3.10 ppm. The ^{1}H NMR spectra of ps-BBOX turnover mixture before adding enzyme and 60 minutes after adding enzyme showed slower hydroxylation of SB_011 compared with h-BBOX (Figure 4.4 b); note mildronate reacts efficiently with h-BBOX but not ps-BBOX [11,16]. The ps-BBOX turnover assay contained 200 μM SB_011, 600 μM 2OG, 100 μM $Fe^{(II)}$, and 0.5 mM L-ascorbate and the reaction was started via adding ps-BBOX (140 nM final concentration). Higher enzyme and substrate concentrations were used in ps-BBOX turnover assays as the ps-BBOX is less active than h-BBOX [15,16].

Another GBB analogue which showed reaction with ps-BBOX was SB_015 which, like SB_011, is structurally similar to GBB, hence SB_015 may be expected to be hydroxylated at its C-3 position if it binds to the BBOX in a similar manner to GBB. The ^{1}H NMR time course of SB_015 turnover with ps-BBOX is shown in Figure 4.5. The turnover sample included 200 μM SB_015, 600 μM 2OG, 100 μM $Fe^{(II)}$, and 0.5 mM L-ascorbate and the reaction was started by adding ps-BBOX (1 μM final concentration). The turnover of SB_015 with ps-BBOX revealed formation of new set of peaks over time

(Figure 4.5). In particular, two singlet peaks corresponding to the NMe_2 group of the product were observed to form over time (Figure 4.5). The latter observation is likely because the two methyl groups in the product $N(Et)Me_2$ moiety are diastereotopic due to a chiral centre at the C-3 position. Unlike ps-BBOX, treatment of SB_015 with h-BBOX did not show any reaction. The h-BBOX turnover sample contained 50 μM SB_015, 400 μM 2OG, 50 μM $Fe^{(II)}$, and 0.5 mM L-ascorbate and the ^1H NMR spectra did not show any product formation over a reasonable time (2 hours) after adding 50 nM h-BBOX (Figure Appendix 4.I).

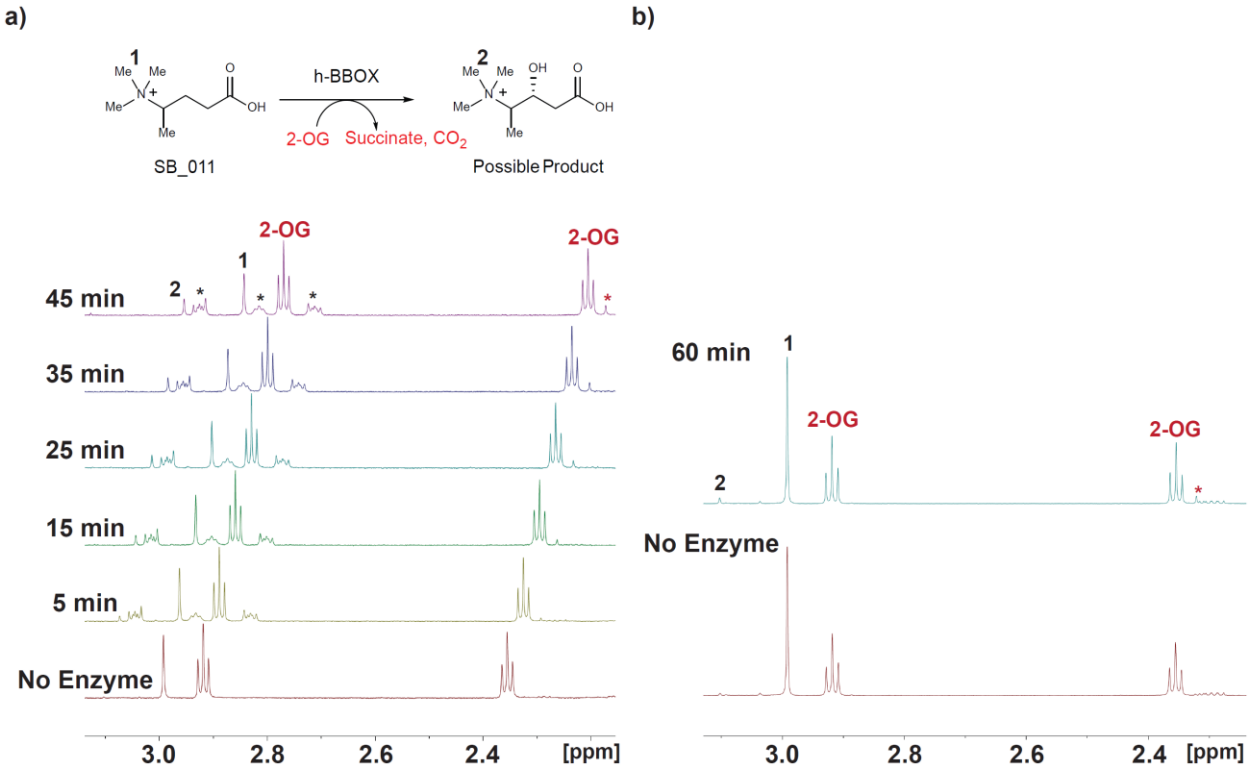


Figure 4.4: The ^1H NMR spectra of SB_011 turnover with **(a)** h-BBOX and **(b)** ps-BBOX at specific time points. The NMe_3 peaks of SB_011 and the product are labelled numerically, and the impurities from h-BBOX batch are labelled with black asterisks. The peak corresponding to succinate is labelled with a red asterisk.

4.2.2: BBOX Inhibitor Protein Binding Assay

The binding affinities of GBB and BBOX inhibitors to ps-BBOX were examined using CPMG edited ^1H NMR spectroscopy. In order to obtain binding curves, samples containing GBB (or other GBB analogues) were prepared in the presence $Fe^{(II)}$ and a 2OG analogue, N-oxalylglycine (N-OG), the latter was used to prevent BBOX catalysis.

It has been observed that the presence of 2OG or its analogues promotes substrate (GBB) binding to BBOX [22]. Relatively high concentrations of N-OG were used to almost saturate BBOX with N-OG. The CPMG edited ^{1}H NMR spectrum of the NMR sample without protein was obtained. Subsequently, the sample was titrated with ps-BBOX solution and the CPMG ^{1}H NMR spectrum was obtained to provide information on binding affinity as described above (Section 4.1.2). The binding assay of SB_011 is shown in Figure Appendix 4.II.

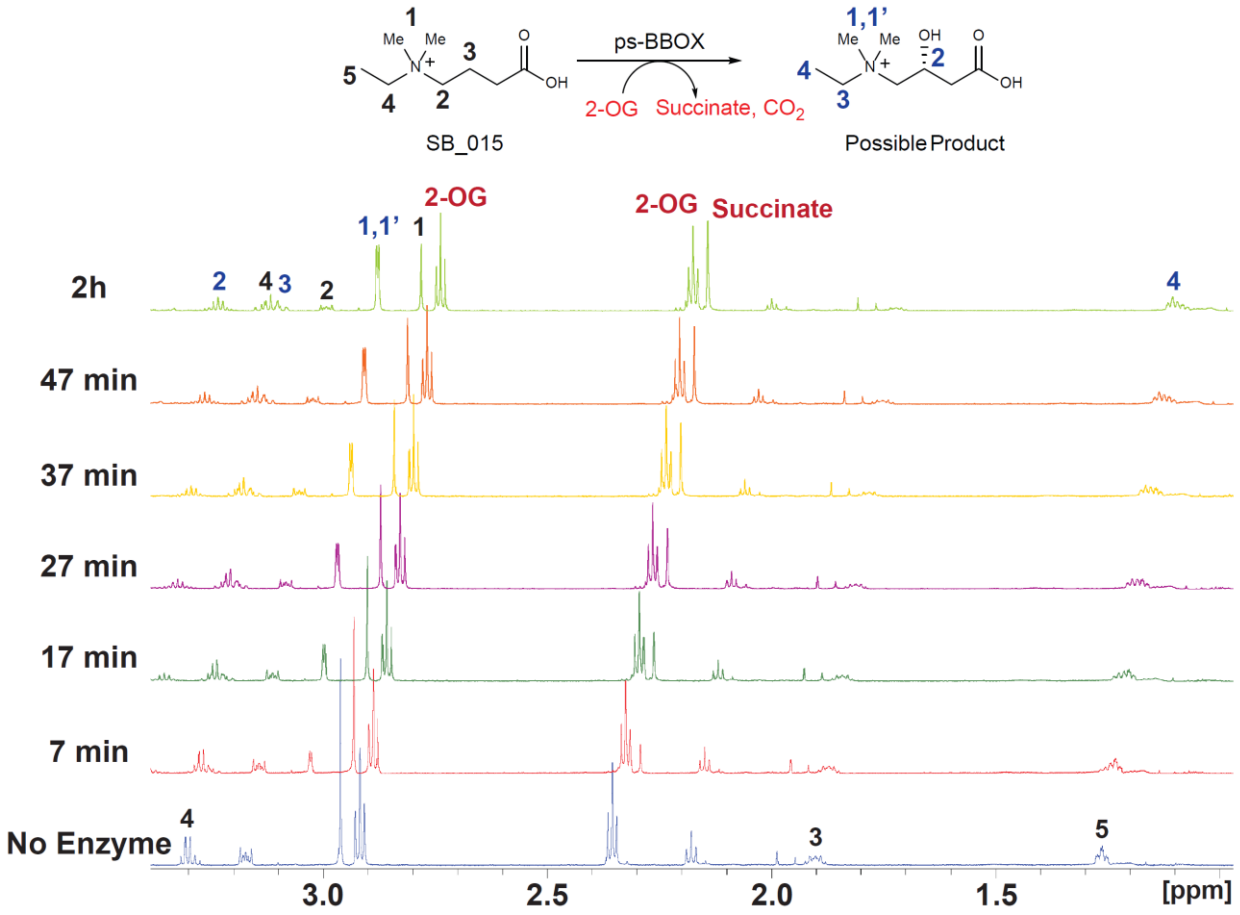


Figure 4.5: The ^{1}H NMR spectra of SB_015 turnover with ps-BBOX at specific time points. The substrate and product peaks are labelled in the reaction scheme and the spectrum with black and blue numbers, respectively.

The binding of GBB to ps-BBOX was examined and the CPMG edited ^{1}H NMR spectra of samples containing GBB and co-substrates at various ps-BBOX concentrations (up to 30 μM) were obtained (Figure 4.6 a). The NMR sample (before ps-BBOX titration) contained 20 μM GBB, 700 μM N-OG, 250 μM $Fe^{(II)}$, and 30 μM trimethylsilylpropanoic

acid (TSP, an internal standard). The GBB NMe_3 peak intensity was observed to decrease with ps-BBOX titration and it almost disappeared at 30 μM ps-BBOX (Figure 4.6 a). The NMe_3 peak was chosen to examine GBB binding because it is a singlet, does not overlap with other peaks, and corresponds to nine equivalent protons. Therefore, monitoring the NMe_3 peak rather than other GBB peaks is preferred in order to optimize the sensitivity of the assay. The ratio of the GBB NMe_3 peak intensity in samples with psBBOX to that of the sample without protein (I/I_0) is proportional to the concentration of free GBB in solution. The latter parameter (I/I_0) was plotted versus ps-BBOX concentration to obtain a binding curve, which was used to compare binding affinities of GBB and the GBB analogues (Figures 4.2 and 4.6 b). All GBB analogues shown in Figure 4.2 were tested for their binding affinity to ps-BBOX; the results are discussed below.

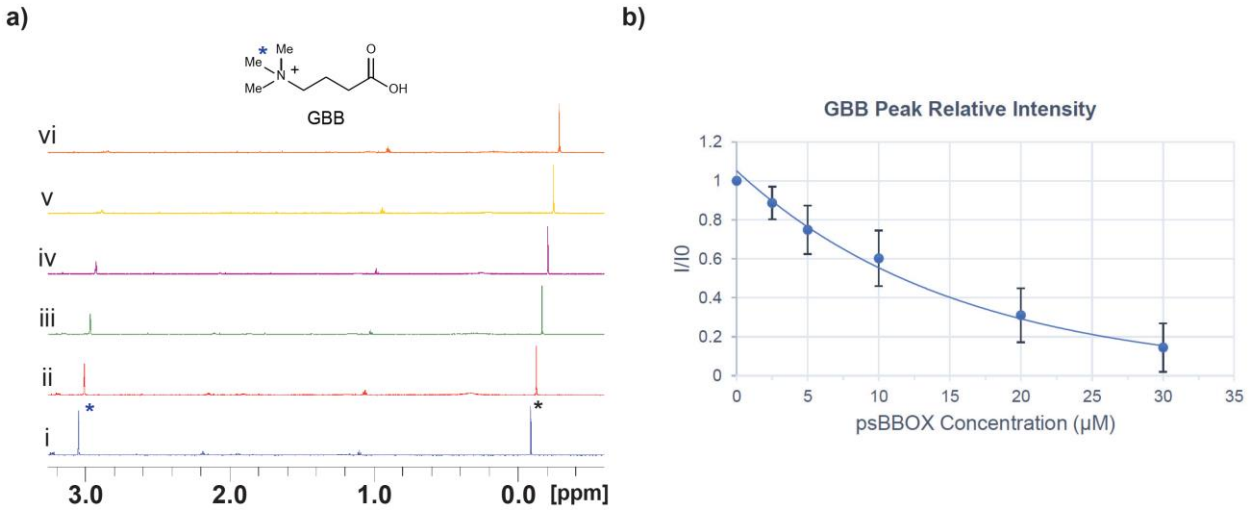


Figure 4.6: **(a)** CPMG edited ^1H NMR spectra of the sample containing 20 μM GBB, 700 μM N-OG, 250 μM $Fe^{(II)}$, and 30 μM TSP (internal standard) without ps-BBOX (i), and with 2.5 μM (ii), 5 μM (iii), 10 μM (iv), 20 μM (v), and 30 μM (vi) ps-BBOX concentrations. The GBB NMe_3 and TSP $SiMe_3$ peaks are labelled with blue and black asterisks, respectively. **(b)** The GBB NMe_3 relative peak intensity with respect to the sample without ps-BBOX (I/I_0) versus ps-BBOX concentration. The error bars are standard deviations from three replicate experiments.

Mildronate showed weaker binding to ps-BBOX compared to GBB (Figure 4.7). The mildronate NMe_3 peak depleted slower than GBB and did not completely disappear with 30 μM ps-BBOX (Figure 4.7 a). According to the obtained binding curve, almost 50 percent of mildronate was bound to the ps-BBOX with 30 μM enzyme (Figure 4.7 b).

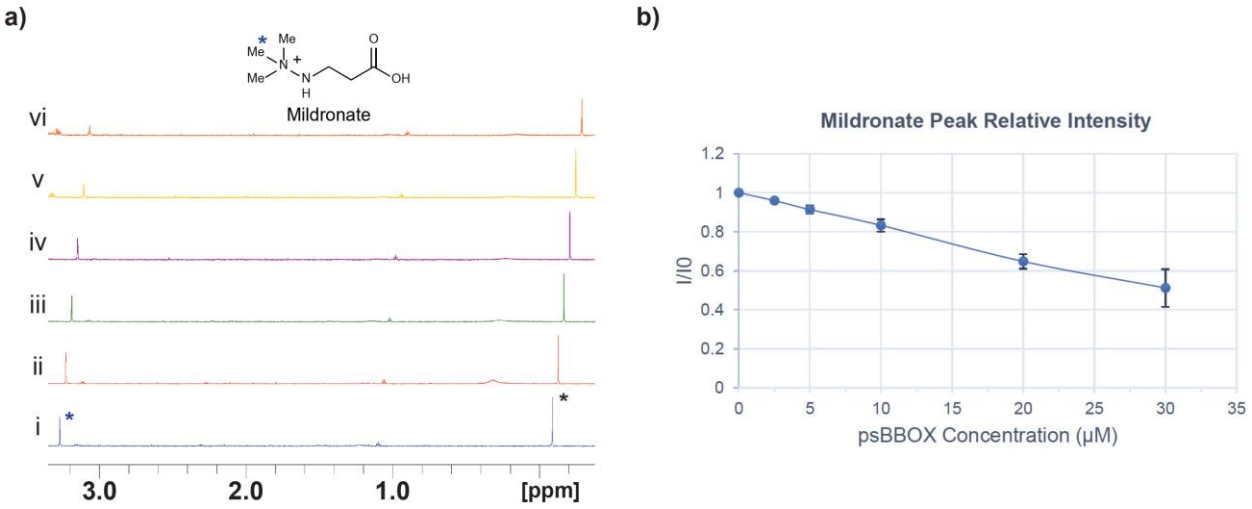


Figure 4.7: **(a)** CPMG edited ^{1}H NMR spectra of the sample containing 20 μM mildronate, 700 μM N-OG, 250 μM $Fe^{(II)}$, and 30 μM TSP (internal standard) without ps-BBOX (i), and with 2.5 μM (ii), 5 μM (iii), 10 μM (iv), 20 μM (v), and 30 μM (vi) ps-BBOX concentrations. The mildronate NMe_3 and TSP peaks are labelled with blue and black asterisks, respectively. **(b)** The diagram of mildronate NMe_3 relative peak intensity with respect to the sample without ps-BBOX (I/I_0) versus ps-BBOX concentration. The error bars are standard deviations from three replicate experiments.

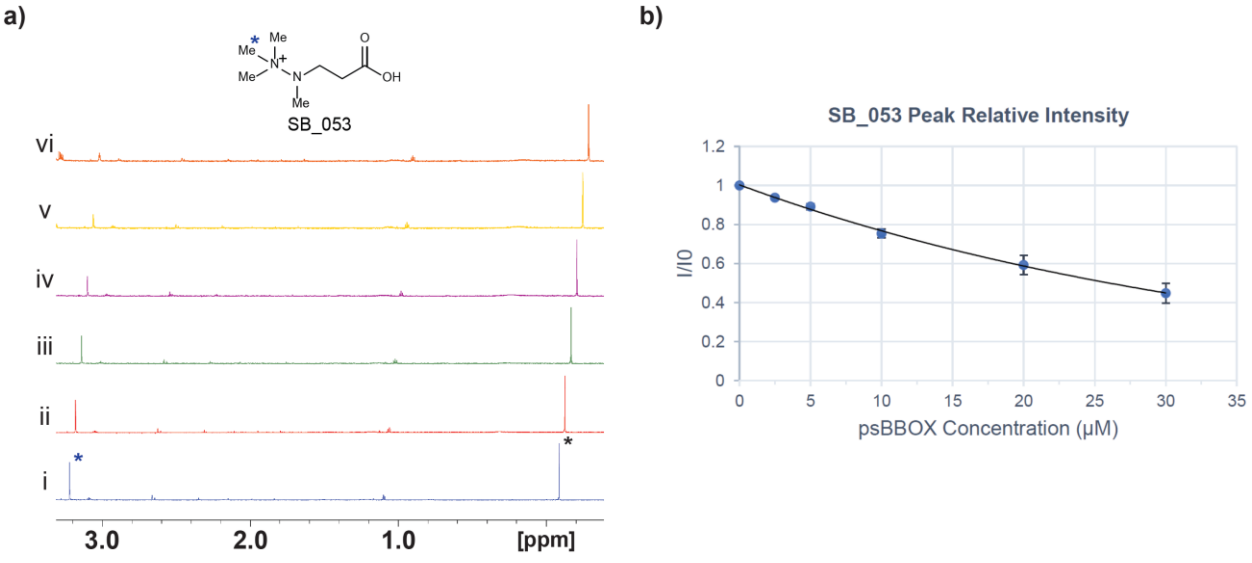


Figure 4.8: **(a)** CPMG edited ^{1}H NMR spectra of the sample containing 20 μM SB_053, 700 μM N-OG, 250 μM $Fe^{(II)}$, and 30 μM TSP (internal standard) without ps-BBOX (i), and with 2.5 μM (ii), 5 μM (iii), 10 μM (iv), 20 μM (v), and 30 μM (vi) ps-BBOX concentrations. The SB_053 NMe_3 and TSP peaks are labelled with blue and black asterisks, respectively. **(b)** SB_053 NMe_3 relative peak intensity with respect to the sample without ps-BBOX (I/I_0) plotted versus ps-BBOX concentration. The error bars are standard deviations from three replicate experiments.

CompoundSB_053, which is mildronate derivative (a methyl group is attached to the mildronate NH in SB_053), showed slightly stronger binding affinity to ps-BBOX than mildronate (Figure 4.8). The CPMG edited ^{1}H NMR spectra of SB_053 titration with ps-BBOX (Figure 4.8 a) and its corresponding binding curve (Figure 4.8 b) showed faster depletion of the SB_053 NMe_3 peak compared to mildronate. Therefore, addition of a hydrophobic group to the mildronate NH may increase the compound's binding affinity to ps-BBOX.

Compound SB_170 (in which an ethyl group substitutes for one of the NMe_3 methyl groups in SB_053) showed higher affinity towards ps-BBOX than mildronate and SB_053 (Figure 4.9). The CPMG edited ^{1}H NMR spectra of the SB_170 sample titrated with ps-BBOX and its binding curve are shown in Figures 4.9 a and 4.9 b, respectively. Despite showing faster depletion of the NMe_2 peak than those observed with mildronate and SB_053, the binding affinity for SB_170 is less than for GBB. The changes in binding affinity can indicate that substituting the methyl groups in the substrate NMe_3 can increase the binding affinity to ps-BBOX.

Compound SB_015 is a close GBB derivative, with an ethyl group substituted for one of the GBB methyl groups. The binding affinity of SB_015 to ps-BBOX was comparable to that of GBB (Figure 4.10). Compound SB_015 showed the strongest binding affinity to ps-BBOX among the GBB and mildronate analogues tested. As mentioned above, the observation of a higher binding affinity of SB_015 than other analogues showed how modifications in the substrate / ligand NMe_3 group can potentially increase the binding affinity.

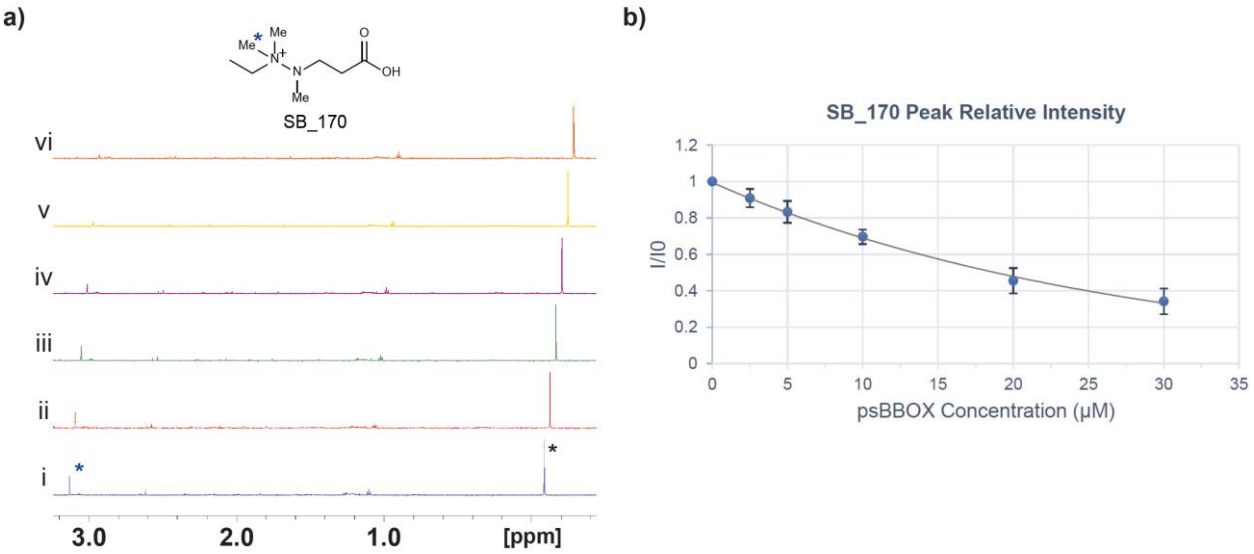


Figure 4.9: **(a)** CPMG edited ^{1}H NMR spectra of the sample containing 20 μM SB_170, 700 μM N-OG, 250 μM $Fe^{(II)}$, and 30 μM TSP (internal standard) without ps-BBOX (i), and with 2.5 μM (ii), 5 μM (iii), 10 μM (iv), 20 μM (v), and 30 μM (vi) ps-BBOX concentrations. The SB_170 NMe_2 and TSP peaks are labelled with blue and black asterisks, respectively. **(b)** SB_170 NMe_2 relative peak intensity with respect to the sample without ps-BBOX (I/I_0) versus ps-BBOX concentration. The error bars are standard deviations from three replicate experiments.

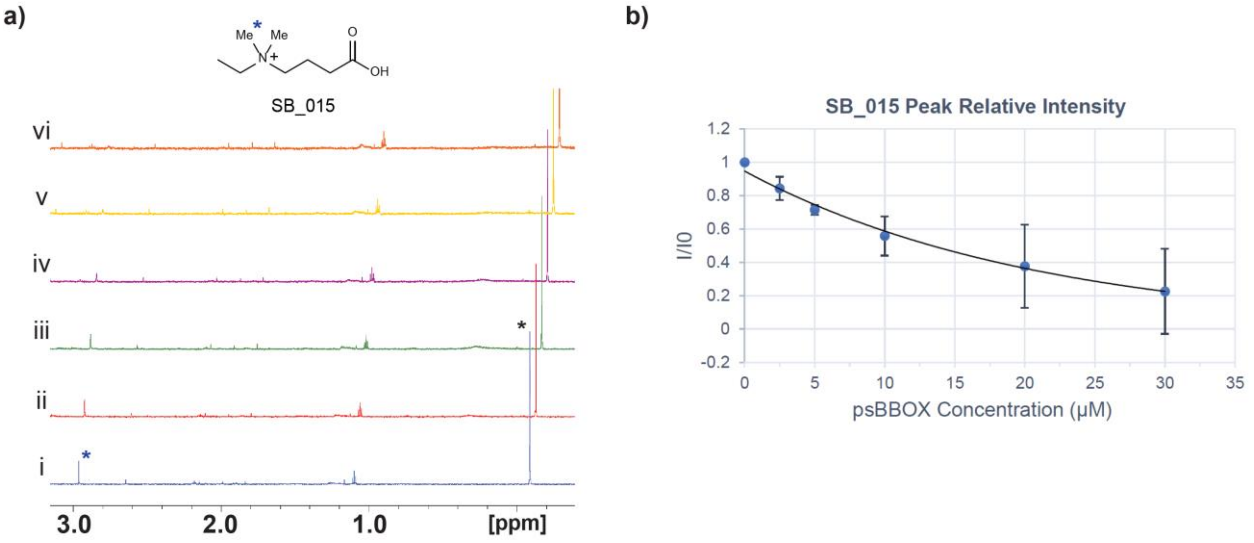


Figure 4.10: **(a)** CPMG edited ^{1}H NMR spectra of the sample containing 20 μM SB_015, 700 μM N-OG, 250 μM $Fe^{(II)}$, and 30 μM TSP (internal standard) without ps-BBOX (i), and with 2.5 μM (ii), 5 μM (iii), 10 μM (iv), 20 μM (v), and 30 μM (vi) ps-BBOX concentrations. The SB_015 NMe_2 and TSP peaks are labelled with blue and black asterisks, respectively. **(b)** SB_170 NMe_2 relative peak intensity with respect to the sample without ps-BBOX (I/I_0) versus ps-BBOX concentration. The error bars are standard deviations from three replicate experiments.

4.2.3: Examining the Binding Mode of SB_133

One of the most potent BBOX inhibitors identified is the N-acyl sulfonamide SB_133 (designed and synthesized by Dr. S. Basak). It was considered that SB_133 may occupy either the 2OG binding site or both the 2OG and GBB binding sites in BBOX [20]. In order to examine the binding mode of SB_133, competitive binding experiments were conducted using CPMG edited ^{1}H NMR spectra. If the inhibitor competes with both GBB and 2OG, both their corresponding peak intensities should increase upon inhibitor titration [20].

In the first experiment, a sample containing 20 μM GBB, 300 μM N-OG (to prevent catalysis), and 250 μM $Fe^{(II)}$ was titrated first with 30 μM ps-BBOX and the intensities of the N-OG and GBB peaks were observed (Figure 4.11 a). The latter observations indicated that GBB and N-OG bind to ps-BBOX, as expected. The sample was then treated with the inhibitor SB_133, with two 20 μM portions of the inhibitor being added The results showed that SB_133 addition caused an increase in both the GBB and N-OG peak intensities (Figure 4.11 a), implying that SB_133 competes with both GBB and N-OG in ps-BBOX. Moreover, N-OG displacement was observed when its concentration (300 μM) was much higher than the SB_133 concentration (up to 40 μM). The latter could reflect the higher binding affinity of SB_133 compared to N-OG and / or cooperative binding to BBOX [22].

A second experiment was conducted to further investigate whether SB_133 occupies both N-OG and GBB binding sites in ps-BBOX. An NMR sample was prepared containing 20 μM GBB, 20 μM SB_133 and 250 μM $Fe^{(II)}$ and its CPMG edited ^{1}H NMR spectrum was obtained (Figure 4.11 b). After the addition of 20 μM ps-BBOX, only the SB_133 peak intensities in the aromatic region were observed to decrease; the GBB peak did not change (Figure 4.11 b), indicating that SB_133 binds to ps-BBOX, preventing GBB from binding. The sample was then treated with N-OG at a relatively high concentration (520 μM); a relatively high N-OG concentration was used due to its lower binding affinity compared to SB_133. Treatment with N-OG caused the GBB peak to decrease and the SB_133 aromatic peaks to be partially recovered (Figure 4.11 b). The binding of GBB

upon SB_133 displacement with N-OG also indicated that SB_133 occupies (or disrupts) both of the GBB and N-OG binding sites.

In another experiment, displacement of 2OG and GBB was examined with SB_133 to confirm SB_133 binding mode. Instead of $Fe^{(II)}$, $Mn^{(II)}$ was used as an active site binding metal ion to prevent catalysis. $Mn^{(II)}$ also possesses the highest number of unpaired electrons across the first-row transition metals due to its $3d^5$ electronic configuration; $Mn^{(II)}$ exhibits a strong paramagnetic effect that broadens the NMR peaks of molecules coordinating to it, in this case 2OG and GBB [23,24], causing their peak intensities to decrease. Less enzyme is required for binding assays in the $Mn^{(II)}$/2OG method compared to the $Fe^{(II)}$/N-OG method [20], something beneficial in the case of binding experiments with the scarce h-BBOX which was available in smaller quantities. Figure 4.11 c shows the CPMG edited ^1H NMR spectra of a sample containing 20 μM GBB, 300 μM 2OG, and 100 μM $Mn^{(II)}$ which was treated with 15 μM ps BBOX, and then SB_133 was added three times (20 μM each time) to the sample. Both the GBB and 2OG peaks were recovered after SB_133 treatment, supporting the proposal that the inhibitor competes with both GBB and 2OG for binding to ps-BBOX.

The aforementioned competitive binding assay was then employed to examine whether SB_133 can occupy both GBB and 2OG binding sites in h-BBOX (Figure 4.12). The initial sample contained 20 μM GBB, 300 μM 2OG, and 100 μM $Mn^{(II)}$ which was treated with 15 μM h-BBOX. The depletion of GBB NMe_3 and 2OG methylene peaks indicates binding of both GBB and 2OG to h-BBOX (Figure 4.12 a). The titration of the latter sample with SB_133 showed recovery of GBB and 2OG peaks implying that SB_133 competes with both GBB and 2OG molecules (Figure 4.12 a). It is notable that the 2OG methylene peaks after h-BBOX addition do not decrease as much as ps-BBOX (blue and red spectra in Figure 4.12 a). Therefore, 2OG binding affinity to h-BBOX is likely to be weaker than its affinity to ps-BBOX. The GBB methylene and 2OG NMe_3 peak relative intensities with respect to the sample without protein was plotted to quantify the displacement levels of GBB and 2OG (Figure 4.12 b).

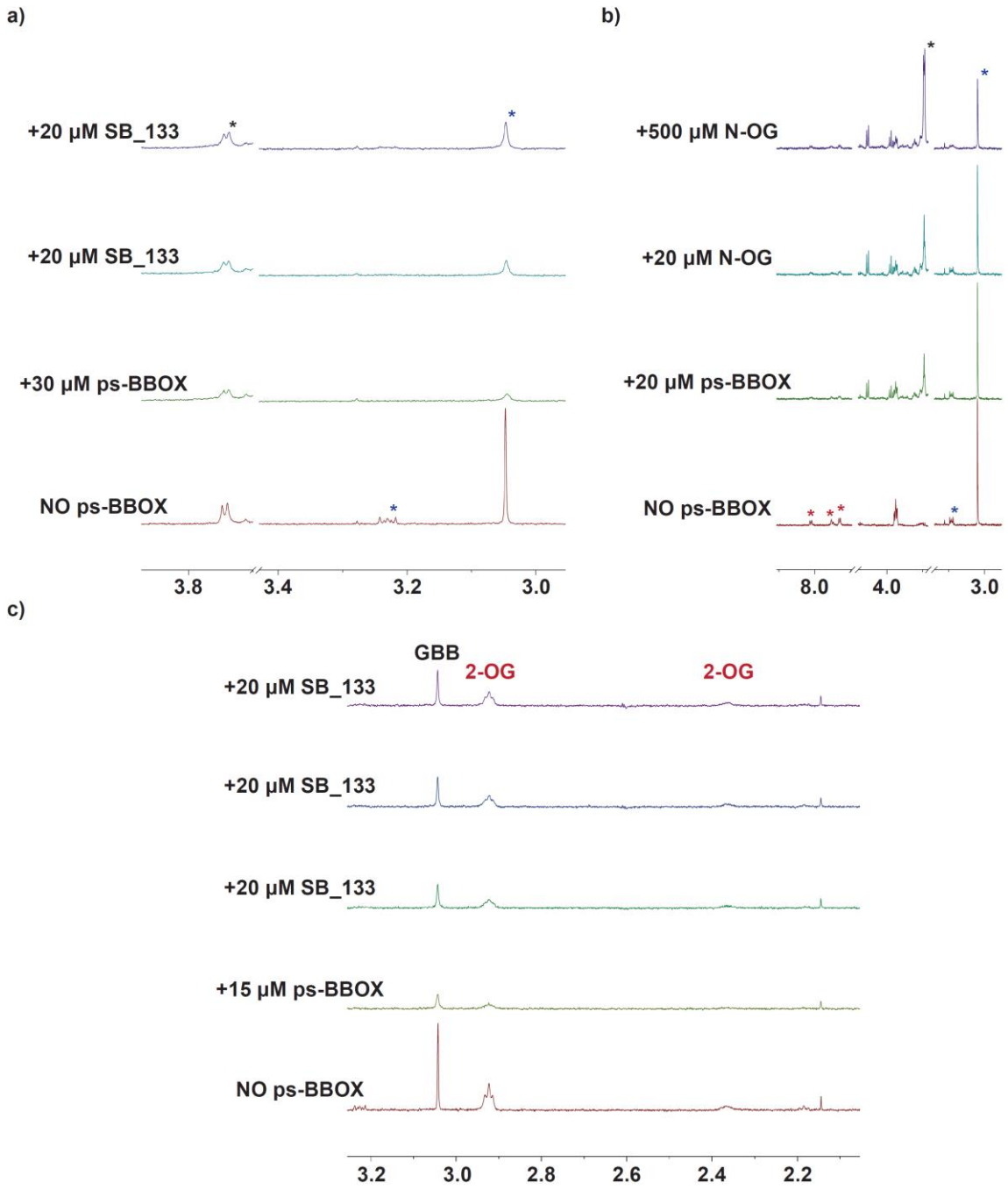


Figure 4.11: Competitive binding assay (to ps-BBOX) between SB_133 and N-OG/2OG. **(a)** The CPMG edited ^{1}H NMR spectra of the sample containing 20 μM GBB, 300 μM N-OG, and 250 μM $Fe^{(II)}$ titrated with ps-BBOX and SB_133. The N-OG and GBB peaks are labelled with black and blue asterisks, respectively. **(b)** CPMG edited ^{1}H NMR spectra of the sample containing 20 μM GBB, 20 μM SB_133, and 250 μM $Fe^{(II)}$ titrated with ps-BBOX and N-OG. The SB_133 aromatic peaks, N-OG peak, and GBB peaks are labelled with red, black, and blue asterisks, respectively. (c) The CPMG edited ^{1}H NMR spectra of the sample containing 20 μM GBB, 300 μM 2OG, and 100 μM $Mn^{(II)}$ titrated with ps-BBOX and SB_133.

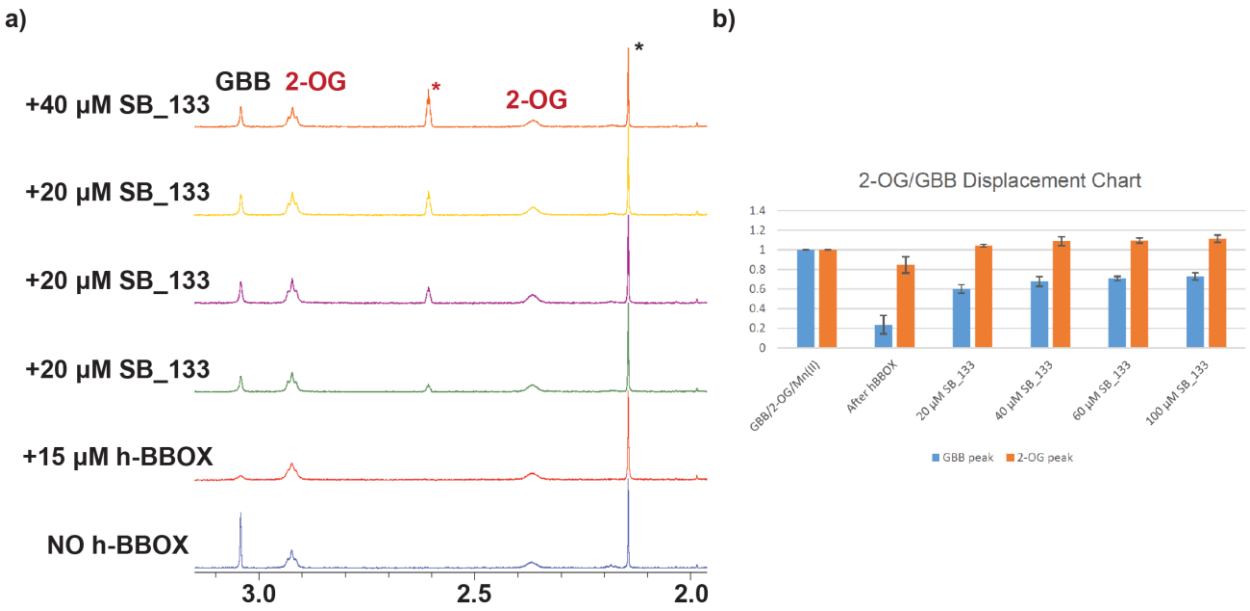


Figure 4.12: Competitive binding assay (to h-BBOX) between 2OG/GBB and SB_133. **(a)** The CPMG edited ^{1}H NMR spectra of the sample containing 20 µM GBB, 300 µM 2OG, and 100 µM $Mn^{(II)}$ titrated with h-BBOX and SB_133. The acetone (internal standard) and DMSO (present in SB_133 batch) peaks are labelled with black and red peaks, respectively. **(b)** GBB NMe_3 and 2OG methylene relative peak intensities with respect to the sample without h-BBOX showing recovery of GBB and 2OG peaks with SB_133. The error bars are standard deviations from three replicate experiments.

4.2.4: Conclusion

In this study, a range of GBB and mildronate analogues (provided by Dr. S. Basak) was examined for the turnover by h-BBOX and ps-BBOX. Following initial studies with GBB, evidence was accrued that SB_011 undergoes hydroxylation as catalysed by h-BBOX and ps-BBOX, whereas SB_015 undergoes hydroxylation with ps-BBOX, but not h-BBOX. The other new compounds tested (SB_053, SB_170) were not observed to undergo hydroxylation. CPMG NMR-based binding assays between ps-BBOX and GBB/mildornate analogues showed that substitution on of one of the substrate NMe_3 methyl groups can increase the BBOX binding affinity. Competitive binding experiments showed that the potent N-acyl sulfonamide inhibitor SB_133 occupies both GBB and 2OG binding sites in both h-BBOX and ps-BBOX.

4.3: Methods

4.3.1: Expression and Purification of Pseudomonas BBOX

A codon optimized plasmid for expression to produce Ps-BBOX in *E. coli* BL21 cells was provided by Dr. E. Salah; the Ps-BBOX sequence contained an N-terminal hexa histidine tag (His-Tag) with an *N*-terminal thrombin protease cleavage site.

The ps-BBOX plasmid was transformed into the *E. Coli* BL21 cell line using the heat shock method. Initially, 2 μL of the IPNS vector solution (~50 ng/μL) was mixed with 20 μL of *E. coli* (BL21) solution, and after incubation in ice for 20 minutes, the cells were shocked at 42 °C for 15 seconds (known as heat shock). The cells were dissolved in 200 μL of nutrient rich SOC medium (New England Biolabs, USA). Subsequently, the cell mixture was incubated at 37 °C for 45-60 minutes to initiate expression. The cell mixture was then grown on a 2YT (2x yeast extract tryptone) agar plate containing 50 mg/L kanamycin, and the plate was incubated at 37 °C overnight. Single colonies from grown 2YT agar plates were picked to inoculate 100 mL of a starting culture (2YT medium, 50 mg/L kanamycin). The starting culture was then incubated overnight at 37 °C with shaking at 180 rpm. The grown starting culture was then diluted into 6 L of the larger scale medium (with 1:10 v/v ratio). The large-scale media were incubated at 37 °C and the cell growth was checked via measuring optical density at 600 nm (OD_{600}). Once the OD_{600} had reached 0.8, β-D-1-thiogalactopyranoside (IPTG) was added to the media to a final concentration of 500 μM. Subsequently, the cell cultures were incubated at 18 °C for at least 18 hours with shaking at 180 rpm. The cells were harvested via centrifugation (11000 g, 8 min, 4 °C) and the collected pellets were stored at -80 °C.

To purify ps-BBOX, 25 g of cell pellets were resuspended in binding buffer A containing 50 mM Tris, 200 mM NaCl, and 5 mM imidazole at pH 7.5 (1:5 w/v ratio). Small quantities of DNAase I, phenylmethylsulfonyl fluoride, and lysozyme were added to the resuspended cell mixture. The cell mixture was then stirred for 20 minutes at room temperature, then for 20 minutes at 4 °C. Subsequently, the cells were lysed via sonification (60% amplitude, 9.9 s pulse on, 9.9 s pulse off, 16 minutes total time). The lysed cells were centrifuged (58000 g, 30 min, 4 °C) and the supernatant was filtered using a 0.45 μM filter.

The filtered cell lysates were loaded onto the nickel His-Trap column (5 mL HisTrap HP, GE Healthcare, USA) that had been pre-equilibrated with 25 mL (5 CV) of binding buffer A. Subsequently, the column was washed with 100 mL (20 CV) of binding buffer A to remove any unbound proteins and small molecules from the lysate. Then ps-BBOX was collected via eluting the column with a linear gradient from buffer A to 100% buffer B (in 20 CV) containing 50 mM Tris, 200 mM NaCl, and 500 mM imidazole at pH 7.5. The fractions showing UV absorption at 280 nm in the nickel his-trap chromatogram were analyzed by SDS-PAGE. The fractions showing ~46 KDa molecular weight proteins (corresponding to ps-BBOX) were collected, and concentrated using 10000 molecular weight cut-off (MWCO) spin concentrators (Merck Millipore, USA) at 3000 g and 4 ^{o}C. To reduce the imidazole concentration in the protein sample, the solution was spin-concentrated down to ~3 mL volume. The concentrated protein sample was then diluted to 15 mL with binding buffer A. The mixture was spin-concentrated to ~7 mL and topped up with buffer A to 15 mL. The final mixture was treated with thrombin protease overnight at 4 ^{o}C to cleave the N-terminal hexa-histidine tag.

The cleaved hexa-histidine tag and the thrombin protease was removed from the ps-BBOX sample using reverse His-trap method. Thus, the ps-BBOX mixture was applied to the nickel affinity column (5 mL HisTrap HP, GE Healthcare, USA) pre-equilibrated with buffer C (50 mM Tris, 200 mM NaCl, and 20 mM imidazole at pH 7.5) and the flowthrough was collected (W1). The column was then washed four times (1CV each step) with buffer C and fractions (W4-W5) were collected. The column was then eluted twice (1 CV each step) with elusion buffer B and the eluted fractions (E1, and E2) were collected. All fractions were analyzed by SDS-PAGE; relatively pure ps-BBOX was observed in the W1 and W2 fractions. The W1 and W2 fractions were collected and spin concentrated via centrifugation (10000 MWCO, Merck Millipore, USA) at 3000 g and 4 ^{o}C to give a ~4 mL volume. The concentrated protein solution was then loaded into dialysis cassette (4-12 mL capacity, 10000 MWCO, Thermo Scientific) that had been pre-saturated with buffer D (50 mM Tris, 200 mM NaCl, 50 mM EDTA, and 5 mM 1,10-phenanthroline at pH 7.5). The dialysis cassette filled with the protein solution was stirred in 400 mL of buffer D at 4 ^{o}C for two hours.

The dialyzed protein mixture was concentrated to 1.8 mL volume in a spin concentrator (10000 MWCO, Merck Millipore, USA) via centrifugation at 3000 g and 4 ^{o}C. The concentrated protein solution was applied to a Superdex 75 column (300 mL, GE Healthcare, USA) that had been pre-equilibrated with buffer E (50 mM Tris, and 200 mM NaCl at pH 7.5). The column was then eluted with 300 mL buffer E and the fractions showing relatively pure ps-BBOX (in SDS-PAGE) were collected. The collected ps-BBOX fractions were concentrated to ~50 mg/mL using spin-concentrators (10000 MWCO, Merck Millipore, USA) via centrifugation at 3000 g and 4 ^{o}C and stored at -80 ^{o}C.

4.3.2: BBOX NMR Studies

All turnover and binding experiments were performed using a Bruker Avance III 600 MHz spectrometer equipped with a 5 mm BB-F/^{1}H Prodigy N_2 cryoprobe. The NMR solutions for both binding and turnover assays were: 50 mM Tris-d_{11} buffer and 80 mM KCl at pH 7.50, and all samples contained 10% D_2O (v/v) to lock the signal. Standard Bruker 5mm tubes were used (500 µL sample volume). The PROJECT – CPMG pulse sequence (includes replicative [t-180$^{o}_{y}$-t-90$^{o}_{y}$-t-180$^{o}_{y}$-t]$_n$ pulses) [19] was used with 32 ms total CPMG time to supress protein broad resonances. The raw spectra were processed with an exponential window function (line broadening was set at 0.3) and the peaks were referenced using acetone methyl peak as internal standard (2.16 ppm). All NMR spectra were obtained at 298 K. The NMR data were analysed using Bruker topspin 3.6.5 (Bruker, Germany, www.bruker.com) and MestReNova 15.0.0 (MestReLabs, Spain, www.mestrelab.com). The ps-BBOX ligand binding assay (to obtain binding curves) and h-BBOX competitive binding assay were repeated at least three times.

4.4: References

[1] J. D. Hulse, S. R. Ellis, and L. M. Henderson. Carnitine biosynthesis. β-Hydroxylation of trimethyllysine by an a-ketoglutarate-dependent mitochondrial dioxygenase. *J. Biol. Chem.* **1978** 253, 1654–1659.

[2] G. Lindstedt. Hydroxylation of γ-butyrobetaine to carnitine in rat liver. *Biochemistry* **1967** 6, 1271–1282.

[3] G. Lindstedt, S. Lindstedt, and I. Nordin. Purification and properties of γ-butyrobetaine hydroxylase from Pseudomonas sp AK 1. *Biochemistry* **1977** 16, 2181-2188.

[4] S. Englard, J. S. Blanchard, and C. F. Midelfort. γ-Butyrobetaine hydroxylase: stereochemical course of the hydroxylation reaction. *Biochemistry* **1985** 24, 1110-1116.

[5] F. M. Vaz, and R. J. A. Wanders. Carnitine biosynthesis in mammals. *Biochem. J.* **2002** 361, 417-429.

[6] G. S. N. Naidu, I. Y. Lee, E. G. Lee, G. H. Kang, and Y. H. Park. Microbial and enzymatic production of L-carnitine. *Bioprocess Biosyst. Eng.* **2000** 23, 627–635.

[7] E. P. Brass, C. L. Hoppel, and W. R. Hiatt. Effect of intravenous L-carnitine on carnitine homeostasis and fuel metabolism during exercise in humans. *Clin. Pharmacol. Ther.* **1994** 55, 681–692.

[8] B. Z. Simkhovich, Z. V. Shutenko, D. V. Meirena, K. B. Khagi, R. J. Mezapuke, T. N. Molodchina, I. J. Kalvins, and E. Lukevics. 3-(2,2,2-Trimethylhydrazinium) propionate (THP)-a novel gamma-butyrobetaine hydroxylase inhibitor with cardioprotective properties. *Biochem. Pharmacol.* **1988** 37, 195-202.

[9] M. Dambrova, E. Liepinsh, and I. Kalvinsh. Mildronate: cardioprotective action through carnitine-lowering effect. *Trends Cardiovasc. Med.* **2002** 12, 275-279.

[10] C. Liao *et al.* Identification of BBOX1 as a Therapeutic Target in Triple-Negative Breast Cancer. *Cancer Discov.* **2020** 10, 1706-1721.

[11] I. K.H. Leung, T. J. Krojer, G. T. Kochan, L. Henry, F. von Delft, T. D.W. Claridge, U. Oppermann, M. A. McDonough, and C. J. Schofield. Structural and Mechanistic Studies on γ-Butyrobetaine Hydroxylase. *Chem. Biol.* **2010** 17, 1316-1324.

[12] L. Henry, I. K. H. Leung, T. D. W. Claridge and C. J. Schofield. γ-Butyrobetaine hydroxylase catalyses a Stevens type rearrangement. *Bioorg. Med. Chem. Lett.* **2012** 22, 4975-4978.

[13] H. K. Greenblatt, D. J. Greenblatt. Meldonium (Mildronate): A Performance-Enhancing Drug? *Clin. Pharmacol. Drug Dev.* **2016** 5, 167-169.

[14] A. M. Rydzik, R. Chowdhury, G. T. Kochan, S. T. Williams, M. A. McDonough, A. Kawamuraac, and C. J. Schofield. Modulating carnitine levels by targeting its biosynthesis – selective inhibition of γ-butyrobetaine hydroxylase. *Chem. Sci.* **2014** 5, 1765-1771.

[15] A. M. Rydzik, I. K. H. Leung, G. T. Kochan, M. A. McDonough, T. D. W. Claridge, Prof. C. J. Schofield. Oxygenase-Catalyzed Desymmetrization of N,N-Dialkyl-piperidine-4-carboxylic Acids. *Angew. Chem. Int. Ed.* **2014** 53, 10925-10927.

[16] A. M. Rydzik, I. K. H. Leung, G. T. Kochan, N. D. Loik, L. Henry, M. A. McDonough, T. D. W. Claridge, and C. J. Schofield. Comparison of the substrate selectivity and biochemical properties of human and bacterial γ-butyrobetaine hydroxylase. *Org. Biomol. Chem.* **2014** 12, 6354-6358.

[17] M. D. Shortridge, D. S. Hage, G. S. Harbison, R. Powers. Estimating protein-ligand binding affinity using high-throughput screening by NMR. *J. Comb. Chem.* **2008** 10, 948-958.

[18] J. A. Johnson, N. M. Olson, M. J. Tooker, S. K. Bur, and W. C. K. Pomerantz. Combined Protein- and Ligand-Observed NMR Workflow to Screen Fragment Cocktails against Multiple Proteins: A Case Study Using Bromodomains. *Molecules* **2020** 25, 3949.

[19] J. A. Aguilar, M. Nilsson, G. Bodenhausen and G. A. Morris. Spin echo NMR spectra without J modulation. *Chem. Commun.* **2012** 48, 811-813.

[20] A. Khan, R. K. Leśniak, J. Brem, A. M. Rydzik, H. Choi, I. K. H. Leung, M. A. McDonough, C. J. Schofield and T. D. W. Claridge. Development and application of ligand-based NMR screening assays for γ-butyrobetaine hydroxylase. *Med. Chem. Commun.* **2016** 7, 873-880.

[21] A. Khan. NMR Spectroscopy Studies of Enzyme Function and Inhibition. University of Oxford, **2016**.

[22] R. K. Leśniak, A. M. Rydzik, J. J. A. G. Kamps, A. Kahn, T. D. W. Claridge, C. J. Schofield. ^{19}F NMR studies on γ-butyrobetaine hydroxylase provide mechanistic insights and suggest a dual inhibition mode. *Chem. Commun. (Camb.)* **2019** 55, 14717-14720.

[23] Paramagnetism in Experimental Biomolecular NMR. C. Luchinat, G. Parigi, E. Ravera, Eds. *R. Soc. Chem., Camb.* **2018** 1-316.

[24] I. Bertini I, C. Luchinat, G. Parigi, R. Pierattelli. NMR spectroscopy of paramagnetic metalloproteins. *Chembiochem.* **2005** 6, 1536-1549.

4.5: Appendix 4.I

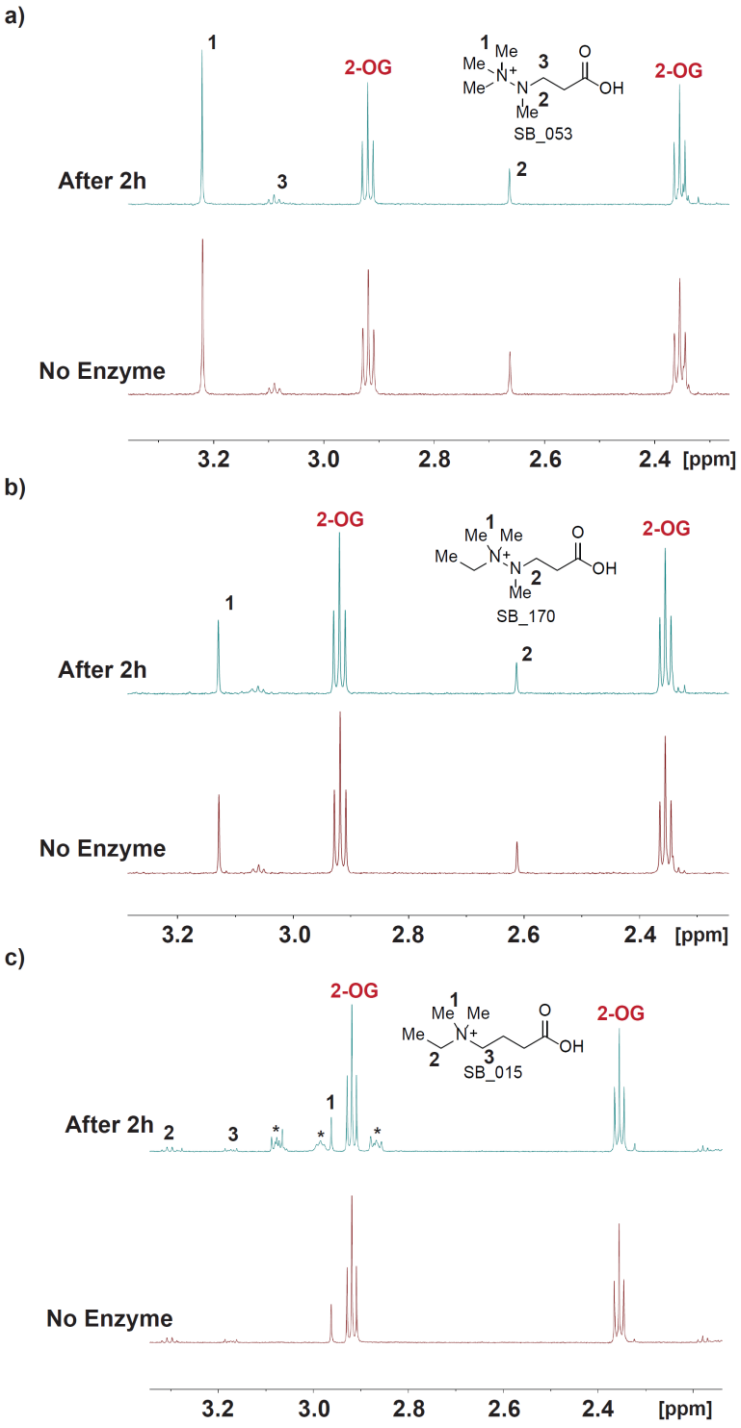


Figure Appendix 4.I: Turnover assay of the **(a)** SB_053, **(b)** SB_170, and **(c)** SB_015 with h-BBOX. The samples contained 50 μM substrate, 400 μM 2OG, 50 μM $Fe^{(II)}$, and 0.5 mM sodium L-ascorbate, and the reaction initiated via adding 50 nM h-BBOX. The corresponding peaks of h-BBOX impurities are labelled with asterisks.

4.6: Appendix 4.II

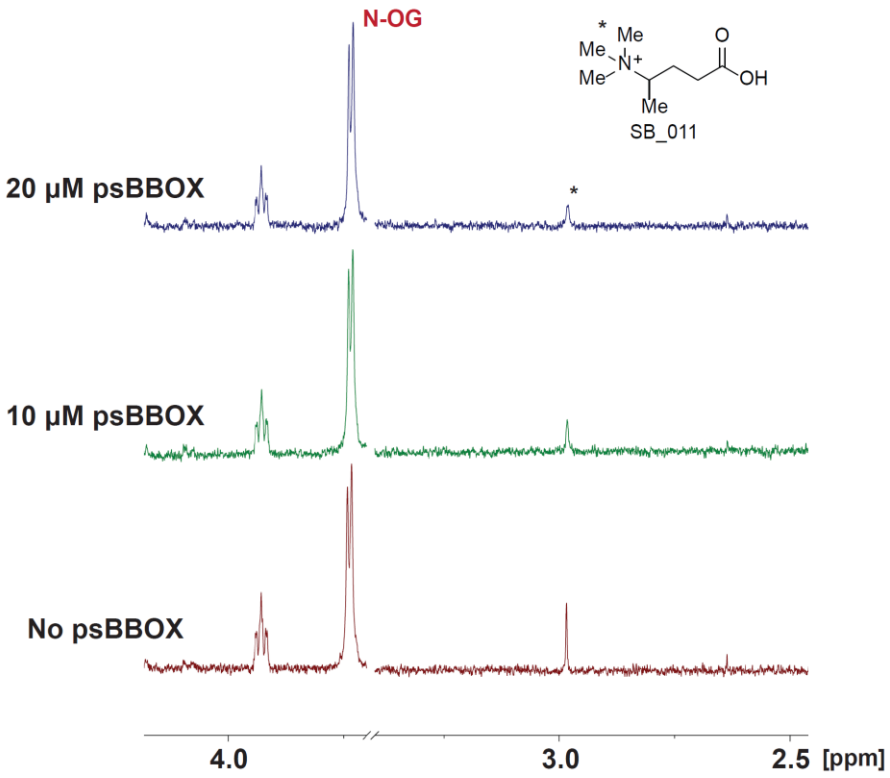


Figure Appendix 4.II: The binding assay of SB_011 with ps-BBOX. The first sample contained 10 μM SB_011, 700 μM N-OG, and 250 μM $Fe^{(II)}$, psBBOX was then added to the sample up to 20 μM concentration. SB_011 NMe_3 methyl peak is labelled with an asterisk.

Chapter 5: Summary of Results and Suggestions for Future Work

The results described in Chapters 2-4 concern experimental studies on two structurally related $Fe^{(II)}$-utilizing oxidizing enzymes – IPNS which catalyzes the key ring forming steps in the microbial biosynthesis of the penicillin antibiotics and BBOX which catalyzes the final step in the biosynthesis of L-carnitine, a molecule vital in lipid metabolism. The use of NMR spectroscopy was a unifying theme in terms of analytical studies carried out – protein observed NMR as described in Chapter 2 and small-molecule NMR as described in Chapter 3, where NMR studies were essential for assignment of product structures and, as described in Chapter 4, where NMR was used to inform on inhibitor binding to BBOX and mechanism of action.

5.1: Summary of Experiments in Chapter 2 and Future Work

Chapter 2 of the thesis describes expression trials of IPNS in different media and IPNS 2D protein NMR spectroscopy. The work aimed to optimize IPNS production using modern methods, with respect to producing labelled protein for protein observed NMR studies. Initially, the expression levels for recombinant IPNS in *E. coli* BL21 cell line were examined, using the pCOLD vectors. Optimization of cells grown in TB autoinduction media (with different concentrations from 35 g/L to 95 g/L) and 2YT media (with different IPTG induction levels up to 1000 μM) were carried out. IPNS was subsequently purified using nickel ion affinity chromatography resin and the expression levels were analyzed with SDS-PAGE (as shown in Figure 2.1 a). IPNS showed optimal yield in 2YT media with 500 μM IPTG applied during the induction phase. The so-optimized condition was further used for production of IPNS mutants, as described in Chapter 3.

Subsequently, IPNS expression in unlabelled and labelled minimal M9 media were examined (as detailed in Table 2.1). Uniformly ^{15}N labelled IPNS was produced (Section 2.2.2). ^{1}H-^{15}N HSQC spectra showed overlapping peaks in the central region (6.5-9.0 ppm and 110-125 ppm in ^{1}H and ^{15}N dimensions, respectively), in both samples containing IPNS:$Zn^{(II)}$:ACV (Figure 2.3) and IPNS:$Fe^{(II)}$:ACV (Figure 2.5). The superimposed HSQC spectra of IPNS:$Zn^{(II)}$:ACV and IPNS:$Fe^{(II)}$:ACV samples (Figure 2.6) showed almost identical peaks, indicating that the $Fe^{(II)}$ bound to IPNS and ACV is likely diamagnetic, consistent with previous studies [1]. Importantly substitution with $Zn^{(II)}$

does not significantly change the IPNS structure, meaning that studies on the IPNS:$Zn^{(II)}$:ACV complex can be carried out under aerobic conditions, something that is preferable from an ease of operation perspective.

To enhance the resolution in the HSQC spectra of IPNS, a TROSY-edited ^{1}H-^{15}N HSQC spectrum of ^{15}N labelled IPNS was obtained - this showed slightly better resolution (Figure 2.11). To further enhance the resolution, IPNS expression was investigated in ^{2}H and ^{15}N labelled M9 medium. The non-exchangeable protons of the resulting recombinant IPNSs were highly deuterated, an approach which can enhance spectroscopic resolution by minimizing dipole-dipole interactions with backbone NHs [2-4]. The TROSY-edited HSQC spectra of per-deuterated ^{15}N-labelled IPNS showed further enhancement in resolution compared to the non-deuterated IPNS (Figure 2.13). Therefore, the combination of protein per-deuteration and the TROSY effect can cooperatively minimize the peak overlapping, which could be helpful for IPNS NMR peak assignments for the future.

The procedures in Chapter 2 were used in the production of IPNS mutants as described in Chapter 3. Time limitations due to the pandemic and a desire to focus on the work described in Chapters 3 and 4, precluded further protein observed NMR work on wildtype IPNS. Nonetheless, the optimized methods described here will be useful for future NMR studies on IPNS in solution, including with respect to understanding dynamic motions induced by substrate binding and during catalysis as well as the effects of mutations and substrate analogues on the outcome of reactions, in the former case as described in Chapter 3.

5.2: Summary of Experiments in Chapter 3

Chapter 3 of the thesis describes studies focusing on the consequences of mutations on key residues of IPNS which are known to connect the IPNS active site motions with the motions in α-helix 3 at the surface (Figure 3.3) [5]. It was proposed that mutations of Ser_{281} would weaken the interaction between the ACV valine carboxylate and the edge of the active site, whereas mutations on Gln_{280} and Leu_{282} would disrupt the interactions between IPNS β-strand 11 and α-helix 3. In all mutants, higher flexibility was anticipated for the ACV valine residue, compared to WT IPNS, something which it was

envisaged could affect the kinetics or selectivity of IPNS catalysis. The desired expression vectors of the mutants (including S281A, S281T, S281C, Q280A_L282A, Q280A, and L282A) were prepared using polymerase chain reactions on the wildtype IPNS vector (Section 3.2.1) and the mutants were subsequently expressed and purified using the optimized methods described in Chapter 2.

Turnover of S281A_IPNS showed formation of a new product, because new methyl peaks were observed the CPMG edited ^{1}H NMR spectrum (Figure 3.7). LC-MS analysis showed two turnover-related products with m/z = 608.16 and m/z = 360.12 (Figure 3.10). To further characterize the new product structures, large scale turnover of S281A_IPNS was prepared and the products were purified using HPLC. The first isolated product (m/z = 608.16) was shown to have TCEP in its structure (NMR spectra shown in Figures 3.12 and 3.13) and, like the second isolated product (m/z = 360.12), showed a different ^{1}H NMR spectrum compared to IPN (Figure 3.14). It was hypothesized that S281A_IPNS forms a new product isomeric with IPN (as IPN has same m/z value), and the turnover with TCEP forms an adduct with m/z = 608.16. Therefore, large-scale turnover of S281A_IPNS was prepared without TCEP, which only formed the product with m/z = 360.12. Purification and structural characterization of the product with m/z = 360.12 revealed a structure with a thiazole ring (Figure 3.16). Therefore, S281A_IPNS formed a new product (isomeric to IPN) bearing a thiazole ring; turnover in presence of TCEP showed an additional product also with a thiazole ring, which was attached to TCEP. Figure 5.1 shows a scheme for S281A IPNS forming the new products in the presence and absence of TCEP.

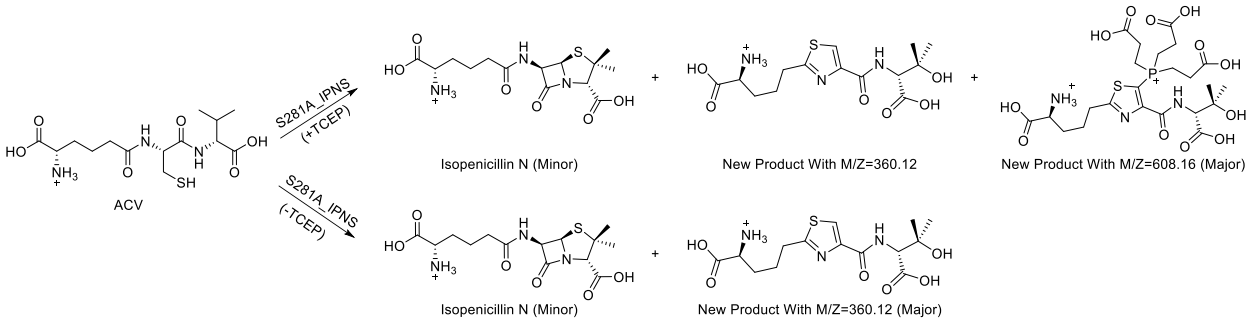


Figure 5.1: A scheme for reaction of S281A_IPNS with ACV, forming the new products bearing a thiazole ring. Isopenicillin N was formed as a minor product.

As shown in Section 3.2.8, other mutations on IPNS Ser_{281} residue (S281T and S281C in Figure 3.26) as well as mutations to the Gln_{280} and Leu_{282} residues (Q280A_L282A and L282A in Figure 3.28) showed evidence for formation of the new product with a thiazole ring. Further work on structures of the intermediates is desirable; if the results are validated they will support the hypothesis that increased or altered mobility of β-strand 11 and / or of the ACV valine group can alter the catalytic outcome.

Section 3.2.10 described time course studies of S281T_IPNS in the presence and absence of TCEP. Although repeats are desirable, evidence was presented (by ^1H NMR) that in turnover without TCEP, the ACV substrate valine is hydroxylated prior to the thiazole ring formation (Figure 3.34 a). An apparent intermediate (observed at early stages of turnover) with m/z = 378.13 was observed by LC-MS analysis (Figure 3.34 b). Therefore, the proposed intermediate appears to have a hydroxylated valine group (a structure is proposed in Figure 3.35); this intermediate can then convert into the product via loss of one H_2O. Time course study of the turnover in the presence of TCEP, gave LC-MS evidence for two intermediates with m/z values of 628.19 and 626.18 (Figure 3.36). It was also observed that TCEP reacts with one of the turnover intermediates, rather than the turnover product (Sections 3.2.11 and 3.2.12). Therefore, it is proposed that TCEP reacts with the intermediate containing an ene-thiol and hydroxylated valine group (m/z=378.13), as shown in Figure 3.39.

Considering the time course experiments and the nature of the mutations leading to altered IPNS catalysis, two possible mechanisms were proposed for the formation of the new products (Section 3.2.14). Both mechanisms involved altered pathways compared to WT IPNS after the thioaldehyde-forming step. In the first possible mechanism, the distal water molecule derived from the peroxide cleavage step converts the thioaldehyde into ene-thiol. In the second proposed mechanism, the distal water molecule forms a hydrated thioaldehyde. The first mechanism forms the previously described intermediate with ene-thiol and hydroxy valine groups. The second mechanism goes through an intermediate with thiazoline ring and hydroxyvaline group, also with expected m/z value of 378.13. Both proposed intermediates convert to the product with the thiazole ring via loss of an H_2O molecule. Figure 5.2 shows both proposed

mechanisms (named as A and B) starting from the thioaldehyde intermediate, which is assumed to be a branch point in altered catalysis pathway.

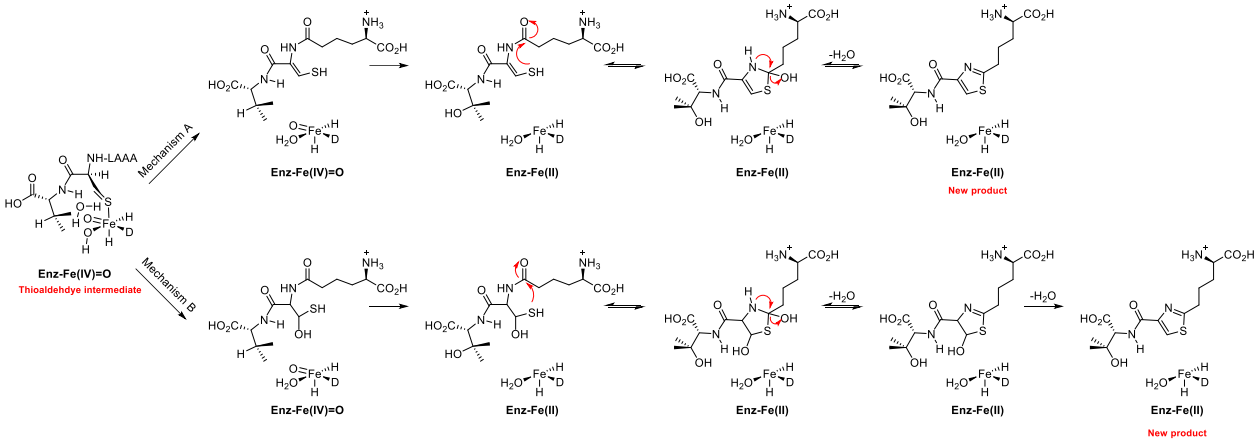


Figure 5.2: Proposed mechanisms (labelled A and B) of formation of the product with thiazole ring in catalysis of S281A_IPNS and other mutants forming the new product. The steps after thioaldehyde intermediate formation are shown. Note in both mechanisms the thiol S may (re)ligate with the Fe to enable ACV valine hydroxylation.

The S281A, S281C, and Q280A_L282A mutants of IPNS were crystallized in complex with $Fe^{(II)}$ and ACV under anaerobic conditions (by Dr. P. Rabe). The crystal structures revealed similar global structures when compared with WT_IPNS, with the notable exception that the residues observed in the C-terminal region were apparently 'truncated' in the mutants, implying that they did not adopt a fixed conformation (Figure 3.47). The latter observation is likely related to the increased mobility of ACV in the mutants, which in turn causes increased mobility of the C-terminal α-helix. Note that the ACV LAAA carbonyl group interacts with C-terminal Thr_{331} residue. Consequently, in all the IPNS mutants crystallized, poor electron density was observed in the C-terminal region making it impossible to build the model for the last amino acids. Previous work has shown evidence for mobility of the IPNS C-terminal region [6].

The active site structure in the mutants showed a different ACV binding mode compared to ACV structure in WT_IPNS, with a different valine orientation and with the ACV Cys thiol group facing away from $Fe^{(II)}$ (Figures 3.48, 3.49, and 3.50) . Interestingly, the S281C_IPNS active site showed two conformations of ACV, one was similar to the ACV structure in WT_IPNS, and the second was similar to the altered conformation as

observed in S281A and Q280A_L282A mutants. The latter observation is consistent with formation of both IPN and the new product (with a thiazole ring) as observed for S281C_IPNS turnover. These structures are also of interest because they show that substrates can bind to the IPNS active site without ligation to the $Fe^{(II)}$.

The combined results described in Chapter 3 are exciting because they demonstrate how apparently subtle modifications in the second coordination sphere can have profound effects on the outcomes of IPNS catalysis. To what extent the results are relevant from a general enzymology perspective is presently unclear. Modelling studies have provided evidence for correlated dynamic motions during catalysis by 2OG dependent oxygenases [7], throughout these studies it was assumed that the wildtype reaction was occurring, though potentially with altered kinetics. The results presented here suggest both active site and more distant mutations can have more dramatic effects. These can be studied in future work on 2OG dependent oxygenases and IPNS, in both cases by mutations in combination with substrate analogues. As described in Chapter 1, IPNS has been shown to accept multiple ACV analogues in some cases giving products with unexpected ring systems [8-13]. It will be interesting to combine these substrate analogues, as well as deuterated versions of ACV, with the mutants described here and others designed to alter conformational dynamics during catalysis.

5.3: Summary of Experiments in Chapter 4

Chapter 4 focuses on another $Fe^{(II)}$ dependent oxidizing enzyme, BBOX, which is 2OG dependent and catalyzes the final step in L-carnitine biosynthesis [14-16]. As BBOX has become a therapeutic target for myocardial infarction [17,18], a set of potent inhibitors and competitive substrates (by Dr. S. Basak) were tested for turnover and binding to BBOX. Amongst the compounds tested, SB_011 showed a hydroxylation reaction with both human (h-BBOX) and a *pseudomonas* BBOX (ps-BBOX) (Figure 4.4), and SB_015 showed hydroxylation with ps-BBOX but not with h-BBOX (Figure 4.5).

The binding affinities of the inhibitors towards ps-BBOX were examined using CPMG-edited ^{1}H NMR spectra. The obtained binding curves (Section 4.2.2) showed that substitution of the methyl groups in the γ-butyrobetaine substrate NMe_3 to a more hydrophobic group can enhance the protein binding affinity.

The binding mode of another potent inhibitor, N-acyl sulfonamide SB_133, was examined using competitive binding assays. It was observed that SB_133 can displace both 2OG and GBB, as a result of occupying both GBB and 2OG binding sites in both h-BBOX and ps-BBOX.

The collected observations on BBOX, further highlight the power of small-molecule NMR studies on enzymes to inform on modes of reaction and mechanisms of inhibition.

5.4: References

[1] V. J. Chen, A. M. Orville, M. R. Harpel, C. A. Frolik, K. K. Surerus, E. Munck, *et al*. Spectroscopic studies of isopenicillin-N synthase- a mononuclear nonheme Fe-2+ oxidase with metal coordination sites for small molecules and substrate. *J. Biol. Chem.* **1989** 264, 21677-21681.

[2] T. D. W. Claridge. High-Resolution NMR Techniques in Organic Chemistry. 3rd edition *Elsevier* **2016**.

[3] D. P. Frueh. Practical aspects of NMR signal assignment in larger and challenging proteins. *Prog. Nucl. Magn. Reason. Spectrosc.* **2014** 78, 47-75.

[4] K. Pervushin, R. Riek, G. Wider, and K. Wüthrich. Attenuated T_2 relaxation by mutual cancellation of dipole–dipole coupling and chemical shift anisotropy indicates an avenue to NMR structures of very large biological macromolecules in solution. *Proc. Natl. Acad. Sci.* **1997** 94, 12366-12371.

[5] P. Rabe *et al.*, X-ray free-electron laser studies reveal correlated motion during isopenicillin N synthase catalysis. *Sci. Adv.* **2021** 7, eabh0250.

[6] P. Rabe, C. C. Walla, N. K. Goodyear, J. Welsh, R. Southwart, I. Clifton, J. D. S. Linyard, A. Tumber, T. D. W. Claridge, W. K. Myers, and C. J. Schofield. Spectroscopic studies reveal details of substrate-induced conformational changes distant from the active site in isopenicillin N synthase. *J. Biol. Chem.* **2022** 298, 102249.

[7] R. Ramanan, S. S. Chaturvedi, N. Lehnert, C. J. Schofield, T. G. Karabencheva-Christova, and C. Z. Christov. Catalysis by the JmjC histone demethylase KDM4A integrates substrate dynamics, correlated motions and molecular orbital control. *Chem. Sci.* **2020** 11, 9950-9961.

[8] J. E. Baldwin, and M. Bradley. Isopenicillin N Synthase: Mechanistic Studies. *Chem. Rev.* **1990** 90, 1079-1088.

[9] J. E. Baldwin, R. M. Adlington, S. E. Moroney, L. D. Field, and H.-H. Ting. Stepwise Ring Closure in Penicillin Biosynthesis. Initial β-Lactam Formation. *J. Chem. Soc. Chem. Commun.* **1984** 15, 984-986.

[10] A. Daruzzaman, I. J. Clifton, R. M. Adlington, J. E. Baldwin, and P. J. Rutledge. The Interaction of Isopenicillin N Synthase with Homologated Substrate Analogues δ-(L-α-Aminoadipoyl)-L-homocysteinyl-D-Xaa Characterised by Protein Crystallography. *ChemBioChem* **2013** 16, 599-606.

[11] J. E. Baldwin, G. P. Lynch, and C. J. Schofield. Isopenicillin N Synthase: A New Mode Of Reactivity. *Tetrahedron* **1992** 48, 9085-90100.

[12] J. E. Baldwin, R. M. Adlington, B. P. Domayne-Hayman, G. Knight, and H.-H. Ting. Use of the Cyclopropylcarbinyl Test to detect a Radical-like Intermediate in Penicillin Biosynthesis. *J. Chem. Soc., Chem. Commun.* **1987** 1661-1663.

[13] A. J. Long, I. J. Clifton, P. L. Roach, J. E. Baldwin, P. J. Rutledge, and C. J. Schofield. Structural Studies on the Reaction of Isopenicillin N Synthase with the Truncated Substrate Analogues δ-(L-α-aminoadipoyl)-L-cysteinyl-glycine and δ-(L-α-aminoadipoyl)-L-cysteinyl-D-alanine. *Biochemistry* **2005** 44, 6619-6628.

[14] J. D. Hulse, S. R. Ellis, and L. M. Henderson. Carnitine biosynthesis. β-Hydroxylation of trimethyllysine by an α-ketoglutarate-dependent mitochondrial dioxygenase. *J. Biol. Chem.* **1978** 253, 1654–1659.

[15] G. Lindstedt. Hydroxylation of γ-butyrobetaine to carnitine in rat liver. *Biochemistry* **1967** 6, 1271–1282.

[16] S. Englard, J. S. Blanchard, and C. F. Midelfort. γ-Butyrobetaine hydroxylase: stereochemical course of the hydroxylation reaction. *Biochemistry* **1985** 24, 1110-1116.

[17] B. Z. Simkhovich, Z. V. Shutenko, D. V. Meirena, K. B. Khagi, R. J. Mezapuke, T. N. Molodchina, I. J. Kalvins, and E. Lukevics. 3-(2,2,2-Trimethylhydrazinium) propionate (THP)-a novel gamma-butyrobetaine hydroxylase inhibitor with cardioprotective properties. *Biochem. Pharmacol.* **1988** 37, 195-202.

[18] M. Dambrova, E. Liepinsh, and I. Kalvinsh. Mildronate: cardioprotective action through carnitine-lowering effect. *Trends Cardiovasc. Med.* **2002** 12, 275-279.